INTERACTION OF LIQUID DROPLETS WITH LOW-TEMPERATURE, LOW-PRESSURE PLASMA

A Thesis
Presented to
The Academic Faculty

By

Tony Lee Jones

In Partial Fulfillment
Of the Requirements for the Degree
Master of Science in Mechanical Engineering

Georgia Institute of Technology

May, 2005

INTERACTION OF LIQUID DROPLETS WITH LOW-TEMPERATURE, LOW-PRESSURE PLASMA

Approved by:

Dr. Said I. Abdel-Khalik, Chair
School of Mechanical Engineering
Georgia Institute of Technology

Dr. Minami Yoda
School of Mechanical Engineering
Georgia Institute of Technology

Dr. Sheldon M. Jeter
School of Mechanical Engineering
Georgia Institute of Technology

Date Approved: April 1, 2005

ACKNOWLEDGEMENTS

I would like to express my gratitude to all those who assisted me in this endeavor. First, I would like to thank my faculty advisor, Dr. Said Abdel-Khalik for his guidance and understanding as I worked through this project. His willingness to freely give of his expertise and life experience was essential and greatly appreciated. I would also like to thank the members of my thesis committee, Dr Minami Yoda and Dr. Sheldon Jeter for their advice and support. Their ideas and suggestions greatly enhanced this project.

I am especially grateful for the help, support, and advice I received from Dennis Sadowski. He always opened his door and went far beyond just doing his job. I would not have completed this work without him. I would also like to thank several members of the department staff. This project would not have been constructed were it not for the technical expertise and support of John Graham, Shop Manager; Vladimir Bortkevich, Electronics Lab Supervisor; and Kyle French, Electrical Engineer.

I would like to thank my laboratory colleagues for their willingness to help: Chad Dillon, Celine Lascar, and Vladimir Novak. I would especially like to thank Dr. Sam Durbin and Timothy Koehler for always providing a spare set of hands; great ideas; and, above all, encouragement.

Lastly, and most importantly, I would like to thank my wife and son for always being there with love and support despite the late hours and frustration that I at times brought home. They make me the man I am.

TABLE OF CONTENTS

LIST OF TABLES

LIST OF FIGURES

SUMMARY

In conceptual inertial fusion reactors, the chamber walls must be protected from the incident photons, ions, and neutrons that result from the target explosions. One way this can be accomplished is through a sacrificial liquid wall composed of either liquid jets or thin liquid films. The x-rays produced by the exploding targets deposit their energy in a thin liquid layer on the wall surface or in the surface of liquid jets arrayed to protect the wall. The partially vaporized liquid film/jet forms a protective cloud that expands toward the incoming ionic debris which arrives shortly (a few μs) thereafter. The charged particles deposit their energy in the vapor shield and the unvaporized liquid, thereby leading to further evaporation. Re-condensation of the vapor cloud and radiative cooling of the expanding plasma allow the energy deposited in the liquid to be recovered prior to the next target explosion (~ 100ms).

Chamber clearing prior to the next explosion represents a major challenge for all liquid protection systems, inasmuch as any remaining liquid droplets may interfere with beam propagation and/or target injection. Therefore, the primary objective of this research is to experimentally examine the interaction between liquid droplets and low-temperature, low-pressure plasmas under conditions similar to those expected following inertial fusion target explosions and the subsequent expansion. The data to be obtained in this research will be useful in validating mechanistic chamber-clearing models to assure successful beam propagation and target injection for the subsequent explosion.

A low-temperature, low-pressure plasma was created by evacuating a glass chamber containing two flat copper plates. The plates, when energized with a radio frequency (RF) generator, created a low-temperature (approx. 500-600°C), low-pressure (approx 1-40 Torr) plasma. A liquid droplet delivery system that could produce and introduce one to three drops into the plasma was developed and tested. Photographs can be taken at the top and bottom of the plasma inside the glass chamber to measure the change in droplet volume. A study of the droplet delivery system showed that repeatable drops of controllable volume could be produced at chamber pressures as low as 20 Torr. At the low end of the pressure range (about 20–50 Torr), the use of degassed water was required to avoid the formation of gas bubbles that interfered with reliable drop delivery; good control over the droplet generation was demonstrated in the 40-50 Torr range. In all cases, the plasma generation system was found to work extremely well for operating durations below 30 minutes; for longer operation times, overheating of the chamber components became a serious issue.

CHAPTER 1

INTRODUCTION

1.1 Motivation and Objectives

1.1.1 Fusion Power

Plasma, the fourth state of matter, is the most abundant form in existence in the universe. It rarely occurs naturally on the earth's surface but is evident every time a neon or fluorescent light is turned on. These everyday uses of plasma pale in comparison to its potential to be a relatively limitless supply of power. Fusion in plasma is the power source of the stars, including the Sun. In a fusion reaction, lightweight elements are combined at high temperatures and densities resulting in a release of energy typified by Einstein's famous equation, $E = mc^2$. The enormous gravitational forces of a star confine the plasma long enough for the fusion reaction to occur. On Earth, other approaches are required to contain the atoms until fusion may occur. In inertial confinement fusion, a tiny pellet of hydrogen isotopes is compressed and heated by intense energy beams so quickly that fusion occurs before the atoms can blow apart. The combination of deuterium (D) and tritium (T) is of particular importance given the relatively low input energy and the abundance of deuterium in the world's water supply. The inertial fusion energy (IFE) concept seeks to harness the energy released by igniting DT fuel capsules in a reactor chamber on a cyclical basis several times per second.

Beginning in 1994, the US Department of Energy declassified large portions of its inertial confinement research program, including the physics of indirect-drive targets. Figure 1.1 shows the basic steps to achieve fusion in an indirectly-driven IFE microexplosion. The DT fuel is contained in a high atomic weight shell known as a hohlraum. First, the inner surface of the hohlraum is rapidly heated with heavy-ion or laser driver beams; it, in turn, emits X-rays which heat the surface of the fuel. A rocket-like blowoff of high-pressure plasma is ejected from the fuel surface, forcing an inwardly focused compression wave propagating towards the center of the fuel. Ignition is achieved as the temperature and pressure near the center reach values of up to O(100 million K) and O(100 Gbar), respectively. After fusion is initiated at this central "hot spot," the thermonuclear reaction propagates radially outward into the remaining fuel. The process is similar for a direct drive IFE reaction except that the driver beams

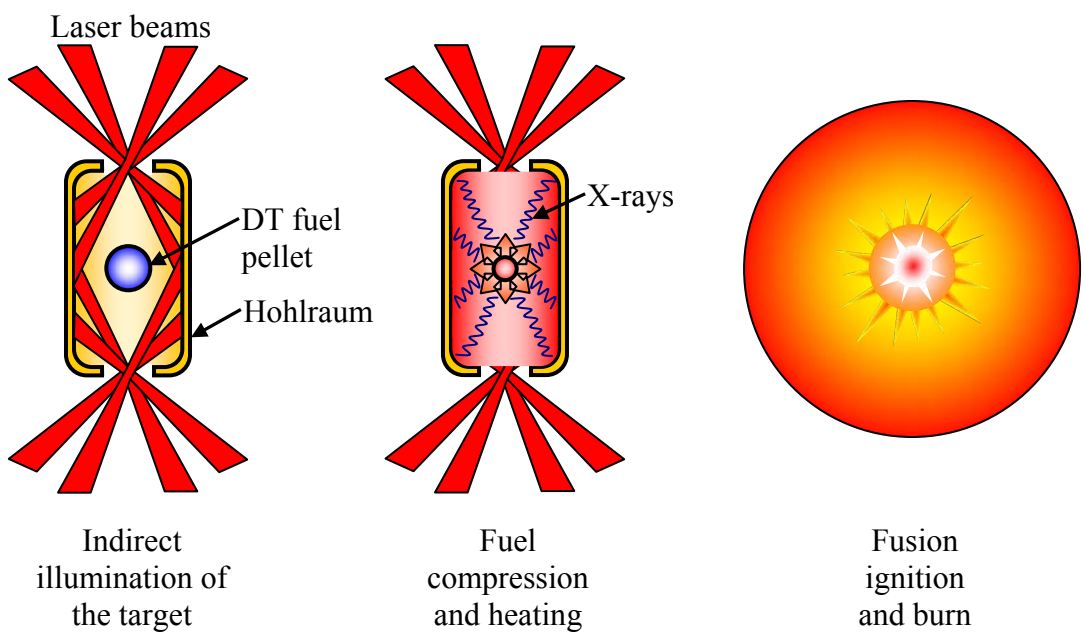

Figure 1.1. Illustration of the Indirect-Drive Ignition Process in IFE (Durbin, 2005).

illuminate the DT pellet directly. This type of driver requires a high degree of driver symmetry in order to assure a successful microexplosion.

The issue of chamber survival is of central importance for the successful commercial operation of an IFE power plant. Current target designs yield energy releases of O(100 MJ), a large portion of which (~30%) is composed of energetic X-rays and ions while the remainder is carried by the fusion neutrons. If exposed directly to the target threat spectrum, the chamber first walls would quickly deteriorate due to spallation (when a fast particle bombards a heavy atomic nucleus, some neutrons are "spalled," or knocked out, in a nuclear reaction called spallation) (Battelle, 2005), high thermal stresses, evaporation, and other mechanisms. Several ideas have been proposed to protect the first wall many of which involve a liquid barrier. Such liquid protection schemes require however, that the chamber be cleared of the barrier material, whether in the liquid, vapor, or plasma state; this issue, called chamber clearing, is addressed by this Master's thesis.

The DT fuel capsule ignition is an extremely precise event requiring exact timing and location. If a droplet of the protective fluid remained in the chamber there are several ways that successful ignition could be disrupted. Target trajectory would be affected should the target strike any drops of coolant during injection. The laser or ion beams could be attenuated or blocked, which could prevent ignition in either the direct or indirect driven systems. For direct drive systems, the presence of liquid droplets in the chamber could impact the illumination symmetry, thereby preventing target ignition. Thus the chamber must be cleared prior to each cycle. Several conceptual inertial fusion reactors are relying on the resulting plasma environment in the chamber core to

completely vaporize all fluid droplets and thus ensure chamber clearing through continuous vacuum pumping. Although plasmas and their properties have been studied since the later half of the nineteenth century, the majority of this work has been on the electrical and magnetic properties of plasma. The effects of plasma on a fluid droplet have to this point been looked at only theoretically. No experimental work has been done to determine how long a fluid droplet would survive in a plasma environment. The determination of how long a droplet will last is crucial to determine if in fact plasma can effectively clear all liquid from a given space and can thus provide an effective means of chamber clearing.

1.1.2 Objectives

The primary objective of this research is to experimentally examine the interaction between liquid droplets and low-temperature, low-pressure plasmas under conditions similar to those expected following inertial fusion target explosions and the subsequent expansion. The data to be obtained in this research will be useful in validating mechanistic chamber-clearing models to assure successful chamber clearing. This will require construction of a plasma chamber as well as a way to introduce a liquid droplet into the chamber. The change in volume of the droplet must be determined. First images are taken of the droplet as it enters the plasma and after exposure to the plasma. The volume of the droplet at any location can then be calculated from these images by assuming that the droplets are essentially axisymmetric and the two dimensional images are diametric slices of an ellipsoid.

The remainder of this thesis is organized as follows. Chapter 2 gives a brief overview of the literature available on liquid protection schemes in IFE and previous

investigations on interactions between droplets and vapor clouds. Chapter 3 describes the experimental apparatus used in this investigation, including developmental and discarded design options; and procedures used. Experimental results that were used in developing the apparatus are reported in Chapter 4. Chapter 5 summarizes the conclusions of this investigation and offers recommendations for future work and improvements to the test apparatus. Appendix A gives tables of the raw data. Appendix B contains tables of material properties used in selection of an appropriate test liquid. Appendix C contains the Matlab code which was used for image processing. Finally, details of the error analysis are included in Appendix D.

CHAPTER 2

BACKGROUND AND LITERATURE REVIEW

2.1 Chamber Wall Protection

Because of the great abundance of fuel and lack of harmful greenhouse gas byproducts, fusion energy has an immense potential for solving the world's growing energy needs. One of the key factors that determine the economic feasibility of a commercial fusion energy station is the issue of containing the plasma. Fusion energy has been under development for over 40 years, but it has not been demonstrated that an economically feasible power plant can be built; the small scale units that have been built to date are capable of only brief bursts of high power (Bova, 1971). One approach to confinement is the inertial fusion energy concept. Here, the fusion comes from bombarding a solid DT fuel capsule with laser energy or heavy ion beams. This results in a miniature thermonuclear explosion and creation of a plasma core which yields energy just as the sun does. The energy from the plasma is captured, the spent plasma is evacuated, and another cycle is begun. Although IFE lacks extensive research and development, the potential exists for production of a great amount of power. Therefore an increased interest and effort has been shown toward IFE research including construction of the National Ignition Facility (NIF) at Lawrence Livermore National Laboratory (LLNL).

The NIF, a facility with 192 lasers capable of delivering a collective 1.8 MJ of energy, is developing laser ignition technology for both commercial and military applications. However, there still remains much to be studied before a commercially feasible IFE power plant can be produced. A key issue to ensure a plant operating lifetime of at least thirty years is the development of a method to protect the first walls of the target chamber.

The energy released from the exploding DT pellet consists of x-rays, energetic neutrons, photons, and ionized debris that eventually deposit their energies on the chamber first wall. The energy deposition from the x-rays and charged particles takes place in a very thin layer of the first wall. This results in intense heating and if left unchecked results in rapid wall erosion from the photon and ion irradiation. The first wall must be protected from numerous destructive mechanisms including: evaporation, spallation, and macroscopic destruction resulting from shock wave destruction, high thermal stresses and intergranular pores explosion. A simple way to do this would be to make the reaction chamber large enough to reduce the radiation flux incident upon the chamber first walls. This is economically unfeasible as the capital costs and maintenance of such a huge device are prohibitive.

Another way of providing first wall protection is to use a liquid to shield the first wall from damaging radiation. Here, the x-rays deposit their energy in a liquid layer rather than on the wall surface as above which prevents destruction of the first wall. Currently, there are two proposed methods of producing a liquid shield: thick liquid jets or a thin liquid film.

2.2 Liquid Protection in Conceptual Fusion Power Plants

2.2.1 Thick Liquid Jet Protection in Fusion Power Plants

Thick liquid protection designs rely on arrays of stationary and/or oscillating jets to shield the chamber (Figure 2.1). Here, "thick" denotes that the characteristic length of the protective flows is greater than the mean attenuation length of the fusion neutrons. A

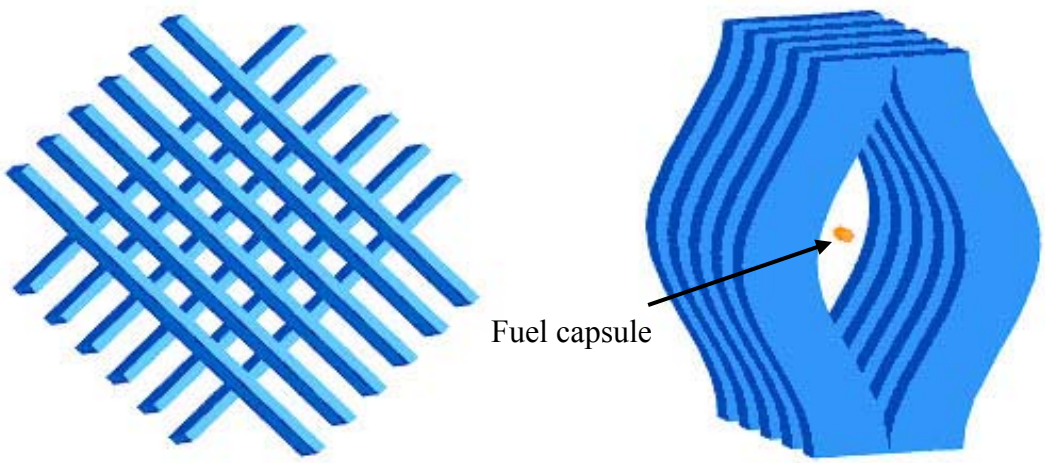

Figure 2.1. Sketches of Liquid Sheets Forming the Stationary Lattice (left) for Protecting the Front and Back Walls and the Array of Obliquely Oscillated Flows (Right) for Protecting the Sidewalls (Durbin, 2005).

neutronically thick blanket of liquid lithium or molten FLIBE (Li_2BeF_4) absorbs radiation (including neutrons) to protect the first wall, provide heat transfer, and breed tritium (a major component of fuel for IFE). The stationary lattice forms a protective grid through which drivers and targets may propagate while shielding the front and back walls of the chamber. The oscillating pocket provides shielding for the chamber sidewalls and dynamically clears the center of the chamber of debris prior to the injection of the next

fuel target. Annular and cylindrical jets have also been proposed as alternatives to liquid sheets (Maniscalco and Meier, 1977; Abbot, *et al.* 2001).

Burke and Cutting (1974) and Seifritz and Naegele (1975) were among the first to introduce the concept of using liquid jets as a "protective blanket". The High-Yield Lithium-Injection Fusion Energy (HYLIFE) reactor concept was described three years later in a formal design by Monsler, *et al.* (1978). Due to fire hazards associated with the liquid lithium coolant chosen for HYLIFE-I, a new design, HYLIFE-II, was developed. The HYLIFE-II power plant design proposed in Moir, *et al.* (1994) uses liquid sheets of molten Flibe (Li_2BeF_4) to form a protective pocket that allows target injection and driver propagation (Figure 2.2). Details of the first publications on HYLIFE-II were published

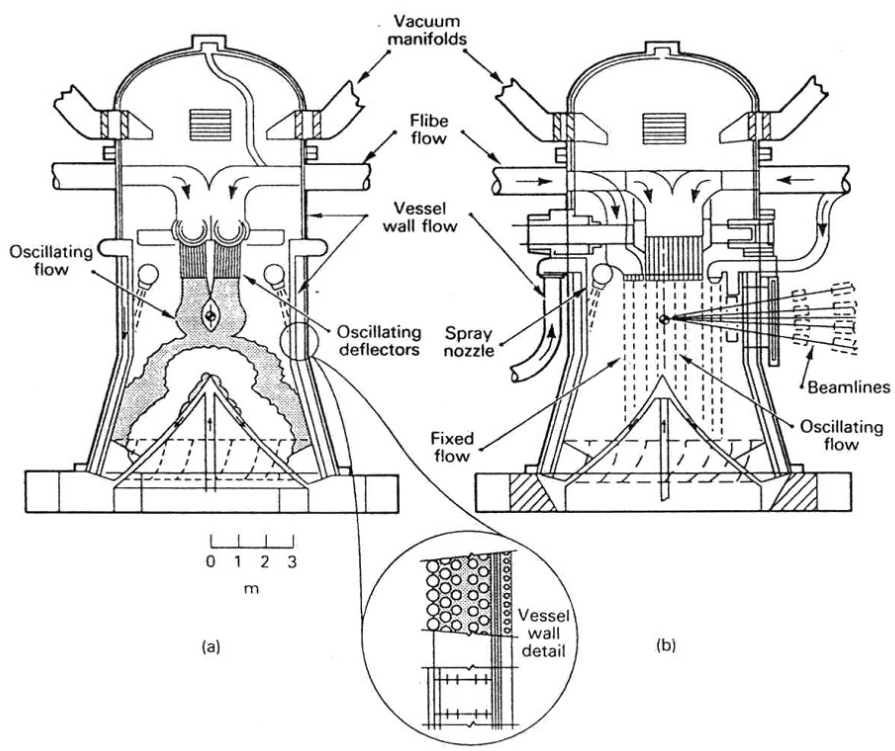

Figure 2.2. Orthogonal Views of the HYLIFE-II Reaction Chamber (Moir, *et al*., 1994).

by Moir, *et al.* (1991) and Moir (1992). While the original HYLIFE design was based on a target gain (defined as the ration between power output and power input) of 400 with a laser energy input of 4.5 MJ, the HYLIFE-II design is based on a moderate gain of 70 and a driver energy input of 5 MJ, assuming a heavy ion driver. This lower gain translates to a target yield reduction from 1800 MJ to 350 MJ and an increased pulse rate from 1.5 Hz to 6 Hz. Further information on the status of the HYLIFE-II development can be found in Moir, *et al.* (1994), Moir (1995), and House (1999). It has also been suggested that liquid first walls could be used in magnetic fusion reaction chamber designs (Moir, 1997). In a recent study, the advanced power extraction (APEX) study by Abdou, *et al.* (2001) confirmed the potential benefits of using liquid protection in an MFE reactor design.

Thick liquid protection has the potential of greatly reducing capital and operating costs by decreasing reactor chamber size and increasing chamber lifetime. However, there are issues involved with thick liquid protection. For maximum protection, the distance between jets must be minimized while still allowing driver propagation and target injection. This requirement means surface fluctuations of the liquid sheets must be minimized. Neutronics calculations for the HYLIFE-II lattice of slab jets show that, for final laser focus magnet lifetimes in excess of 30 years, a standoff distance between the jet free surface and the edge of the driver beam of only 5 mm is necessary (Latkowski and Meier, 2001). Experiments have also shown that this close surface tolerance is achievable (Durbin, 2005).

Durbin (2005) also looked at the turbulent breakup of the protective flows and resulting droplet generation which also pose a threat to driver and target propagation

inside the chamber. Droplets or jet fragments could prove catastrophic for heavy ion beam propagation given the close proximity described above. Figure 2.3 summarizes the clearance issues affecting beam-to-jet interfaces. Target trajectory and survival would also be affected should the target encounter any droplets of coolant in the chamber prior to ignition. Additionally, disruption of the jets due to the effect of the thermonuclear explosion provides another source of droplets within the chamber. Therefore, knowledge of the survivability of droplets in an environment closely simulating the chamber would be useful.

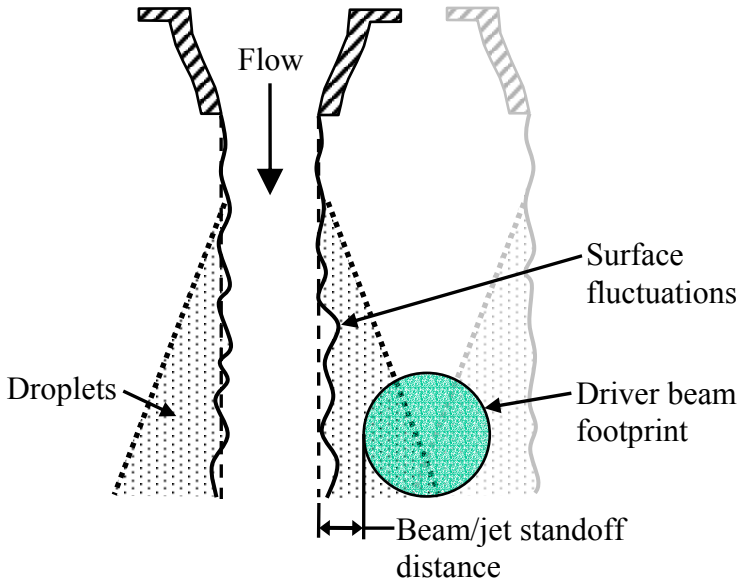

Figure 2.3. Illustration of Driver Interface Issues in Thick Liquid Protection. For Efficient Shielding the Beam/Jet Standoff Should Be Minimized without Causing Interference from Free-Surface Fluctuations and Droplets Due to Primary Breakup (Durbin, 2005).

2.2.2 Thin Film Protection in Fusion Power Plants

Numerous studies have been conducted (Abdel-Khalik and Hunter, 1978; Peterson, 1996; Peterson, *et al.,* 2002; and Peterson and Scott, 1996) to investigate the

thermal-mechanical effects of various target yields and target designs (*i.e.* spectra) on different wall materials. Additional studies have clearly shown a need for protecting the first wall (Raffray, *et al*., 2002; Mollendorff, *et al*., 1996; and Kulcinski, *et al*., 2002); thin liquid layers which do not significantly attenuate the fusion neutrons can adequately protect the first wall from the x-rays and ions produced by the explosion (Hassanein and Abdel-Khalik, 2002). Several designs have been proposed that employ a thin layer of liquid protection that covers the interior of the first wall. One of the first IFE wall protection proposals is the wetted porous wall concept, developed by Los Alamos in 1972 (Booth, 1972; and Williams, *et al*., 1974). Latter designers also utilized this technique. Hiball (1981) employed a wetted wall concept in a heavy ion beam fusion reactor. A wetted porous wall liquid protection scheme was proposed in the OSIRIS reactor design, which consisted of a chamber first wall of porous carbon fabric with a layer of Flibe seeping along the inner surface (Bourque, *et al.*, 1992). PROMETHEUS-L was a laser-driven design, while PROMETHEUS-H was a heavy-ion-driven design, both of which used a similar protection scheme consisting of a thin film of liquid lead to protect a porous SiC first wall (Waganer, *et al*., 1992; Abdou, *et al*., 1993; and Waganer, 1994). Table 2.1 and Figure 2.4 show a summary of design parameters in the Prometheus-L/H designs as well as a 3-D model of the original thin liquid film protective scheme.

An essential element of thin layer protection schemes is the characterization of the target yield and spectrum. Both indirect and direct driven target designs can be analyzed. Reactor chamber designs with dry walls are subjected to x-ray and charged particle spectra to determine the requirements for shielding. Reactor chamber designs with dry

Table 2.1 Comparison of the Design Parameters of the Prometheus-L/H Conceptual Reactor Designs (Abdou, *et al*., 1993; Waganer, 1994; and Osirus Report, 1992).

Design Parameter	Prometheus-L	Prometheus-H
Total pellet yield, [MJ]	497	719
X-ray yield, [MJ]	31	46
Ionized debris yield, [MJ]	107	159
Repetition rate, [Hz]	5.6	3.6
Cavity radius, [m]	5	4.5
Cavity height, [m]	5	4.5
Cavity surface area, [m^2]	471	382
Cavity volume, [m^3]	916	668
Non-condensable gas pressure (273 K), [Pa]	1.5	1.5

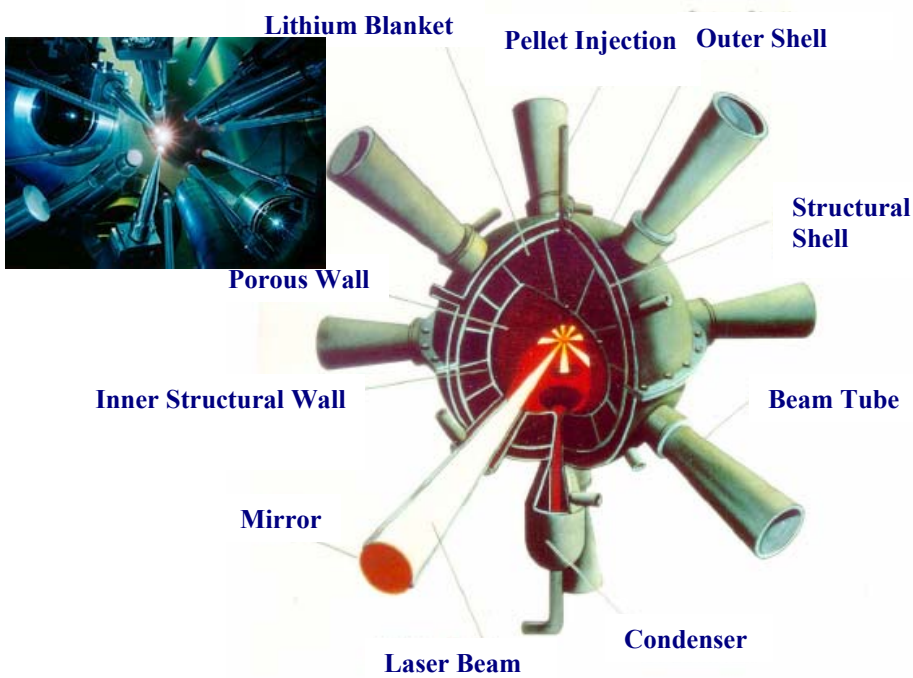

Figure 2.4 Conceptual 3-D Model of the Original Thin Liquid Film Protection Scheme for the Inertial Fusion Energy IFE System and Close-Up of the DT Implosion Process (Mollendorff, *et al*., 1996; and Hiball, 1981).

walls subjected to the x-ray and charged particle spectra represent a reference for the required shielding by thin liquid film protection. Therefore, dry wall chambers with direct drive targets were analyzed (Raffray, *et al*., 2002; Mollendorff, *et al*., 1996; and Kulcinski, *et al*., 2002) by investigating target heating which gives an indication of upper limits on chamber gas as well as chamber wall temperature (Abdel-Khalik and Hunter, 1978; Peterson, 1996; Peterson, *et al*., 2002; and Peterson and Scott, 1996). Incident energy and particle fluxes were calculated and the thermal responses reported in several studies (Raffray, *et al*., 2001; and Renk, *et al*., 2003). Figure 2.5 and 2.6 show the detailed spectrum and temperature response for the direct drive target. These figures give an indication of the severity of the conditions that an unprotected wall would be subjected to and the depth of protection layer required.

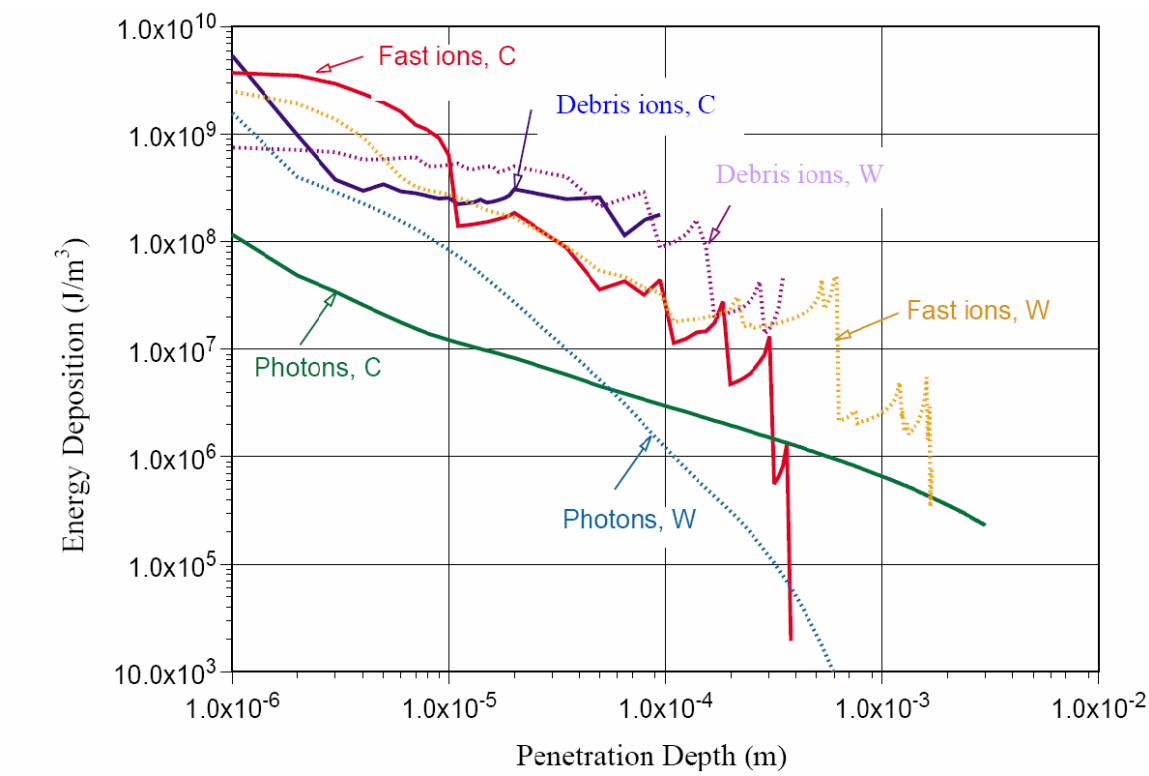

Figure 2.5 Photon and Ion Attenuation in Carbon (C) and Tungsten (W) for Direct-Drive Spectra without Protective Chamber Gas (Raffray, *et al*., 2001).

For indirect drive targets, the penetration depth of the charged particles is thinner, and thus the thermal response may exceed the limiting sublimation temperature for many of the commonly proposed wall materials such as carbon and tungsten. Figure 2.7 shows the attenuation of charged particles in carbon and tungsten targets for indirect drive spectra with no wall protection. Thus the thin liquid wall protection provides the required protection to allow chamber survival at practical sizes.

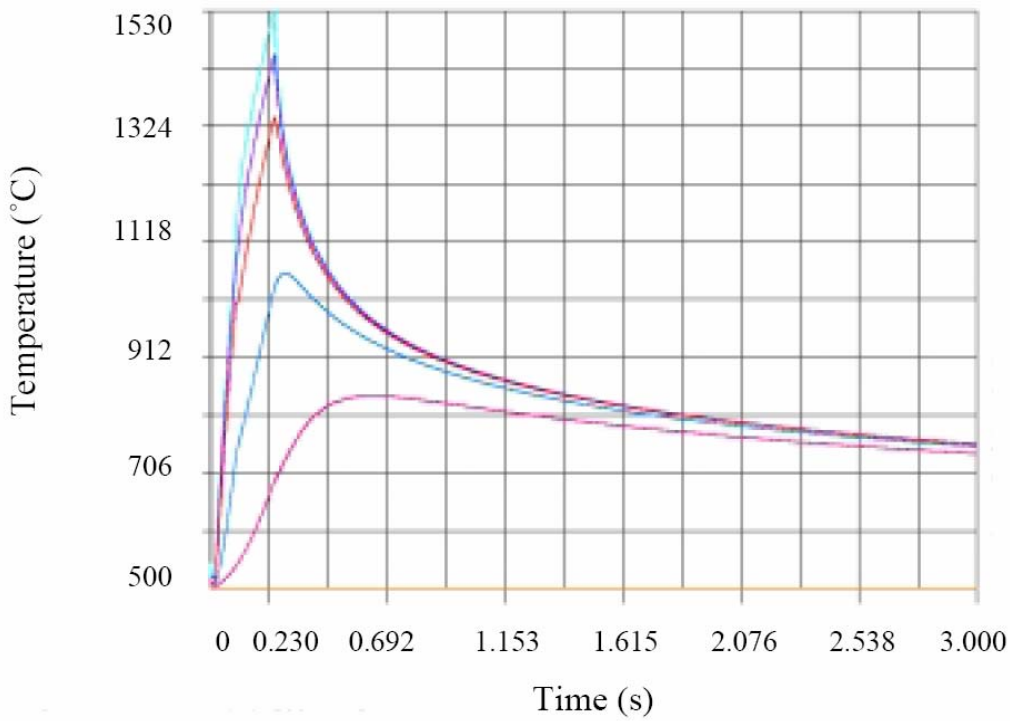

Figure 2.6 Temperature Histories for Carbon Flat Wall Under Energy Deposition from Direct Drive Spectra without Protective Chamber Gas (Raffray, *et al*., 2001).

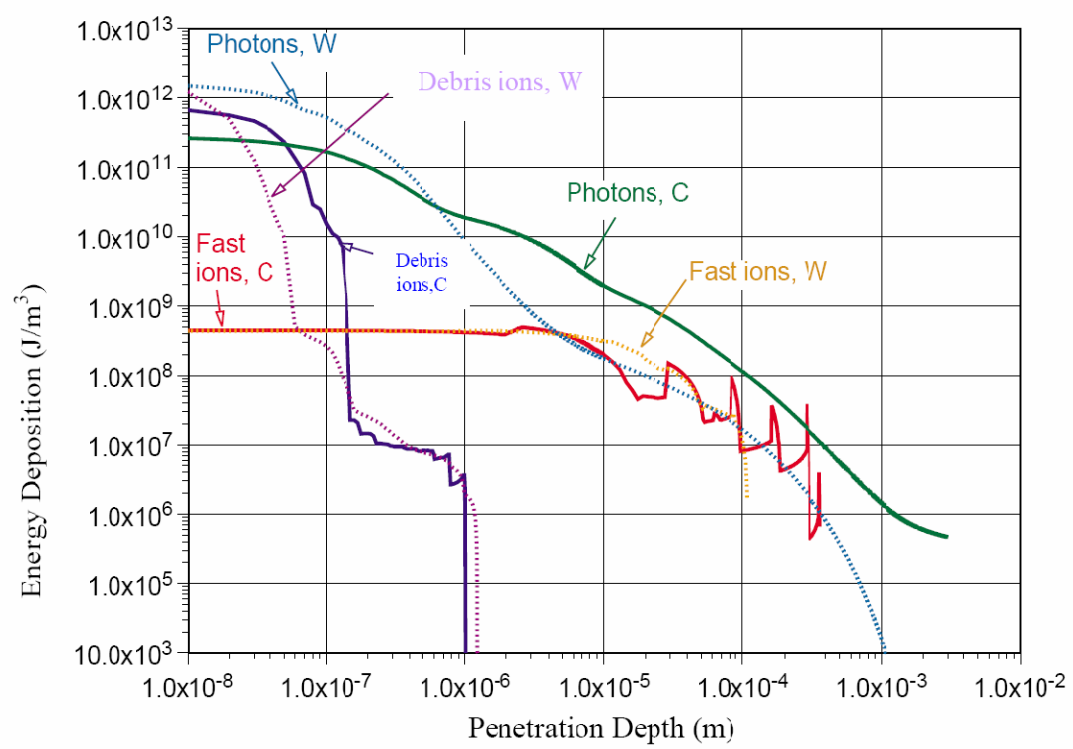

Figure 2.7 Photon and Ion Attenuation in Carbon (C) and Tungsten (W) for Indirect-Drive Spectra without Protective Chamber Gas (Raffray, *et al*., 2001).

Waganer, *et al*. (1992) introduced in the Prometheus-L study a novel concept of a thin (0.4-0.6 mm) film of liquid lead that is injected through a porous first wall of silicon carbide. Lead was chosen because its high-Z nature resulting in efficient photon attenuation. The x-rays produced by exploding targets deposit their energy in the thin liquid surface layer. The partially vaporized liquid film forms a protective cloud that expands toward the incoming ionic debris which arrives shortly (a few μs) thereafter. The charged particles deposit part of their energy in the vapor shield and the remaining energy (20-200MJ) is deposited in the remaining film, thereby leading to further evaporation. Re-condensation of the vapor cloud and radiative cooling of the expanding plasma allow the energy deposited in the liquid to be recovered prior to the next target explosion

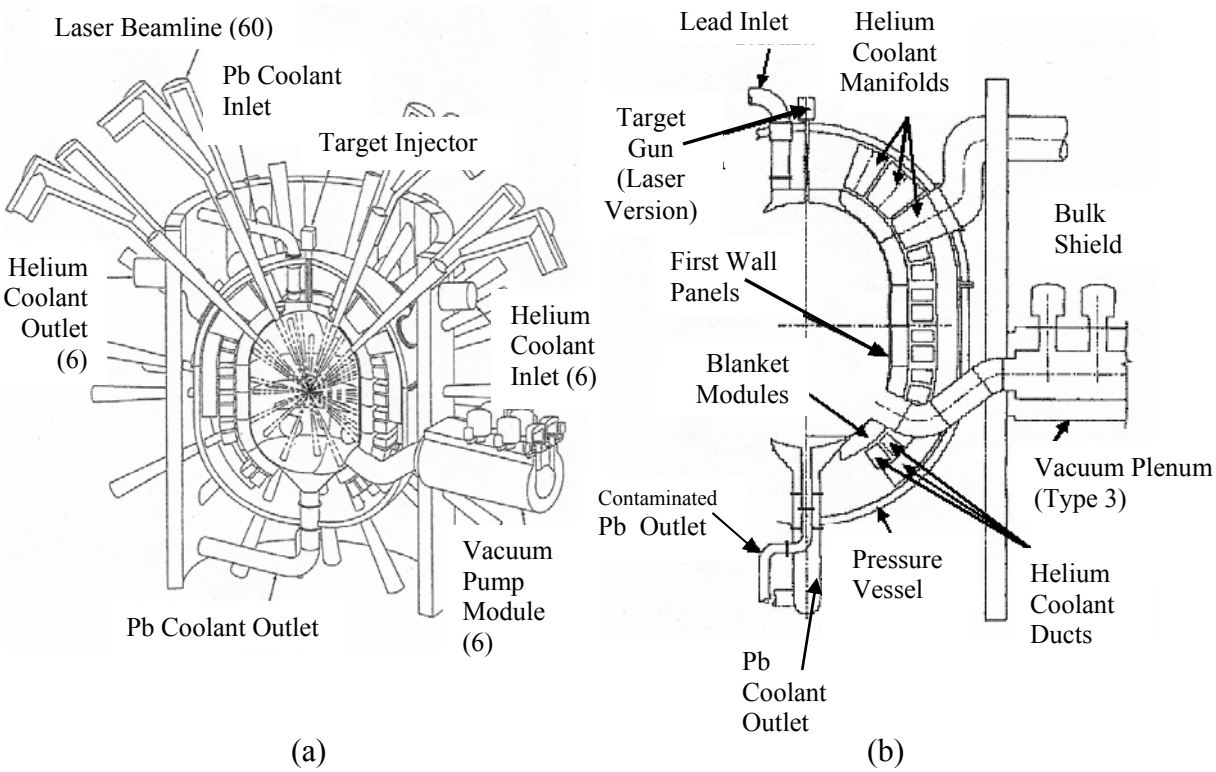

Figure 2.8 Conceptual Model of the Prometheus-L Thin Liquid Protection Scheme for the Inertial Fusion Energy IFE System: (a) Three-Dimensional Model, and (b) Two Dimensional Section (Williams, *et al.*, 1974; and Waganer, *et al.*, 1992).

(~100ms). This occurs over a relatively longer time period which limits first wall heating, degradation, and thermal stresses. Figure 2.8 is a conceptual model of the Prometheus-L fusion laser reactor chamber.

2.2.3 Chamber Clearing

In the HYLIFE-II design, the oscillating pocket attempts to address the issue of chamber clearing. However, the potential still exists for droplets from the clearing jets themselves to form an aerosol in the chamber. Additionally, to completely clear the chamber core, the jets would impact each other and their separation could cause droplets to remain in the core. With the thin liquid concept, droplets falling from the upper end

cap of the chamber could disrupt the target introduction as well as attenuate the driver beams. Also, the presence of droplets from the microexplosion exists as there is no way to dynamically clear the chamber with a thin liquid film; vacuum pumping at rates equivalent to the removal of the entire chamber volume between explosions would be energetically prohibitive. With either, thick liquid jet or thin film protection, the potential exists for liquid droplets to be present in the chamber. The liquid vapor outside of the chamber core will recondense, but it will do so either on the first wall or on the jets themselves, where the temperature is much lower. To completely clear the chamber, all of the liquid in the chamber core will have to be completely evaporated in the explosion and resulting plasma field. If this occurs, then the chamber is cleared and the next target is successfully introduced and the laser/ion beams can propagate.

The question of chamber clearing has been recognized and studies have been done to determine the dynamics of a single droplet of a liquid metal in an "infinite" vapor media, *i.e.*, plasma (Konkashbaev, *et al.*, 2003). These studies have determined that the droplet may actually survive for a time that exceeds the time between explosions (~100ms). Figure 2.9 shows the results of simulations on a lead droplet with an initial radius of 10 microns. The curves in the figure show the relative values of droplet radius (R/R_0), temperature (T_{out}/T_{out0}), pressure difference ($\Delta P = 1-P_{out}/P_{in}$), flux difference ($\Delta S = 1-S_{out}/S_{in}$), and heat flux difference ($\Delta W = 1-W_{out}/W_{in}$) given as a function of time. Of key note is the fact that after 100 ms, the radius has decreased by only 0.2%. If these simulations are accurate then the presence of plasma in the chamber core cannot solely guarantee chamber clearing prior to introduction of the next target.

$R_0 = 10$ micron, $T_0 = 800$ K, $P_0 = 0.1$ Torr

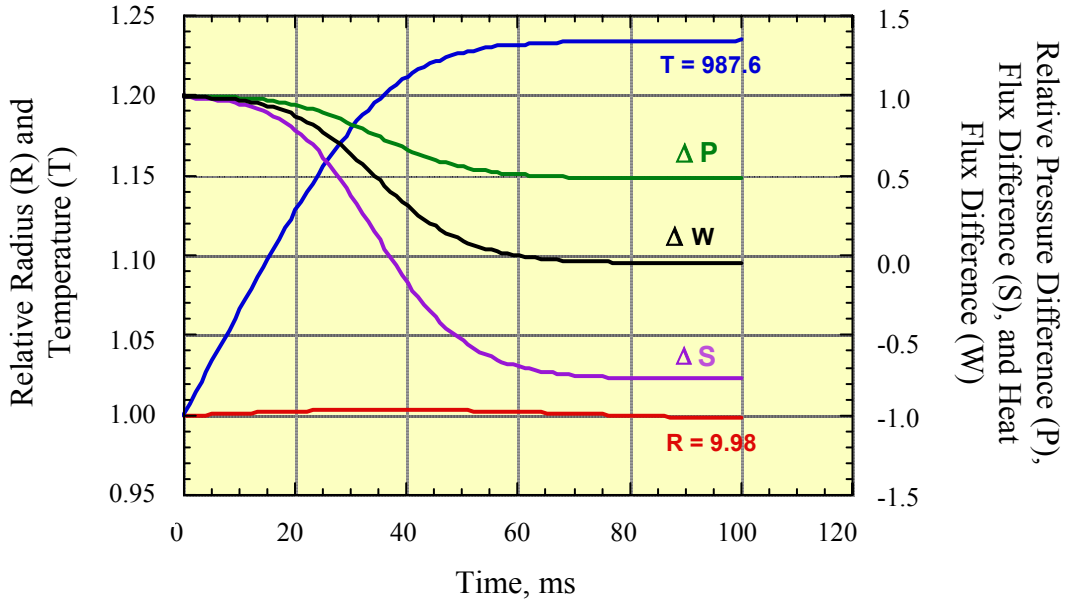

Figure 2.9 Simulated Properties of Pb Droplet in Pb Plasma (Konkashbaev, *et al*., 2003).

Both methods (thick liquid jets and thin films) of first wall protection are susceptible to problems with liquid droplets preventing complete chamber clearing; further research is necessary to both validate the current models and provide information on the survivability of a liquid droplet in a plasma environment. Therefore, this investigation has been undertaken in order to provide the database necessary to validate chamber clearing models and provide data on droplet life.

CHAPTER 3

EXPERIMENTAL APPARATUS AND PROCEDURES

An experimental apparatus was designed, constructed, and instrumented to examine the behavior of single liquid droplets falling through a low-temperature, low-pressure plasma. The main functional requirements of the apparatus are to:

1) Create a sealed enclosure in which the plasma can be confined
2) Provide a system where the pressure inside the enclosure can be precisely controlled
3) Provide the means to create and steadily maintain the low-temperature, low-pressure plasma of different compositions
4) Provide a system for delivery of single liquid droplets with controlled sizes to the plasma, and
5) Provide the means to quantitatively measure the change in liquid droplet volume, due to evaporation, as it moves through the plasma.

This chapter will describe the experimental apparatus and procedures. First we will discuss the apparatus (Figure 3.1) and its development. We will discuss each portion of the apparatus in the order that it was built to include descriptions of unsuccessful attempts. The second portion of this chapter will then discuss procedures used in various experiments to test individual portions of the apparatus during development.

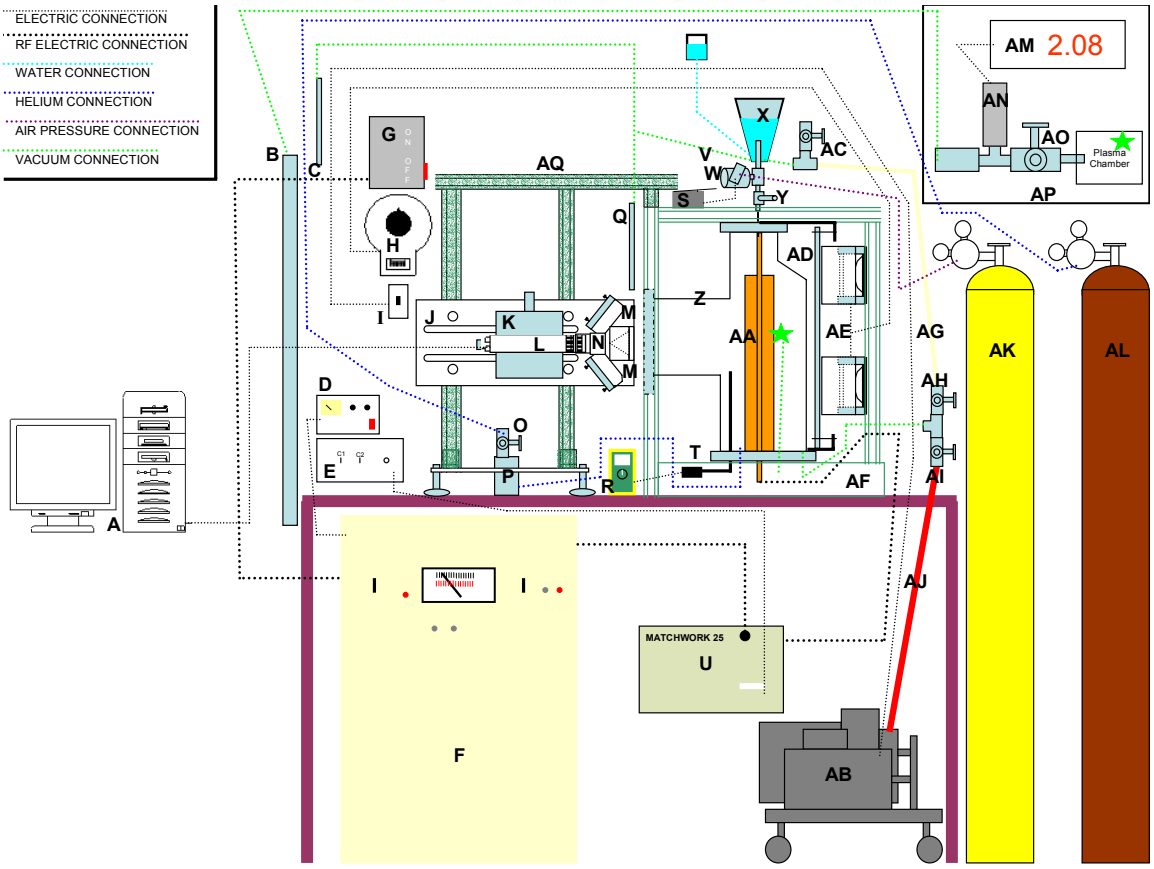

Figure 3.1 Complete Experimental Apparatus Schematic (Shown) and All Subsystem Schematics (AVI, 17M, jones_tony_l_200505_ms_Apparatus_Schematic.avi).

3.1 Experimental Apparatus

3.1.1 Vacuum/Pressure System

A detailed listing of the vacuum system components is found in Table 3.1. There are several key components of the vacuum/pressure system which are schematically shown in Figure 3.2. These consist of a T-shaped glass vessel which serves as the vacuum chamber, the vacuum pump, three plates used to seal the vacuum chamber, two pressure gauges, and several valves.

The three plates and the T-shaped glass vessel together form what is referred to as

Table 3.1. Detailed List of the Vacuum/Pressure System Hardware Components.

Item ID	Description	Manufacturer	Model	Serial number
B	MANOMETER 29 inch U-Tube Absolute Pressure Mercury Manometer	Meriam Instrument	11AA10WM	-
I	VACUUM PUMP SWITCH	-	-	-
O	L SERIES SHUTOFF VALVE	Swagelok	SS 4LA	-
P	LEAK VALVE	Granville-Phillips	Series 203	708221
Z	GLASS PLASMA CHAMBER	Unknown	-	-
AB	VACUUM PUMP	Welch Vacuum	DuoSeal1376	118
AH	SHUTOFF VALVE Stainless Steel Toggle Valve 1/4 in. Tube Fitting	Swagelok	SS-1GS4	-
AI	SHUTOFF VALVE	Mueller/B&K Ind	110-522	-
AJ	VACUUM HOSE	-	-	-
AL	COMPRESSED HELIUM TANK	Airgas	UN1046	S29217
AM	DIGITAL PRESSURE GAUGE READOUT UNIT	Digivac	200	-
AN	THERMOCOUPLE VACUUM GAUGE TUBE Mild Steel, 1/8 in NPT Thread	Varian	Type 0531	-
AO	SHUTOFF VALVE Stainless Steel 1-Piece Ball Valve 1/4 in. Tube Fitting/Angle Pattern	Swagelok	SS-42S4-A	-

the plasma chamber (Z). The glass vessel is approximately 17 in tall; the diameters of the open ends of the Tee are 6“ for the bottom and center of the Tee and 4” for the top, all of which are sealed by attaching 3 plates (Figure 3.3). Both the top and bottom plates are made of Bakelite in order to resist the high temperatures in the plasma chamber while the front plate (on the central leg of the Tee) of the plasma chamber is made of polycarbonate since it does not contact the plasma. All three plates were fabricated on site and all are clamped to the glass vessel through the use of a split ring and flange bracket. The seals

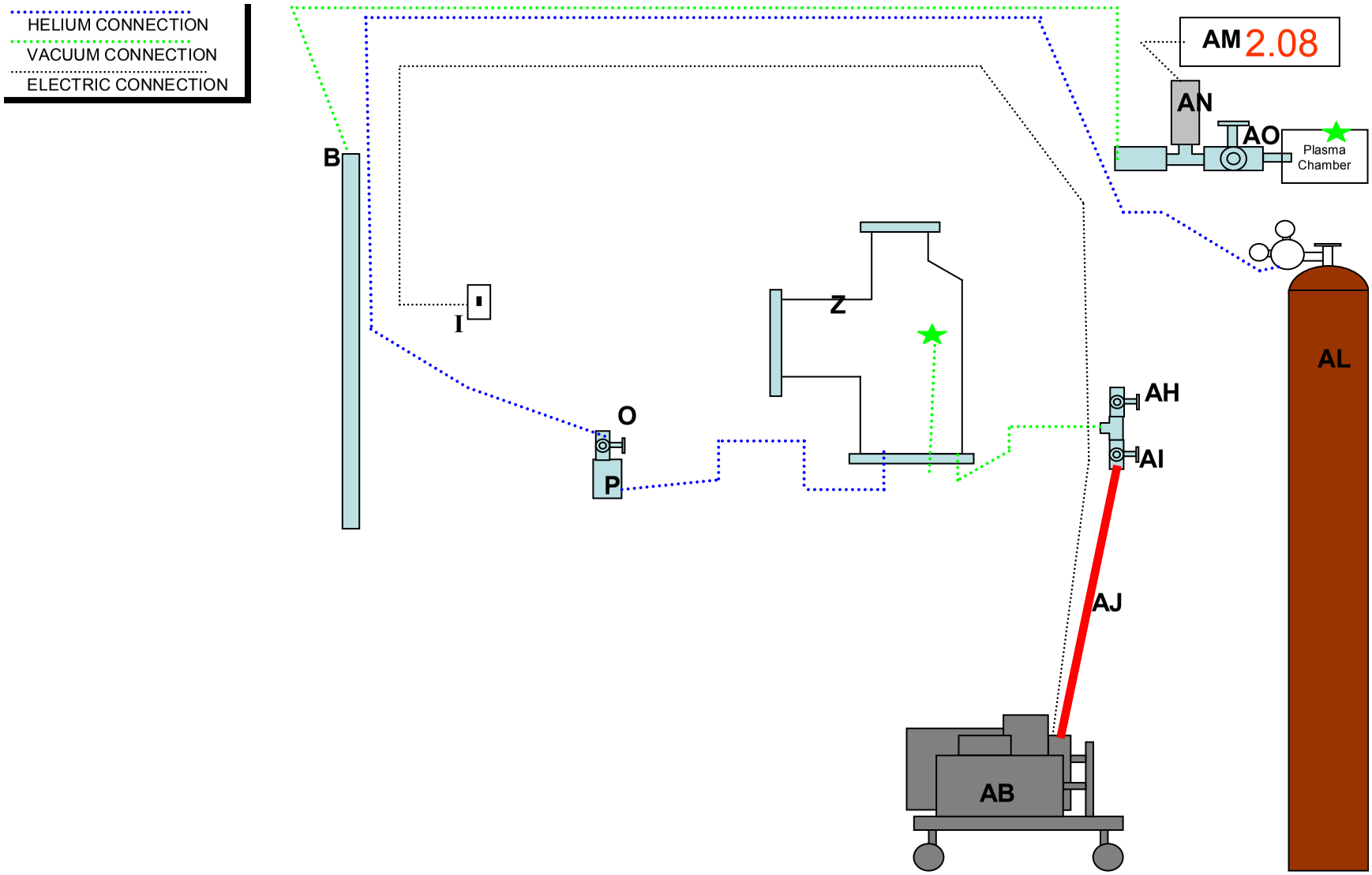

Figure 3.2 Vacuum / Pressure System Schematic.

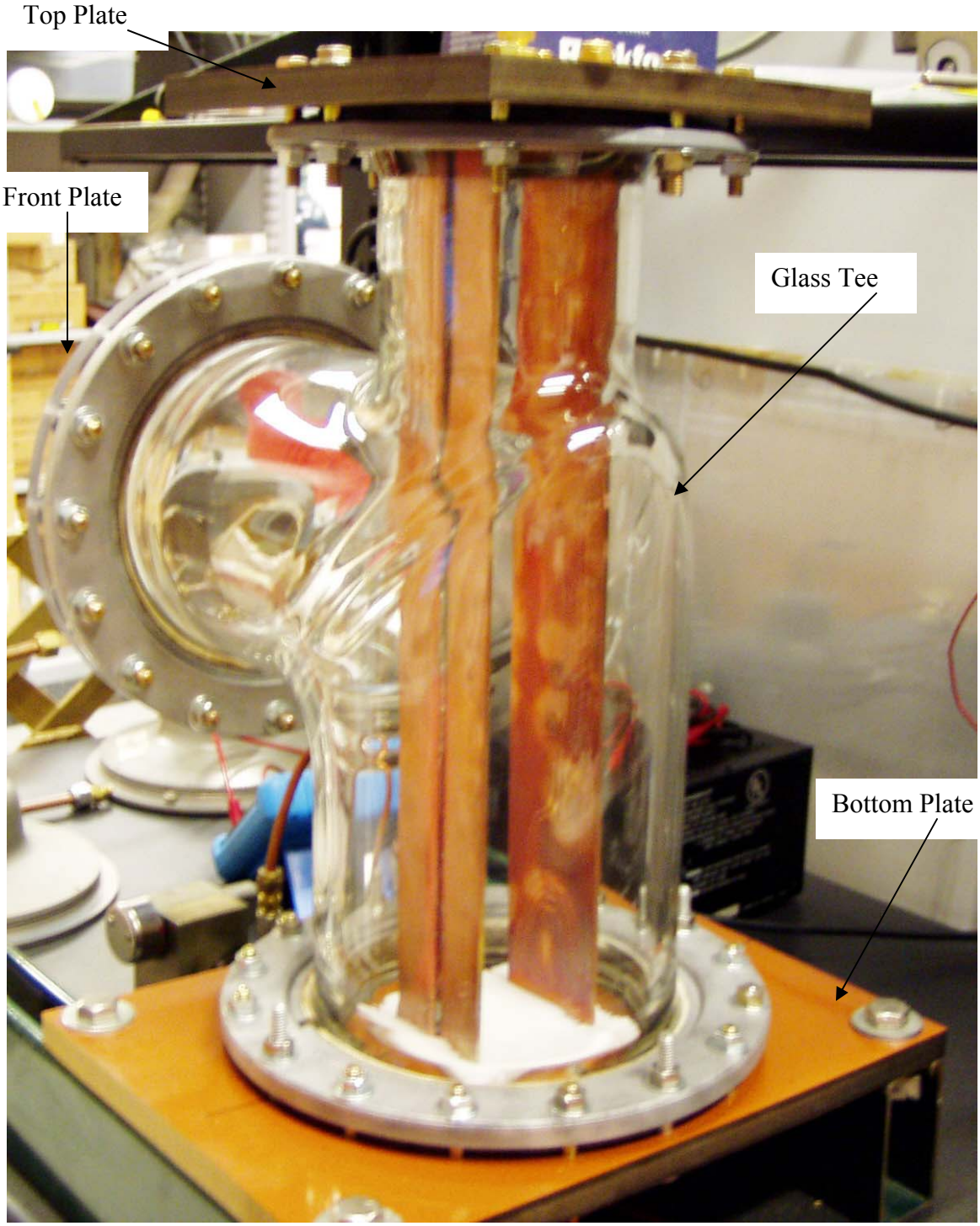

Figure 3.3 Plasma Chamber (Z) with All Components Annotated.

are made airtight through O-ring grooves which are cut into all three plates. Care was taken to ensure that the flange connections were tightened in a uniform manner to ensure that the O-ring was compressed about the entire seal. Additional care has to be given to the polycarbonate front plate as it began to crack due to over-tightening during the last month of the experiment.

The front polycarbonate plate has no ports on it and serves simply as a viewing window for the imaging system. The bottom plate has 6 holes through it; three of these are for the vacuum system connections, one hole is the primary draw for the vacuum pump (AB), one is the tap for the plasma chamber pressure gauges (B & AN) and the last hole is used to introduce helium gas for experiments using helium plasma. All of these connections are made with ¼" Swagelok fittings. The other three holes are for the two electrode plates (AA) to pass through and a small hole for the thermocouple (T) to pass through (see description of the RF system). The top plate has only two holes that are equipped with Swagelok fittings for ¼" diameter openings; the central one allows introduction of the liquid droplets, while the second is used as a feed-through for a Langmuir probe.

The key component of the vacuum system is the vacuum pump, a DUOSEAL model 1376 made by Welch Vacuum (AB). This pump is a single-phase, two-stage, belt-driven high-vacuum pump driven by a 1 hp motor and is rated at 10.6 CFM displacement. It is designed to generate an ultimate vacuum of $1x10^{-4}$ Torr (Figure 3.4). After cleaning the pump, replacing the oil, and attaching the pump directly to the digital pressure gauge

Figure 3.4 DUOSEAL Model 1376 Vacuum Pump (AB).

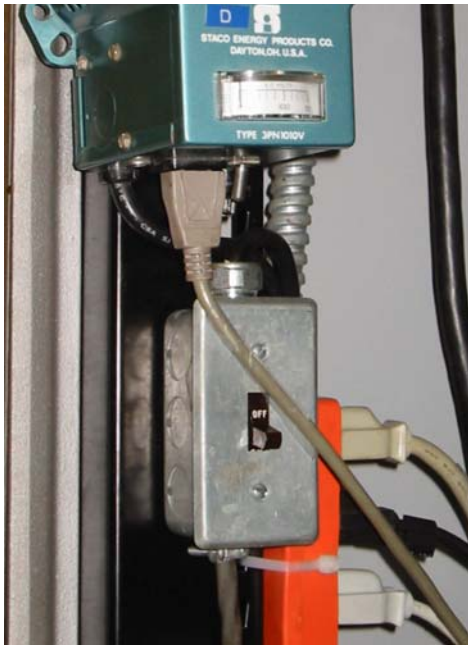

Figure 3.5 Pump Switch (I).

(AM & AN) we were able to measure an absolute pressure of ~0.013 Torr. The difference between design and actual performance is due to the age of the pump and the losses associated with the connections. For convenience and safety, a switch (I) was inserted in the pump power line; the switch was mounted on the work table (Figure 3.5).

The pump was connected to the chamber by a red vacuum hose (AJ) with an inner diameter of 0.8125 in and two hose clamps. A shutoff valve (AI), which is normally used on natural gas appliances, was placed on the chamber end to prevent back gassing when the pump was turned off. Later, a second shutoff valve (AH) was added to isolate the liquid supply from the main vacuum draw as necessary; all of these connections are shown in Figure 3.6. In order to simulate conditions within an inertial fusion reactor chamber, it is necessary to produce and maintain a helium plasma and to regulate and control the pressure level; both of these requirements are met with two valves and a helium tank. The helium tank (AL), a standard gas cylinder supplied by AirGas Co, was equipped with a regulator to step the pressure down and a shutoff valve to turn off the gas supply. The gas supply is connected to a Series 203 leak valve (P) made by Granville-Phillips Co; this valve is rated to provide a continuously variable flow from 400 to 10^{-10} cm^3/s. Since the leak valve is designed only to meter the flow and would be damaged if used as a shutoff valve, an L-series Swagelok metering valve (O) was placed downstream of the exit of the leak valve (Figure 3.7) to isolate the chamber from the leak valve and provide further control of the flow rate. The shutoff valve is then connected to the plasma chamber through the port on the bottom plate mentioned above; all connections are made with ¼" plastic tubing. By running the vacuum pump (AB) continuously and varying the amount of gas that is let in through the leak valve (P) a constant, controllable, pressure

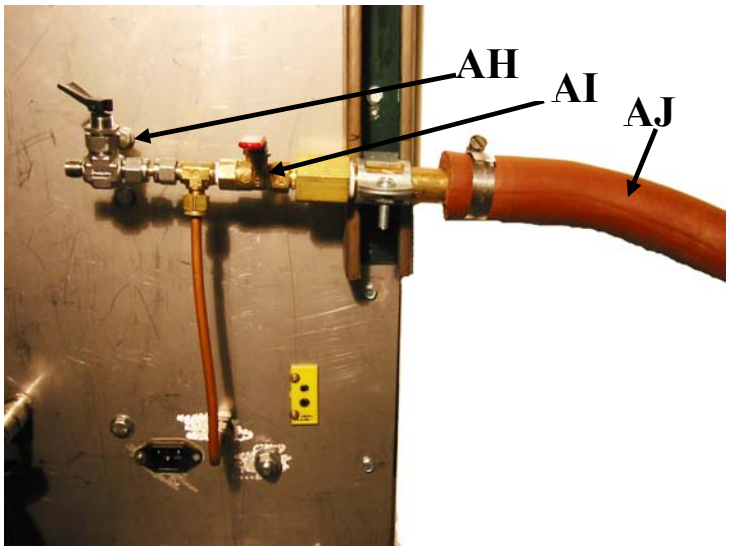

Figure 3.6 Chamber Vacuum Connections Showing Vacuum Hose (AJ), Pump Shut Off Valve (AI), and Fluid Supply Shut Off Valve (AH).

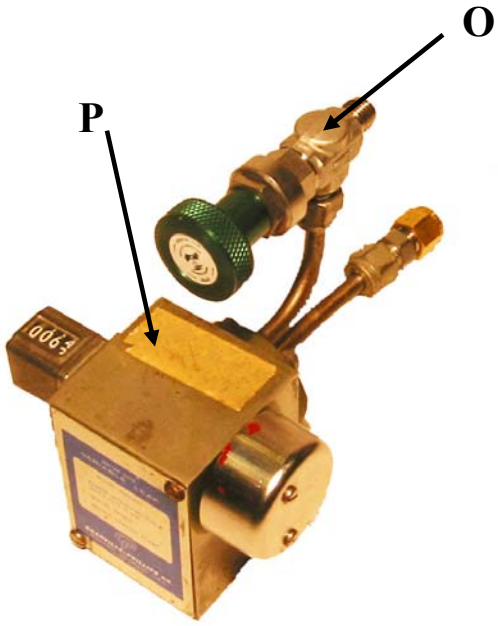

Figure 3.7 Leak Valve (P) and Helium Shut Off Valve (O).

can be maintained inside the vacuum chamber (Z).

To rapidly fill the chamber with helium gas, the leak valve (P) is fully opened and the pump (AB) is turned off. Since helium is lighter than air (and any injected liquid vapor), when the pump (AB) is turned back on, any gas in the chamber other than helium settles to the bottom where the vacuum port is located and the unwanted gas and vapor are removed by the pump. This process is repeated several times to ensure that the chamber contents are predominantly helium; the contents of the chamber can be confirmed when the chamber contains plasma since the color of the plasma depends on the gas, with a purple plasma indicating the presence of air (~ 70% nitrogen) while a light yellow plasma indicates that the chamber gas is mainly helium.

In order to accurately measure the pressure within the chamber, a U-tube mercury manometer (B) is used in series with a digital pressure gauge (AN & AM). The manometer (Figure 3.8) is accurate to ± 1 Torr; the digital pressure gauge provides measurements below 1 Torr. The manometer is manufactured by Meriam Instrument Co; it has a range of 29" and is capable of measuring absolute pressure from 730 Torr down to 3 Torr $\pm$ 1 Torr. It is permanently mounted to the table that is used to hold the experiment and is attached to the plasma chamber through a ¼" plastic tube.

The second pressure measurement device is composed of two parts: a Varian type 0531 thermocouple vacuum gauge tube (AN) and a digital readout device (AM) developed by Digivac Co (Figure 3.9). The gauge tube is attached to the plasma chamber through a special ¼" Swagelok tee fitting. One branch of the tee fits the gauge tube directly, another attaches to the ¼" tube leading to the manometer, and the last branch leads to a shutoff valve (AO). The pressure gauge shutoff valve is a Swagelok model

Figure 3.8 U-Tube Manometer (B).

Figure 3.9 Varian Thermocouple Vacuum Gauge Tube (AN), Digivac Model 200 Digital Pressure Gauge Readout Unit (AM), and Pressure Gauge Shut Off Valve (AO).

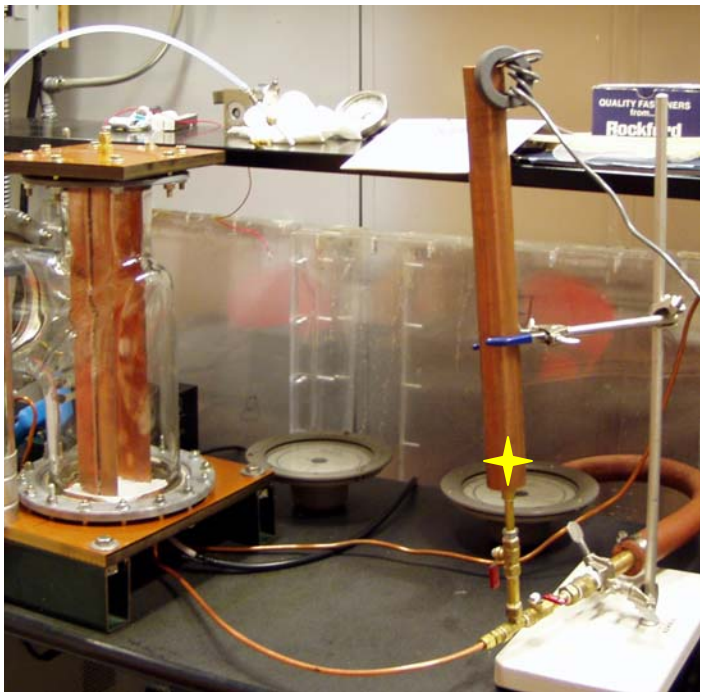

Figure 3.10 Initial Location of Varian Thermocouple Vacuum Gauge Tube (AN) and Attempts to Shield from RF Interference.

SS-42S4-A Stainless Steel 1-Piece Ball Valve (Figure 3.9). This was installed to allow the chamber to be isolated from the pressure gauges in case future research in this facility introduces droplets of material that could harm the pressure sensors or interact with mercury. This feature was also useful when testing for vacuum leaks, as will be discussed later.

The digital gage worked well until the RF generator (F) was utilized. When the digital pressure gauge (AM) was running and the RF Generator was switched on, severe interference resulted, giving completely inaccurate readings on the pressure gauge. Figure 3.10 shows an initial crude attempt to shield the vacuum gauge tube (located inside the copper pipe denoted by the star). Notice that the ¼" copper tubing leads from the plasma chamber to the gauge tube directly with no grounding; also notice that the vacuum tube is on the same line as the main vacuum draw. Both of these features changed in the final

design since the initial crude shielding attempts were unsuccessful and ultimately resulted in two destroyed gauge tubes. The pressure tap had to be moved from the main vacuum line in order to place it in a Faraday Cage. Moving this pressure tap also fortuitously led us to the discovery of an erroneously low reading of chamber pressure, as described in the next paragraph. Details on the successful RF shielding will be discussed later in this chapter.

In this first location, when the pump was turned on, the pressure reading would drop quickly to ~2 Torr and then drop down to ~0.033 Torr; upon pump shutoff the pressure would spike immediately up to ~0.5 Torr and then slowly increase. Initially it was thought that there was a leak in the plasma chamber (Z); however, when the pressure tap was moved into the Faraday cage, the pressure in the chamber would not go below ~0.09 Torr. We then realized that the initial low reading was due to a Bernoulli effect and this was removed by taking the pressure tap out of the main vacuum line.

3.1.2 Plasma Generation System

To discuss the plasma generation system we will start with the electrodes (AA) and follow the power supply back. Then we will look at some of the ancillary devices that are grouped with the plasma system. A list of system components is in Table 3.2 and a schematic of the power system is contained in Figure 3.11.

The copper electrodes (AA) provide the means to generate capacitively coupled plasma. They were initially constructed by cutting two copper plates down to the dimensions of 2.6” by 16”, machining a groove down the long axis and soldering a 20” long ¼” diameter copper rod to the back. After running the plasma, we observed that having the electrodes extend all of the way to the top of the plasma chamber was not

desirable as the needle from the liquid droplet supply system was immersed in the plasma and subject to excessive heating. Reducing the plate height while maintaining the rod at the same length did not resolve this problem. Finally, constructing a new set of electrodes with plates 2.8” x 12.25” and machining spacer blocks from round ceramic to hold the electrodes in place solved the problem.

Table 3.2. Detailed list of the Plasma Generation System Hardware Components.

Item ID	Description	Manufacturer	Model	Serial Number
D	Adjustable Dual Tracking DC Power Supply 0-15 V DC	Micronta (Radio Shack)	22-121	10A7
E	Matching Network Control Unit On/Off with 2 Capacitor Control Switches	Capovani Brothers Inc.	Custo m Built	Custom Built
F	RF Generator 13.56 MHz 230Vac input 1000Watt into 50 ohms output	ENI	HF-1T	341
G	220V MAIN SWITCH	General	-	-
R	LCD Digital MultiMeter Power 9V Battery Temperature Measurement Range -20 to 1300 C -4 to 2373 F	Omega	HHM29	0400-0022
T	K Thermocouple Probe, 1/8 inch(3.2mm) diameter, ungrounded junction, 12 inch(300mm) length Chromel / Alumel	Omega	KQXL-18U-12	-
U	Automatic Matching Network 13.56 MHz 125Vac 50-60 Hz input 50 ohms input 10-1000 ohms output	ENI	MW-25	108R
AA	Copper Electrodes	Custom Built	-	-
AF	Large Faraday Cage	Custom Built	-	-
AP	Small Faraday Cage	Custom Built	-	-
AQ	Work Stand	Custom Built	-	-
AU	Langmuir Probe	Custom Built	-	-
AV	Work Stand	Custom Built	-	-

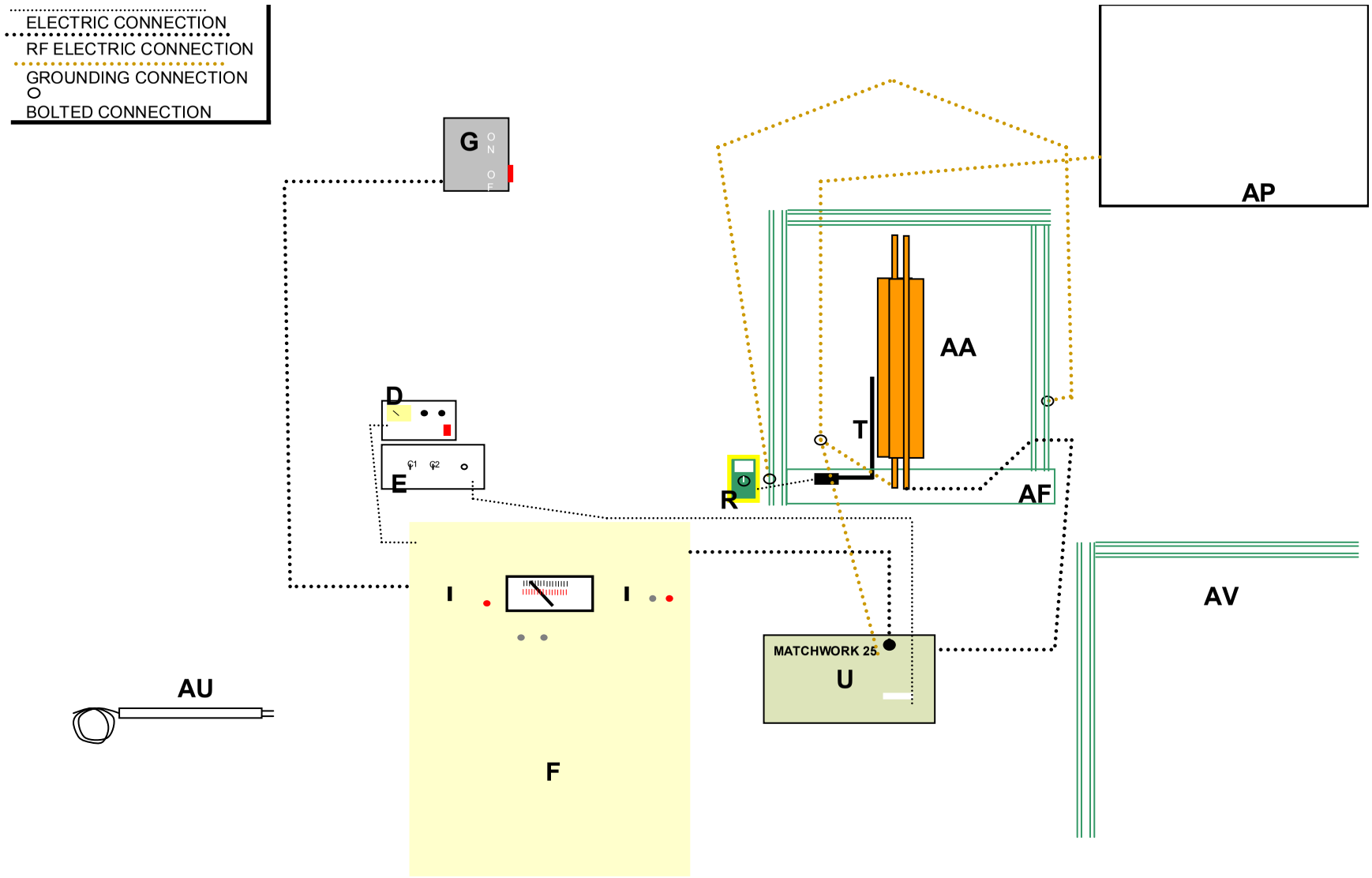

Figure 3.11 Schematic of Plasma System Including Peripheral Components.

During the early stages of development, the plasma was not run for long (> 1 hr) periods. When data collection began, however, the plasma was often left on for extended periods to allow the temperature in the chamber to stabilize. Eventually, the solder holding the electrodes' plates and rods melted off, thereby separating the plates from the rods. To avoid de-soldering due to excessive heating, the 2.8" x 12.25" electrode plates were vacuum brazed to withstand temperatures up to 1300° C. An undesirable side effect of the brazing process is that the plates are annealed during brazing, becoming extremely malleable. The first set of brazed electrodes was deformed significantly during re-installation, rendering them unusable. The second set of plates was cut to 2.6" x 12.25",

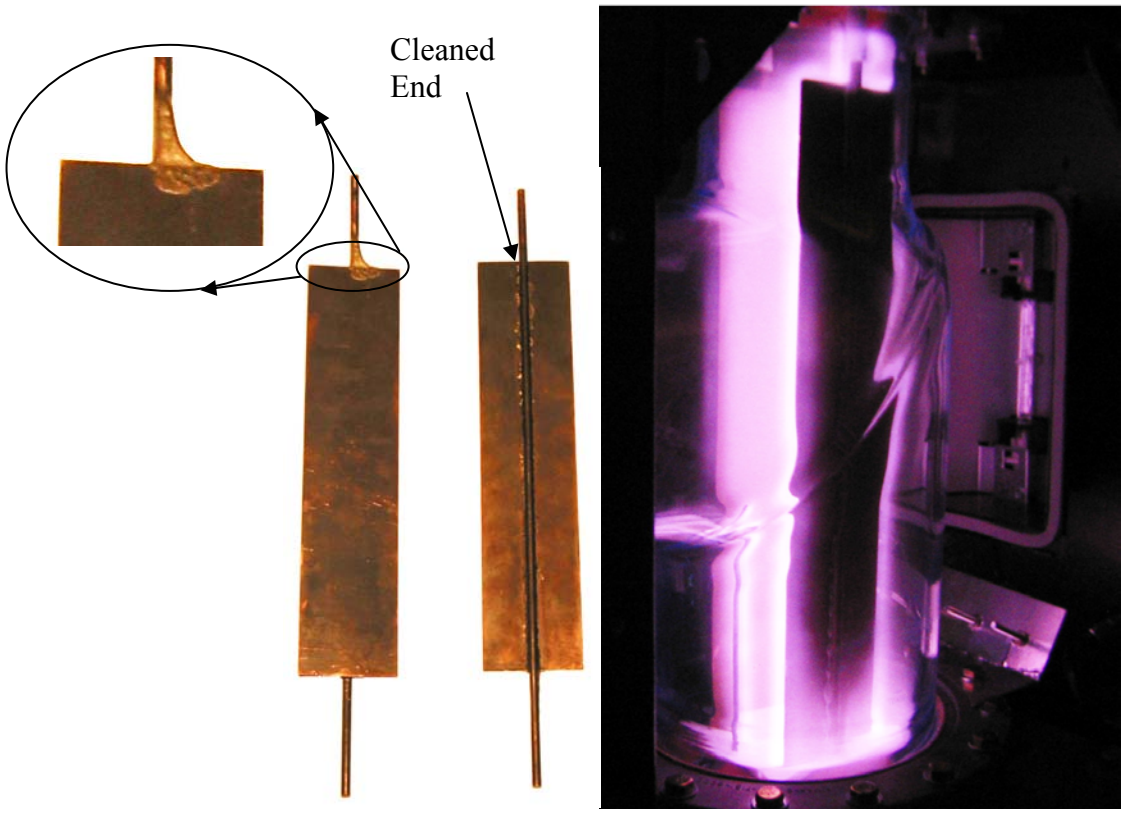

Figure 3.12 Copper Electrodes (AA) Prior To Post-Brazing Clean-Up (Left) and After; Right Image Shows Electrodes in Operation with a Nitrogen Plasma.

brazed, and cleaned by removing the old solder that had collected at one end (Figure 3.12).

Great care was then taken during re-installation of the second set of electrode plates to ensure that the plates were not excessively deformed. A Teflon plate at the bottom of the plasma chamber with grooves that keep the plates in position and parallel to each other was used during the re-installation. The electrode rod is inserted through the hole in the Teflon and then through the holes in the bottom plate. The plates are locked in with ¼" Swagelok fittings using Teflon ferrules, and the ceramic spacers are placed on the top of the rod. The ceramic spacers fit into recesses in the top plate of the plasma chamber. Finally, the electrodes are attached to the cable that energizes them with custom built clamps (Figure 3.13).

The cable that connects the electrodes (AA) and the matching network (U) was built in-house; it consists of one type N connector on a coaxial cable with two ring clamps on the other end (Figure 3.14). The neutral lead was built by unwinding the outside of the coaxial cable and putting it in heat-shrink tubing. The matching network (Figure 3.15) is an ENI model MW-25 Tuning Unit (U). The MW-25 consists of two components; the RF Tuning Unit (U) and the Control Unit; a control unit (E) that allows the MW-25 Tuning Unit (U) to operate in the manual mode (Figure 3.16) was custom-built by Capovani Brothers Inc (CBI). The two toggle switches on the front of the CBI control box (E) controls the settings of two variable capacitors inside the tuning unit and allows the operator to manually match the impedance of the generator to the plasma.

In addition to the control box the MW-25 tuning unit (U) is connected to a 1000 Watt, 13.56 MHz ENI HF-1T RF generator (F). It has an input of 220 VAC, a variable

output of 0-1000 Watts of RF power into a 50 ohm load and is comprised of all solid state components (Figure 3.17). The output of the RF generator (F) is attached to the input of the MW-25 (U) by means of a standard N type connector coaxial cable. The RF generator

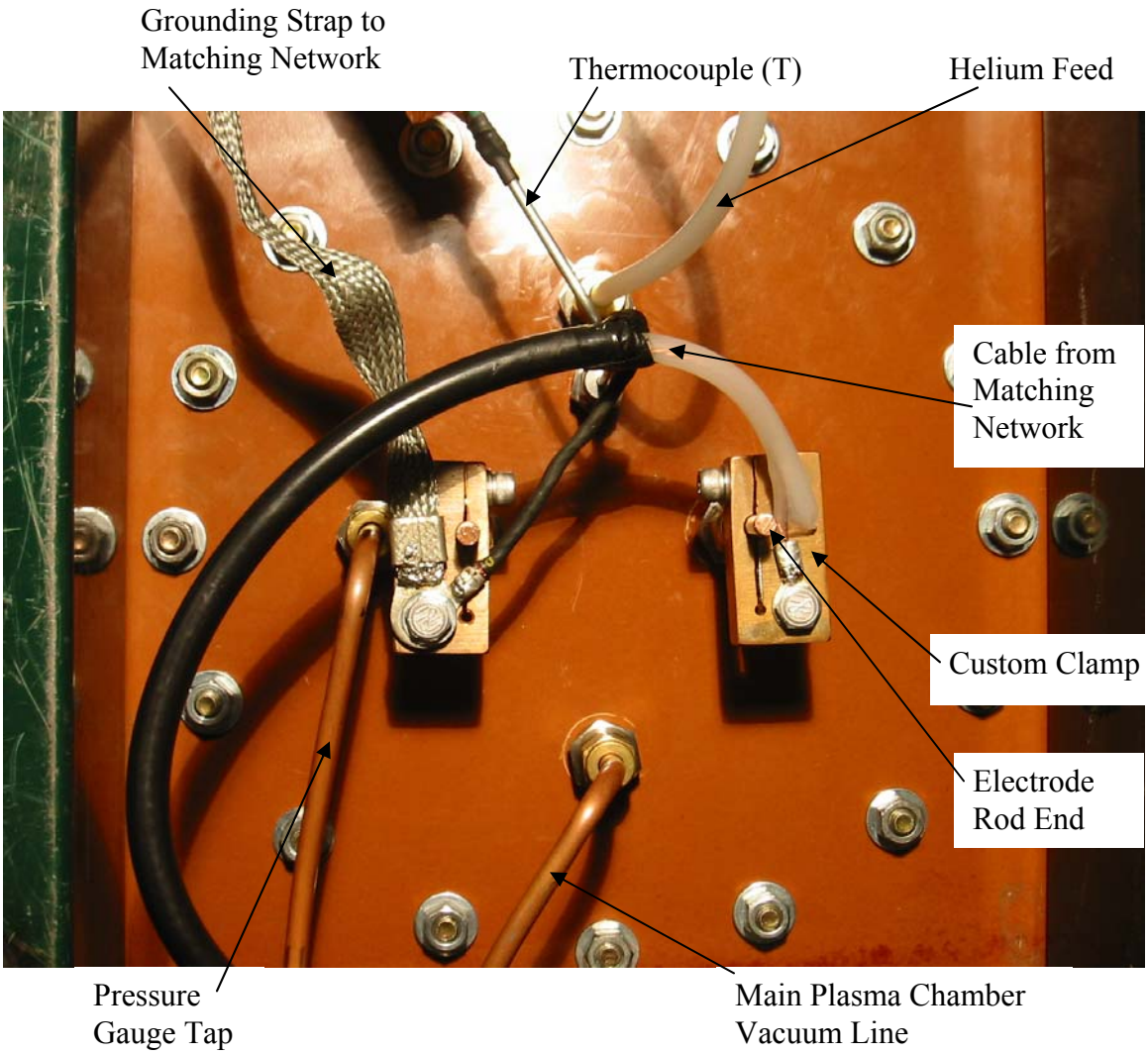

Figure 3.13 Bottom View of Plasma Chamber Showing Custom Electrode Clamps and Connections.

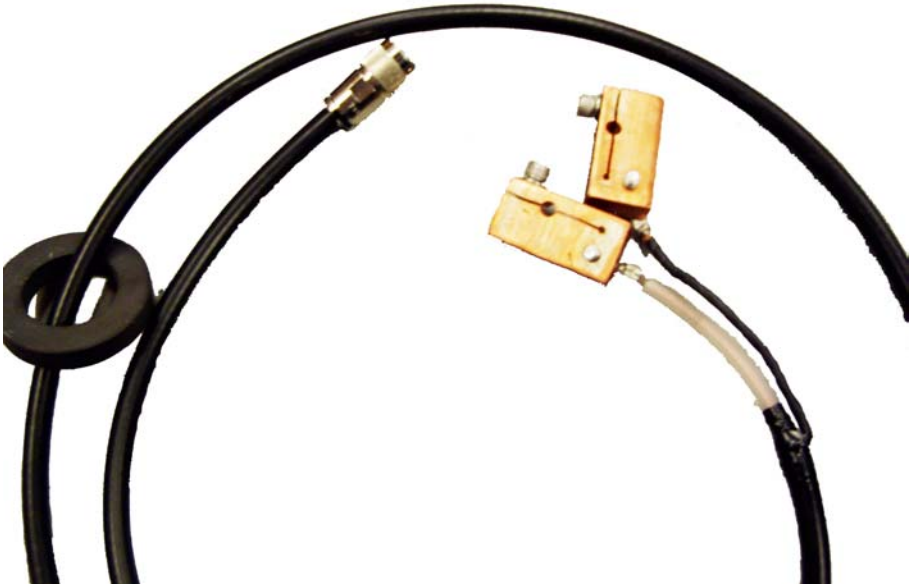

Figure 3.14 Custom RF Cable for Connection from Electrodes to Matching Network.

Figure 3.15 Matchwork MW-25 Tuning Unit (U).

Figure 3.16 Micronta DC Power Supply (D) and the CBI Custom Built Matching Network Control Unit (E).

Figure 3.17 ENI HF-1T 1000 Watt 13.56 MHz RF Generator (F).

(F) was purchased from Ocean Surplus; it had been previously modified for remote operation only and required a variable 0-10 VDC driver signal to adjust the output; this signal is provided by a Micronta 22-121 (Figure 3.16) Adjustable Dual-Tracking DC Power Supply (D) which is attached to the external input (Figure 3.18) on the back of the RF generator (F).

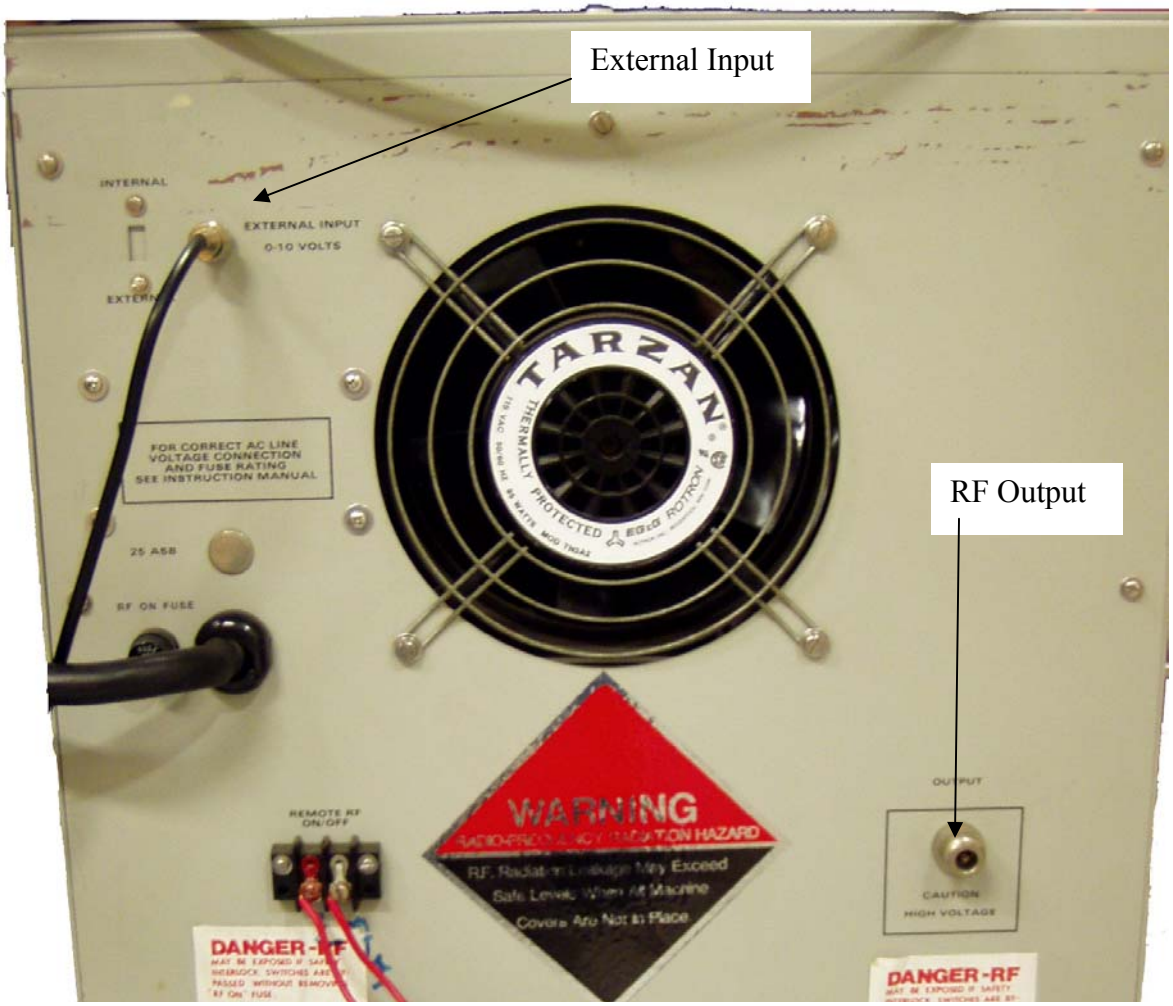

Figure 3.18 Rear of RF Generator Showing Attachments for DC Power Supply (D) and Matching Network (U).

When the RF generator is operated, the electrode plates in the plasma chamber become large capacitors which drive the plasma; they also become large antennas that broadcast RF energy throughout the lab. As mentioned previously in section 3.1.1, when the digital pressure gauge (AM) was running and the RF Generator (F) was switched on severe interference resulted, thereby producing completely inaccurate readings from the pressure gauge, which were due to electrical currents in any ungrounded metal exposed to broadcast RF energy. Initial attempts to fix this problem were, as discussed previously,

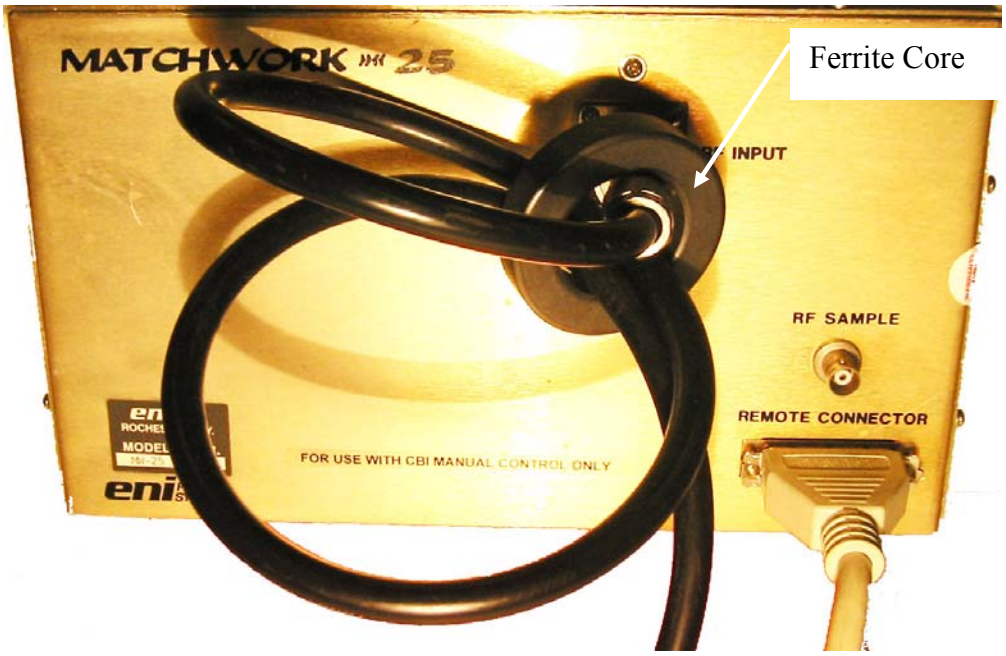

Figure 3.19 Initial Faraday Shielding on RF Cables.

unsuccessful. The first solution that was tried was to place ferrite cores on all cabling to try to remove currents set up in the wires. This was successful in the RF cables (Figure 3.19) as turning the generator on with the cables (routed through ferrite cores) attached to the generator but not the plates resulted in no interference. As soon as the plates were attached the problem returned. We then attempted to place the digital pressure gauge inside a Faraday cage as shown in Figure 3.10 and Figure 3.20. These efforts were unsuccessful and resulted in the destruction of the vacuum gauge tube (AN). In order to fix the problem we had to control the RF emissions from the electrodes (AA).

The problem was solved by constructing a large Faraday cage (AF) around the entire plasma chamber. The frame of the cage was composed of lengths of unistrut bolted together to form a rectangular box. This box was covered on the top, bottom, and 2 sides by 0.020” thick stainless steel sheets (Figure 3.21); the back was covered with a 0.050”

Figure 3.20 Initial Faraday Shielding on Digital Pressure Gauge Readout (AM).

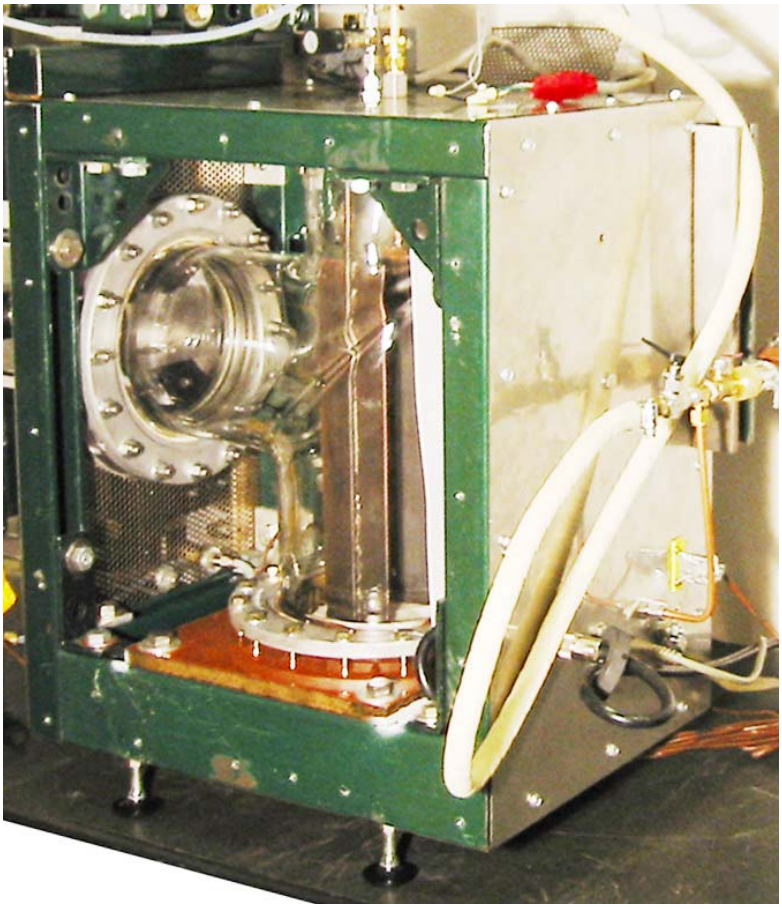

Figure 3.21 Large Faraday Cage (AF) Showing Thicker Back Panel, Thinner Top Panel, and Unistrut Frame Construction through Open Right Side.

thick sheet (thicker to function as the primary location to mount bulkhead connections to pass through items; Figure 3.22) of stainless steel, while the front was covered by a 0.036" thick perforated steel sheet with an open area of 51% and 0.1875" holes staggered on 0.25" centers. A hole was cut in the front perforated sheet to allow unobstructed vision through the polycarbonate cover plate of the vacuum chamber's side opening (Figure 3.23).

The perforated steel front cover was cut from a 40"x 36" size sheet; the remaining portion of this sheet was bent into a box shape with two open sides; which comprises the small Faraday cage (AP). This was then mounted to the front left side of the large Faraday cage (AF) and a sheet of aluminum was bent to form a shelf inside the cage. Figure 3.24 shows a view of the rear of both cages and by looking at the upper right hand corner the relative size of the two cages can be seen. Within the small cage (AP) the thermocouple vacuum gauge tube (AN) and digital readout device (AM) are mounted. Figure 3.25 shows a close in view of the small Faraday cage. This is an earlier configuration of the vacuum hookup, as the precursor to the pressure shut off valve (AO) is seen. In the figure the digital readout device (AM) has been disconnected from the vacuum gauge tube (AN) and a copper tube that gives further shielding to the vacuum gauge tube (AN) is sitting on the bottom of the small Faraday cage (AP). In the top right the aluminum shelf which holds the digital readout device (AM) is seen. Another feature of the small cage is an access door which swings up on the two hinges seen near the center of Figure 3.26. The bottom of the small Faraday cage (AP) is permanently mounted to the left side of the large Faraday cage (AF) and has been fitted with a

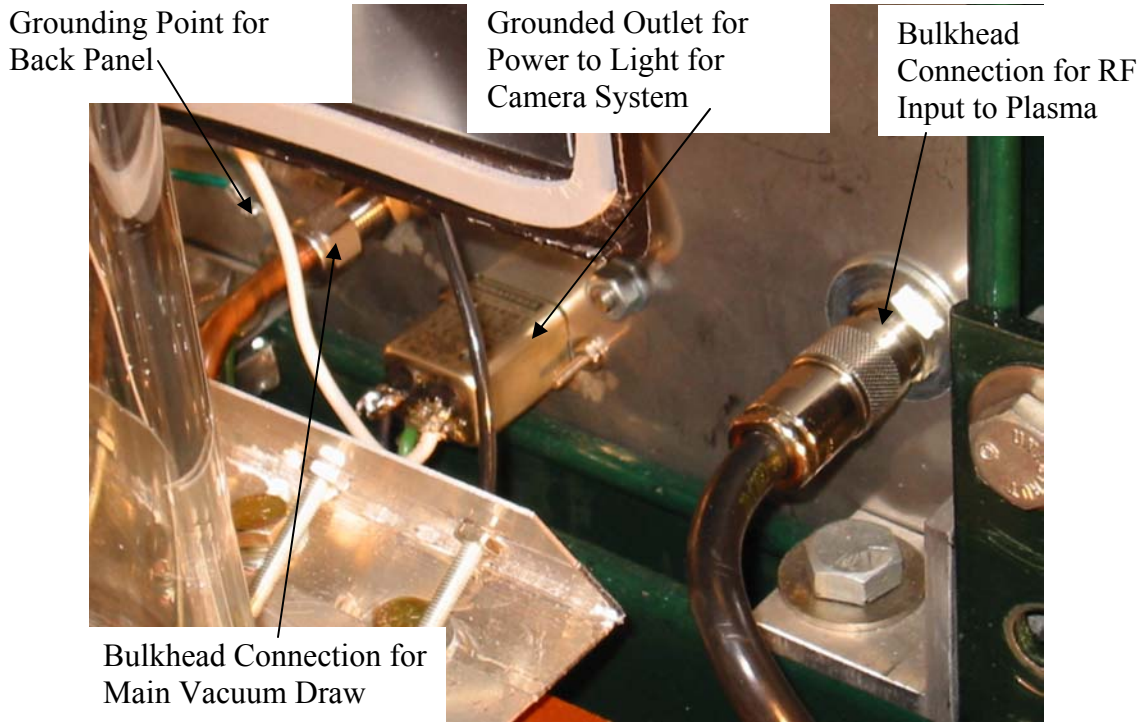

Figure 3.22 Detail of Pass Through Points in Back Plate of Large Faraday Cage.

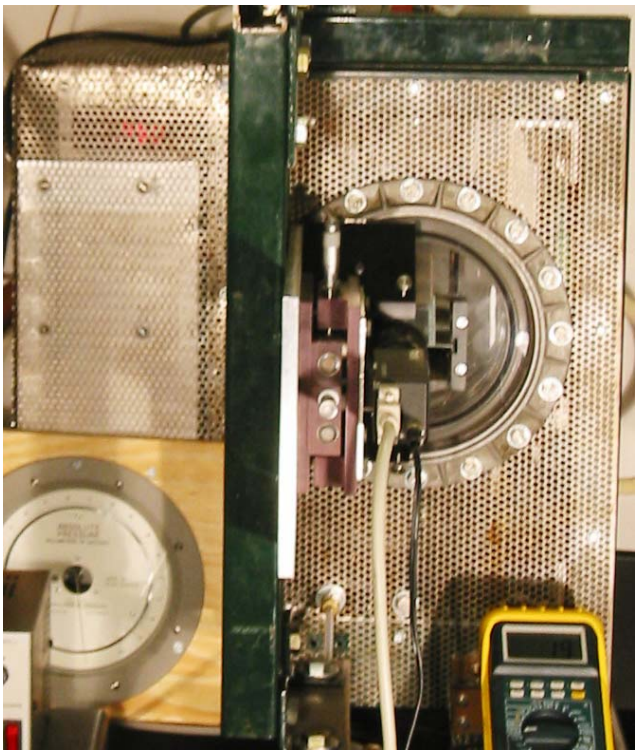

Figure 3.23 Front of Large Faraday Cage Showing Front Perforated Cover Plate with Hole for Viewing.

grounded shielded outlet. In this manner, power for the digital pressure gauge enters the small cage without causing RF interference.

Great care was taken to ensure that all connections were grounded to the cage. One should realize that, for every electrical and vacuum connection depicted by lines on the apparatus schematic diagrams throughout this chapter, two connections are implied; *i.e*. from the device to the interior of the Faraday cage and from the exterior of the cage to the desired final location. By doing all connections in this manner, every piece of metal is directly connected to the Faraday cages.

Figure 3.24 Back of Large (AF) and Small (AP) Faraday Cages.

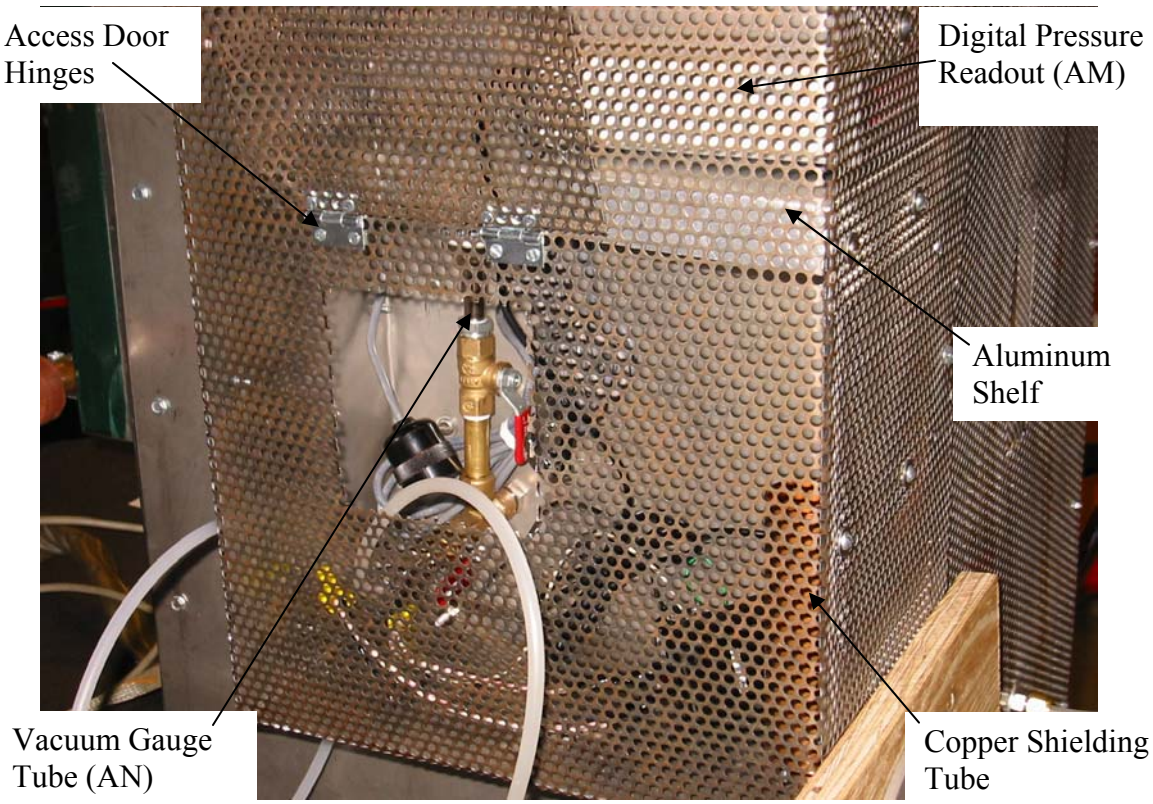

Figure 3.25 Close Up View of the Small Faraday Cage (AP).

From different locations on the large Faraday cage (AF), three grounding straps are tied to earth ground (Figure 3.11); a large 1.5" wide grounding strap leads from the front perforated panel and unistrut frame to earth ground on the wall cabinet, a small 0.6" grounding strap leads from the back panel (where most of the pass through connections are made) to the same earth ground, and another 0.6" grounding strap leads from the right side panel and unistrut to the ground on the rear of the MW-25 matching network (U). This last grounding strap is tied to the small Faraday cage (AP) and to the ground electrode inside the plasma chamber via a short length of 0.6" grounding strap (Figure 3.13 shows one end of this strap) on the inside of the large Faraday cage (AF). By

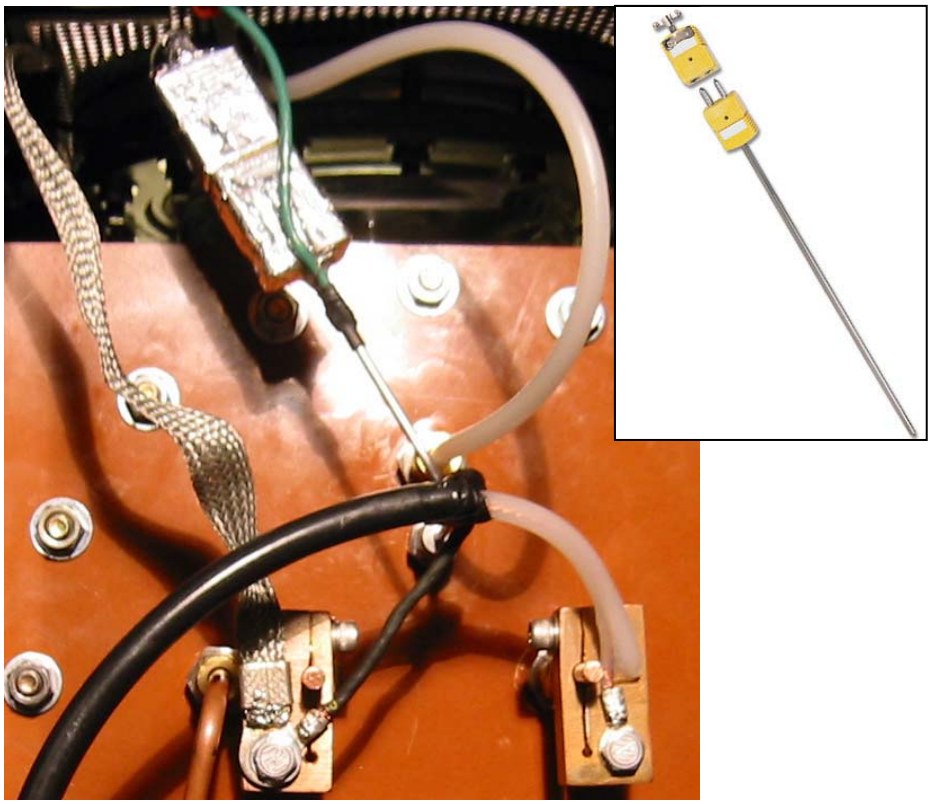

Figure 3.26 Detail of Thermocouple Insertion (T) (Inset: Catalog Picture of Unmodified Thermocouple).

Figure 3.27 Omega LCD Digital MultiMeter (R), Grounded Cable and Outlet.

measuring potential difference with a multimeter, all of the panels were found to be tied into earth ground. The final result of all of this RF shielding was that when the RF generator (F) and digital pressure gauge (AM & AN) were run at the same time, the maximum amount of interference caused was 0.6 Torr, which established the expected error in the pressure measured using the digital pressure gauge.

The bulk plasma temperature was measured using a standard ungrounded, 1/8 inch diameter, 12 inch long, Chromel/Alumel, K series thermocouple (T), bent at a right angle, and inserted into the bottom of the plasma chamber through a hole in the bottom plate. Figure 3.26 shows a close in view of the thermocouple; seen in the picture is the thermocouple plugged into a quick disconnect shielded cable. Since this is an ungrounded probe the Chromel and Alumel wires inside the probe do not make contact with the probe body, and thus do not receive any RF interference. The thermocouple and the cable plug are both wrapped in metallic tape and the probe body is tied to the ground wire of the shielded cable by the green jumper wire. In this manner the data cable coming from the thermocouple receives no RF interference. This cable leads to the rear wall of the large Faraday cage and into an outlet. A second grounded and shielded cable leads from the outlet to an Omega LCD digital multimeter (R) which is powered by a 9V Battery and has a temperature measurement range of -20° to 1300° C (Figure 3.27). Since there are few metal parts and no contact with ground, the RF interference does not affect the multimeter. Typical operation is for the unit to read ~20° C when turned on and immediately raise to ~200° C or higher when immersed in plasma and then slowly climb

until the temperature levels at 400-600° C depending on the composition, pressure, and RF power input to the plasma.

A Langmuir probe is used to determine the electron temperature, electron density, and electric potential of plasma. It operates by inserting one or more electrodes into the plasma and varying the electric potential between them or between them and the plasma chamber (Brow, 2005) (Figure 3.28). The measured currents and potentials in this system allow the determination of the physical properties of the plasma. Figure 3.29 shows the typical characteristic curve of a dual Langmuir probe. In a dual probe setup, rather than the plasma chamber serving as a reference, a second probe is placed close to the first and the potential is varied between the two (Fußmann, 2005). At the point where the current is zero, the slope of the characteristic gives the electron temperature. As the applied probe voltage increases on one probe and then the other, electrons are either completely repelled or attracted to the probe; this is the saturation-current. The electron density is deduced from the value of this current (Fußmann, 2005). The advantage of the dual probe is that both of the probes are equally affected by the RF interference and the RF signal can be filtered out, and in some cases eliminated by symmetry (Bourham, 2004). The disadvantage is that the plasma potential cannot be determined.

In this experiment, a dual Langmuir probe (AU) was constructed (Figure 3.30). The probe was made of two lengths of 0.009" Tungsten wire placed in a ceramic ¼" rod which has two lengthwise holes. To construct the probe, the Tungsten wire was threaded through the ceramic tube and stretched between two vices. The wire was then cemented in place using Varian Torr Seal vacuum epoxy. The two ends of the Tungsten wire were

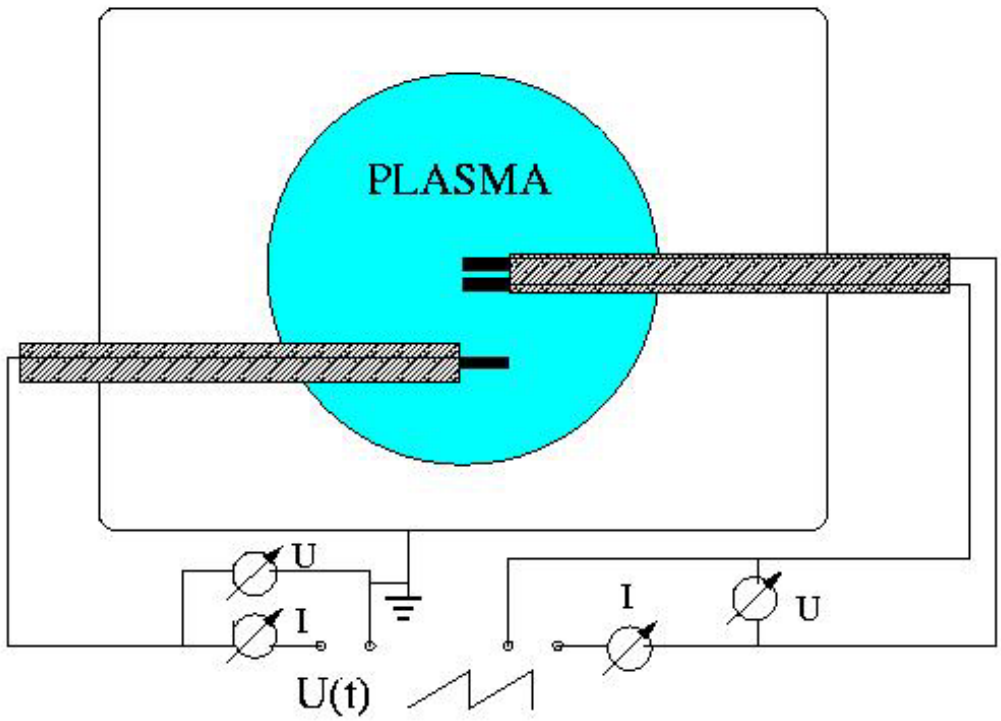

Figure 3.28 Schematic of a Typical Langmuir Probe Setup for Both a Single and Dual Probe (Fußmann, 2005).

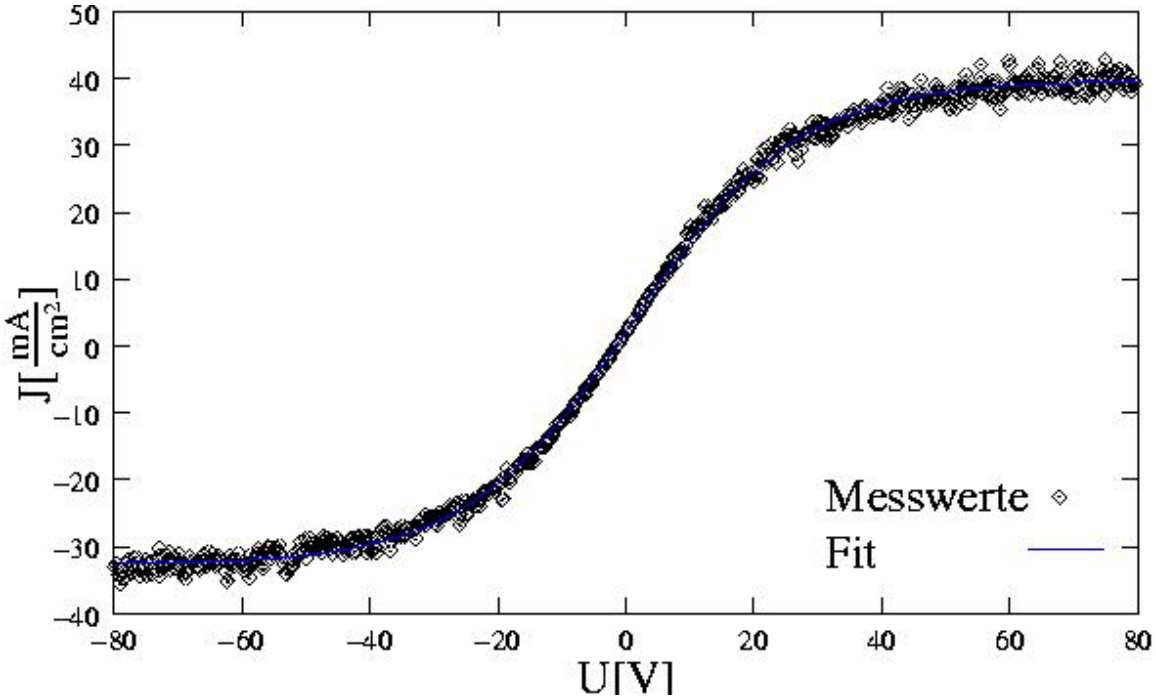

Figure 3.29 Typical Characteristic Curve for a Dual Langmuir Probe (Fußmann, 2005).

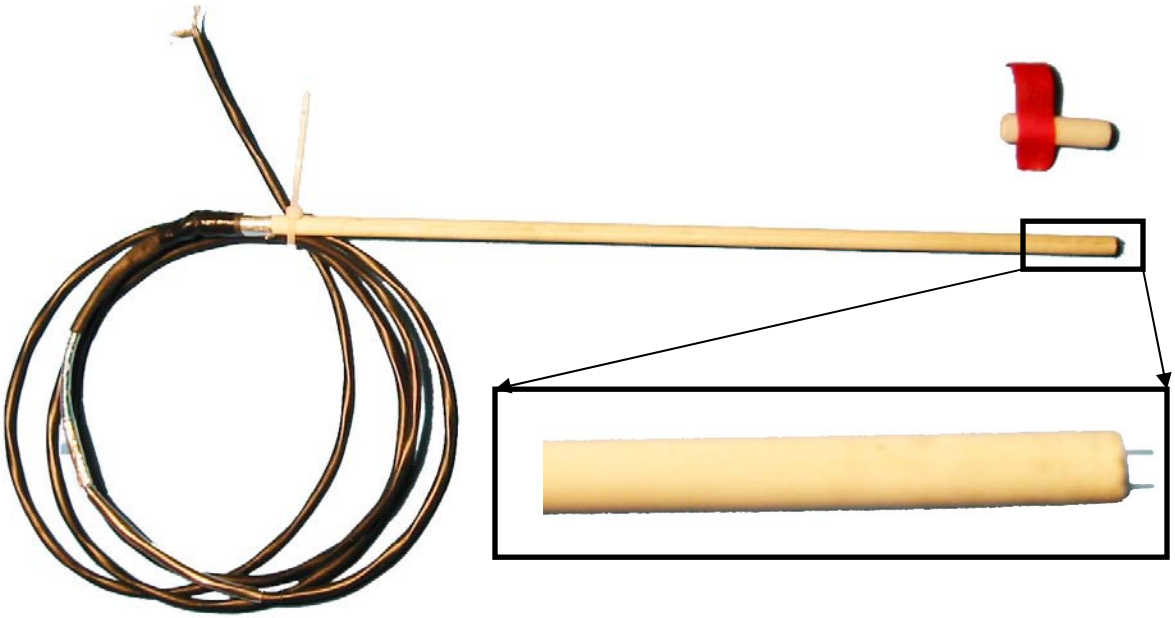

Figure 3.30 Dual Langmuir Probe with Tip Cover (above). Inset Shows Detail of Probe Tip.

then soldered to shielded instrumentation wire, insulated with heat shrink tubing, and wrapped with metallic tape (Figure 3.31). In this manner, the RF interference is prevented from influencing the system except in the Tungsten wire. One probe was destroyed during construction due to the brittle nature of Tungsten wire; to avoid this problem, a cover was built to protect the exposed probe ends. The probe (AU) is inserted into the plasma through the top plate and then spun so that the plane defined by the two probe ends is parallel to the RF electrodes (AA); this ensures uniform interference on both wires and reduces the RF interference to a negligible level. Measurements will be conducted upon installation of a voltage source to power the system and a method to electronically measure the current in the system and the applied voltage.

The last item in the plasma generation system was required by the weight of the RF shielding. Legs had been attached to the bottom of the large Faraday cage (Figure

3.32) to make it easier to move the apparatus around on the table top as well as to allow cabling to be run underneath the system. These legs were not long enough to allow work to be done on the bottom of the system and it became problematic to tip the system on its side. The system was so heavy that a length of unistrut was added to the bottom of the table as it had begun to sag due to the weight of the experiment. The solution to these difficulties was to build a work stand (AV) to allow access to the bottom of the apparatus. The stand was slid as close to the table as possible ensuring that the legs of the test apparatus were outside of the work stand bars. Then the test apparatus was disconnected from all external items and, both the work stand and test apparatus, were slid back so that the apparatus rested on the work stand only. In this position it was easy to remove the bottom panel and legs to access all of the connections on the underside of the experiment.

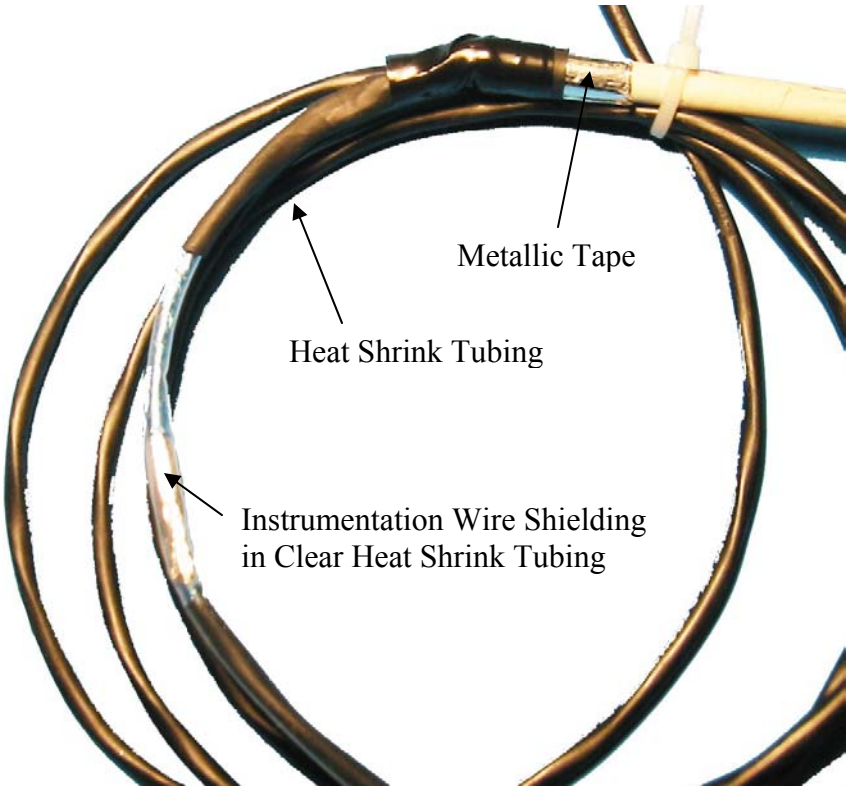

Figure 3.31 Close Up of Langmuir Probe Connection to Instrumentation Wire.

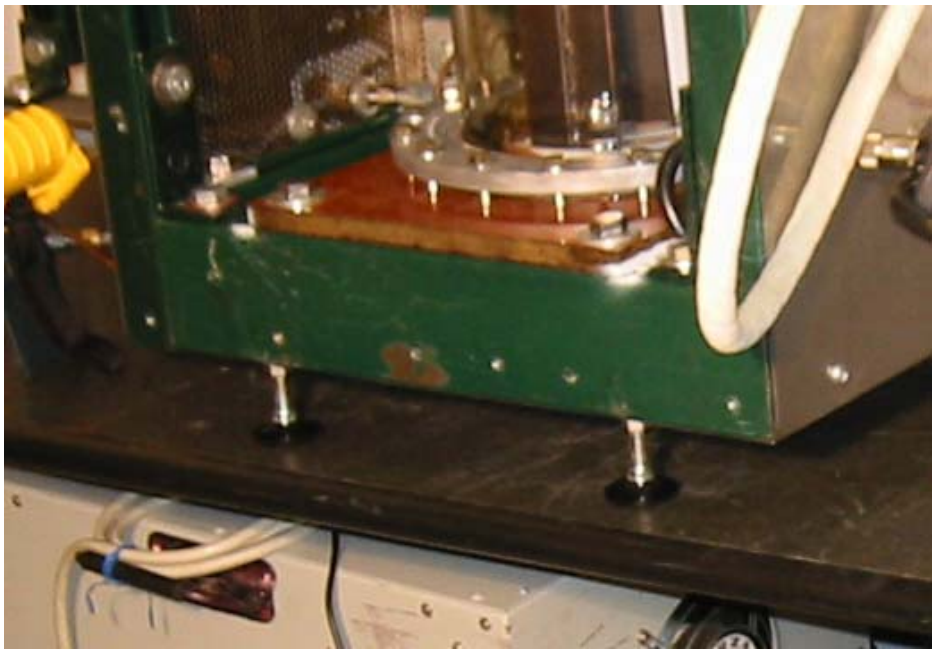

Figure 3.32 Legs of Large Faraday Cage.

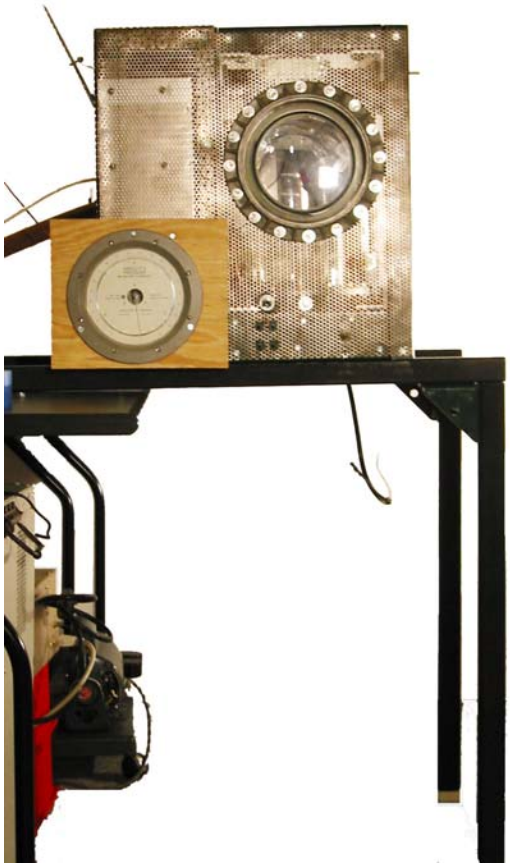

Figure 3.33 Work Stand (AV) in Use to Access the Bottom of the Experiment.

Figure 3.33 shows the work stand in this configuration with the RF cable leading to the copper electrodes hanging out the bottom.

3.1.3 Liquid Droplet Generation System

The next subsystem developed during this investigation was the liquid delivery system. Since the unsuccessful ideas directly contributed to the next (and finally successful) system, we will first discuss the ideas that did not work prior to covering the final liquid droplet generation system. Table 3.3 shows a list of the components of the liquid droplet system and Figure 3.34 is a schematic drawing showing how these parts fit together.

Table 3.3 Detailed List of the Liquid Droplet Generation System Hardware Components.

Item ID	Description	Manufacturer	Model	Serial Number
C	Dial Absolute Pressure Gauge Max Case Pressure 15 psig 0-800 mm of HG Scale	Wallace & Tiernan	-	FA 160-NN15953
Q	Dial Absolute Pressure Gauge Max Case Pressure 15 psig 0-20 mm of HG Scale	Wallace & Tiernan	-	FA 160-NN16036
S	Bump Switch	Micro	Type Z	-
V	Pneumatic Shutoff Valve	Nupro	B-4HK	-
W	Solenoid Valve	SMC	NVZ110	-
X	Modified 500 mL Sampling Flask	Pyrex	5340	-
Y	Stainless Very Fine Metering Valve, 1/4 in. Tube Fitting, Vernier Handle	Swagelok	SS-SS4-VH	-
AC	Brass Needle Valve, 1/4 in. Tube Fitting, Regulating Stem	Swagelok	B-1RS4	-
AG	Gum Rubber Vacuum Hose	Unknown	-	-
AK	Compressed Air Tank	Airgas	UN1002	S24462

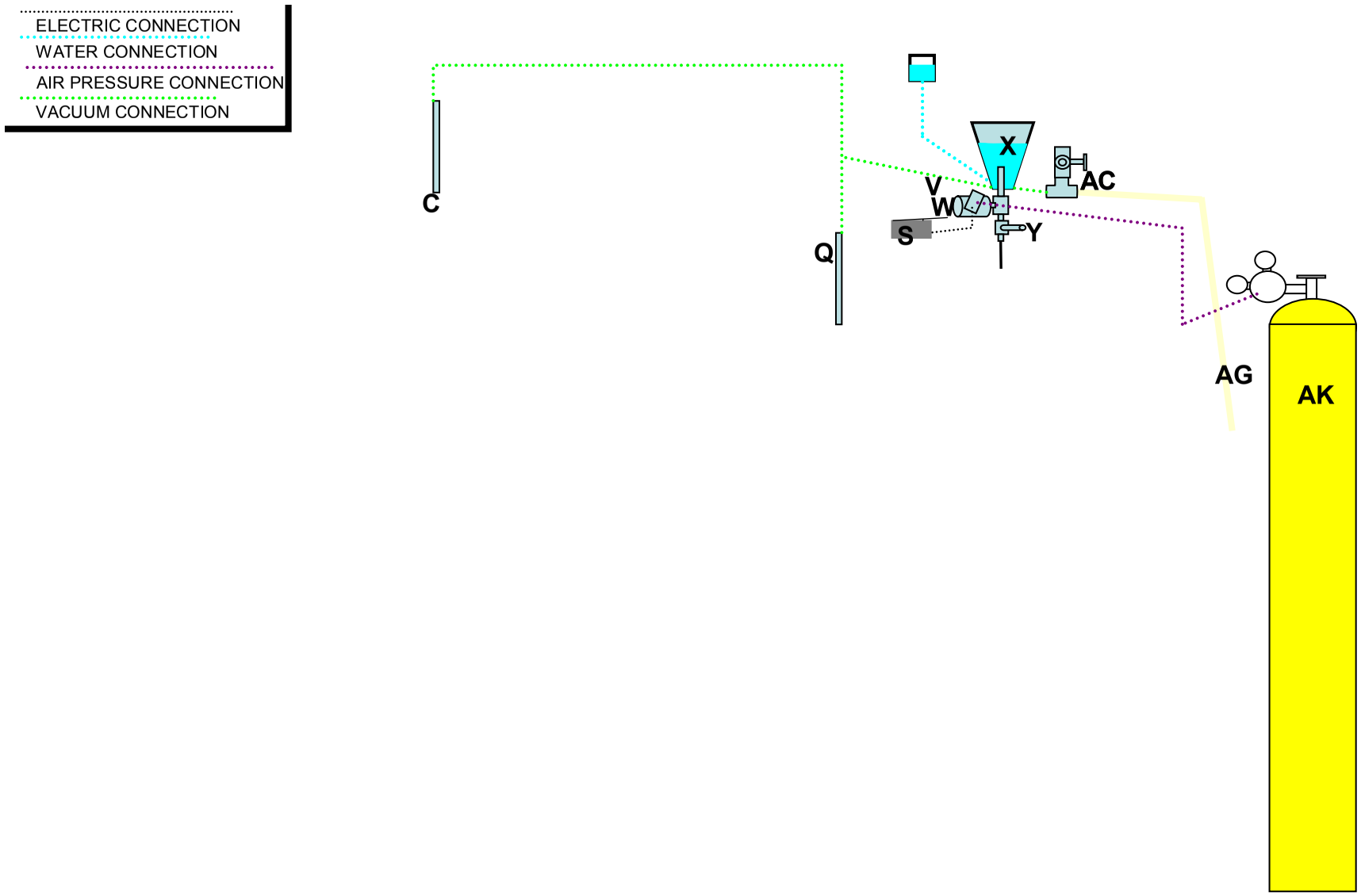

Figure 3.34 Schematic of Liquid Droplet Generation System.

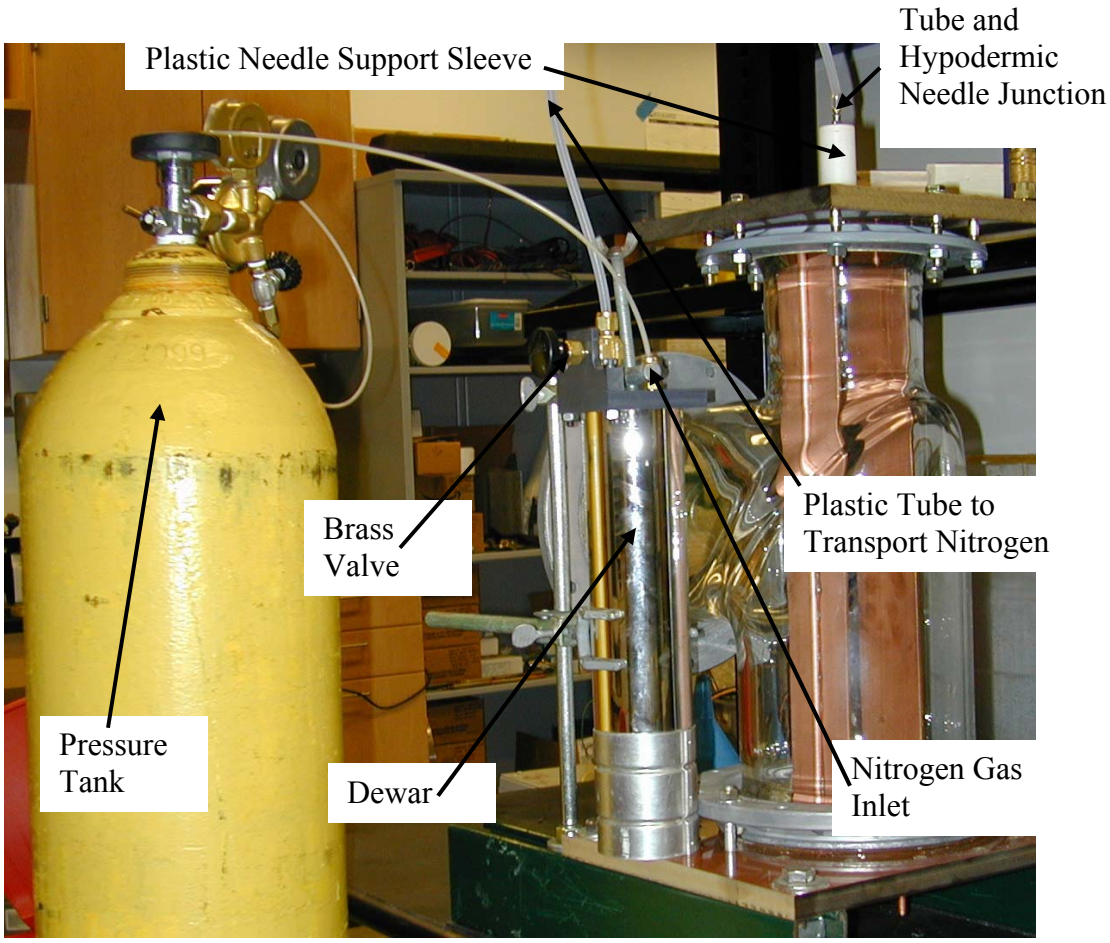

Figure 3.35 First Droplet Setup: Nitrogen Drop in Nitrogen Plasma.

The original idea for this experiment consisted of placing a drop of liquid nitrogen into nitrogen plasma. Figure 3.35 depicts the initial setup to try to accomplish this; the system included a dewar to keep the liquid nitrogen in a liquid state, a tube to transport the nitrogen to the top of the apparatus where it would be fed into the plasma chamber through an 18 gauge needle. The needle was press-fit through the center of a ¼" diameter cylinder of Teflon to resist the heat of the plasma chamber which was in turn placed in a ¼" Swagelok valve with a Teflon ferrule to pass through the geometric center of the top plate. A plastic sleeve was placed around the top of the hypodermic to provide support and prevent movement of the needle which would cause leaks in the system. The top of

the dewar was sealed with a plastic plate which had fittings for the liquid nitrogen to be fed from the bottom of the dewar and a second fitting for applying pressure to the dewar through nitrogen gas to force the liquid nitrogen up through the brass valve, the plastic tube, the 18 gauge needle, and ultimately into the chamber.

This system did not function because of boiling, as liquid nitrogen boils at room temperature and the reduced pressure of the nitrogen gas in the plasma chamber caused the liquid to boil even faster. The result was that instead of liquid droplets being introduced into the plasma chamber, we observed nitrogen vapor exiting the needle. What we learned from this was twofold; first the droplet would have to be composed of a material that was a liquid near room temperature and had a vapor pressure that was as low as possible. The second lesson learned from this experiment was that pressurizing the droplet supply was not necessary. This fact was determined when we were running tests to ensure that liquid would flow through the system. Instead of liquid nitrogen pressurized by nitrogen gas, water pressurized by air was used (the pressure tank shown in Figure 3.33 is actually an air tank). When water was placed in the dewar and the valve at the top of the dewar was opened the vacuum in the plasma chamber pulled water rapidly through the system, thereby introducing a continuous stream into the plasma chamber. When the pressure in the Dewar was removed the water flowed into the chamber but it did so in an inconsistent manner due to the leaks in the interface between the tube and the hypodermic needle.

In order to determine an appropriate candidate for a replacement liquid Table 3.4 was developed; the table shows the name, chemical formula, temperature range over which the values are applicable, and the vapor pressure at 20° C for substances with

vapor pressures less than 10 torr. Since none of these compounds were deemed acceptable it was felt that it would be possible to cool the droplet supply, so compounds with acceptable values at 0° C are found in Table 3.5 (the complete list is in Appendix B). It was therefore decided that experiments for this initial study would be conducted using water.

Table 3.4 Common Substances with Acceptable Vapor Pressures at 20° C. (Yaws, 1995)

		Temperature Range		TEMP (K) 293.15
NAME	FORMULA	Tmin	Tmax	Vapor Press (Torr)
ASTATINE	At	279	607	6.95E-06
FRANCIUM	Fr	267	879	1.42E-05
SULFURIC ACID	H2S04	283.15	603.15	3.26E-05
MERCURY	Hg	234.31	1735	1.28E-03
SULFAMIC ACID	H3N03S	293.15	373.15	6.00E-03
IODINE	I2	242	819.15	2.60E-01
HYDROGEN PEROXIDE	H202	272.74	730.15	1.37E+00
CARBON SUBSULFIDE	C3S2	287.15	403.95	1.48E+00
BORIC ACID	BH303	293.15	401.15	1.94E+00
PHOSPHORUS TRIBROMIDE	PBr3	280.95	448.45	2.18E+00
CHLOROSULFONIC ACID	CIH03S	193.15	700	2.32E+00
HEXACHLORODISILANE	Si2Cl6	277.15	412.15	3.09E+00
BERYLLIUM BOROHYDRIDE	BeB2H8	274.15	363.15	5.18E+00
THIONYL BROMIDE	SOBr2	266.45	412.65	5.46E+00
OSMIUM TETROXIDE - YELLOW	OsO4	276.35	403.15	5.64E+00
HEXACHLORODISILOXANE	Si20Cl6	268.15	408.75	5.79E+00
VANADIUM TETRACHLORIDE	VC14	247.45	697	5.84E+00
SULFUR MONOCHLORIDE	S2C12	265.75	411.15	6.55E+00
OSMIUM TETROXIDE - WHITE	OsO4	267.55	403.15	6.98E+00
ARSENIC TRICHLORIDE	AsCl3	261.75	403.55	8.27E+00
TITANIUM TETRACHLORIDE	Ti-Cl4	249.05	638	9.40E+00

Attempts were made to identify a suitable metallic element for use as the working fluid for the liquid droplet system; melting point and vapor pressure data for various metals are given in Table 3.6. Gallium, which has a melting point of 30° C and a vapor

Table 3.5 Common Substances with Acceptable Vapor Pressures at ~0° C (Yellow denotes substances with applicable temperatures between 0 ^{o} and 20° C). (Yaws, 1995)

		Temperature Range		TEMP (K) 273.15
NAME	FORMULA	Tmin	Tmax	Vapor Press (Torr)
FRANCIUM	Fr	267	879	1.99E-06
MERCURY	Hg	234.31	1735	2.01E-04
IODINE	I2	242	819.15	3.80E-02
HYDROGEN PEROXIDE	H202	272.74	730.15	2.76E-01
CHLOROSULFONIC ACID	CIH03S	193.15	700	5.31E-01
HEXACHLORODISILANE	Si2Cl6	277.15	412.15	7.51E-01
BERYLLIUM BOROHYDRIDE	BeB2H8	274.15	363.15	9.01E-01
OSMIUM TETROXIDE - YELLOW	OsO4	276.35	403.15	9.94E-01
HEXACHLORODISILOXANE	Si20Cl6	268.15	408.75	1.44E+00
THIONYL BROMIDE	SOBr2	266.45	412.65	1.58E+00
OSMIUM TETROXIDE - WHITE	Os04	267.55	403.15	1.62E+00
SULFUR MONOCHLORIDE	S2C12	265.75	411.15	1.73E+00
VANADIUM TETRACHLORIDE	VC14	247.45	697	1.81E+00
ARSENIC TRICHLORIDE	AsCl3	261.75	403.55	2.30E+00
TITANIUM TETRACHLORIDE	Ti-Cl4	249.05	638	2.73E+00
HYDRAZINE	N2H4	274.68	653.15	2.74E+00
PHOSPHORUS THIOCHLORIDE	PSC13	236.95	398.15	3.69E+00
DEUTERIUM OXIDE	D20	276.97	643.89	3.81E+00
CHROMIUM OXYCHLORIDE	Cr02Cl2	254.75	390.25	4.07E+00
DIIODOSILANE	SiH2l2	276.95	683.81	4.35E+00
WATER	H20	273.16	647.13	4.58E+00
VANADIUM OXYTRI CHLORIDE	VOC13	193.65	400	4.85E+00
STANNIC CHLORIDE	SnCl4	250.45	386.15	5.35E+00
IRON PENTACARBONYL	FeC505	266.65	378.15	7.39E+00
TETRASILANE	Si4H10	245.45	373.15	7.61E+00
TRIBROMOSILANE	SiHBr3	242.65	617.5	8.11E+00
PHOSPHORUS OXYCHLORIDE	POC13	274.33	378.65	8.90E+00

Table 3.6 Metal Vapor Pressure Data. (Eberl, 2004)

			Temperature at Vapor Pressure			
Element	Symbol	Melting Point	10^{-2} Torr	10^{-4} Torr	10^{-6} Torr	10^{-8} Torr
Silver	Ag	962	1027	832	685	574
Aluminium	Al	660	1217	972	812	685
Arsenic	As	817	277	204	150	104
Gold	Au	1064	1397	1132	947	807
Boron	B	2080	2027	1707	1467	1282
Barium	Ba	725	610	462	354	272
Beryllium	Be	1280	1227	997	832	707
Bismuth	Bi	271	672	517	409	347
Carbon	C	3550	2457	2137	1867	1657
Calcium	Ca	839	597	459	357	282
Cadmium	Cd	321	265	177	119	74
Cobalt	Co	1495	1517	1257	1067	922
Chromium	Cr	1857	1397	1157	977	837
Copper	Cu	1083	1257	1027	852	722
Dysprosium	Dy	1409	1117	897	747	625
Erbium	Er	1529	1177	947	777	649
Europium	Eu	822	611	466	361	283
Iron	Fe	1535	1477	1227	1032	892
Gallium	Ga	30	1132	907	742	619
Germanium	Ge	937	1397	1137	947	812
Mercury	Hg	-39	46	7	-44	-72
Indium	In	157	947	742	597	488
Potassium	K	63	208	123	65	21
Lanthanum	La	920	1727	1422	1192	1022
Lithium	Li	181	537	404	306	235
Magnesium	Mg	649	439	327	246	185
Manganese	Mn	1244	937	747	611	505
Molybdenum	Mo	2610	2527	2117	1822	1592
Sodium	Na	98	289	193	123	74
Niobium	Nb	2468	2657	2277	1987	1762
Nickel	Ni	1453	1527	1262	1072	927
Phosphorus	P	44	185	129	88	54
Lead	Pb	328	715	547	429	342
Palladium	Pd	1554	1462	1192	992	842
Platinum	Pt	1772	2097	1747	1492	1292
Rhenium	Re	3180	3067	2587	2217	1947
Rhodium	Rh	1966	2037	1707	1472	1277
Sulfur	S	113	109	55	17	-10

Table 3.6 (continued)

			Temperature at Vapor Pressure			
Element	Symbol	Melting Point	10^{-2} Torr	10^{-4} Torr	10^{-6} Torr	10^{-8} Torr
Antimony	Sb	631	533	425	345	279
Scandium	Sc	1541	1377	1107	917	772
Selenium	Se	217	243	164	107	63
Silicon	Si	1410	1632	1337	1147	992
Tin	Sn	232	1247	997	807	682
Strontium	Sr	769	537	394	309	241
Tantalum	Ta	2996	3057	2587	2237	1957
Tellurium	Te	450	374	280	209	155
Thallium	Tl	304	609	463	359	283
Titanium	Ti	1660	1737	1442	1227	1062
Tungsten	W	3410	3227	2757	2407	2117
Yttrium	Y	1523	1632	1332	1117	957
Ytterbium	Yb	819	557	417	317	247
Zinc	Zn	420	344	247	177	123

Table 3.7 Water Vapor Pressure Data. (Nave, 2005)

Temperature (C)	Vapor Pressure (Torr)		Temperature (C)	Vapor Pressure (Torr)
-10	2.15		40	55.3
0	4.58		60	149.4
5	6.54		80	355.1
10	9.21		95	634
11	9.84		96	658
12	10.52		97	682
13	11.23		98	707
14	11.99		99	733
15	12.79		100	760
20	17.54		101	788
25	23.76		110	1074.6
30	31.8		120	1489
37	47.07		200	11659

pressure in the ultra high vacuum range, was judged to be a suitable candidate. It was, nevertheless, decided that heating the droplet supply system would be problematic, thus water was used as a droplet substance for the initial study; Table 3.7 contains a list of vapor pressures for water at various temperatures.

Now that we had decided on a substance to use, we had to look at a way to get a droplet to grow on the end of a needle rather than shoot into the plasma chamber as a stream. Initially, we looked at a simple hypodermic syringe which was used to test the ability of the camera. This was not a viable option as the only way to do this was to place a thick rubber circle inside the Swagelok fitting in the top plate of the plasma chamber. This required a very fine needle to be able to push through and consequently a very small droplet was produced. Next we looked at actually installing the body of the hypodermic into the Swagelok valve. This had two separate results: first we discovered that the force of the vacuum pulling down in an 18 gauge needle was sufficient to overcome the friction of the plunger in the hypodermic; unless the plunger was held stationary, the water streamed into the plasma chamber. The second result was that the force necessary to sufficiently seal the vacuum chamber ultimately broke the body of the hypodermic.

Next based on results from an unrelated experiment where 1-2 atmospheres of pressure differential was able to be metered at a rate of 1-3 drops at a time we tried to utilize a combination of a stainless steel Swagelok very fine metering valve (Y) (1/4" tube fitting, with a Vernier handle) and a stainless steel Swagelok Toggle Valve (AH) (also with 1/4" tube fittings). A Teflon fitting was machined with a small hole bored lengthwise through it to accommodate an 18 gauge hypodermic needle press fit into the end; the outside of this fitting was a ¼" cylinder for half of its length and custom turned

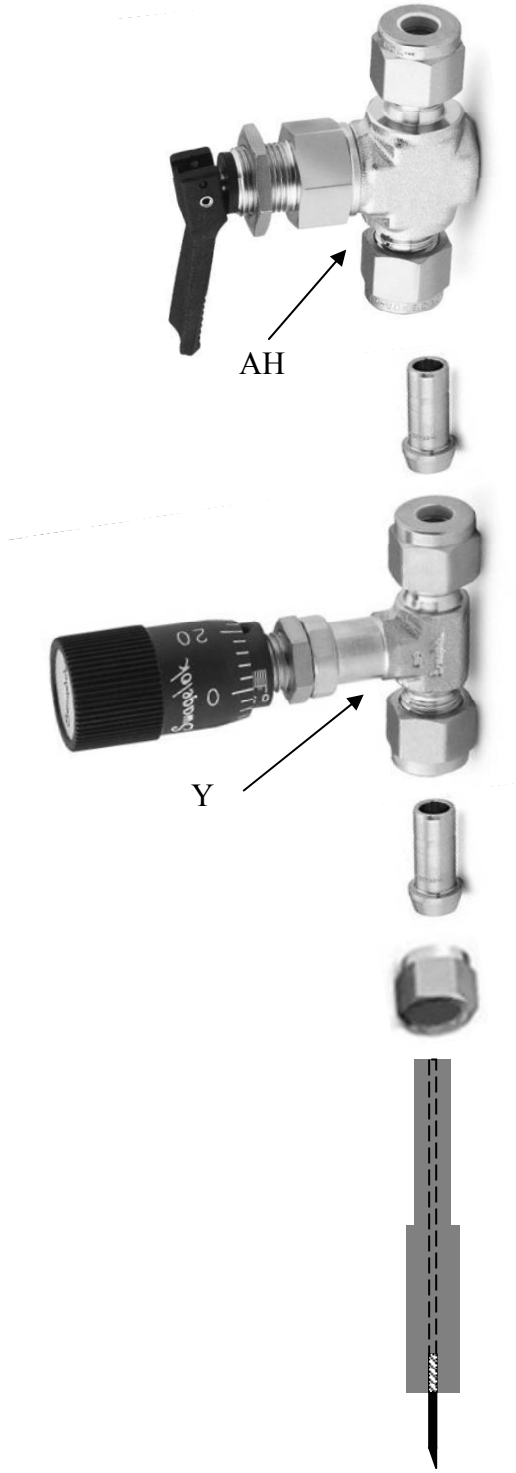

Figure 3.36 Exploded View of Intermediate Water System (Swagelok Caps Removed From Port Connectors and Placed on Valves to Show Relationship).

to fit inside a ¼” Swagelok port to port fitting that connected the valve system above to the Swagelok fitting in the top plate of the plasma chamber (Z). Several configurations were tried with the best being shown in Figure 3.36. With atmospheric pressure on both ends of this system one drop at a time could be metered in; however, at low pressures in the plasma chamber, droplets were difficult to control and further refinement was needed.

The first step of this refinement was to develop a way to draw a vacuum in the liquid supply in order to reduce the pressure head across the system. This was accomplished by taking a PYREX 500 mL sampling flask (X), attaching a vacuum hose (AG) to the sampling tube on the side, boring a ¼” hole in a #7 stopper, and placing a ¼“ copper tube (with a Swagelok nut on the outside end) through the stopper. In this manner the water could be attached to the top of the valve shown in Figure 3.36 and by changing the vacuum system as shown in Figure 3.37, a vacuum could be drawn on the water supply. This system was further refined by: fabricating a split ring and flange device to hold the stopper in place, placing a tee fitting and shutoff valve (AC) on the vacuum line to let air into the system as needed, and boring two more holes through the stopper, one for water inlet and a second for pressure measurement.

This last refinement was necessary in order to determine the pressure in the water supply and balance that with the pressure in the plasma chamber (Z). The water supply pressure is measured by two absolute pressure dial gauges (Figure 3.38); a large scale gauge (C) reading from 0 to 800 mm of Hg and a small scale gauge (Q) reading from 0 to 20 mm of Hg.

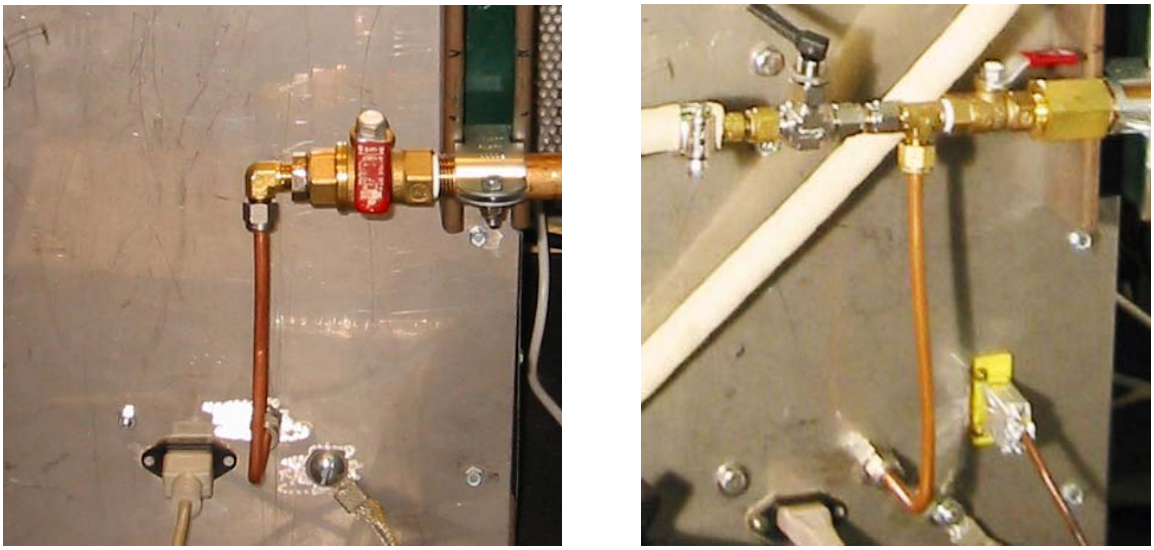

Figure 3.37 Intermediate Vacuum Configuration (Left) and Final Configuration.

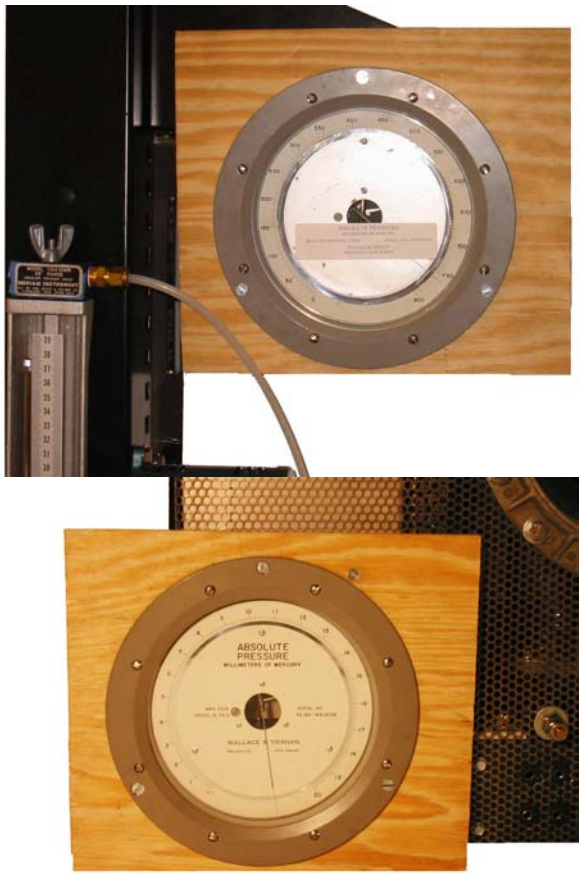

Figure 3.38 Liquid System Pressure Gauges. Large Scale (C-Top) and Small Scale (Q).

Note in Figure 3.37 that the Toggle Valve (AH) is no longer on the water valve system. This change occurred while developing the imaging system as it was seen that a faster response time to opening and shutting the top valve was needed. To accomplish this, the toggle valve (AH) was replaced with two valves: a pneumatically controlled, ¼”

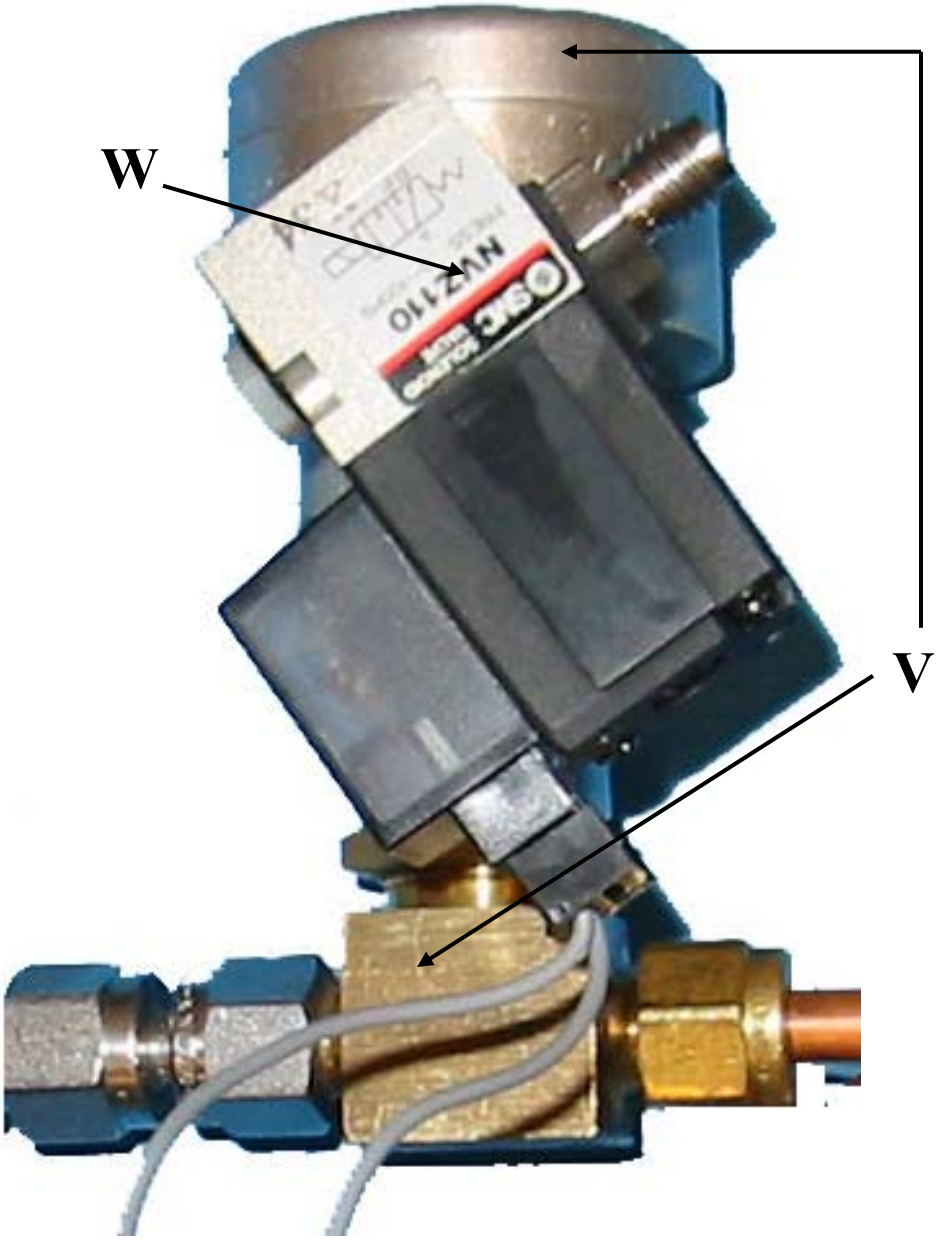

Figure 3.39 Nupro Shutoff Valve (V), and SMC NVZ110 Solenoid Valve (W).

tubing, Nupro B-4HK shutoff valve with a normal closed position (V), and a SMC NVZ110 solenoid valve (W) to control the Nupro shutoff valve (Figure 3.39). Activation of the SMC solenoid valve is accomplished by using a Micro Type Z bump switch (S) and a Micro Type-T mount both set in a custom built mounting block (Figure 3.40). The last new addition was a compressed air tank that is needed to run the pneumatic valve (V).

The complete liquid droplet generation system (minus the air tank) is shown assembled in Figure3.41. With this system, repeatable and controllable droplets can be generated and introduced into the plasma chamber; nevertheless, drops were extremely difficult to manage at low pressures. Figure 3.42 shows typical problems that were seen: air bubbles in the water droplets and droplets that were obviously too small. These problems started at ~75 torr and were highly evident in the 20-50 torr range. Based on these results it was decided that dissolved gases in the water were coming out of solution

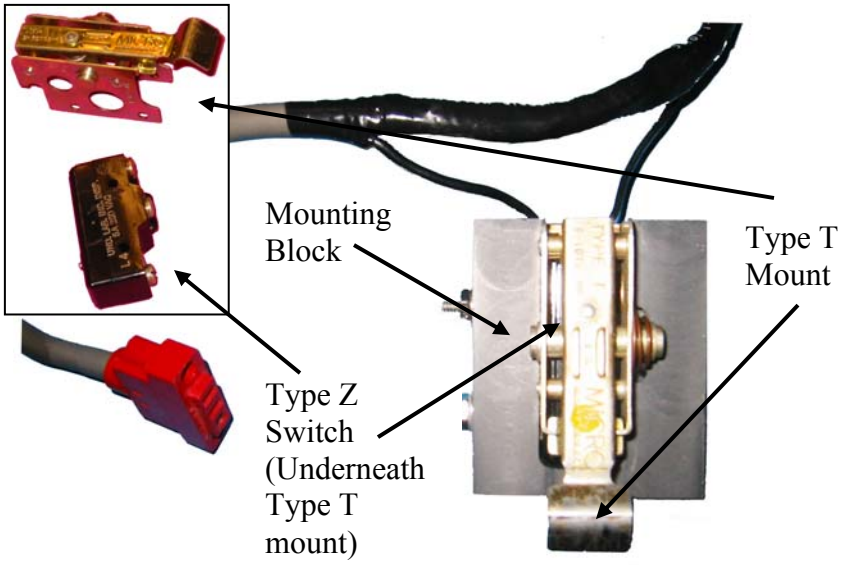

Figure 3.40 Micro Type Z Bump Switch (S) and a Micro Type-T Mount Set in Mounting Block. Inset Shows Both Items Unmounted.

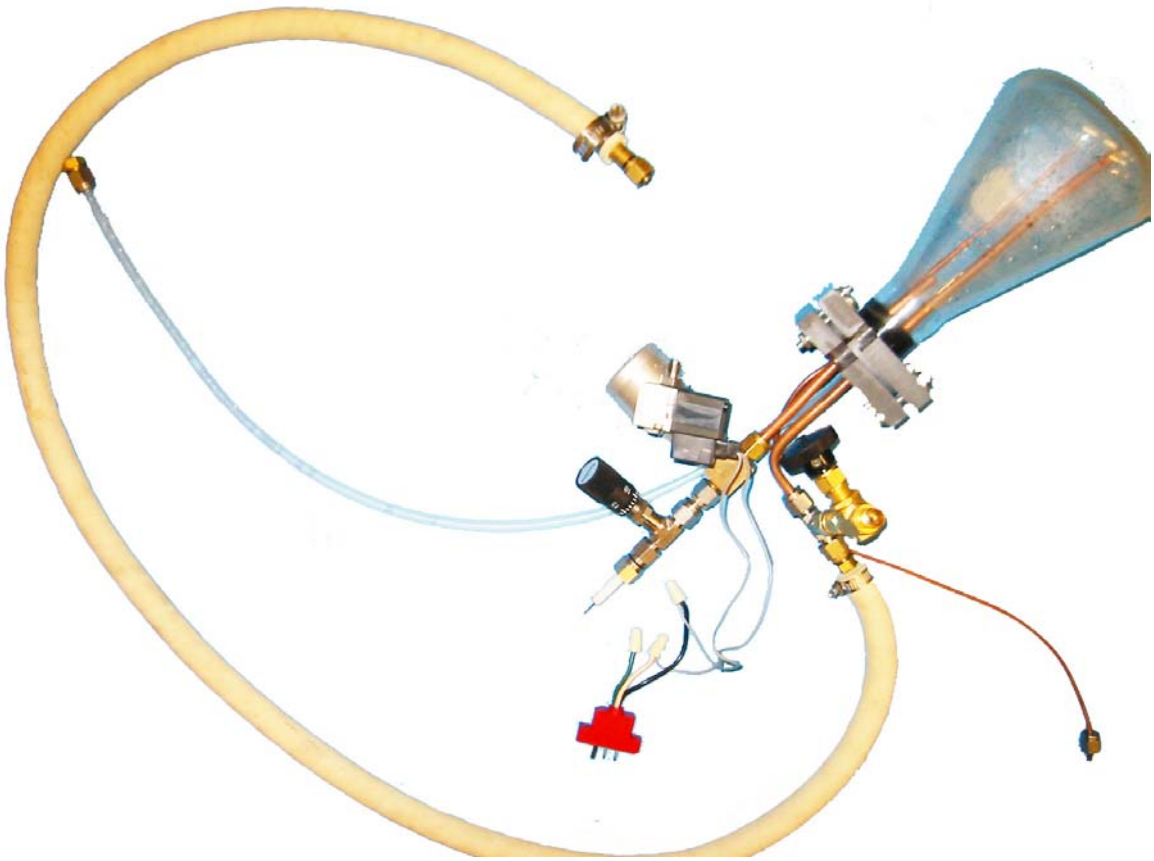

Figure 3.41 Complete Liquid Droplet Generation System.

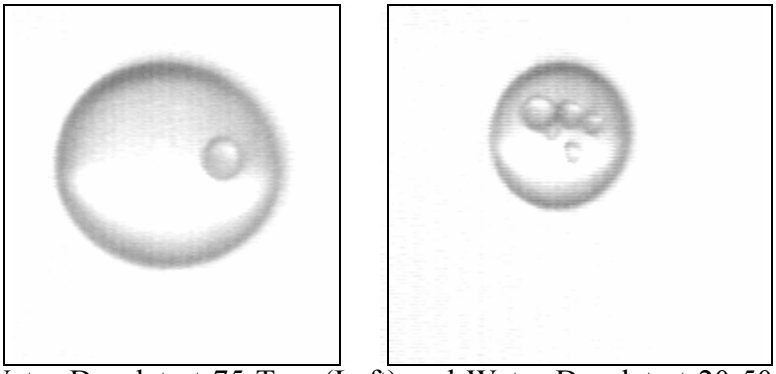

Figure 3.42 Water Droplet at 75 Torr (Left) and Water Droplet at 20-50 Torr (Scale is the Same).

at lower pressures and were causing these problems. The water was heated under vacuum conditions and kept boiling for ~20 min in order to remove the dissolved gasses. The water was then allowed to cool under vacuum. The procedure proved to be successful.

3.1.4 Imaging System

The last sub-system to be developed was the imaging system. Table 3.8 contains a listing of all components of the imaging system and Figure 3.43 shows the system schematic diagram. In this system there were two different configurations used to generate data; a single-view system shown at the bottom of Figure 3.43 and a dual-view system shown in the primary system configuration.

The key component of the imaging system is the camera (L); a Pulnix TM-6710CL (the CL denotes camera link compatible) 120 frame per second, electrically controlled exposure CCD camera was used (Figure3.44). The minimum exposure setting is $1/3200^{th}$ of a second and by using this and the next highest setting ($1/1600^{th}$ sec), it was possible to capture pictures of droplets as seen in Figure 3.42. The setting used resulted in a 200 x 640 pixel image (Figure 3.45); by doing this it was possible to set the long axis of the image parallel to the droplet fall path and zoom closely on the droplet.

The camera is attached to the computer system (A) by a camera link data cable. The cable leads to the input of the Road Runner frame grabber board. This board comes with a standard software package called SDK 4.0 which has basic software to run the board as well as some basic imaging applications. The two applications that are used consist of “R2View.exe” which allows the current view of the camera to be frozen and saved as a picture in BMP format; and “Flow.exe” which saves a series of images in system memory. This series can then be saved as sequentially numbered BMP files or as

Table 3.8 Detailed List of the Imaging System Hardware Components.

Item ID	Description	Manufacturer	Model	Serial Number
A	COMPUTER SYSTEM			
	Dell Computer with Intel Pentium III 497 MHz Processor with 1 GB RAM	Dell	Precision 410	04Z8L
	Road Runner Frame Grabber 32-bit/33MHz bus master PCI Bus Interface Board	Bitflow	R3-PCI-CL23-L R3	-
	Technical Computing Software	Matlab	6.5	-
H	Variable Autotransformer input 120 Vac output 0-140 Vdc rated for 10 amp 1.4 KVA	Staco Energy Products	3PN1010V	-
J	Camera Mount Plate	Custom Built	-	-
K	XY Translation Stage	Newport Research Corp	Model 400	-
L	CCD Progressive Scan Camera	Pulnix	TM 6710CL	000157
M	MIRROR SYSTEM			
	Mirror Mount 3.0" Angled	Edmund Optics Inc	NT36-481	-
	50MM RA Specialty Mirror First Surface Enhanced Aluminum	Edmund Optics Inc	NT47-005	-
	50 x 50mm Mirror 4-6 Wave First Surface Enhanced Aluminum	Edmund Optics Inc	NT43-876	-
N	ZOOM LENS			
	Manual Focus, Manual Iris, F1.8, 12.5-75mm, C-Mount Zoom Lens	Cosmicar	C31204	34625
	Close Up Set	Campro	49mm	-
AD	Diffuser	Custom Built	-	-
AE	300 Watt Dual Halogen Lights	Lumark	LWQ300	-
AQ	Dual View Camera Frame	Custom Built	-	-
AR	Single View Camera Mount Plate	Custom Built	-	-
AS	Single View Camera Frame	Custom Built	-	-
AT	300 Watt Single Halogen Light	Regent	EQ300WL	-
AW	Focus / Scale Rod	Custom Built	-	-

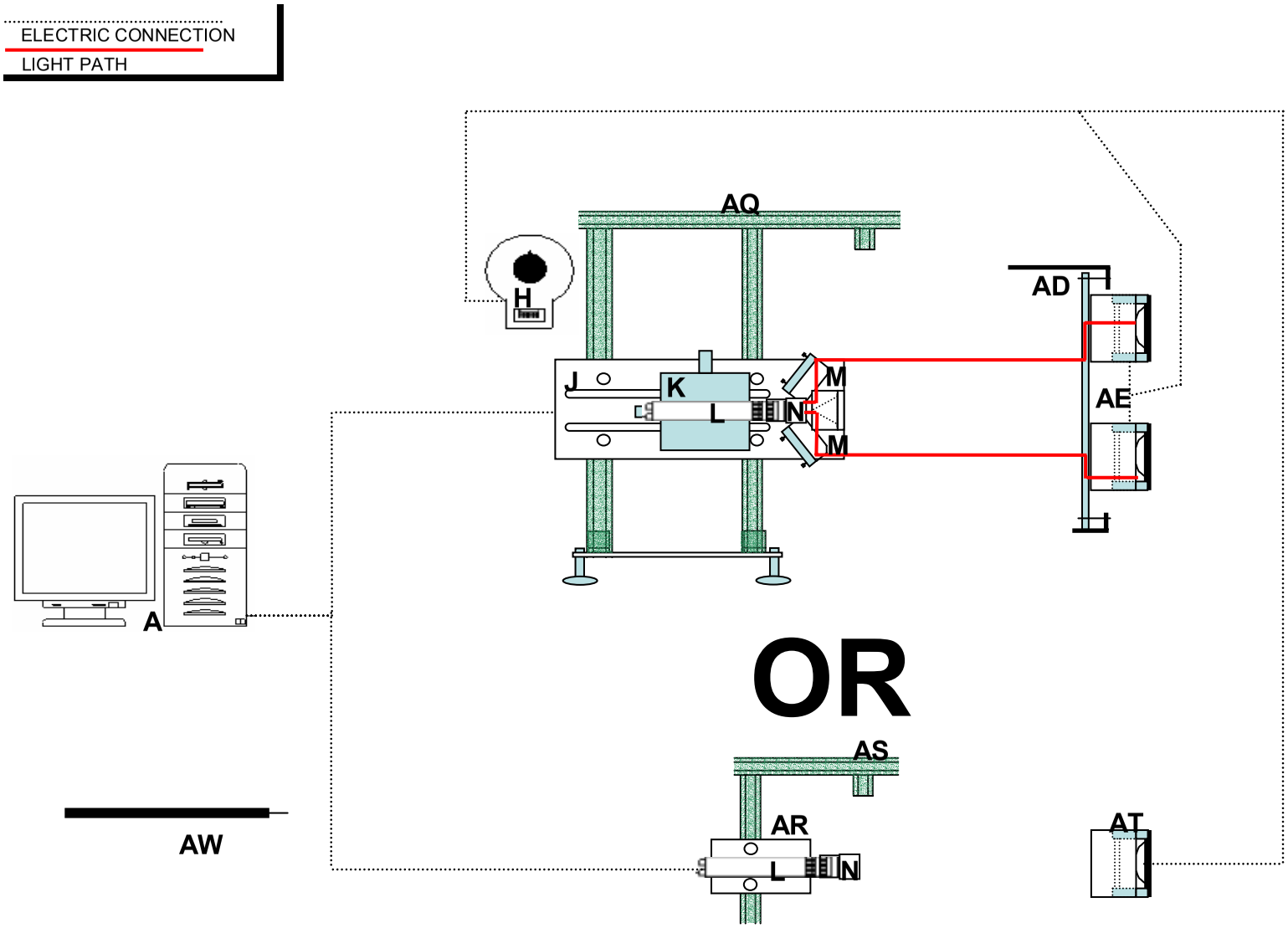

Figure 3.43 Imaging System Components.

Figure 3.44 Pulnix TM-6710CL CCD Progressive Scan Camera.

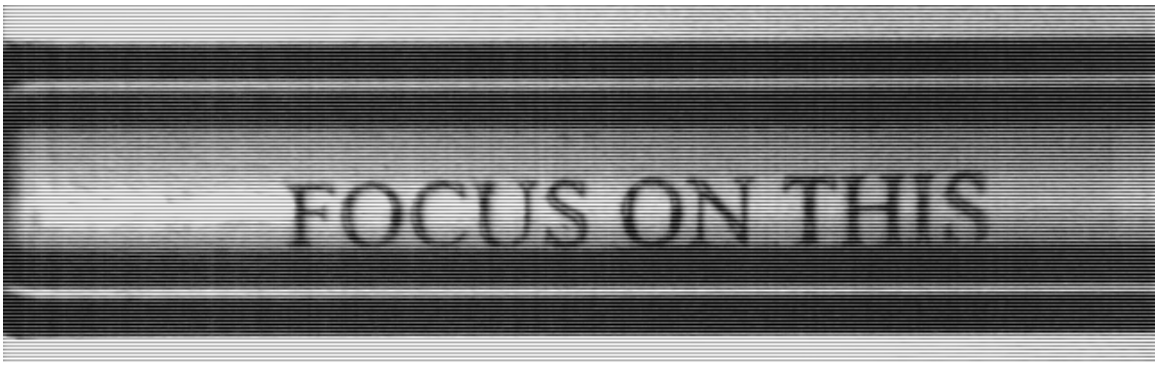

Figure 3.45 Unadjusted Example of Pulnix Camera (L) Output. Image is from the Single Image Setup with a +4 Closeup Lens on the Cosmicar Zoom Lens (N). Picture is of the ¼" Glass Focus Rod (AW) Which Gives a Sense of Scale. The Focus Letters are in Times New Roman Font at a Size 6. Use This As a Comparison (FOCUS ON THIS).

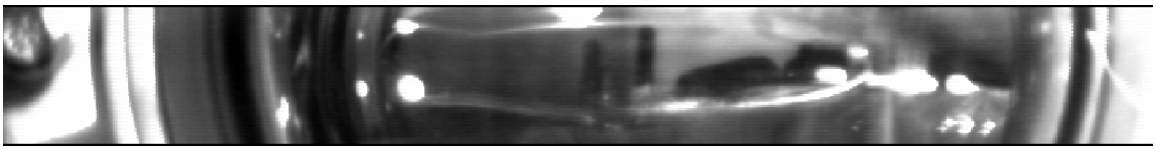

Figure 3.46 First Drop Movie Showing the Feasibility of Using the Pulnix Camera. The Top of the Viewing Window is on the Left. (AVI, 13M, jones_tony_l_200505_ms_ FirstDropletMovie.avi)

a movie in AVI format. Figure 3.46 shows the very first movie that was a result of tests to determine the feasibility of using this camera. There are two elements from this movie that are key indicators of what was needed in the imaging system: a very intense light source is necessary and a zoom lens is definitely required.

The camera is equipped with a C-mount for various lenses. Both imaging setups used a Cosmicar F1.8, 12.5-75mm, manual zoom lens (N). For the single image setup a +4 lens from a Campro closeup lens set is attached to the end of the zoom lens (N) and on the dual image setup the +2 lens from the set is utilized. The combination of a closeup lens and the Cosmicar manual zoom lens are collectively referred to as the zoom lens (N) for the remainder of this document. This combination resulted in an extremely versatile and adaptable setup.

The next part of the imaging system development was the lighting setup. For the initial trial, a halogen light was aimed into the plasma chamber from the right rear. This arrangement was not possible once the large Faraday cage (AF) was put in place. The first attempt to place light inside the large Faraday cage box involved mounting an 18“ long,15Watt, fluorescent light from Lights of America (model number UCL 7000-1) on the inside of the back panel (Figure 3.47). To ensure that no RF interference would be transmitted out, a grounded and shielded outlet was installed (Figure 3.22) in the back of the large Faraday cage (AF). This light resulted in poor quality photographs; the key problem being that the camera and light frequency were out of sequence. Fluorescent lights are designed to turn off and on rapidly, and the frequency of this was completely out of synch with that of the camera taking photos at 120 frames per second. The result is that the image in the AVI films appears bright and well lit and then fades to dimly lit and

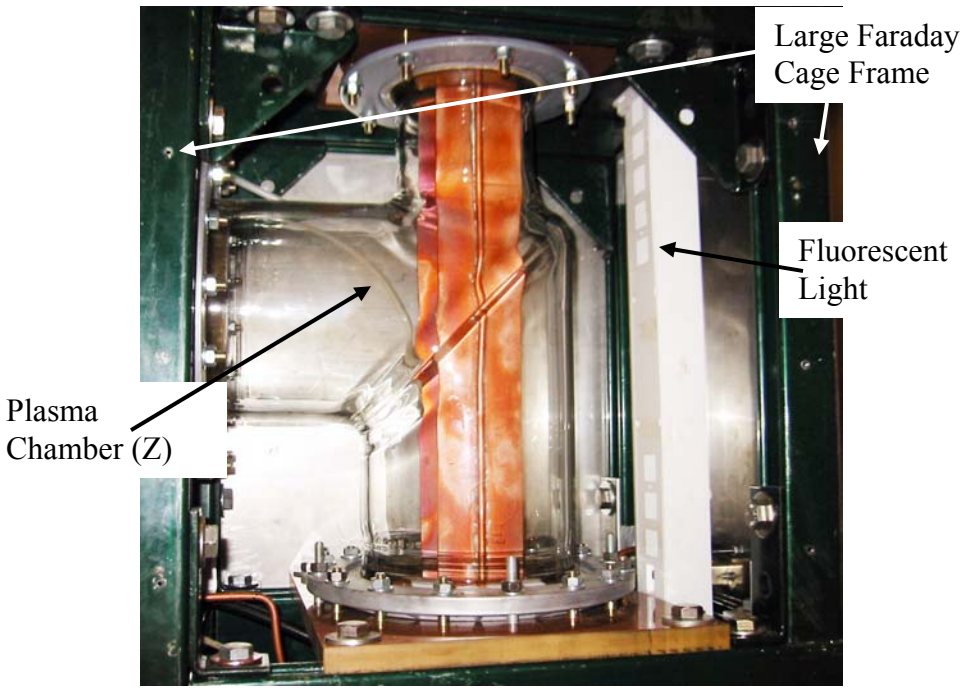

Figure 3.47 Initial Attempt to Light the Plasma Chamber (Z) Using a Fluorescent Light.

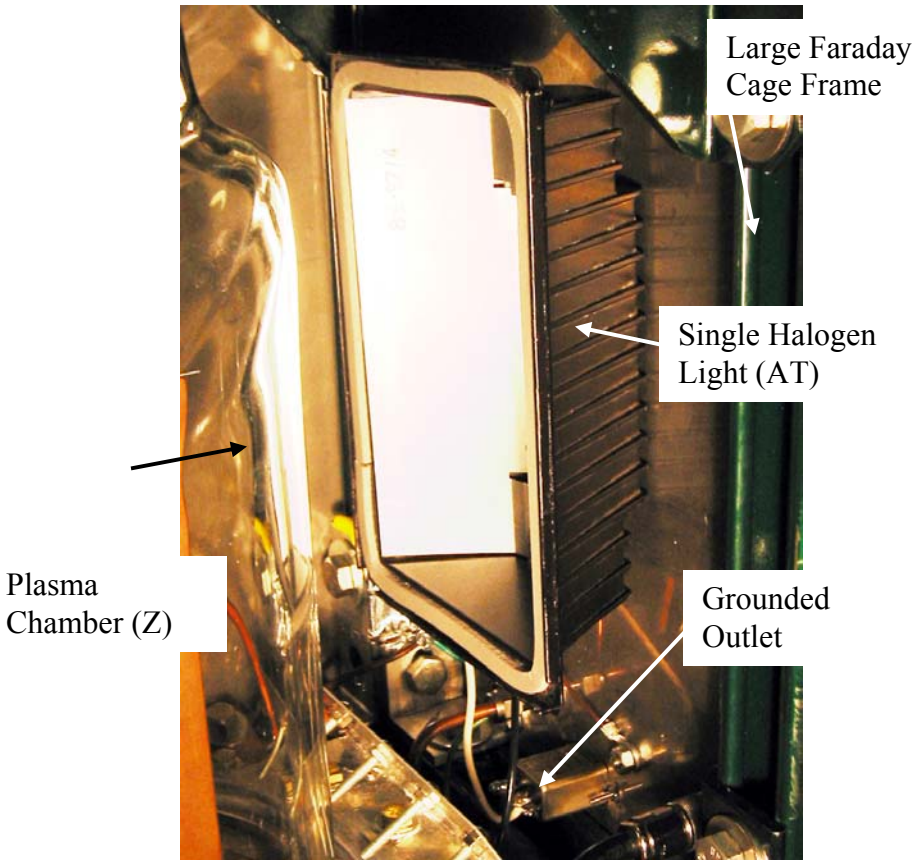

Figure 3.48 Single Halogen Light (AT) Mounted on Back Panel.

returns to brightly lit when illuminated by a fluorescent light.

The next attempt to light the chamber involved using a 300W Regent halogen light (AT). This light, again mounted on the back using the same grounded outlet (Figure 3.48), solved the problem, produced ample light, and in some cases, depending on the camera setting, too much light. Since there is an excessive amount of heat given off by the light, the light was connected to a variable transformer (H) in order to adjust the light level to the lowest usable setting (Figure 3.49). Figure 3.50 shows the first film recorded while trying to determine the best lighting scheme. Here drops were generated approximately where the center of the chamber would be (the plasma chamber (Z) had been removed for this test). The valve seen in the movie is a temporary setup used to trouble shoot vacuum leaks. By noticing that the drops are only visible when passing in front of the valve, we determined the need for a light diffuser to produce a more uniform light source.

Several items were tested to determine the best diffusing material; primary among these were sandblasted glass, specifically designed diffusing film, and white paper. None of these worked very well. It was finally determined that by accepting some light blockage, a 0.055 in thick sheet of Teflon, cut to fit (approx 6.8125”x14”) was the best way to produce uniform lighting. Brackets were fabricated to hold the diffuser (AD) away from the light and were able to generate very good photographs in the center of the viewing window; an example of which is shown in Figure 3.51. The camera itself was positioned in the center using a frame (AS) made of unistrut and a mounting bracket (AR) fabricated from aluminum. This single camera setup was utilized for several tests which will be covered in both the procedures section and results.

Figure 3.49 Staco Energy Products Model 3PN1010V Variable Autotransformer Input 120 Vac, Output 0-140 Vac, Rated for 10 Amp / 1.4 KVA.

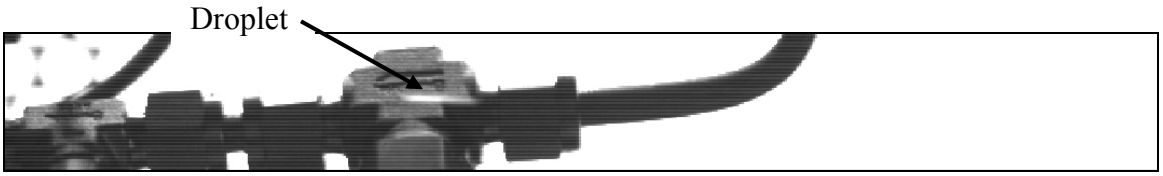

Figure 3.50 Vision Test Movie Taken while Developing Lighting Scheme. Notice Droplet in Front of Valve. (AVI, 52M, jones_tony_l_200505_ms_Vision_Test_ Movie.avi)

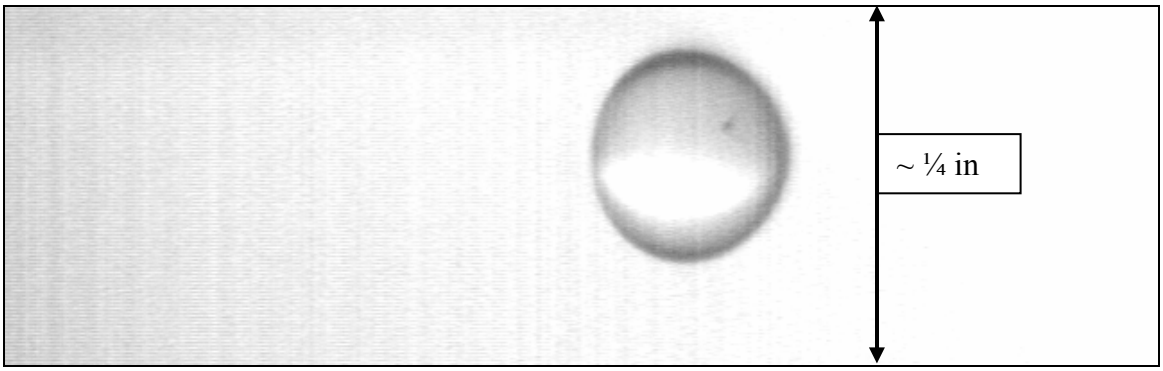

Figure 3.51 Example of View in Center with One Halogen Light.

Since the purpose of the experiment was to quantitatively evaluate the change in droplet size as it passed through the plasma, it was necessary to obtain pictures of the same droplet at the top and the bottom of the viewing window. To try to get this we first attempted to set the camera on a falling mount and synchronize the timing of the droplet release and the camera release. In Figure 3.37 we noted that the Toggle Valve (AH) was exchanged for a pneumatic valve (V) and solenoid (W) to get a faster response time to opening and shutting the water valve system; a change necessitated by this "falling camera" setup (Figure 3.52). Initially we tried to release the camera and droplet by depressing one switch; the switch would activate a Ledex rotary solenoid dropping the camera, and the SMC solenoid valve (W) releasing the droplet. This did not work as the rotary solenoid would bind and not reliably release the camera. We then tried to manually release the camera and have the camera mount activate the Micro Type Z bump switch (S) which would release the drop. This finally worked but the issue of timing presented a problem that was insurmountable; in order to have the droplet in the picture, the timing of the droplet release had to be within $1/30^{th}$ of a second. In chapter four we will discuss the

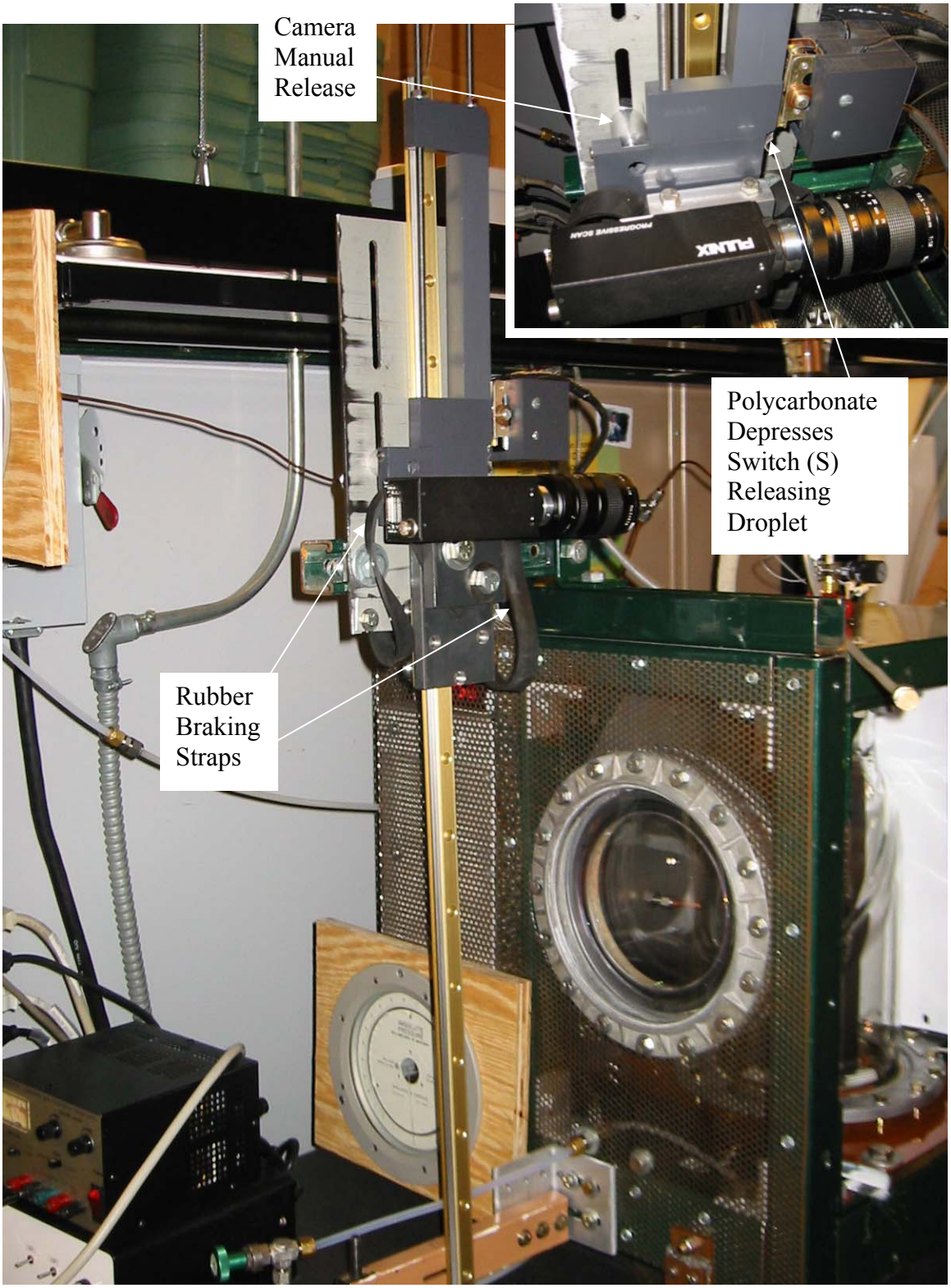

Figure 3.52 Falling Camera Setup. Inset Shows Close-Up View of Connections.

results of the trials that were conducted to determine the timing of the "falling camera" system but suffice it to say that the system did not reliably achieve this level of precision.

The next step, which was successful, consisted of developing a mirror system that allows two images to be seen by the same camera. Initial testing verified that mirrors could be used to look at two places within the plasma at the same time (Figure 3.53). Several components comprise the final mirror system (M) and Figure 3.54 shows how they are positioned. In the center aligned with the axis of the camera is a right angle specialty mirror made from first surface enhanced aluminum on two sides of a prism (Figure 3.55). This mirror splits the camera image into two views; both vertically oriented and diverging from the center. Two mirror mounts (Figure 3.56) are placed equidistant from the right angle mirror, top and bottom, and are each used to hold one 50 x 50 mm first surface aluminum mirror (Figure 3.57). L shaped brackets were built to hold the mirrors flush to the mirror mount face. These mirrors are fixed at approximately 45° to the views coming from the right angle mirror. The diagram in Figure 3.43 details the light path for the dual arrangement. There are two views feeding into the camera; one from the top of the viewing window and one from the bottom of the viewing window.

One of the key requirements for this arrangement is to ensure that the two mirror mounts are equidistant from the right angle mirror so that the focal length of each view is identical (if this is not the case then one image would always be out of focus). This was accomplished by machining a camera mount plate (J) on which all of the hardware was mounted (Figure 3.58). The mirror mounts are equidistant from the center of the camera mount plate (J). Three items (two right angle mirror holding blocks and a right angle mirror mount plate) hold the right angle mirror (Figure 3.54) such that its center is on the

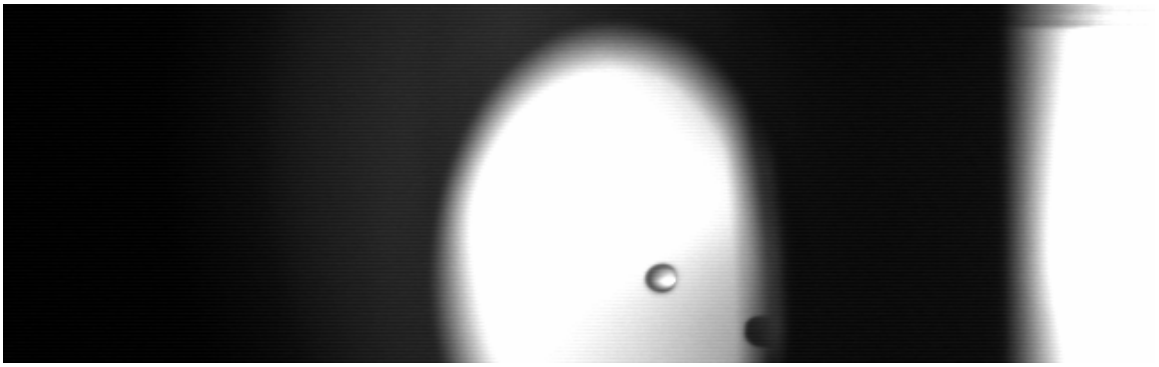

Figure 3.53 Initial Test of Mirror Concept. Droplet is Observed at Bottom of Viewing Window While Camera is Positioned in the Center of the Viewing Window.

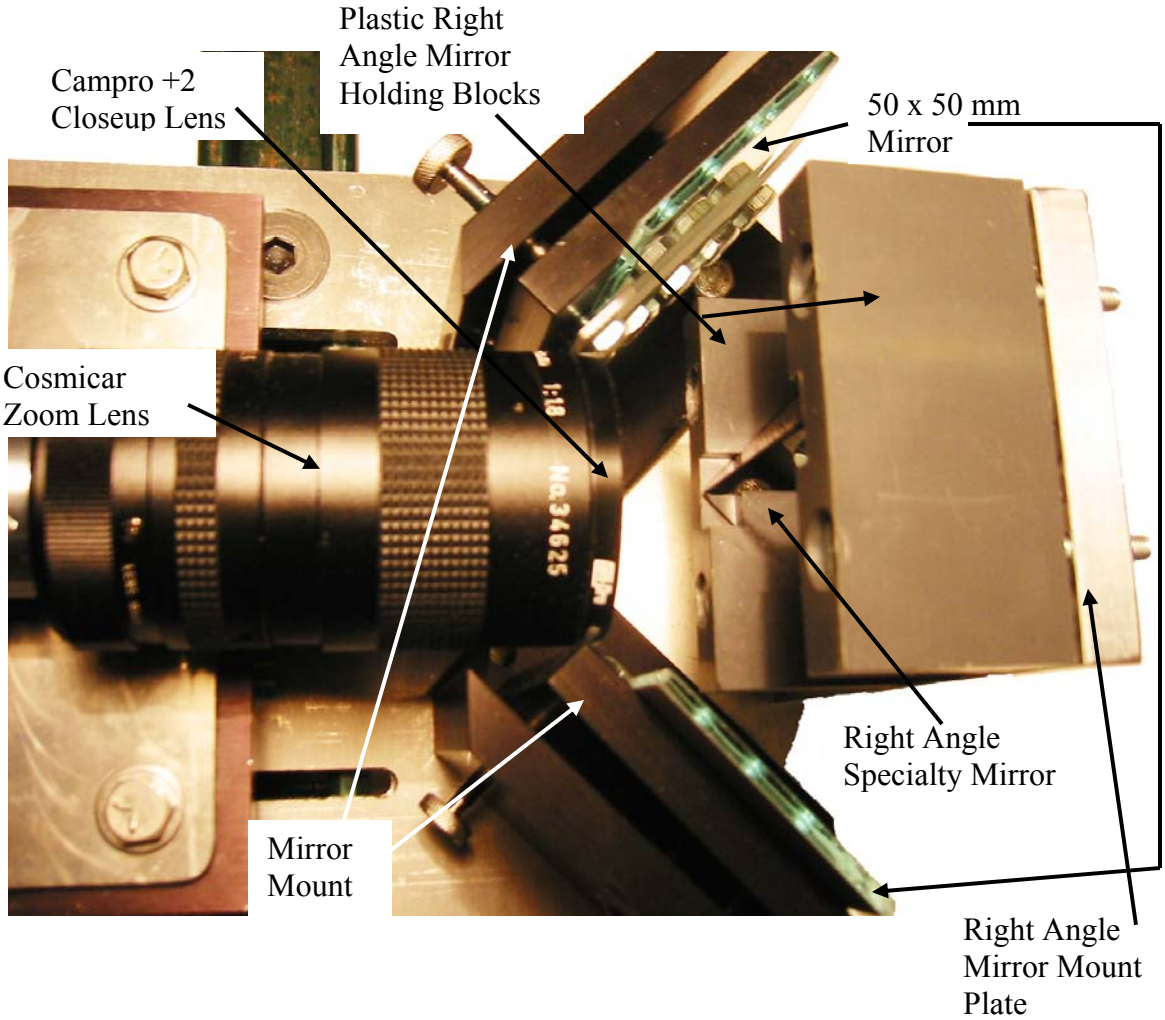

Figure 3.54 Mirror System (M) and Zoom Lens (N).

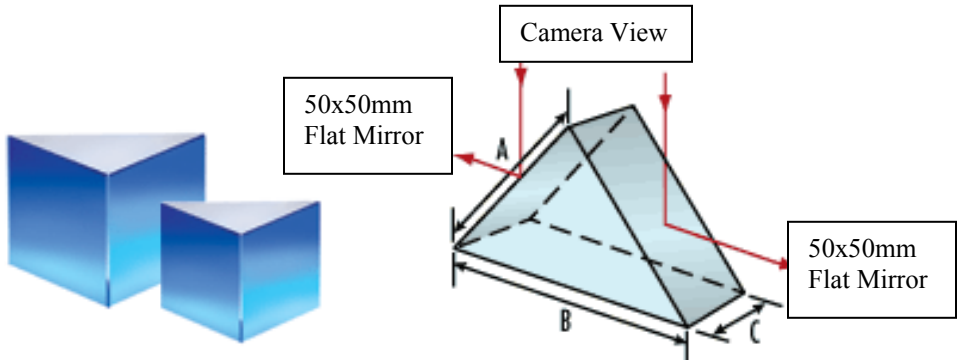

Figure 3.55 Picture of 50MM RA Specialty Mirror First Surface Enhanced Aluminum (Left) and Schematic of How the Light Paths are Bent. Dimensions for the 50mm Right Angle Mirror are: A = C = 50mm, and B = 70.7mm (Edmund, 2005).

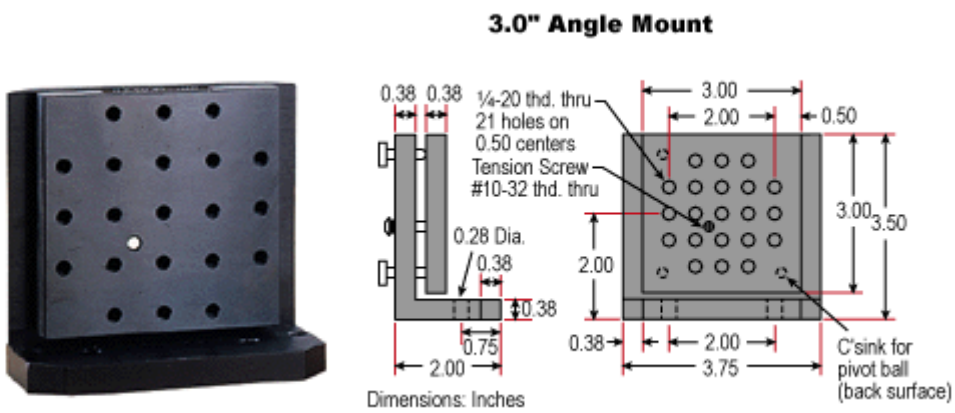

Figure 3.56 Picture of 3in Mirror Mount (Left) and Technical Schematic. The Two Adjustable Screws Provide Very Fine Control of What The Camera Sees in Each View (Edmund, 2005).

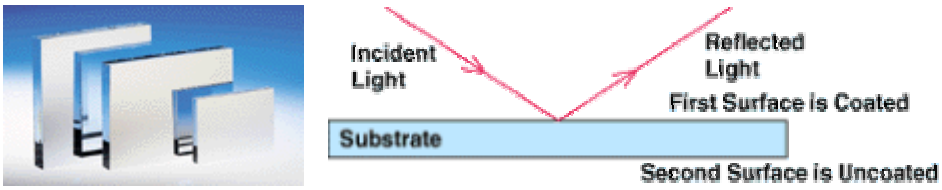

Figure 3.57 Picture of 50 x 50mm 4-6 Wave First Surface Enhanced Aluminum Mirror (Left) and Schematic Showing How the Mirror Works (Edmund, 2005).

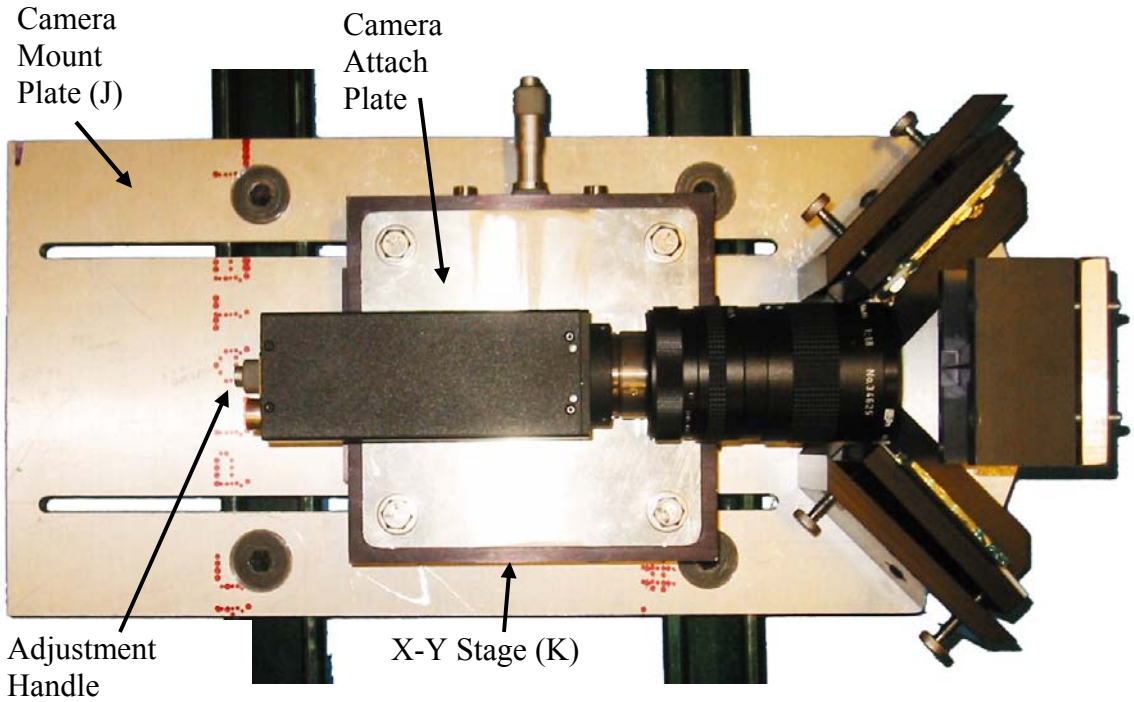

Figure 3.58 Camera Mount Plate with All Equipment Mounted. The Adjustment Handles for the X-Y Stage are Seen Coming From the Top and Left Side of the Stage.

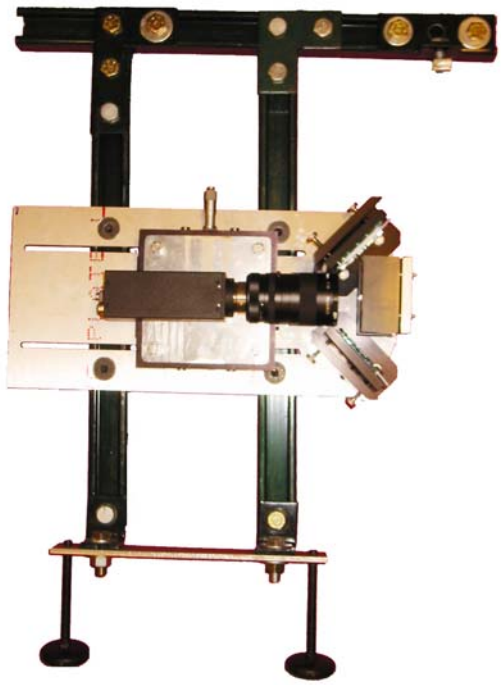

Figure 3.59 Camera Frame (AQ) with Camera Installed. The Nut on the Upper Right Attaches to a Unistrut Bar on the Top of the Large Faraday Cage (AF).

centerline of the camera mount plate (J). Rough positioning of the camera itself is accomplished through the slots milled along the long axis of the plate; for fine adjustment of the camera position, an X-Y translation stage (K) is mounted on the center of the camera plate. The camera (L) is attached to the stage (K) by means of a custom built attaching plate. Due to the weight of all of these items a separate frame (AQ) was built to hold the dual view camera system (Figure 3.59); this frame is attached to a length of unistrut on top of the large Faraday cage (AF). This attachment can be easily moved and the legs on the bottom of the frame (AQ) are adjustable; these, combined with the slots in the camera mount plate, provide a very flexible system. We were now able to view two positions at the same time.

An unexpected result of this setup is that the camera view is not split exactly in half. Figure 3.60 shows that the images from the top and bottom actually overlap with the center of the image, receiving input from both views. This is a benefit when trying to capture the droplet as we can zoom in closer and improve the resolution of the droplet picture. It is a problem because now we have uneven lighting, as the center of the image is receiving twice as much light as either the top or bottom. The fact that the light source is only 3 in long as compared to the 6 in viewing window compounded the problem; the light was strongest where it was also doubled. The magnitude of this problem was not readily evident until we began using edge finding software on the images. The droplets that happened to be captured in the center of the image were too faint to detect. We had to find a better way to light the chamber for the dual image mode.

The solution was to utilize two 300 watt halogen lights (AE). Due to space limitations we had to strip the lights out of their hard shells and use just the light sockets.

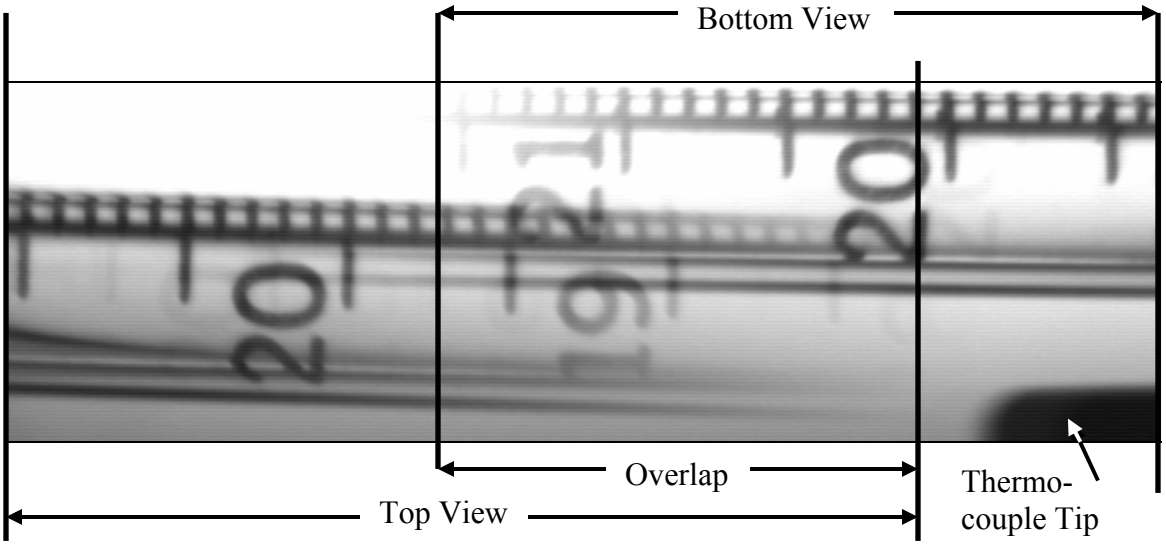

Figure 3.60 Dual Image with Top and Bottom Offset to Show Relation.

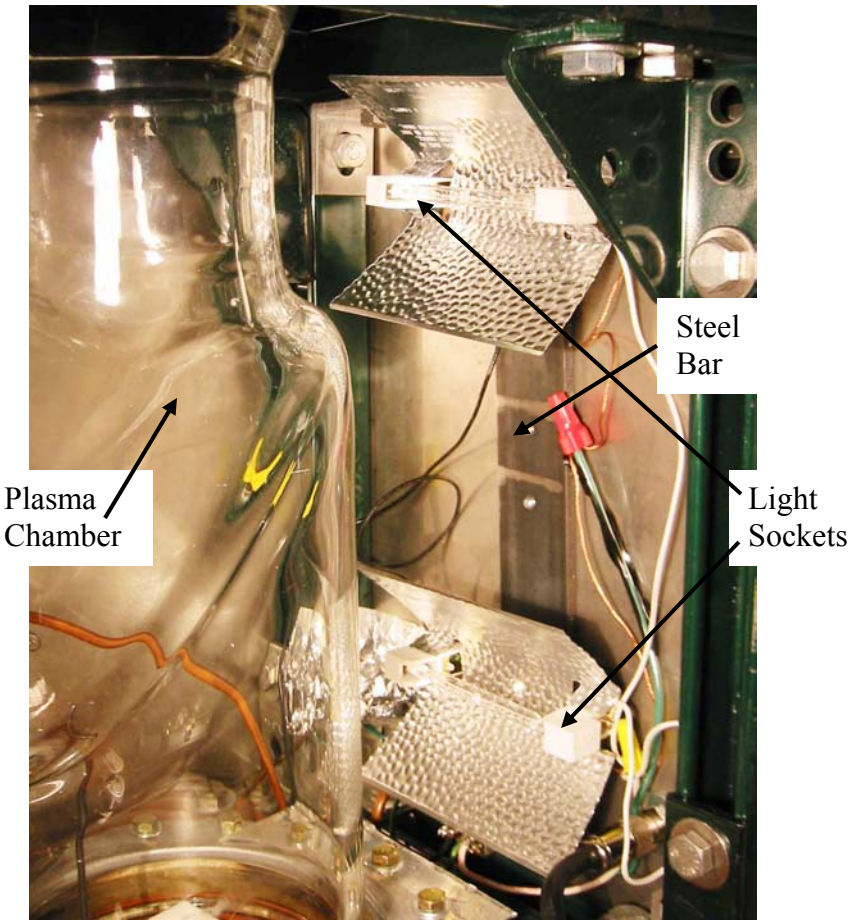

Figure 3.61 Dual Halogen Lamps (AE).

These were mounted to aluminum plates with lengths of magnetic tape on the back. A 0.25” thick steel bar 2”x14” was mounted on the back panel and the magnets were attached to this bar. By placing the two lights (AE) so that they are oriented horizontally, the lighting is generally uniform across the width of the image; by placing one light at the top and one at the bottom (Figure 3.61), the top and bottom of the image has increased light and the enforced relative darkness in the center is offset by the doubling effect of the mirrors. The only down side to this setup is that, now that the light is not shining directly into the mirrors, the amount of light is too low to use the minimum 1/3200th second exposure setting; however, the next higher one (1/1600th) provides excellent images as well (Figure 3.62).

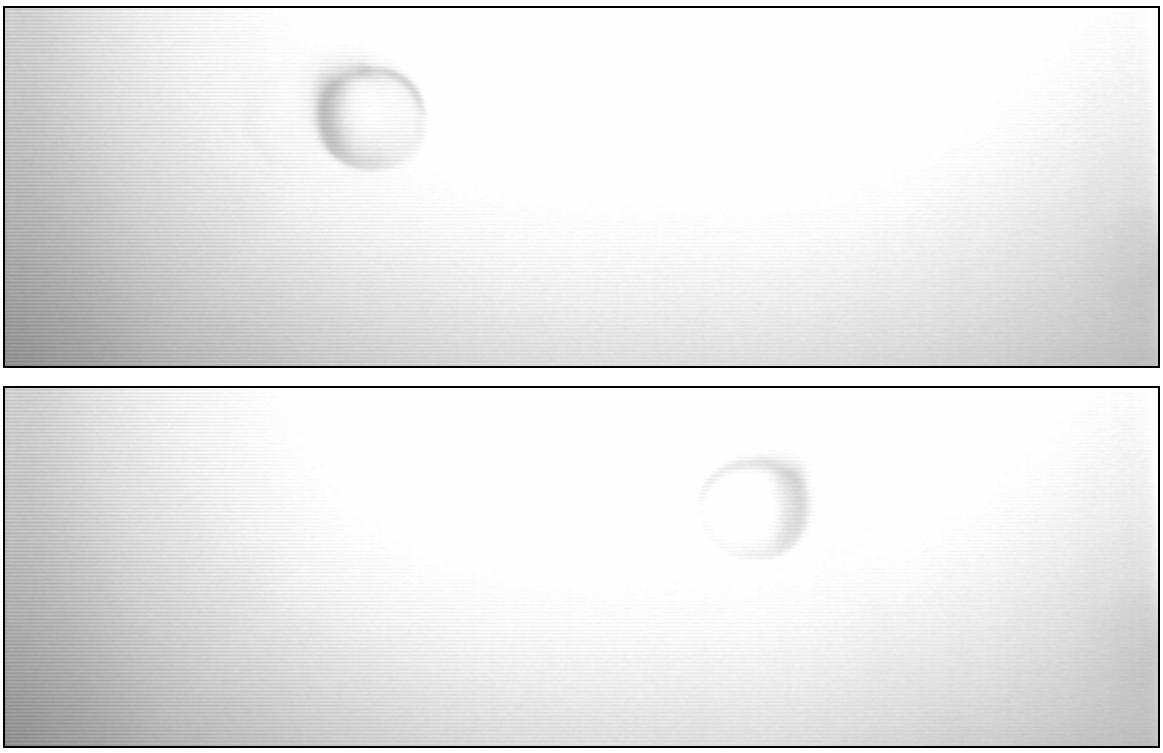

Figure 3.62 Examples of Camera Images with Dual Lighting System in Place. Photo of Top Image (Top) and Bottom Image (Drop is Falling from Left to Right).

For both the single and dual-view mode we needed a way to focus the camera on the location that the droplet would fall through. The easiest way to do this was to take a ¼“ glass rod (AW) and place it through the hole that the liquid droplet system entered. Due to the constrictive nature of the Swagelok fitting, the glass focus rod (AW) lined up nearly perfectly with the path of the water droplet. It was perfect with respect to distance from the camera so, by focusing on a transparency inside the rod with the words “FOCUS ON THIS” printed out in a size 6 font (Figure 3.45), the camera was perfectly focused on the center of the droplet. When taking pictures at the top and bottom of the viewing window, it was necessary to have a way to determine the distance between the two images. This was accomplished by permanently placing a scale with 1mm increments on the focusing glass rod (Figure 3.63). The other change that was made to the glass rod (AW) was to affix the focus tab to the end of the rod to minimize the distortion of looking through the glass.

The last component that has not been discussed is the computer system (A). One part of it was discussed earlier when we covered the camera as we discussed the Road Runner Frame Grabber Bus Interface Board, which is installed as hardware in the main computer system (Figure 3.64). The primary part of the computer system is the Dell Precision 410 computer with an Intel, Pentium III, 497 MHz Processor. The software used to run the frame grabber card was discussed earlier; but another key piece of software is Matlab 6.5 which is installed in the computer system as well. This computing software was used to analyze images and determine droplet volumes, the details of which will be covered in the next section.

Figure 3.63 Focus / Scale Rod (AW) Detail.

Figure 3.64 Computer System (A) Used for Experimental Data Collection and Analysis.

3.2 Experimental Procedures

3.2.1 Initial Apparatus Setup

For every test there were several details that required checking before detailed setup could begin. The first item that was checked was the reliability of the vacuum system. As the system was assembled, every piece was tested to see how well it would hold a vacuum. All tubing had to hold a pressure of 0.1 Torr for at least several hours before assembling the next piece. Once the chamber was placed in the system, the system was evacuated to a pressure of $\leq$ 0.1 Torr; it was then left overnight; sealing is judged to be adequate if the pressure does not rise above 5 Torr in a 16 hour period.

The second item checked was calibration of the digital pressure gauge. The vacuum pump was connected directly to the digital pressure gauge and the manometer, both were then read and adjustments made to the digital pressure gauge until it read the same ($\pm$ 1 Torr) as the manometer reading for pressures below 20 Torr.

3.2.2 Falling Camera Test

The first test conducted was to determine the timing involved in the falling camera setup. To do this the camera was removed from the rail carriage, mounted in the single view configuration, and the single halogen light was rewired to be triggered by the falling carriage. The timing between the depression of the trigger, indicated by the initiation of light from the halogen, and the first photo of the droplet at the center of the viewing window was determined as described in the next few paragraphs. This time lag was used to adjust the camera placement; fine tuning of the falling camera position was done using adjustments on the apparatus. A movie was captured that started with a blank screen, grew to a bright light and then showed a droplet falling through the center of the

viewing window (Figure 3.65). The first step in this test is to focus the image and align the camera; this is done prior to installing the liquid droplet generation system. The focus rod is inserted through the liquid droplet generation insertion point in the center of the top plate to both focus the image and provide an estimate of the size scale (this was prior to the 1 mm scale being applied to the rod). Using the "R2View.exe" application, an image of the complete rod is captured which gives the scale as 0.00153mm/pixal (0.25"/163 pixels) and an indication of how well the image is focused (Figure 3.66).

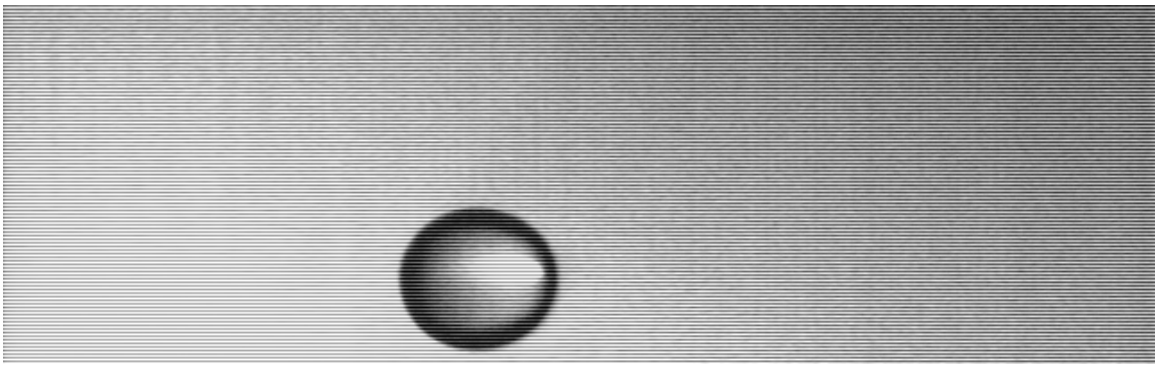

Figure 3.65 Falling Camera Test Movie, Trial #3 (Frame #65 Shown). (AVI, 9M, jones_tony_l_200505_ms_FallingCameraMovie_10Dec#3.avi)

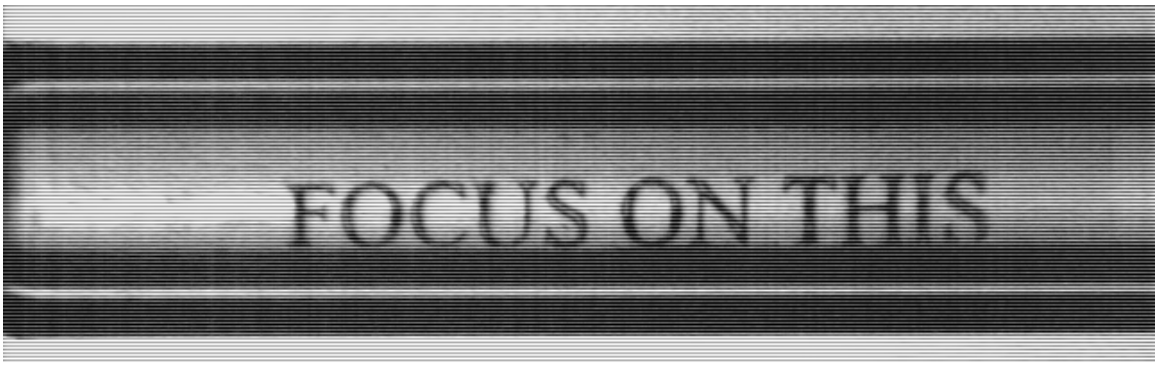

Figure 3.66 Focus Image for 10 DEC, 2005 Falling Camera Test Showing ¼" Diameter Focus Rod for Scale.

To ensure uniform droplet size prior to triggering, the bump switch (S) was depressed (with the Vernier handle completely open) to fill the valve bodies (V & Y). The Vernier handle was turned slowly until a droplet formed and fell. Once the droplet detached, the reading of the Vernier handle was recorded and the handle was turned for 4.76 turns (this figure was arrived at by dropping several drops and determining an average number of turns). This resulted in a droplet grown on the end of the needle but still not falling.

The camera (L) was triggered through the "Flow.exe" application to start recording a movie, the rail carriage was allowed to fall (triggering the single halogen light (AT) and the pneumatic shutoff valve (V)), and the images were stored to the hard drive of the computer. This procedure was performed 33 times. By watching the movie, the approximate frame of first light and the first frame showing a droplet were determined. These images were saved as bitmaps and the pictures were placed in a Microsoft powerpoint presentation (Figure 3.67). By completely darkening the lab and viewing the powerpoint slide show, the frame of first light can be determined to the nearest frame. In the given example the first apparent light shows after frame #9. This was done on 15 of the 33 data sets as it became apparent after a few trials that this setup would not have the necessary precision to synchronize the fall of the camera with the droplet.

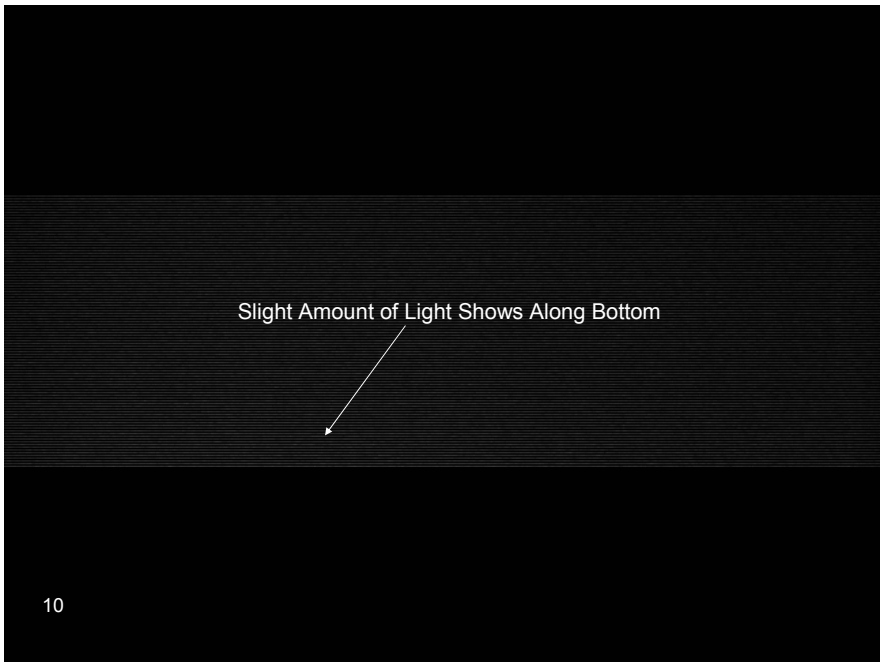

Figure 3.67 Determination of First Appearance of Light. Frame Ten from Trial #3 of the Falling Camera Test Shown. (AVI, 17M, jones_tony_l200505_ms_FallingCameraLight Determination_10Dec#3.avi)

3.2.3 Droplet Generation Test

The next test performed was to determine the repeatability of the fluid droplet generation system. For this test, the camera (L) was placed in the single-view configuration in the center of the viewing window and the image was aligned, focused, and a scale of 0.00113 mm/pixel was determined by using the 1mm markings on the scale/focus (AW) rod. The bump switch (S) was depressed (with the Vernier handle completely open) to fill the valve bodies (V & Y), the camera was triggered to begin recording a movie, and the Vernier handle was turned slowly until a droplet formed and fell. The movie was observed to determine the frames (one or two) that contained pictures of a droplet; these frames were saved as raw data. For each successful picture, the pressure was recorded from both the manometer (B) for the plasma chamber (Z) pressure and the two dial pressure gauges (C & Q) for the fluid supply flask (X) pressure.

The only exception to this was for the lower pressure measurements where the dial pressure gauges had a gap and readings were unreliable.

The above process was conducted at various pressures. In order to ensure that the pressures in the fluid supply (X) and the plasma chamber (Z) were equal, the vacuum pump (AB) was operated until the desired pressure was achieved; the pump shutoff valve was closed, and the pressure was allowed to equalize. For tests at atmospheric conditions no pump was utilized and the readings were all at the same pressure; under vacuum conditions, leaks caused the pressure to vary. The pump was operated until the lower pressure was reached and was turned off; data was collected until the pressure reached the upper desired pressure and the pump would be operated until the chamber was at the lower pressure again. This process was repeated until the desired number of data points was obtained; the utilized ranges, based on the manometer (B) readings, were: 245-333 Torr, 67-112 Torr, and 31-47 Torr.

The series of pictures were then fed into Matlab 6.5 and manipulated to get an estimate of the volume; there are seven matlab code files which control this process (the text for these codes is contained in Appendix C). Dropcomparison.m is the overall program that calls out each of the subroutines, tracks and records the results of each loop, and determines the standard deviation, using a built in matlab code. The first subroutine, Scale.m determines the scale of the image by reading in the scale bitmap image and receiving user input on the number of 1mm markings contained and the number of pixels covered. The pixel count from each scale image is determined by finding the centerline of the two outside lines in the scale image and calculating the difference between the two. This is the only source of bias error as the results of this calculation are applied to all

volume calculations in each trial. Detailed looks at the scale image for all trials show that this bias uncertainty (U_b) ranges from $7.0*10^{-6}$ in/pixel to $9.1*10^{-6}$ in/pixel (Table 3.9). These values were determined using $\pm$ 1.2 pixels as the uncertainty for the pixel count and $\pm$ 0.1 mm as the uncertainty of the scale rod.

Table 3.9 Scale Bias Errors.

	Length		**Pixels**	**Scale**	**Scale U_b**	
Trial	**mm**	**in**	**#**	**in/pixel**	**mm/pixel**	**in/pixel**
ATM	17	0.669	598	1.13E-03	1.8E-04	7.0E-06
300						
75						
20-50						
Degas	18	0.709	598	1.19E-03	1.8E-04	7.0E-06
Top	29	1.142	525.5	2.17E-03	2.3E-04	9.1E-06
Bot	30	1.181	543	2.18E-03	2.2E-04	8.8E-06

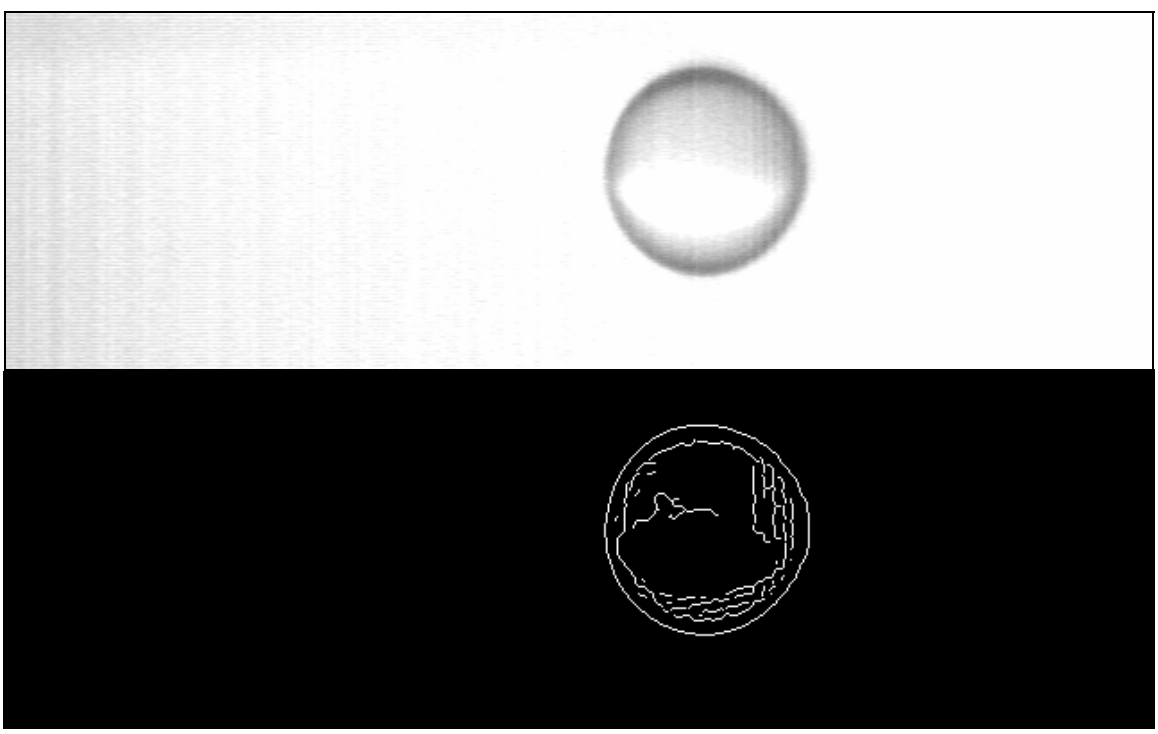

Figure 3.68 Sample Results of Edgefind.m Subroutine. Original Raw Data Image (Top) is Converted into a Binary Image Showing the Edge of the Droplet.

Next, the Edgefind.m subroutine reads a droplet image and returns a binary bitmap figure that is the edge of the droplet. This uses an internal matlab routine called edge.m which takes an intensity image as its input, and returns a binary image of the same size, with 1's where the function finds edges and 0's elsewhere; it is set to use “The Canny Method” to find the edges. This method finds edges by looking for local maxima of the gradient of an image. The gradient is calculated using the derivative of a Gaussian filter. The method uses two thresholds, to detect strong and weak edges, and includes the weak edges in the output only if they were connected to strong edges. This method is therefore less likely than the others to be "fooled" by noise, and more likely to detect true weak edges. When using Edgefind.m, the user adjusts these thresholds, in an iterative manner, until a circular drop appears (Figure 3.68).

Once the user is satisfied with the edge image, the next subroutine, Fillup.m is initiated. Here the two outermost “1’s” of each horizontal pixel row were determined and the values in between were converted to “1’s” as well. This results in a binary two-dimensional projection of the droplet. The next subroutine, Reduce.m, cuts the extraneous parts of the image away to reduce the amount of data that the remainder of the program must analyze (Figure 3.69).

Figure 3.69 Example of Output from Reduce.m. Compare to Figure 3.68 on Previous Page.

The last two subroutines are used to calculate the volume from this two-dimensional image. DropStats.m uses an internal matlab function, regionprops.m, which calculates the major axis, minor axis, orientation, eccentricity, and solidity of the filled in image. This subroutine then saves each parameter as a separate variable to be stored by Dropcomparison.m. The last of the subroutines, VolumeCalc.m, asks for user input to determine if the droplet should be rotated about the major or minor axis; if the droplet is compressed then rotation about the major axis is appropriate, if elongated rotate about the minor axis (Figure 3.70). The subroutine uses the standard volume for an ellipsoid. All of these subroutines were automatically run on each image (except for scale.m which is only operated on the scale image) in a loop. At the end of the loop an average volume and standard deviation were calculated.

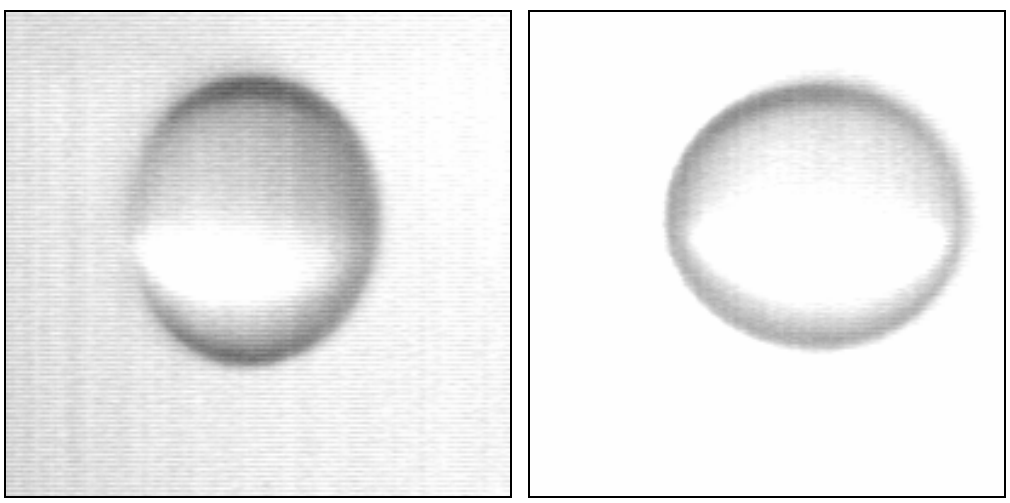

Figure 3.70 Examples of Droplets that are Compressed (Left) and Elongated.

3.2.4 Degassed Liquid Droplet Generation Test

In section 3.1 the method for degassing water was discussed; once the water was

degassed, it was placed in several nalgene bottles, which were numbered in the order that they were drawn from the degassing chamber, and sealed with as little air in the nalgene bottles as possible.

The testing procedure performed using degassed water was identical to the test performed for droplet generation testing with one exception; getting the degassed water into the fluid supply. To accomplish this, the plasma chamber and the water supply were both placed under vacuum (~20 Torr absolute pressure); a nalgene bottle containing the degassed water was placed near the end of the plastic tube leading into the fluid supply (X). The nalgene bottle was opened, the Swagelok cap on the plastic tube was removed, and the tube was rapidly placed into the nalgene bottle; the vacuum in the fluid supply drew the degassed water in. From this point on the procedure for the 20-50 Torr range was followed. By using degassed water acceptable results were generated at these intermediate pressures.

3.2.5 Dual-View Droplet Size Test

Once acceptable results with the droplet generation were produced; testing was necessary to determine the abilities of the dual-view imaging system. For this test, normal water was utilized under atmospheric conditions to focus the investigation on the abilities of the imaging system. The camera (L) was set up in the dual view mode, the image was aligned, focused, and a scale of 0.002175 mm/pixel was determined by using the 1mm markings on the scale/focus (AW) rod and the Scale.m subroutine. Additionally it was determined that the distance from the top of the upper view to the bottom of the lower view was ~ 5.87 inches, nearly the entire available length. The bump switch (S) was depressed (with the Vernier handle completely open) to fill the valve bodies (V & Y), the

camera was triggered to begin recording a movie, and the Vernier handle was turned slowly until a droplet formed and fell. The movie was observed to determine the frames (~10) that contained pictures of the droplet passing across the viewing window; these frames were saved as raw data. The pictures were saved so that their frame relationships were preserved; the default file naming system for the camera is to place six zeros followed by the frame number. For example, if frame numbers 15-23 contained the desired data for trial #X, the file name typed in would be Date#X and the computer would have 9 bitmap files named: Date#X0000000, Date#X0000001, Date#X0000002…Date#X0000009. These files would be quickly analyzed, pictures from the middle frames with no view of the droplets would be deleted, and the extraneous zeros would be erased so that a file name would be 15FEB#3-8 denoting the 8th frame of the third experiment.

The data was divided into top and bottom views, and the separate data sets were analyzed using modified versions of the seven matlab files discussed in 3.2.2. There were two key modifications required: the ability to screen out the tip of the thermocouple which can be seen in the bottom pictures (Figure 3.71) and the ability to adjust the Edgefind.m and Fillup.m files so that a user could leave some extraneous parts on the edge picture and filter these parts out during the fillup processing. The last modification is a result of having too much light near the center of the viewing area; periodically, the droplets in the bottom view would be captured close to the center of the captured image and the edge program would have difficulty finding the edge at the top of the droplet (Figure 3.72).

Two things were done to alleviate this problem. First the Fillup.m program was adjusted to allow the user to cut away unwanted leftover portions of the edgefind.m program which allowed a lower threshold to be set (Figure 3.73). If this didn't work then the image was opened in Microsoft paint, zoomed in until individual pixels were visible, and the pixels at the top of the droplet were darkened to allow the edge to be found by the computer (Figure 3.74). Through a combination of these two methods, all of the droplets were analyzed and the volumes corresponding to the top and bottom images were compared.

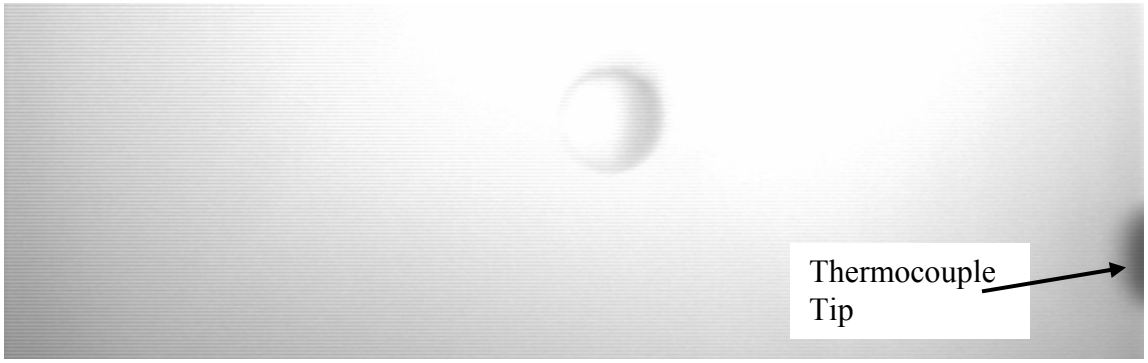

Figure 3.71 Example of Bottom View from Dual-Image Test (15FEB#4-8).

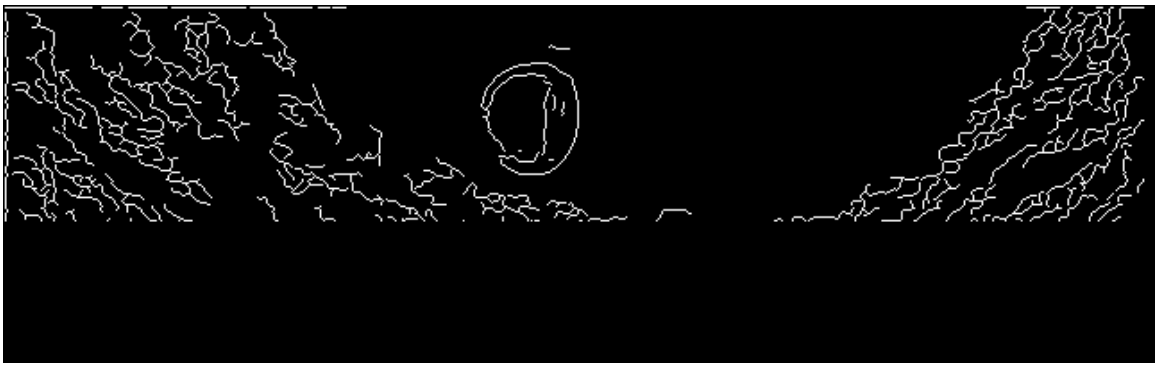

Figure 3.72 Example of Incomplete Droplet with Threshold set to 0.15 (15FEB#8-8).

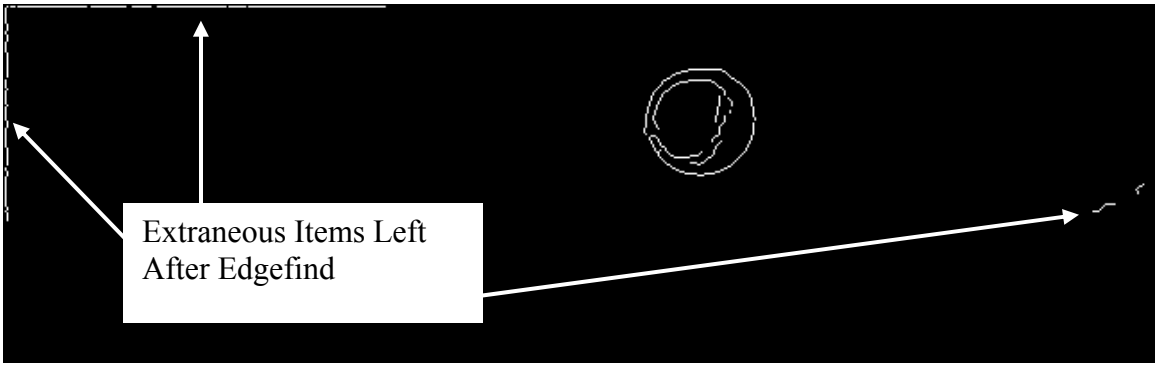

Figure 3.73 Example of Lowering Threshold (From 0.3 to 0.2) to Get a Circle Leaving Unwanted Items (Example Shown is 15FEB#6-8).

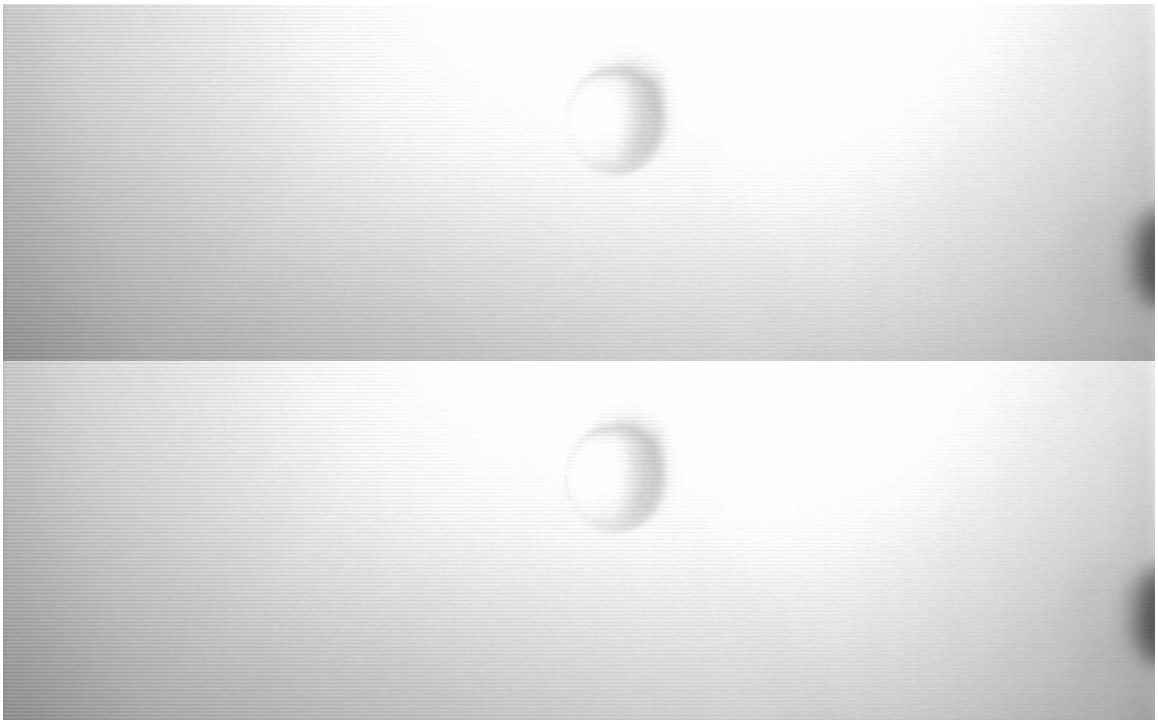

Figure 3.74 Comparison of Original (Top) and Altered Photos (15FEB#30-8).

CHAPTER 4

RESULTS AND DISCUSSION

This chapter includes the results of all tests conducted during this investigation. As indicated earlier, the primary outcome of this thesis was the design, construction, and testing of an experimental test facility which allows the behavior of single liquid droplets within a low-temperature, low-pressure plasma to be investigated. The results will be discussed in the order that the trials were conducted. Primarily, the results show that reproducible drops can be generated and the dual image collection system is capable of producing reliable images of a droplet as it enters and exits the plasma.

4.1 Falling Camera Test

Thirty-three total trials were conducted at atmospheric pressure; only 15 trials of the 33 were completely analyzed because after a few sets it became quickly apparent that the falling camera system would not be precise enough to synchronize the descent of the droplet and camera. Trials 1-2 were ignored due to a lack of uniformity in the droplet setup. From rough tests while developing the lighting system, it was found that the time for a droplet to pass across the viewing window was 8-9 frames (~0.066-0.075s). Looking at Table 4.1 the fall times varied from 0.2083s to 0.4583s with an average time of 35.7s and a standard deviation S = 0.0802s; the standard deviation of the time is greater than the time for the droplet to pass across the entire viewing window. The data was sorted by the values for the 2nd Vernier setting and it appeared that the time varied as

a function of the setting of the Vernier handle on the micrometer valve, rather than the expected constant time. Figure 4.1 shows the data with the Micrometer setting on the x axis and the time of fall as the dependant variable. The line represents a linear regression fit with an R^2 value of 0.54. Obviously there is not a linear relationship, but the setting of the Vernier scale has a direct effect; with a few exceptions, there is a clear trend toward longer times for a lower setting. This setting is completely arbitrary and not able to be adjusted to a particular setting. The only way to get a falling camera to work would be to have the droplet initiate the drop of the camera. This would require a device to accelerate the camera (as the droplet falls faster than the camera) and a second device to determine the exact instant of droplet detachment. Based on these two requirements, it was decided to change to the dual-view camera approach.

Table 4.1 Falling Camera Test Results.

Trial	Vernier Setting		Frame Number		Frame	Fall Time
#	1st Drop	2nd Drop	1st Light	1st Picture	Count	(s)
3	11.15	6.21	9	64	55	0.4583
4	11.21	7.02	32	64	32	0.2667
5	12.05	7.11	19	52	33	0.2750
6	10.16	5.22	8	63	55	0.4583
7	11.13	6.19	13	55	42	0.3500
8	11.2	7.01	9	40	31	0.2583
9	13.06	8.12	12	41	29	0.2417
10	12.07	7.13	9	35	26	0.2167
11	12.12	7.18	4	34	30	0.2500
12	11.09	6.15	6	48	42	0.3500
13	12.06	7.12	3	38	35	0.2917
14	10.21	6.02	3	46	43	0.3583
15	12.19	8	5	34	29	0.2417
16	13.02	8.08	4	33	29	0.2417
17	11.18	6.24	4	29	25	0.2083
				AVG	35.7	0.2978

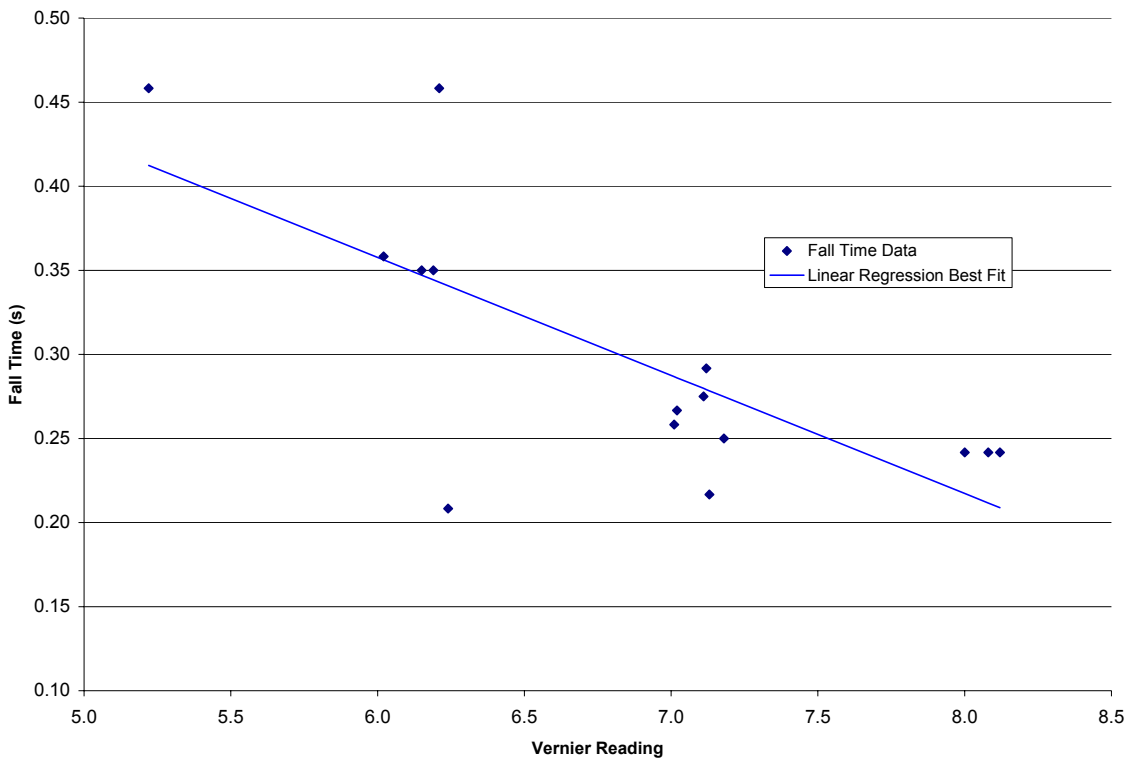

Figure 4.1 Illustration of Non-Constant Fall Time for Falling Camera Experiment.

4.2 Droplet Generation Test

Next the ability of the liquid droplet generation system was studied to determine its ability to produce uniform, reliable fluid drops. There were four individual tests performed at various pressure values. Each was conducted in the same manner; however, the results were very different. A complete table of results showing values for every trial can be found in Appendix A.

4.2.1 Atmospheric Pressure Test

The ability of the liquid droplet generation system to produce drops with atmospheric pressure on both sides was expected to be very good based on the observations made while assembling the system; consistent drops were allowed to fall into the ambient air with a high degree of control. The fluid droplet generation system

was installed in the apparatus; fifty trials were conducted at atmospheric pressure and volumes were calculated from the images taken by the camera. The drops were able to be grown and controlled easily with only one person required to operate the experiment. The average volume was found to be $1.20*10^{-3}$ in^3 with a standard deviation of $2.16*10^{-5}$ in^3.

When an Anderson-Darling normality test was performed, the data was not normal. Using the three sigma rule, the three largest data points (trials #5, #48, and #49) were disregarded as being outlying (Figure 4.2). The average value of the 47 remaining points was $1.19*10^{-3}$ in^3 with a standard deviation of $1.49*10^{-5}$ in^3 which corresponds to an uncertainty of 1.25% and a 95% confidence limit of 2.5%. Figure 4.3 shows a plot of the 47 data points with a normal curve for comparison; the P value for this data is 0.242 which is normal. The uncertainty above accounts for random error only; the bias error generated by uncertainty in the scale measurement (discussed in section 3.2.3 - see Table 3.9) must be accounted for. A multiplier of 2 is applied to the standard deviation and the resulting value (U_a) is combined with the bias uncertainty (U_b) of $2.2*10^{-5}$ in^3, to generate a total uncertainty of $3.7*10^{-5}$ in^3 with a 95% confidence interval.

The pixel values for the major and minor axis were extremely good as well; the major axis had an average value of 120.10 pixels with a standard deviation of 2.12 pixels, while the average minor axis was 110.21 pixels with a deviation of 3.76 pixels. If these values are used to calculate a volume (with the scale of 0.00113261 in/pixel), the result is $1.18*10^{-3}$ in^3 which is within the standard deviation for the measured volume. This value requires a combination of 70% with rotation about the major axis and 30% with rotation about the minor axis (Figure 3.72); these fractions were estimated based on the distribution of droplet orientations (Figure 4.4).

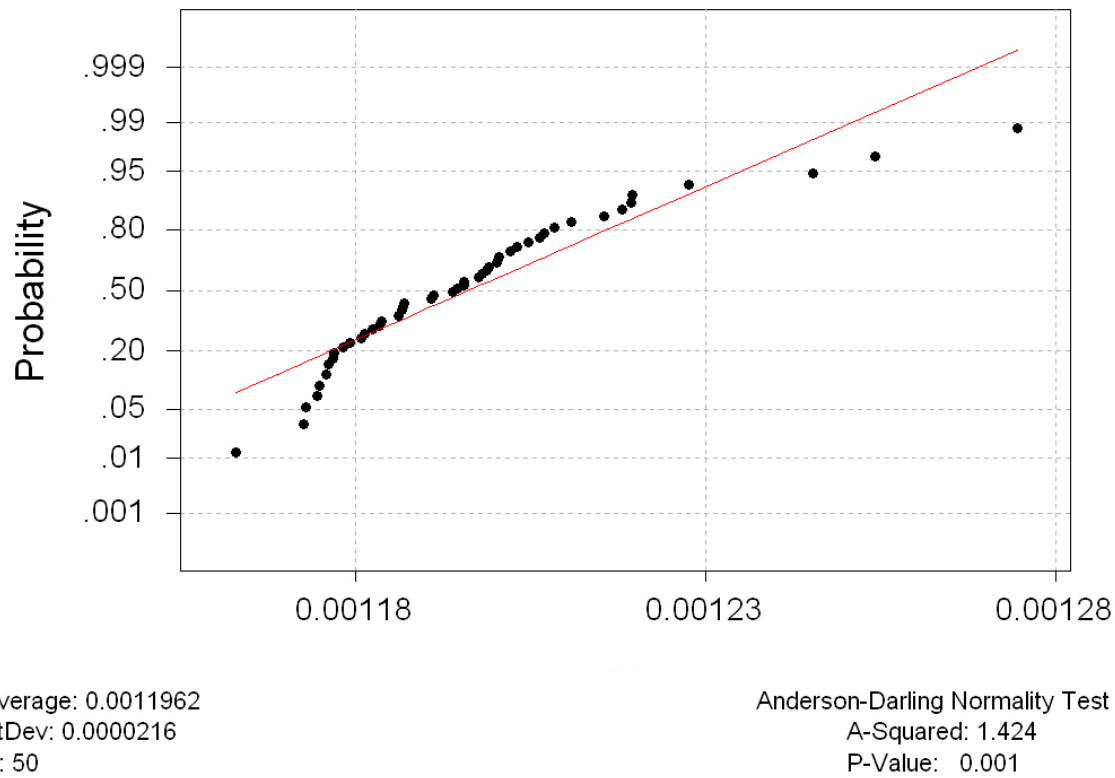

Figure 4.2 Normal Probability Plot from Anderson-Darling Test on All Atmospheric Data Points.

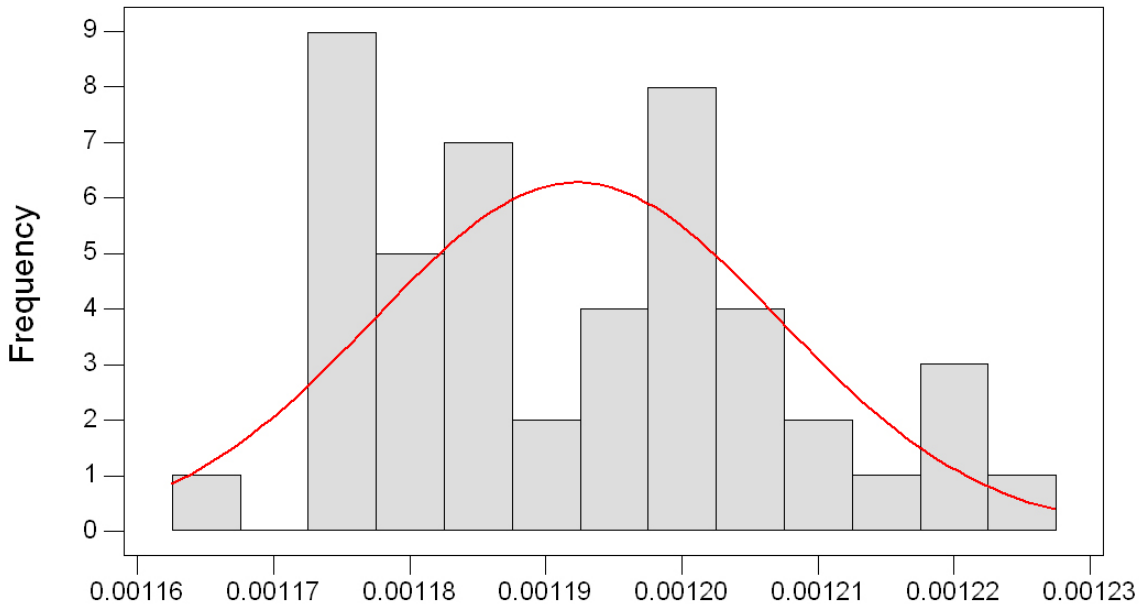

Figure 4.3 Histogram of Adjusted Atmospheric Droplet Volume.

Notice that only 3 orientations fall outside of 10° from either perfectly vertical or perfectly horizontal, indicating a smooth release with the droplet necking down, detaching from the needle, and then oscillating from compression to elongation (Figure 3.71) until surface tension forms a perfect sphere. It is also interesting to note that the majority (68%) were compressed showing a tendency toward a uniform path/behavior as the droplet fell.

Variation in the droplet eccentricity was observed; Figure 4.5 shows the two extremes with the values ranging from 0.136 to 0.527. Recall that for an ellipse, eccentricity is a scalar that represents the ratio between the distance between foci and the major axis length; it varies between 0 and 1 with 0 being a perfect circle and 1 a straight line. For the droplets examined here, an average eccentricity of 0.38 with a standard deviation of 0.12 (over 30%) was observed which signifies a wide disparity in the data with respect to eccentricity; however, this did not have a negative effect on the volume calculations. This would indicate that the shape (compressed, elongated or circular) of the droplet cross section does not have a negative effect on the volume calculations, providing the proper volume formula is applied. It also means that the droplets deform as they fall through the ambient, and that the captured image may vary significantly depending on the evolution of the droplet geometry.

The last measured value referred to as solidity measured the amount of open space within the area used by the DropStats.m subroutine to calculate the major and minor axis. This value should be above 95% for reliable results and the values for this test, with an average of 98.03% and a standard deviation of 0.60%, were excellent. In the table showing all data, a final column entitled accuracy depicts a subjective rating on how

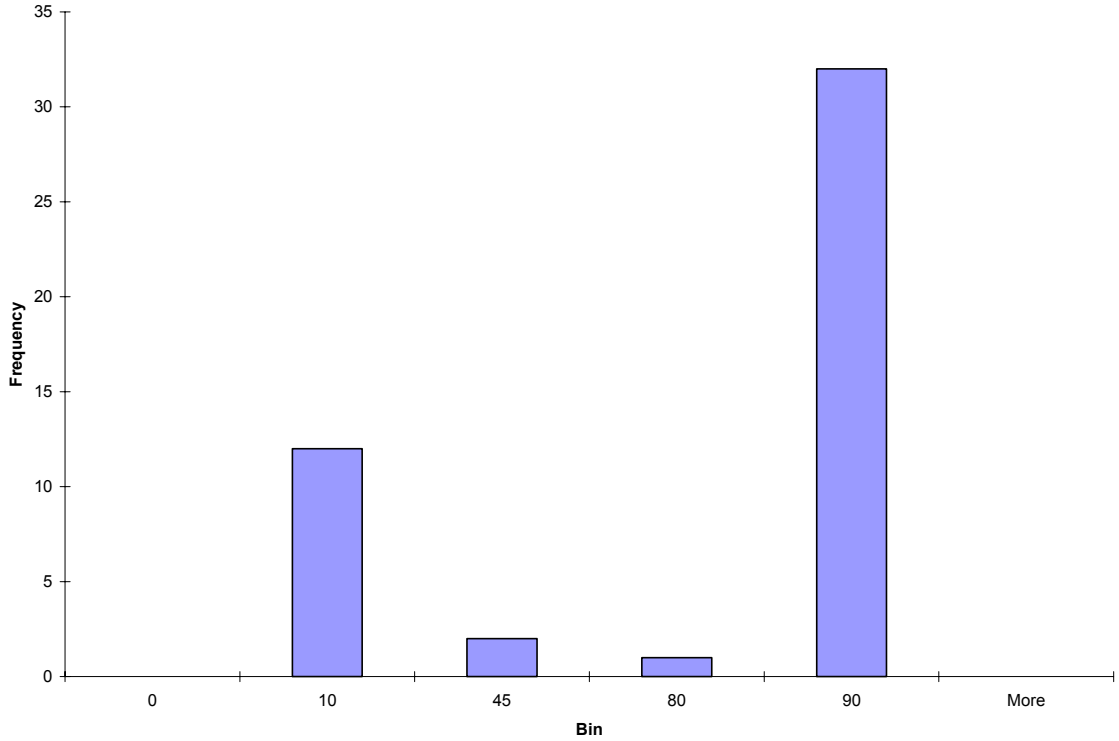

Figure 4.4 Orientation Distributions for Atmospheric Droplet Test.

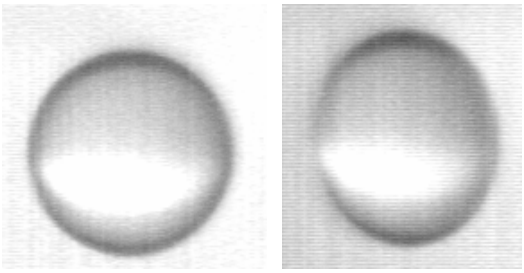

Figure 4.5 Extreme Examples of Difference in Eccentricity for Atmospheric Test. Nearly Circular (Eccen=0.136 14JAN#16, Left) and Flattest (Eccen=0.609 14JAN#48).

Figure 4.6 Examples of Substandard Fill. L to R Trial #2, #4, #5, and #7.

well the Edgefind.m and FillUp.m depicted the droplet cross section. A value of one in this column denotes a satisfactory fill while a three denotes an unsatisfactory result. Of the 47 trials in the adjusted data set, 13 were deemed to be substandard, several examples of which are shown in Figure 4.6.

4.2.2 300 Torr Test

Next, the vacuum pump was operated until a pressure of ~250 Torr was measured in the vacuum chamber by the manometer; the actual range of pressures for the 30 trials in this test was 267-345 Torr. The procedure was the same as for the atmospheric test, which allowed controlled droplet production by one person. Again, the results were very good with an average volume of $1.20*10^{-3}$ in^3 (identical to that determined in the atmospheric test) and a standard deviation of $2.56*10^{-5}$ in^3. The data was not normal

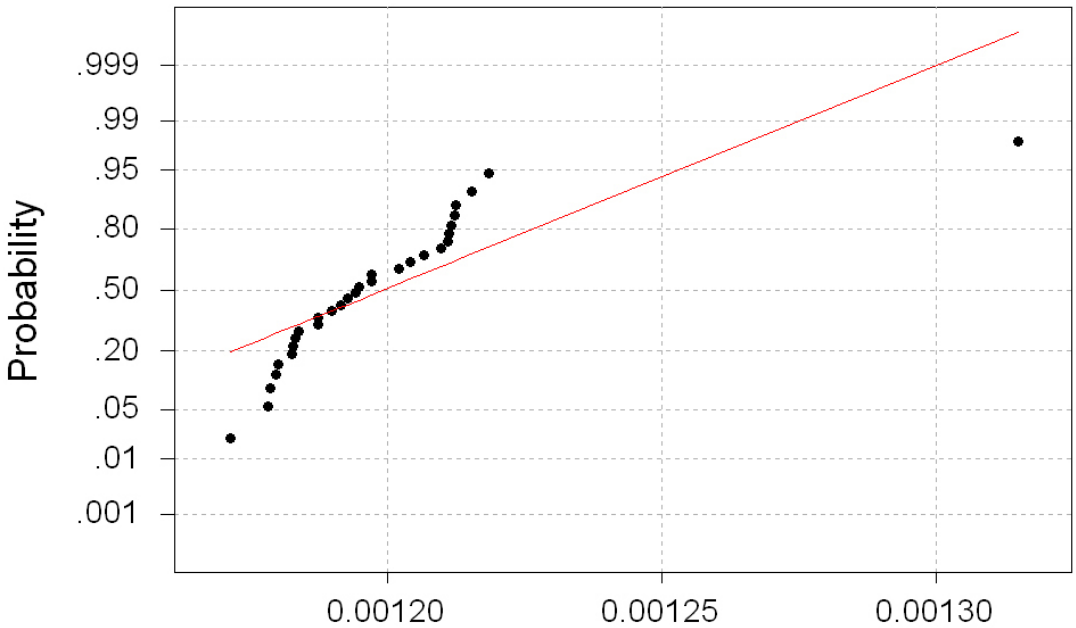

Average: 0.0011994
StDev: 0.0000256
N: 30

Anderson-Darling Normality Test
A-Squared: 2.143
P-Value: 0.000

Figure 4.7 Normal Probability Plot from Anderson-Darling Test on All 300 Torr Points.

(Figure 4.7) and based on the three sigma rule, as used above; the highest data value was discarded (trial #17). The remaining 29 points generate an average volume of $1.20*10^{-3}$ in^3 and a standard deviation of $1.36*10^{-5}$ in^3. The bias error for this test was $2.2*10^{-5}$ in^3 which, when combined with the standard deviation, gives a 95% confidence limit of $\pm$ $3.5*10^{-5}$ in^3, the smallest uncertainty of any test. Figure 4.8 shows a histogram of the adjusted data with a normal curve for comparison. These 29 points are not normal; with a P value of 0.087 the distribution is judged to be inconclusive.

The major and minor axis both had very good consistency with a 120.26 pixel average and a standard deviation of 2.17 pixels. The minor axis was 110.35 pixel average and deviation of 3.45 pixels both of which are extremely close to the same numbers for the atmospheric tests. These numbers generate a volume of $1.19*10^{-3}$ in^3 with 21 trials rotated about the major axis and 8 about the minor axis. Figure 4.9 gives a breakdown of the distribution of the orientations. Again, the majority (72.4%) was compressed and only 2 were outside of 10° off of perfectly vertical / horizontal. The eccentricity was completely random without a distinct pattern as the error was 29.14% based on an average of 0.379 and a deviation of 0.110. The solidity of the images averaged to 98.11% $\pm$ 0.35% representing a 0.36% uncertainty. These values represent an improvement over the numbers at atmospheric conditions and show that the repeatability of droplets can be accomplished under vacuum conditions.

4.2.3 75 Torr Test

The next test was conducted at pressures ranging from 67-112 Torr. At these pressures, it became somewhat difficult to get droplets to slowly grow and drop from the needle. When the Vernier handle was fully open droplets would fall until the valve

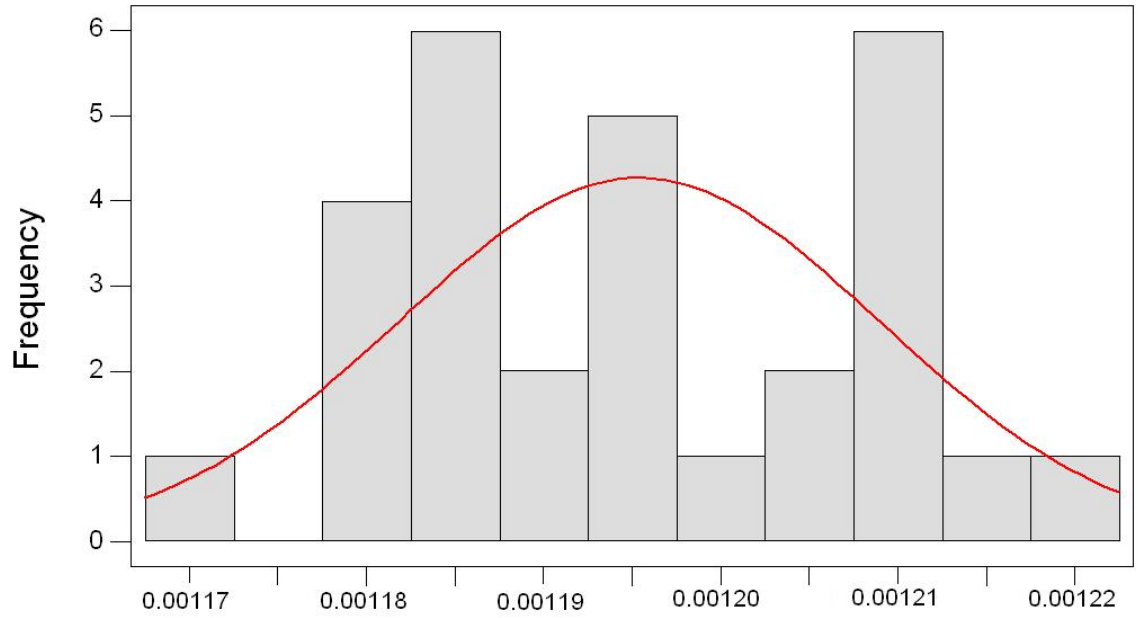

Figure 4.8 Histogram of Adjusted 300 Torr Droplet Volume.

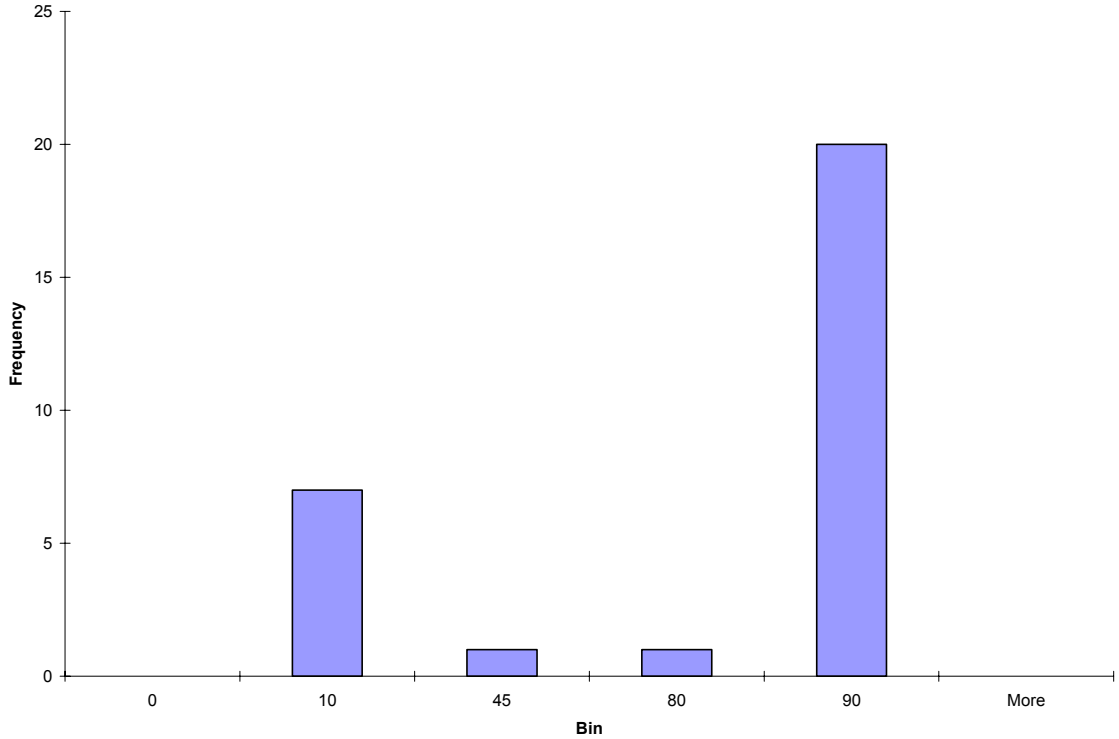

Figure 4.9 Orientation Distributions for 300 Torr Droplet Test.

system was empty. Only the lower half of the traverse on the Vernier handle could be used. This meant that the vacuum pump had to be started and stopped at regular intervals. The average volume determined at these pressures was $1.20*10^{-3}$ in^3 with a standard deviation of $3.67*10^{-5}$ in^3. This data also required several points be discarded (Figure 4.10), and by the three sigma rule the largest three points (trials #1, #20, and #28) were discarded as outlying. Using the remaining 27 points, an average value of $1.19*10^{-3}$ in^3 was calculated with a standard deviation of $1.86*10^{-5}$ in^3 which results in an uncertainty of 1.56%. A 95% confidence interval of $\pm$ 3.6% is generated after the scale bias error of $7.0*10^{-6}$ in/pixel is accounted for. The adjusted data set has good normality as seen in Figure 4.11; the P value for this data is 0.314.

The major and minor axis data, as with both of the first tests, was very reproducible with an average major length of 119.88 pixels $\pm$ 1.40 pixels and a minor length of 110.79 pixels $\pm$ 2.78. These values represent errors of 1.17% and 2.51% respectively and generate a volume of $1.18*10^{-3}$ in^3 by rotating 17 images about the major axis and 10 about the minor. These numbers are not as evident based on the orientation distribution as seen in the two previous tests but are determined by using 45° as a division point. Figure 4.12 shows the distribution based on the pervious criteria of 10° from vertical or horizontal; note the large number that are outside these limits. This along with the observation that the droplets were more difficult to control, indicates that the droplet release from the needle is not as consistent as the first two trials. Figure 4.13 shows that at these pressures the droplets first demonstrated the effects of dissolved gases on the droplet generation.

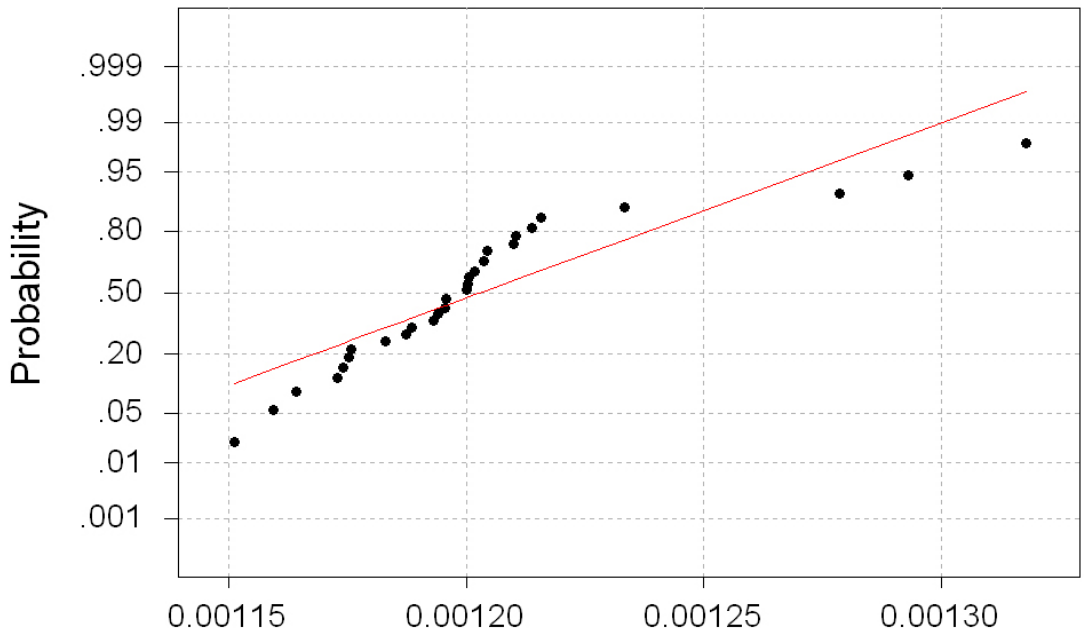

Average: 0.0012031
StDev: 0.0000367
N: 30

Anderson-Darling Normality Test
A-Squared: 1.967
P-Value: 0.000

Figure 4.10 Normal Probability Plot from Anderson-Darling Test on All 75 Torr Points.

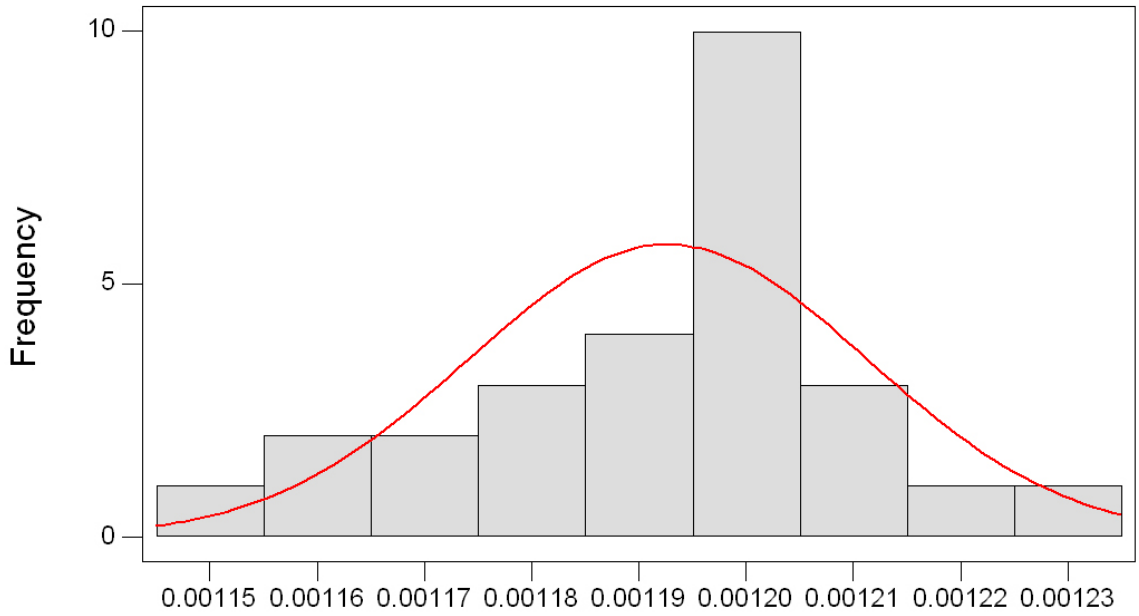

Figure 4.11 Histogram of Adjusted 75 Torr Droplet Volume.

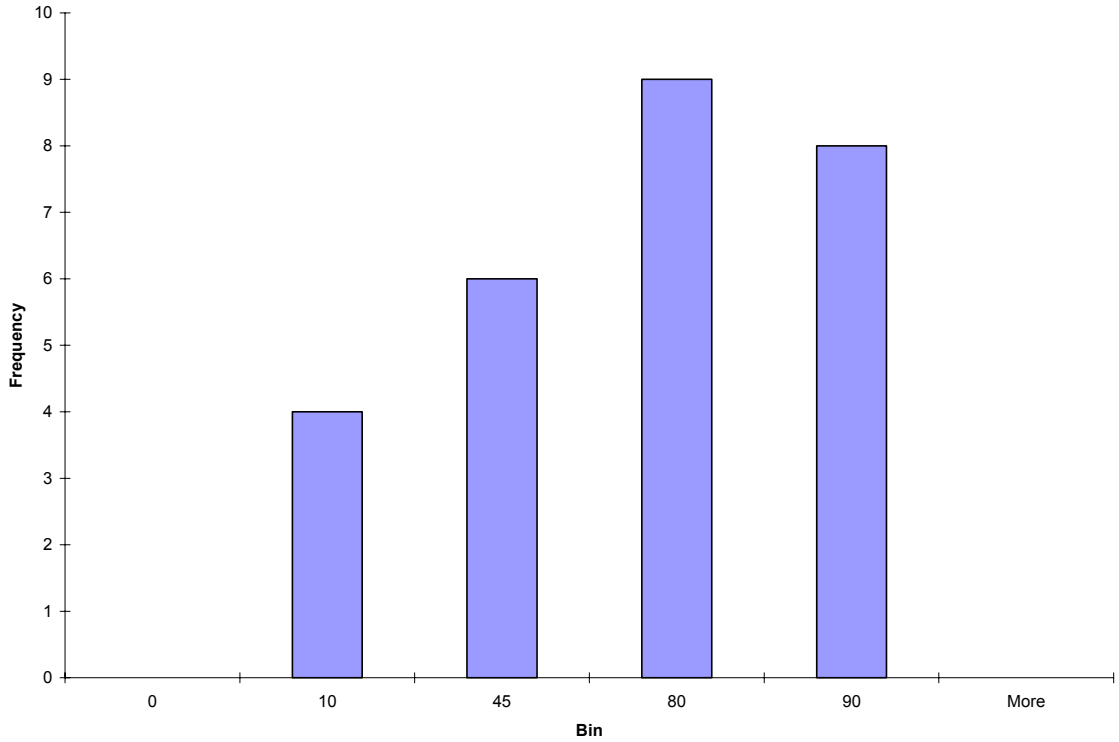

Figure 4.12 Orientation Distributions for 75 Torr Droplet Test.

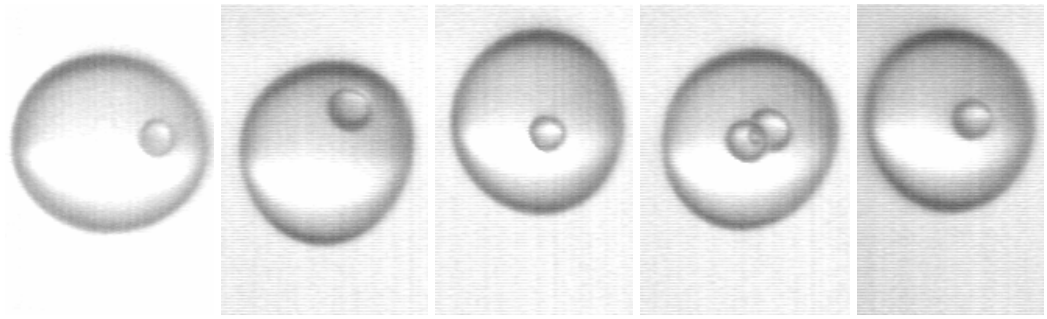

Figure 4.13 Gas Bubble Images from 75 Torr Droplet Generation Test.

The eccentricity of these images was as widely-varying as the first two sets with an average of 0.372 and an uncertainty of 21.13% based on the standard deviation of 0.079. The solidity of the images was very good with an average value of 98.2% and a standard deviation of only 0.4%. Of the 27 images in this adjusted test only 5 were judged to have a substandard fill.

4.2.4 20-50 Torr Test

The last test performed to validate the reproducibility of droplet size was attempted in the 20-50 Torr range. All data points were actually taken in the 30-50 Torr range because the apparatus was too difficult to manage in the 20-30 Torr range. Two people were required as getting droplets to form required manipulation of both the Vernier knob on the pneumatic shutoff valve (V) and the bump switch (S) at the same time; one operator performed this function while the second operator triggered the camera and recorded the pressure. The pressure in the water chamber was not recorded as there is a gap from 20 to 50 Torr that the gauges do not cover; even though the high range gauge (C) goes to zero the indicated pressure never went below 50 Torr, while the lower range gauge (Q) was reading below 20 Torr. Droplets would not form easily and control of the timing of fall was difficult at best; nevertheless, data was collected and the results were poor. Table 4.2 compares the results for all of the different pressures. Note that the adjusted average volumes for the highest three pressures are very close to each other, while the value for the 20-50 Torr test is considerably smaller with an average value of $1.03*10^{-3}$ in^3 (versus $1.19*10^{-3}$ in^3) with a standard deviation of $3.01*10^{-4}$ in^3 (versus $1.36*10^{-5}$ in^3 to $1.86*10^{-5}$ in^5). This is a direct result of the problems caused by the

Table 4.2 Summary of All Droplet Generation Tests.

	AVG Volume	STD DEV
Test	in^3	in^3
ATM (ADJ -3)	1.19E-03	1.49E-05
300 Torr (ADJ -1)	1.20E-03	1.36E-05
75 Torr (ADJ -3)	1.19E-03	1.86E-05
20-50 Torr	1.03E-03	3.01E-04
20-50 Torr (ADJ -10)	1.20E-03	7.79E-05

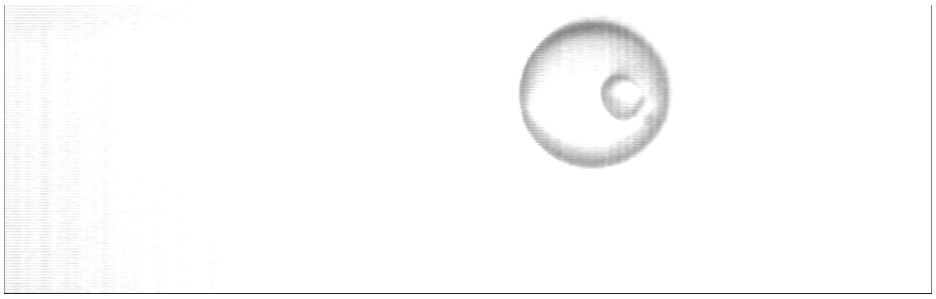

Figure 4.14 Unused Images from 20 Torr Test which Demonstrate Problems with Dissolved Gases in the Water. (AVI, 9M, jones_tony_l_200505_ms_Unused_20Torr_ Images.avi).

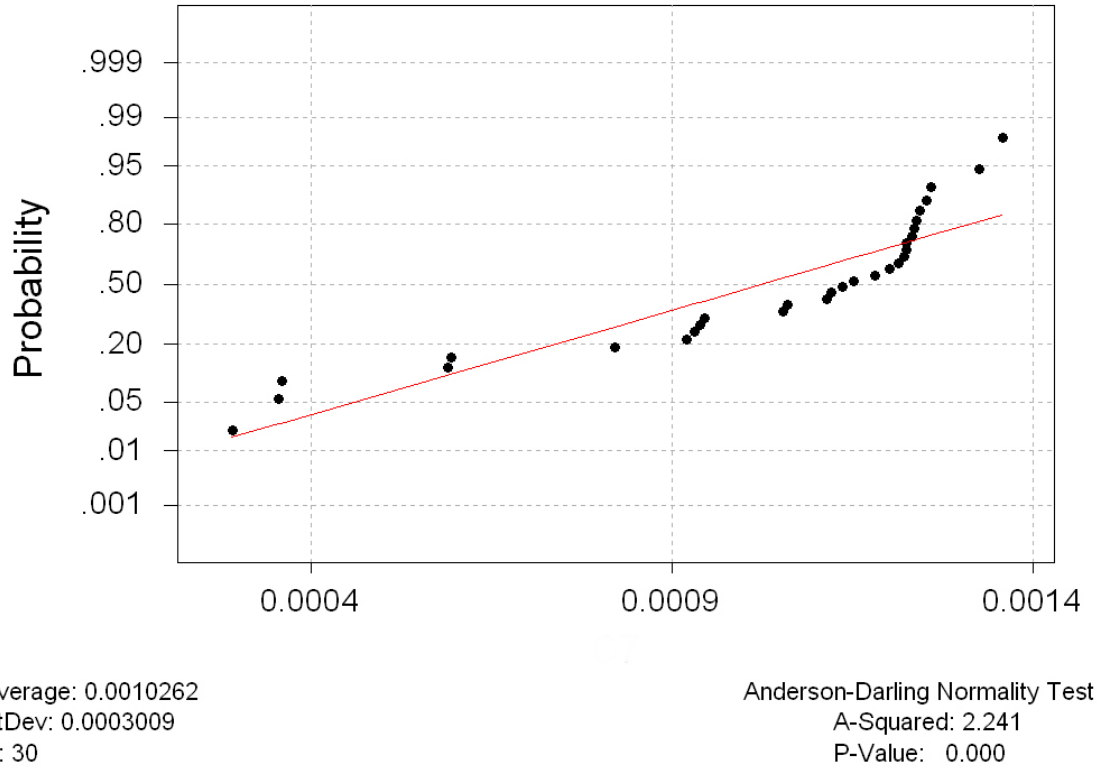

Figure 4.15 Normal Probability Plot from Anderson-Darling Test on All 20-50 Torr Points.

dissolved gases. Figure 4.14 shows a movie of all of the images that were deemed unusable; it is easy to see that: some of the droplets produced are visually smaller that the previous tests, that gas bubbles are present within the droplets, and that the smooth

growth and release of droplets are not happening as droplets are now falling outside of the camera view.

Looking at Figure 4.15, several drops appear to be outliers on the small side. By removing the smallest 10 images, the data becomes normal (Figure 4.16) and the average of the 20 remaining points is $1.20*10^{-3}$ in^3 with a standard deviation of $7.79*10^{-5}$ in^3; this justifies the deletion of the 10 lowest points as the minus three sigma value with these numbers is $9.68*10^{-4}$ in^3. Now the value for volume is more in line with the values seen in the previous tests; however, the standard deviation is still significantly higher than the corresponding values at elevated pressures. Accounting for the bias error from the scale measurement generates a total uncertainty in volume of $1.57*10^{-4}$ in^3 with a 95% confidence interval.

Calculating the volume from the mean values of the major and minor radii does not produce comparably accurate results as was the case for the higher pressures. The average major axis was 113.21 pixels with a standard deviation of 12.93 pixels representing an uncertainty of 11.42%, while the minor axis average was 105.71 pixels with a slightly higher uncertainty of 13.01% from a standard deviation of 13.75 pixels. These numbers improve if the values are calculated based on the 20 largest images; corresponding results are: an average major axis of 119.69 pixels with a standard deviation of 2.75 pixels representing an uncertainty of 2.3% and an average minor axis of 113.37 with a deviation of 3.39 pixels for an uncertainty of 2.99%. These numbers generate a volume of $1.20*10^{-3}$ in^3 with 8 rotated about the major and 12 rotated about the minor axis. Figure 4.17 shows the distributions of the 20 orientations and, just as in the

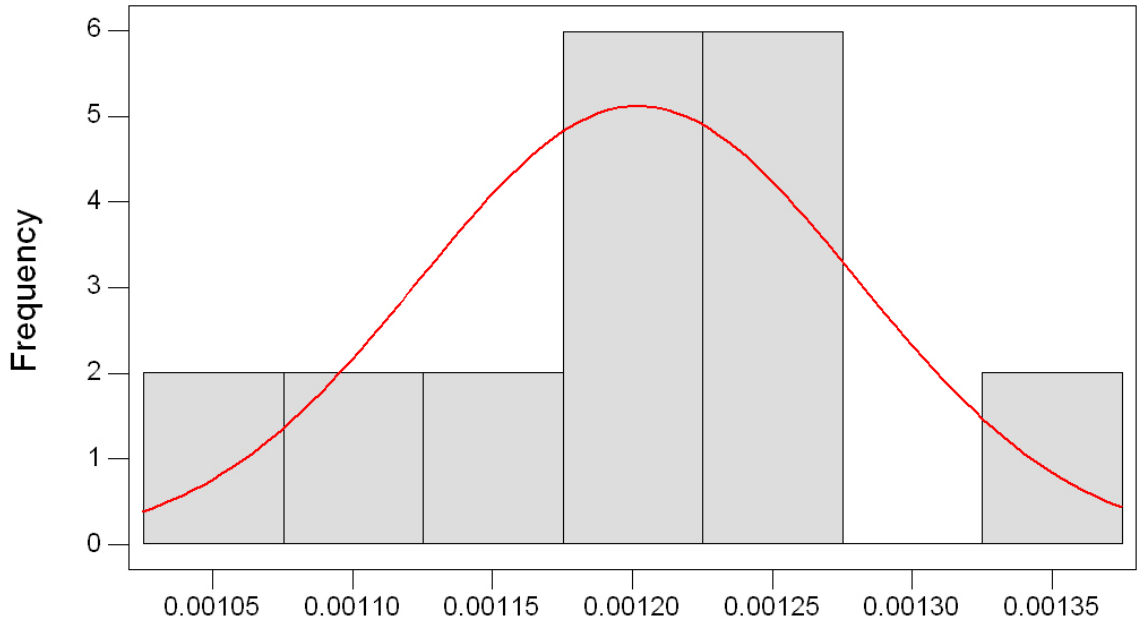

Figure 4.16 Histogram of Adjusted 20 Torr Droplet Volume.

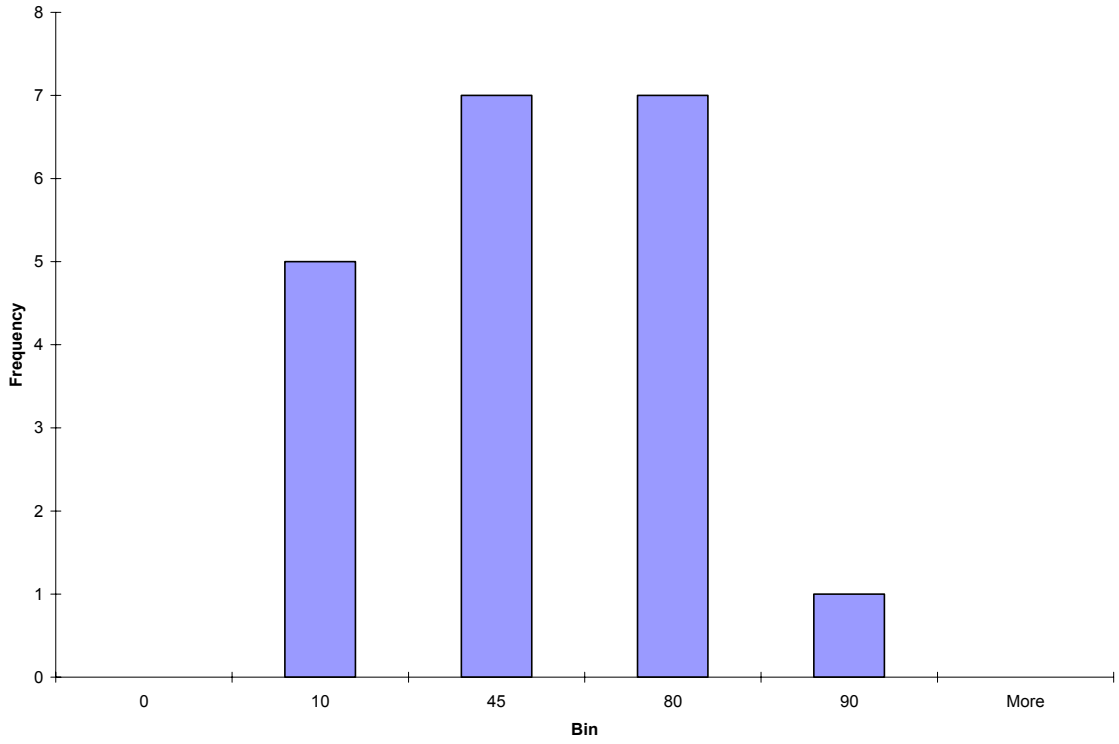

Figure 4.17 Orientation Distributions for Adjusted 20 Torr Droplet Test.

75 Torr test; the orientations indicate that the droplet is not falling smoothly from the needle as only 7 of 20 trials are within 10° of horizontal or vertical.

As is the case for data at the elevated pressures, the eccentricity of the images exhibits large variations; even with a smaller group of 20 images, the average is 0.3 with an uncertainty of 39.9%. It is reassuring to note that this variation in eccentricities still resulted in a standard deviation of less than 10% in volume. The solidity of these 20 images was very high at 98.35% with a standard deviation of only 0.18%. Of these images only one was deemed to have a substandard fill.

4.3 Degassed Water Test

The problems encountered during the droplet generation tests conducted at low pressure were identified as being caused by dissolved gasses in the water coming out of solution as pressure is reduced. Several liters of water were degassed and this fluid was placed in the liquid supply flask (X) while under a vacuum. This made it much easier to control the droplets, so that it was possible to conduct this test with one person as opposed to the two person technique required during the 20-50 Torr size test without degassing. The resulting average volume was $1.17*10^{-3}$ in^3 with a standard deviation of $8.94*10^{-5}$ in^3. These figures appear to contain outlying values based on the three sigma rule (Figure 4.18). By removing the five lowest and two highest values (trials #25, #19, #3, #15, #6, #11, and #18 respectively) an average of $1.19*10^{-3}$ in^3 with a standard deviation of $2.40*10^{-5}$ in^3 is obtained; combining this with a volumetric bias error of $2.1*10^{-5}$ in^3 resulting from the scale bias generates an uncertainty of $5.2*10^{-5}$ in^3 and a 95% confidence limit of 4.4%. The normality of the modified data set associated with these values is judged to be extremely normal (Figure 4.19) as determined by the

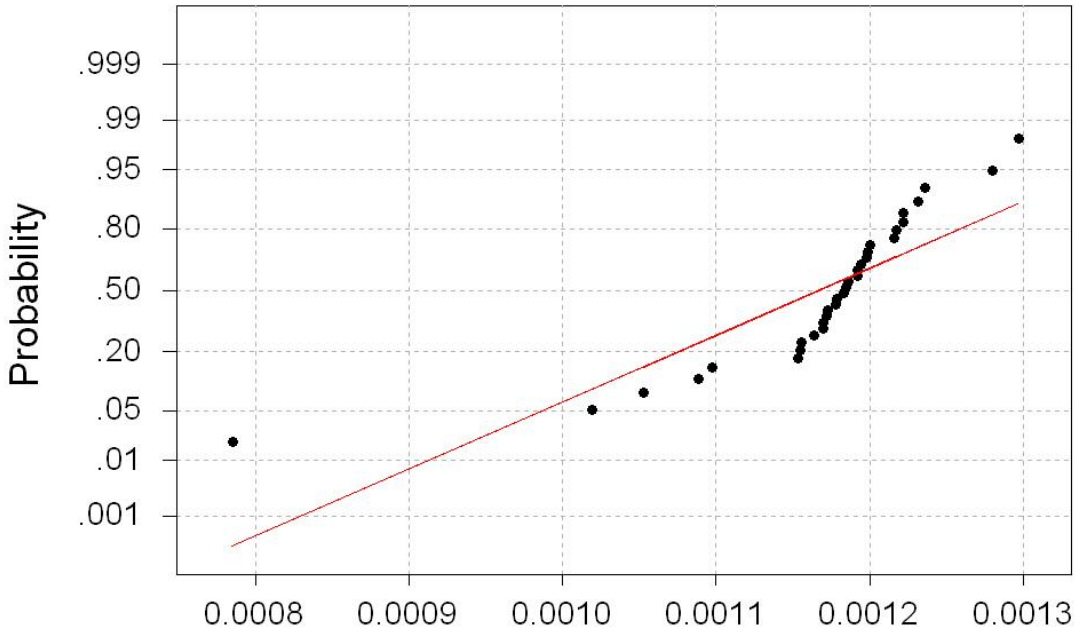

Average: 0.0011672
StDev: 0.0000894
N: 32

Anderson-Darling Normality Test
A-Squared: 2.581
P-Value: 0.000

Figure 4.18 Normal Probability Plot from Anderson-Darling Test on All Degassed Water Points.

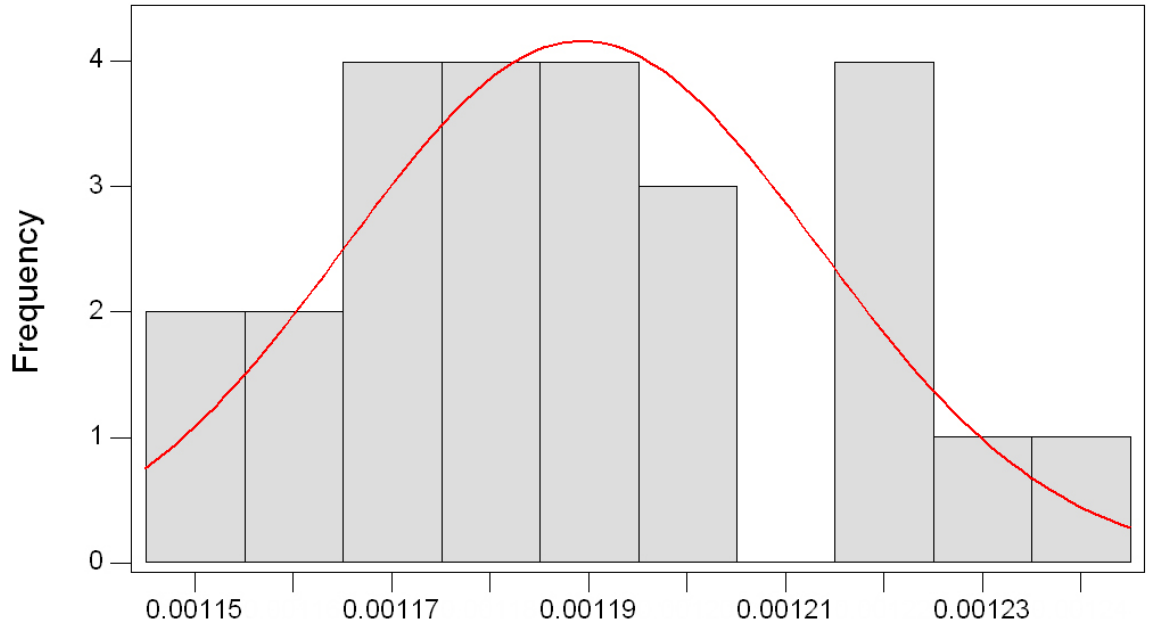

Figure 4.19 Histogram of Adjusted Degas Droplet Volume.

Anderson-Darling normality test; the P value was 0.519, the highest of any trial.

The major and minor axis data significantly improved when degassed water was used; the average major axis was 114.2 pixels with a deviation of 1.72 for an uncertainty of 1.51%, while the average minor axis is 105.77 pixels with an uncertainty of 3.09% from a standard deviation of 3.26 pixels. These values generate a volume of $1.18*10^{-3}$ in^3 with 72% rotated about the major and 28% rotated about the minor axis. Figure 4.20 shows the distribution of the orientations for the droplets which drove this division. It should be noted that the majority (80%) of the droplets is within $\pm$ 10° of perfectly vertical or horizontal as was the case for the droplet generation tests conducted at high pressures where the dissolved gases had little effect. Also, in this case only 7 of the

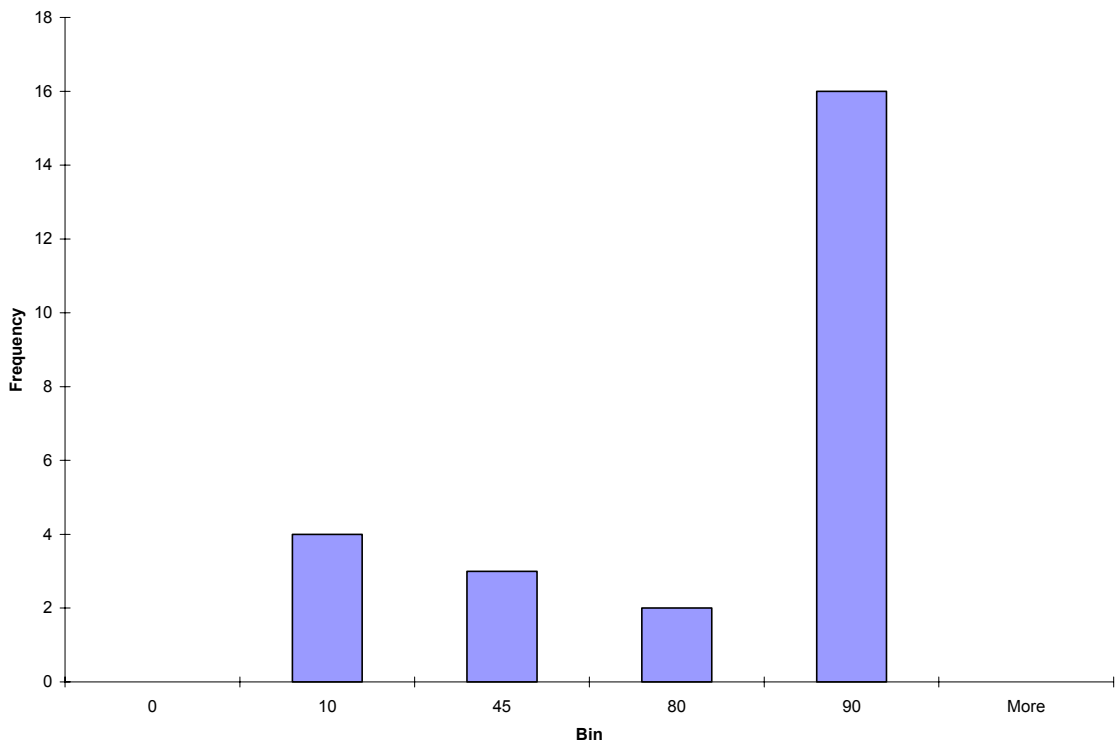

Figure 4.20 Orientation Distributions for Adjusted Degas Droplet Test.

droplets fell outside of the three sigma deviation as opposed to 10 for the 20-50 Torr droplet generation test. Degassing of the fluid appears to be necessary to allow for smooth droplet generation and detachment.

As has been the case with the entire droplet testing so far, the eccentricity has exhibited a large variation, with a standard deviation of 0.112 on an average value of 0.358; this gives an uncertainty of 31.2% but this again appears to have no effect on the volume generated. The solidity is lower than any of the previous tests with an average value of 97.45% but it is very consistent with a standard deviation of only 0.47%. This low average is more than likely a result of several poor fills as 10 of the adjusted data set (40%) were determined to have substandard fills.

4.4 Dual View Droplet Size Test

Experiments have been conducted to assess the abilities of the dual camera system. The camera was set up in the dual view mode and images were recorded at both the top and bottom of the viewing area to see if the same volume would be generated when isothermal conditions prevail. The top and bottom images were processed as two separate groups.

4.4.1 Top View Results

The data for the top view generated an average volume of $1.28*10^{-3}$ in^3 with a standard deviation of $4.65*10^{-5}$ in^3. This data had one outlying data point (trial # 20) on the upper end (Figure 4.21) which was ignored. The adjusted data set generated an average volume of $1.27*10^{-3}$ in^3 with an error of 5.7% based on a standard deviation of $3.50*10^{-5}$ in^3 and a scale bias error of $9.1*10^{-6}$ in/pixel which generates a volumetric bias error of $1.6*10^{-5}$ in^3. This new set was normal (Figure 4.22) with a P value of 0.34 from

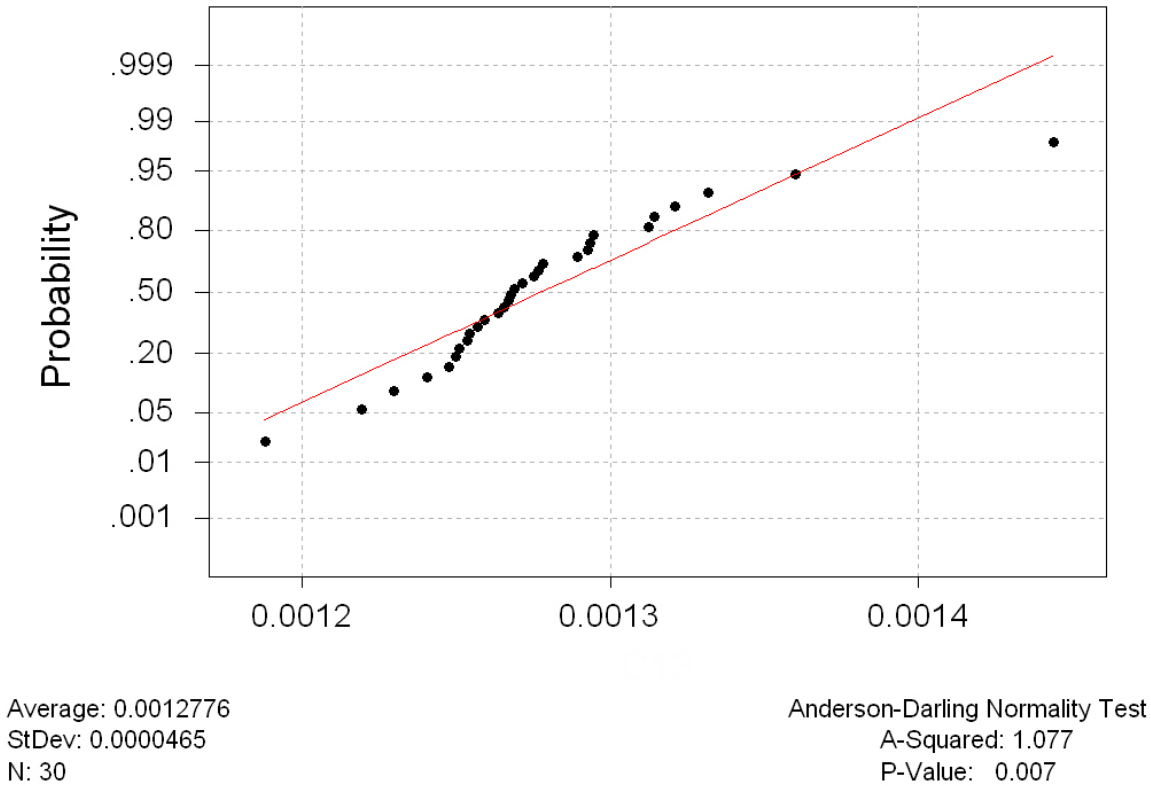

Figure 4.21 Normal Probability Plot from Anderson-Darling Test on All Top View Points.

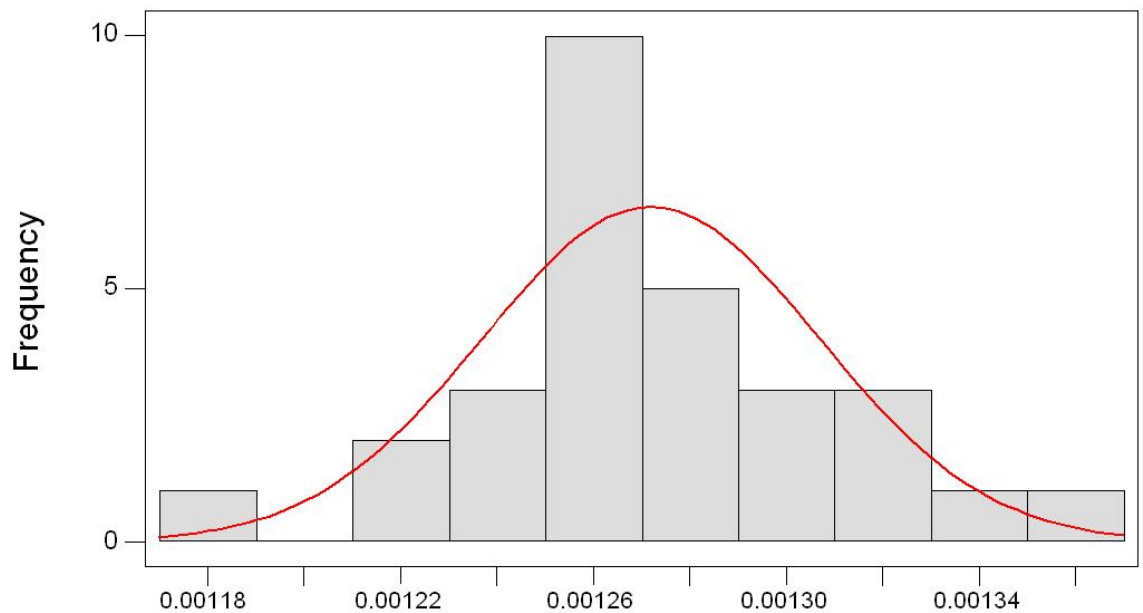

Figure 4.22 Histogram of Adjusted Top View Droplet Volumes.

the Anderson-Darling normality test. Good agreement was obtained with the volume calculated using the mean values of the major and minor axes. The standard deviations in the major and minor axes' measurements were 1.77 and 0.677 pixels, respectively. The average major axis was 65.12 with an uncertainty of 2.71%, while the minor axis average

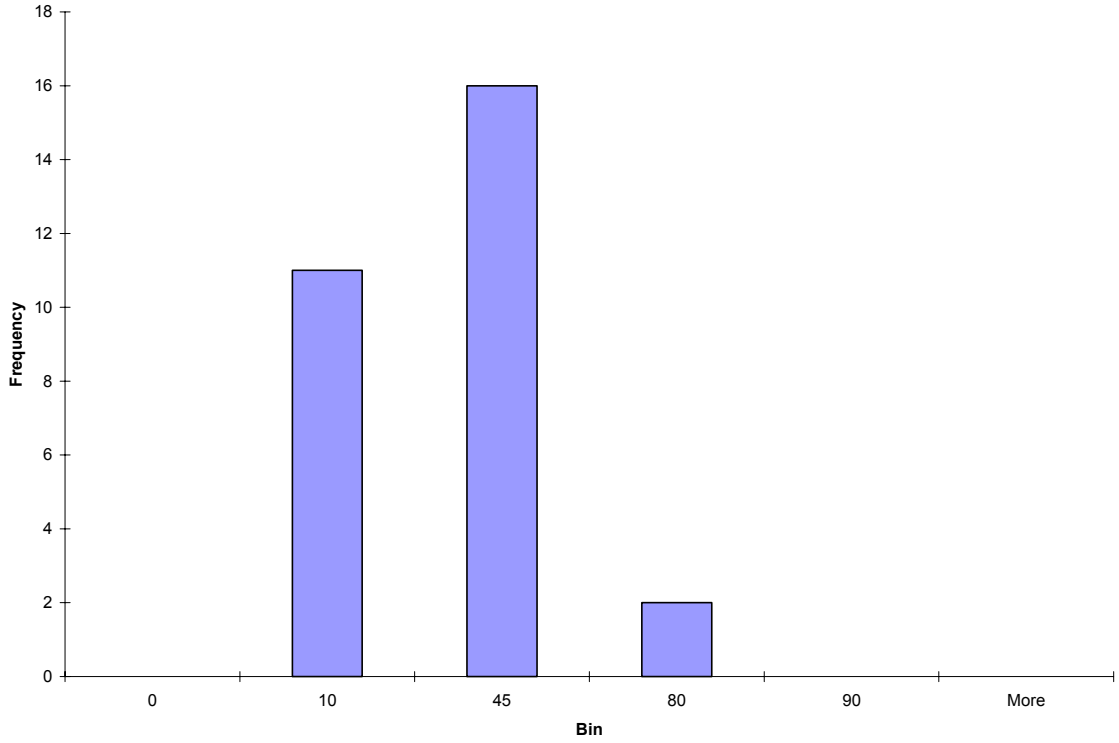

Figure 4.23 Orientation Distributions for Adjusted Top View Droplet Test.

Table 4.3 Orientation Comparison.

Test	AVG Absolute Orientation	Frequency			
		0°-10°	10°-45°	45°-80°	80°-90°
ATM-Size	64.08	12	2	1	32
300 Torr-Size	64.32	7	1	1	20
75 Torr-Size	51.97	4	6	9	8
20 Torr-Size	39.13	5	7	7	1
Degas	59.38	4	6	3	17
Top-Dual View	16.99	11	16	2	0
Bottom-Dual View	27.9	14	8	4	4

was 59.57 pixels with an uncertainty of 1.14%. These values combined to generate a volume of $1.25*10^{-3}$ in^3 with 93.1% rotated about the minor axis and the remaining 2 rotated about the major axis. Figure 4.23 shows the orientation distribution and it is interesting to note that this is only the second time that the frequency of droplets with orientations within 10° of zero is greater than those with orientations within 10° of 90; the previous time was for the 20-50 Torr generation test.

Table 4.3 shows a comparison of droplet orientation distributions. Notice that the average absolute orientation is much higher for trials with the camera mounted in the middle as opposed to the dual image values. The top five entries were taken with the camera in the center of the viewing window, while the top view data was taken with the camera at the top, and the bottom view data was taken with the camera at the bottom of the viewing window. There is not enough data to make a definitive judgment, but it would seem that the placement of the camera has an effect on the primary orientation of the droplets observed, since it captures the droplet at a different point in its oscillation cycle. In the center droplet orientation is above 45° while on the edges it is below 45°.

The eccentricity of the top images follows the trends of all the others in that it had an average of 0.39 with a relatively high standard deviation of 0.083, corresponding to an uncertainty of 21.08%. Again, wide variation in eccentricity does not appear to affect the volume calculations. The solidity of the images in the top was rather low at 96.28%. This is most likely due to the fact that the dual droplet images are smaller due to the necessity to capture a wider field of view; thus an empty pixel in a smaller image is a larger percentage of the fill. The uncertainty in the solidity was only 1.33% so all of the images appear to have this tendency.

4.4.2 Bottom View Results

The bottom view data required additional manipulation to obtain the required results. First, the bottom view had to be lowered in order to further offset the brightness of the image in the center. This caused every picture to include the tip of the thermocouple within the image, which had to be removed. Next, several images required that the pixels on the top of the droplet be darkened in order for the edge finding software to work; this was done on 13 of 30 images. These actions resulted in excellent results as the bottom view data had an average volume of $1.23*10^{-3}$ in^3 with a standard deviation of $2.35*10^{-5}$ in^3; combining this with the volumetric bias error of $1.5*10^{-5}$ in^3 generates an uncertainty of $4.9*10^{-3}$ in^3 with a 95% confidence interval of 4.0%. This data was normal (Figure 4.24) with a P value of 0.339 from the Anderson-Darling normality test; this was the only original data set with no outlying data points according to the three sigma rule (Figure 4.25). The major and minor axis data had excellent agreement as well with an average major axis of 63.72 pixels with a standard deviation of 1.41 pixels for an uncertainty of 2.22%, while the minor axis average was 59.14 with an uncertainty of 2.06% based on a deviation of 1.22 pixels. These values were used to calculate a volume of $1.29*10^{-3}$ in^3 with 8 of 30 trials rotated about the major axis.

As with the top view images, the distribution of the orientations favored those that were horizontal (requiring rotation about the minor axis) with the lower values predominating (Figure 4.26); the largest amount of drops had orientations $< 10^o$. The eccentricity of the images was again widely distributed, as was the case for all previous tests; the average value was 0.36 with an uncertainty of 26.53%. With the uncertainty in the original volume data of 1.91% this again shows that the eccentricity of the droplets

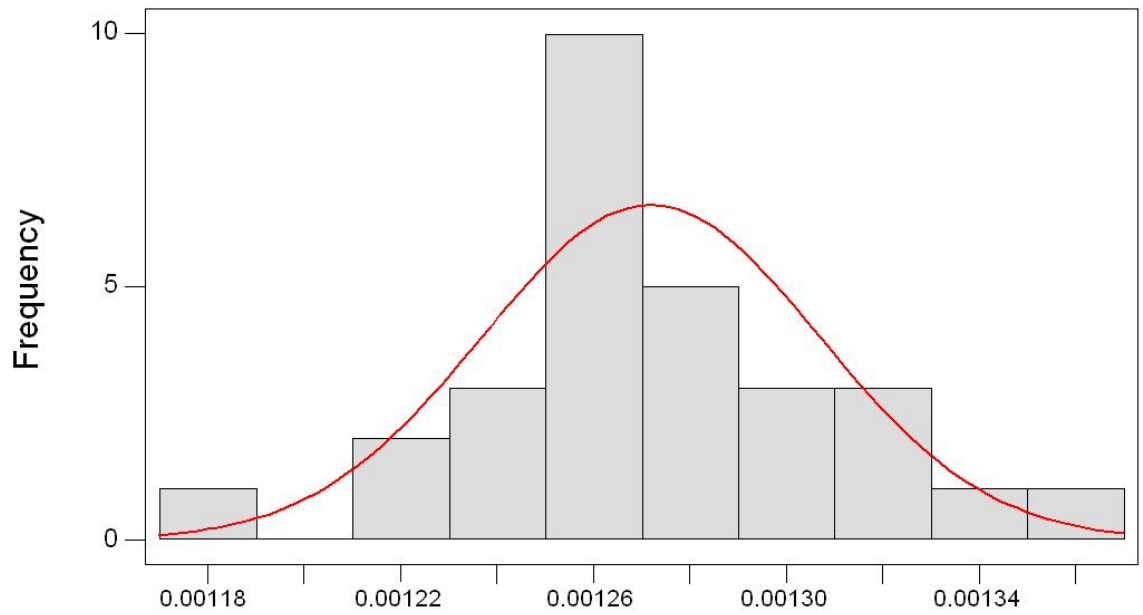

Figure 4.24 Histogram of All Bottom View Droplet Volumes.

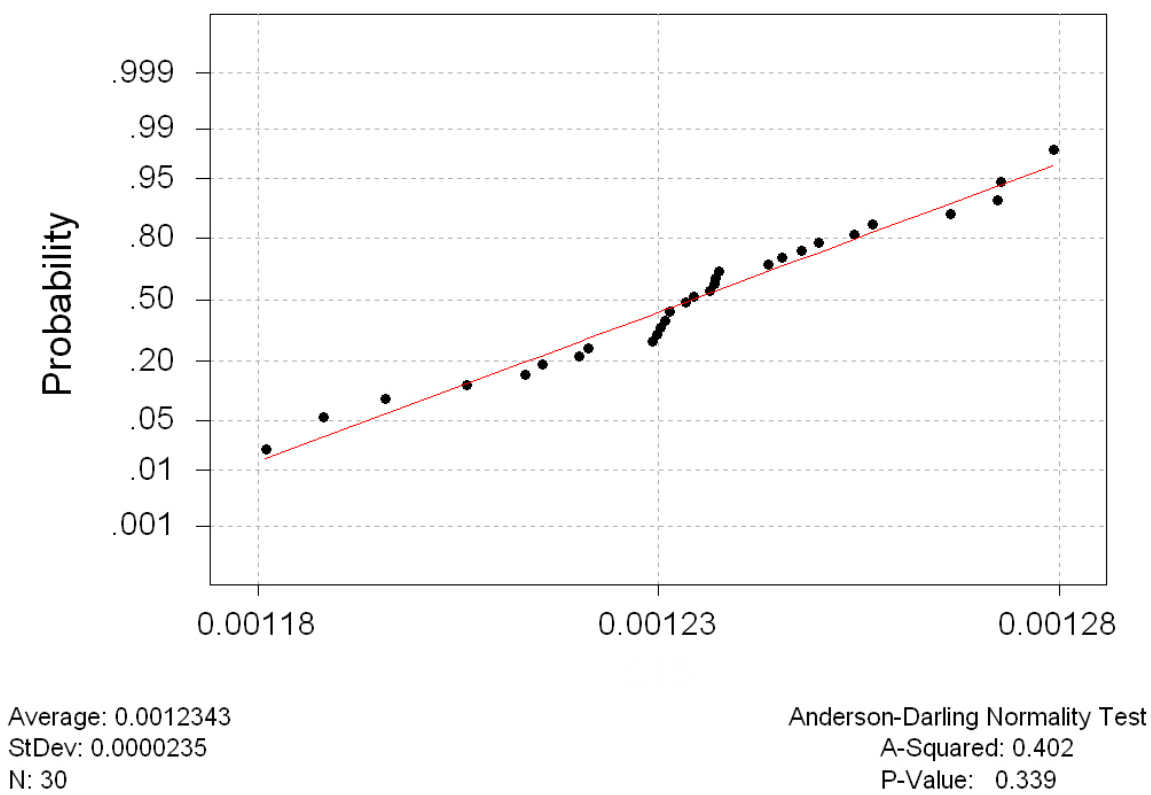

Figure 4.25 Normal Probability Plot from Anderson-Darling Test on All Bottom View Points.

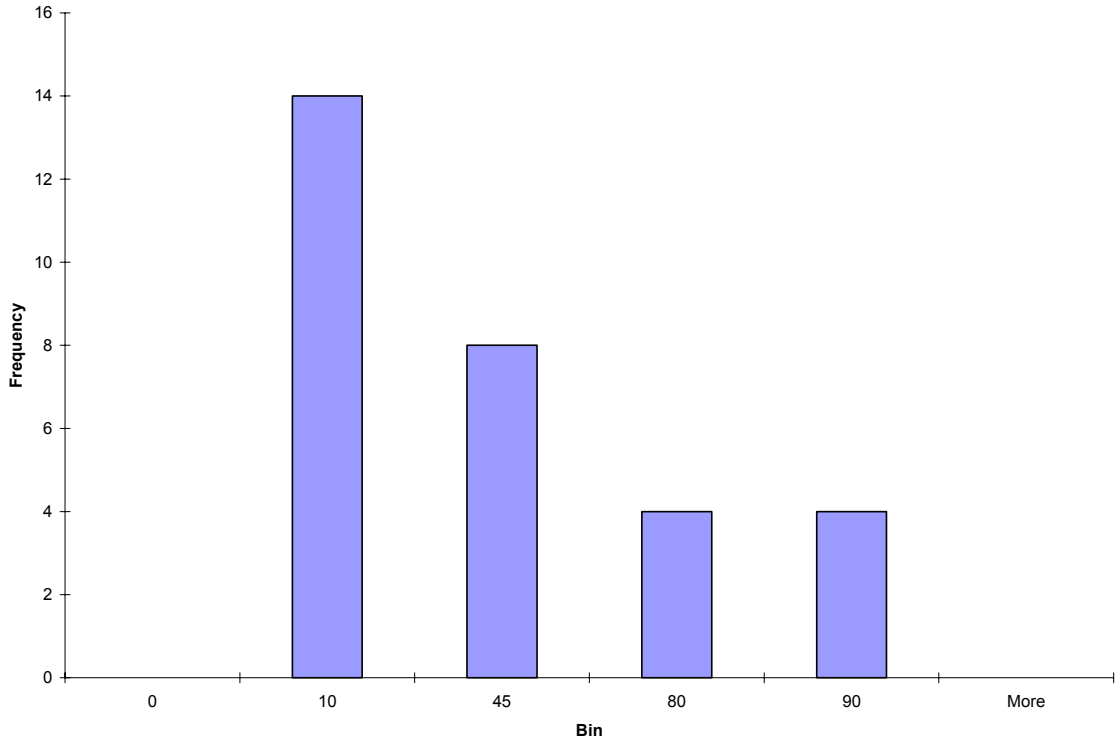

Figure 4.26 Orientation Distributions for All Bottom View Droplet Tests.

has little effect on the volume calculations as long as the proper orientation is applied and revolution about the correct axis is performed. The average solidity of the bottom images was only 96.62%; again, as with the top, this is likely due to the smaller image size. Additionally, this was uniform across the data set as the standard deviation was only 1.21%.

4.4.3 Top and Bottom Comparison

Figure 4.27 is a scale representation of the two ranges and shows their relative location to each other. There is a large degree of overlap and, since two 300 watt halogen lights were operated continuously, any decrease in volume is justified to by the fact that heating from the lights would cause a degree of evaporation. Both of these facts show that the dual camera setup has the ability to accurately measure the change in diameter

for falling droplets. The only provision that would be applied would be if the change in volume is less than the standard deviation in either the top or bottom volumes; were this to happen, the change could not be differentiated from the measurement uncertainty.

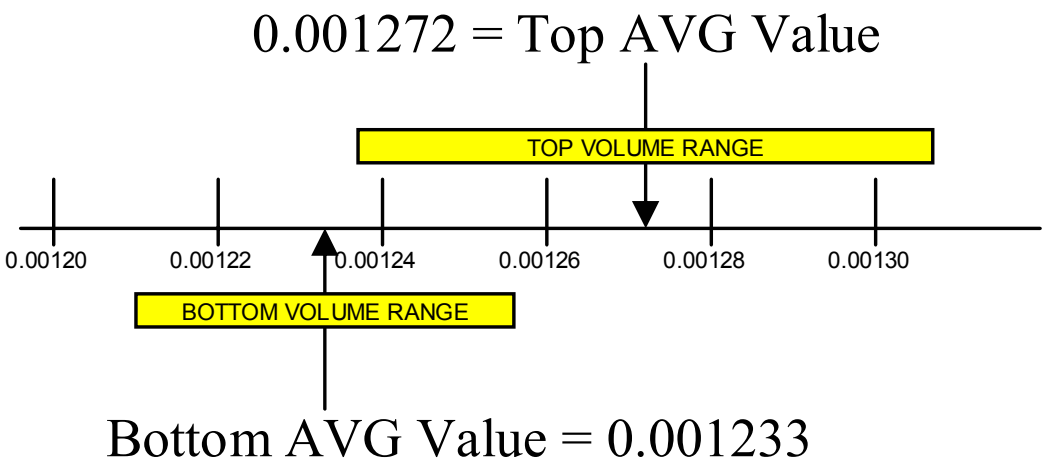

Figure 4.27 Visual Comparison of the Ranges for Top and Bottom Droplet Volumes.

Table 4.4 shows a breakdown of volumes calculated from the top and bottom images. The data points are sorted in ascending order by the middle column which represents the absolute value of the difference between the top and bottom volumes for each trial. It should be noted that the figures that have the worst agreement are those that had no manipulation performed on them for the bottom data; additionally, 3 of 5 poor fills in the top data are represented by these poor matches. If one looks at each individual trial and applies the standard deviations then 21 of 29 trials overlap and are able to be explained by the deviations. The 8 worst matches (trials 3, 11, 15, 17, 19, 22, 28, and 29) have poor fills for half of them and six of the eight have much higher than average top volumes.

Table 4.4 Top and Bottom Trial by Trial Comparison.

TRIAL #	TOP ACCURACY	TOP VOLUME in^3	ABSOLUTE DIFFERENCE in^3	BOTTOM VOLUME in^3	BOTTOM ACCURACY
1	1	1.1878E-03	4.600E-07	1.1882E-03	1
10	3	1.2189E-03	1.082E-06	1.2200E-03	4
6	1	1.2402E-03	2.706E-06	1.2375E-03	1
8	1	1.2763E-03	3.686E-06	1.2726E-03	4
25	1	1.2497E-03	6.128E-06	1.2436E-03	4
14	1	1.2541E-03	6.322E-06	1.2478E-03	3
4	1	1.2473E-03	9.329E-06	1.2566E-03	4
9	3	1.2889E-03	9.629E-06	1.2792E-03	4
12	1	1.2673E-03	1.288E-05	1.2544E-03	4
21	1	1.2534E-03	1.636E-05	1.2371E-03	1
2	1	1.2925E-03	2.031E-05	1.2722E-03	1
18	1	1.2508E-03	2.100E-05	1.2298E-03	4
23	1	1.2590E-03	2.269E-05	1.2363E-03	4
27	1	1.2748E-03	2.481E-05	1.2500E-03	4
30	1	1.2565E-03	2.633E-05	1.2302E-03	4
7	1	1.2632E-03	2.872E-05	1.2344E-03	1
5	1	1.2668E-03	3.539E-05	1.2314E-03	1
16	1	1.2711E-03	4.030E-05	1.2308E-03	4
24	1	1.2778E-03	4.440E-05	1.2334E-03	4
13	1	1.2294E-03	4.842E-05	1.1810E-03	1
26	1	1.2930E-03	5.613E-05	1.2369E-03	1
3	4	1.2687E-03	6.276E-05	1.2060E-03	4
28	1	1.3140E-03	6.867E-05	1.2454E-03	1
22	1	1.2654E-03	6.951E-05	1.1959E-03	1
29	3	1.2943E-03	7.316E-05	1.2212E-03	1
17	1	1.3122E-03	8.305E-05	1.2292E-03	1
15	3	1.3206E-03	8.923E-05	1.2314E-03	1
11	1	1.3315E-03	1.161E-04	1.2154E-03	1
19	3	1.3600E-03	1.467E-04	1.2133E-03	1
AVG		1.2719E-03	3.953E-05	1.233E-03	
STD DEV		3.5000E-05	3.680E-05	2.310E-05	

CHAPTER 5

CONCLUSIONS AND RECOMMENDATIONS

The primary objective of this research was to design, construct, and instrument an experimental test facility to examine the interactions between liquid droplets and low-temperature, low-pressure, plasmas under conditions similar to those expected following inertial fusion target explosions and the subsequent expansion. The data to be obtained from such a facility will be useful in validating mechanistic chamber-clearing models to assure successful beam propagation and target delivery. The experimental apparatus and data acquisition methods have been tested and shown to be effective in producing liquid droplets in a vacuum. Additionally, the ability to capture images of liquid droplets prior to and after passing through the plasma has been demonstrated. These efforts will be crucial to continued study of the interaction of plasma with liquid droplets.

5.1 Conclusions

Based on the results of this research, the following conclusions can be drawn.

1) It was determined that the use of a falling camera to follow the evolution of a single droplet as it falls through the plasma was not feasible using the available equipment. Synchronizing the droplet release and the camera drop was not possible because of variations in the drop release delay time. The ability to film the drop during its entire fall would be desirable, but is not a requirement for acquiring the data required to meet the objectives of this investigation.

2) The results of the volumetric data for the different pressure tests were very encouraging in that all of the adjusted data sets had average values that were in good agreement with each other. The data shows that droplets of a known size can be predictably released into the plasma. For all experiments, the average droplet volume ranged between 1.124×10^{-3} in^3 and 1.280×10^{-3} in^3 and was easily measured by the camera system.

3) Slight variations in the major and minor axes of the droplet images captured by the imaging system were observed at different pressures. The average length of the major and minor axes corresponded to 120.1 pixels $\pm$ 0.5 pixels and 111.5 pixels $\pm$ 1.75 pixels, respectively, for all trials. The operating pressure appears to have little, if any, effect on determining the droplet shape; moreover, the droplet edge-finding algorithm was demonstrated to generate reproducible results.

4) Correct identification of the droplet orientation sharply impacts the accuracy of the volumetric calculations as rotation about the wrong axis can lead to large variations in the resulting volumes of the generated ellipsoids. The method used to identify the droplet orientation can be reliably used when the axes are within 10° of the vertical or horizontal orientations. Volume calculations may become uncertain when the inclination angles are near 45° of the droplet path.

5) Degassed liquids must be used in these experiments to ensure repeatable droplet generation at reduced pressures. When degassed water was used, the droplet orientation distribution at low pressures was similar to those for high pressure with the majority of the droplets having well defined orientations. Use of water without

degassing results in randomly oriented droplet images that directly impact the droplet volume calculation.

6) The droplet eccentricity has little or no effect on the calculated droplet volumes; oscillation of the droplet as it falls through the ambient results in a wide range of eccentricities among the captured images. The uncertainties in the eccentricity values for the adjusted data sets ranged from 21.13% to 39.90%; while the corresponding mean values ranged from 0.105 at 20-50 Torr to 0.527 at atmospheric pressure. The eccentricity uncertainty is higher for the atmospheric case as compared to the 75 Torr trial, but the respective volumetric uncertainties do not follow the same pattern. The only apparent use for the eccentricity would be as an indicator that the orientation should be carefully monitored in these images since a "flat" droplet image will have greater disparities between major and minor axis rotations.
7) The solidity of the captured images provides a good indicator of possible outlying datapoints but seems to have little adverse effect on the volumetric data.
8) Using degassed water in the droplet generation system made it possible to reliably produce droplets, even at low chamber pressures, with a reproducible trajectory within the viewing area. Note that there were only three observations of droplets containing bubbles and no evidence of droplets falling outside of the viewing window in the 20-50 Torr range using degassed water as opposed to 30 occurrences of these types of events at similar pressures using distilled water without degassing. A large decrease in the volumetric uncertainty (from 29.32% to 8.445%) was observed in the low-pressure unadjusted data sets (20-50 Torr) when degassed water was used. Care

must be taken to remove any dissolved non-condensables beforehand for any working fluid used in this test facility.

9) A dual image camera system can successfully detect changes in the volume of a specific droplet as it falls through the ambient environment (*e.g.* plasma). Experiments have shown that the droplet volumes upon entry and near departure of the viewing area were nearly identical under isothermal conditions. A comparison of the inlet and exit (top and bottom, respectively) volume measurements, which should give an indication as to whether the mirrors distorted the images, shows good agreement between these values, suggesting that the current imaging system gives reasonably accurate estimates of volume change.

5.2 Recommendations

This section covers recommendations for future work in three distinct areas: 1) recommended improvements to the current apparatus; 2) recommendations for further experiments; and 3) recommended improvements in the overall methodology.

5.2.1 Improvements to the Current Apparatus

The first improvement to the apparatus should be development of instrumentation for the Langmuir probe to measure the electron temperature of the plasma. The objective of these experiments, namely direct comparisons between data from this facility and calculations from mechanistic chamber-clearing models requires this temperature measurement. A second instrumentation improvement would be to replace the current digital pressure gauge, which operates with a thermocouple pressure sensor, with a wide range diaphragm manometer vacuum gauge. This change is necessitated by the fact that

the thermocouple pressure sensor is sensitive to changes in gas composition whereas the manometer type gauge is not.

Another primary improvement would be incorporating a way to equalize the pressure in the liquid supply (X) and the plasma chamber (Z) in the test facility. One way to accomplish this would be to remove the liquid supply pressure gauges (C & Q), bore a hole through the top plate of the plasma chamber (Z) for a liquid vacuum draw, and move the water shutoff valve (AH) to a position between the liquid supply (X) and the plasma chamber (Z). With these modifications, the pressure at the needle exit and the pressure at the liquid surface could be maintained in equilibrium simply by opening the shutoff valve. The current design has the liquid supply flask equalized with the intake of the vacuum pump.

An additional improvement to the liquid droplet generation system would be to fabricate a combination top plate and liquid supply. The key purpose of this new design would be to allow simultaneous control of the temperature of the liquid supply (X) and liquid control valves (W & Y). The current design limits the temperature to the ambient temperature of the lab so that there is no way to control the temperature of the valves. Hence the ability to either chill or heat a liquid in the liquid supply is limited. This would expand the possibilities for further studies as described in the next section.

An improvement for the vacuum system would be to fabricate a filter for the pump exhaust in order to utilize other liquid droplet materials which may be harmful such as lead or mercury. This filter would have to screw directly into the pump housing and be able to capture the metal vapors (perhaps cryogenically) from the pump exhaust.

The last major improvement to the apparatus would be the installation of a second camera. During the development of the imaging system, the decision was made to use the dual view mirror system in order to avoid issues with determining the time between images, which must be known with great accuracy, in order to compare the droplet volume evolution with chamber-clearing models. Issues arising from attempts to obtain uniform illumination at two different locations at the same time were not anticipated. These issues were somewhat overcome by adjusting the Matlab code to allow lower threshold values and manipulating the images where necessary. A better solution would be to run several tests using the dual-view mirror system to get an accurate time standard and rough volume change data; then use a two-camera system (with an indicator to synchronize the timing of both image sequences) for a rough time standard and accurate volume data due to increased resolution and better lighting. These two data sets would then be used to validate each other.

5.2.2 Recommendations For Further Experiments

The first experiment to be performed should be a full system test using water as the liquid at room temperature with helium plasma at a pressure of 20-50 Torr. The current apparatus is capable of conducting such a test, which will determine to a large extent the scope of future experiments. The next step would be to attempt to conduct the same experiment with chilled water, preferably at pressures as small as 5-10 Torr. This would be the limit of applicable pressures for water; at lower pressures, freezing within the droplet delivery system becomes a major issue. The pressure equalization modification described in the previous Subsection would also probably be required in order to decrease vacuum leaks in the system to operate at this reduced pressure.

The next trial would eliminate the issue of dissolved gases and/or boiling by using a pure liquid metal. Once the apparatus has been modified to allow heating of the liquid supply and valve system, gallium (which has already been purchased) would replace water as the liquid. The liquid supply (X) would be heated to approximately 35°C and the plasma chamber (Z) would be placed in as low of a vacuum as possible to reduce gallium oxidation. A ceramic cup would need to be placed at the bottom of the chamber for easy removal of any remaining fluid. Droplets of gallium would be photographed in the same manner as the water tests.

The next step would be taken only if a safe metal vapor capture system as described in the previous section has been purchased or built. The next recommended liquid would be mercury as this would not require heating. Upon successful testing of this fluid, the final fluid to be tested would be molten lead, which is the actual substance proposed for several thin walled protection schemes and is a metal with a relatively low melting point.

5.2.3 Improvements In The Overall Methodology

This last section describes some considerations that should be taken into account if this test apparatus were to be re-designed and re-built. Based on observations of an experiment at North Carolina State University to study the effects of plasma on a pool of liquid metal; the plasma chamber should be constructed primarily of metal. This would eliminate the need for a Faraday cage as the plasma chamber itself would serve both purposes; it would also decrease by a factor of two the number of vacuum fittings and consequently the number of leaks. The chamber could then be constructed with only five holes: a vacuum draw, a gas introduction port, a liquid introduction port, a liquid vacuum

port, and a pressure sensor port. All other connections (thermocouple readout, Langmuir probe leads, RF supply, etc) could be made with insulated and sealed bulkhead connectors. The plates would be permanently mounted inside and “floated” on ceramic plates to prevent grounding of the electrodes with the plasma chamber.

The imaging system would be similar, except that the viewing port would be two flat clear panels mounted on opposite sides of the plasma chamber. One side would allow observation of the liquid droplets, while the other panel would allow backlit illumination of the droplets. The lights would be mounted outside the chamber to reduce the number of required bulkhead connectors, while keeping the size of the plasma chamber as small as possible.

APPENDIX A

RAW DATA

Table A.1 Data for Falling Camera Test.

TRIAL	VERNIER READINGS		FRAME NUMBER		FRAME	FALL TIME
#	1st DROP	2nd DROP	1st LIGHT	1st PIC	COUNT	(s)
3	11.15	6.21	9	64	55	0.4583
4	11.21	7.02	32	64	32	0.2667
5	12.05	7.11	19	52	33	0.2750
6	10.16	5.22	8	63	55	0.4583
7	11.13	6.19	13	55	42	0.3500
8	11.2	7.01	9	40	31	0.2583
9	13.06	8.12	12	41	29	0.2417
10	12.07	7.13	9	35	26	0.2167
11	12.12	7.18	4	34	30	0.2500
12	11.09	6.15	6	48	42	0.3500
13	12.06	7.12	3	38	35	0.2917
14	10.21	6.02	3	46	43	0.3583
15	12.19	8	5	34	29	0.2417
16	13.02	8.08	4	33	29	0.2417
17	11.18	6.24	4	29	25	0.2083
				AVG	35.7	0.2978

Table A.2 Data for Droplet Generation Test at Atmospheric Pressure.

TRIAL	VOLUME	MAJOR AXIS	MINOR AXIS	ORIENTATION	ROTATION	ECCENTRICITY	THRESHOLD	SOLIDITY	ACCURACY
#	in^3	Pixels	Pixels	Degrees					
1	1.20E-03	117.54	114.22	86.9	maj	0.236	0.2001	0.984	1
2	1.21E-03	122.91	105.36	-88.4	maj	0.515	0.3501	0.967	3
3	1.21E-03	119.07	111.84	88.8	maj	0.343	0.1751	0.983	1
4	1.22E-03	117.40	116.31	35.8	maj	0.136	0.2251	0.983	3
5	1.27E-03	120.67	115.06	6.8	maj	0.301	0.1751	0.982	3
6	1.22E-03	117.57	115.59	17.1	maj	0.182	0.2751	0.985	1
7	1.22E-03	123.14	105.71	-86.9	maj	0.513	0.2001	0.964	3
8	1.19E-03	121.16	106.96	84.8	maj	0.470	0.3001	0.972	3
9	1.20E-03	119.75	110.02	89.1	maj	0.395	0.2251	0.984	1
10	1.19E-03	121.42	113.34	3.5	min	0.359	0.1751	0.983	1
11	1.22E-03	120.60	110.08	88.5	maj	0.408	0.3501	0.983	1
12	1.20E-03	116.87	115.68	69.5	maj	0.142	0.1751	0.984	1
13	1.20E-03	120.80	108.51	88.9	maj	0.439	0.2251	0.979	3
14	1.23E-03	118.74	114.45	82.3	maj	0.266	0.1751	0.983	1
15	1.19E-03	120.71	107.41	-89.9	maj	0.456	0.3251	0.982	1
16	1.18E-03	116.14	115.07	9.6	maj	0.136	0.2001	0.984	1
17	1.19E-03	123.76	112.27	5.2	min	0.421	0.3751	0.985	1
18	1.20E-03	121.07	107.53	-89.3	maj	0.459	0.2501	0.983	1
19	1.16E-03	123.54	111.23	6.2	min	0.435	0.1751	0.984	1
20	1.21E-03	120.57	109.27	-87.1	maj	0.423	0.3001	0.973	3
21	1.20E-03	122.32	105.69	89.0	maj	0.503	0.2001	0.982	1
22	1.18E-03	124.01	111.64	7.0	min	0.435	0.2251	0.983	1
23	1.20E-03	117.04	114.71	8.7	maj	0.199	0.3751	0.982	3
24	1.18E-03	120.25	107.19	-88.8	maj	0.453	0.2251	0.972	3
25	1.20E-03	121.17	107.20	-88.3	maj	0.466	0.2501	0.980	1
26	1.19E-03	121.38	113.71	5.5	min	0.350	0.2001	0.984	1
27	1.20E-03	121.34	107.18	-87.2	maj	0.469	0.3001	0.983	1
28	1.17E-03	121.75	104.00	-89.8	maj	0.520	0.2001	0.980	1
29	1.18E-03	119.92	107.50	87.1	maj	0.443	0.1751	0.975	3
30	1.18E-03	118.34	114.66	3.3	min	0.247	0.1751	0.982	3
31	1.19E-03	117.39	113.14	82.9	maj	0.267	0.2001	0.984	1
32	1.17E-03	119.27	113.77	5.0	min	0.300	0.3251	0.982	1

Table A.2 (continued).

TRIAL	VOLUME	MAJOR AXIS	MINOR AXIS	ORIENTATION	ROTATION	ECCENTRICITY	THRESHOLD	SOLIDITY	ACCURACY
#	in^3	Pixels	Pixels	Degrees					
33	1.20E-03	122.74	104.57	-89.1	maj	0.524	0.2251	0.956	3
34	1.21E-03	122.24	106.18	-89.0	maj	0.495	0.2001	0.982	1
35	1.18E-03	122.24	103.91	-89.4	maj	0.527	0.3001	0.979	1
36	1.19E-03	118.07	111.90	88.4	maj	0.319	0.2001	0.984	1
37	1.17E-03	118.45	110.07	88.3	maj	0.370	0.2251	0.984	1
38	1.19E-03	120.77	113.86	7.8	min	0.333	0.2001	0.983	1
39	1.18E-03	119.99	113.54	6.2	min	0.324	0.2001	0.985	1
40	1.18E-03	121.70	104.35	-88.6	maj	0.515	0.2501	0.976	3
41	1.18E-03	121.66	105.10	-85.8	maj	0.504	0.3251	0.972	3
42	1.18E-03	117.90	111.29	89.0	maj	0.330	0.2001	0.985	1
43	1.17E-03	118.05	110.62	88.2	maj	0.349	0.2501	0.984	1
44	1.18E-03	120.90	106.33	-88.4	maj	0.476	0.2501	0.982	1
45	1.19E-03	117.66	112.63	-89.2	maj	0.289	0.3501	0.982	1
46	1.20E-03	121.28	106.83	-87.4	maj	0.473	0.3001	0.982	1
47	1.20E-03	117.15	114.74	8.7	maj	0.202	0.3251	0.984	1
48	1.25E-03	127.63	101.20	-85.1	maj	0.609	0.2501	0.879	3
49	1.25E-03	125.04	104.70	-86.0	maj	0.547	0.2751	0.915	3
50	1.18E-03	117.15	112.85	87.5	maj	0.269	0.2501	0.983	1
AVG	1.20E-03	120.36	110.02			0.38	0.25	0.98	
STD DEV	2.16E-05	2.413798	3.999879			0.120	0.0599	0.018	
% Error	1.81	2.01	3.64			31.40	24.39	1.83	

Table A.3 Data for Droplet Generation Test at 300 Torr Pressure.

TRIAL	VOLUME	MAJOR AXIS	MINOR AXIS	ORIENTATION	ROTATION	ECCENTRICITY	THRESHOLD	SOLIDITY	ACCURACY	PRESSURE	
#	in^3	Pixels	Pixels	Degrees						H2O	Cham-ber
										Torr	Torr
1	1.18E-03	117.53	112.15	83.9	maj	0.299	0.2001	0.984	1	267	245
2	1.21E-03	117.59	115.00	7.6	maj	0.209	0.2001	0.986	1	270	258
3	1.18E-03	121.24	105.80	88.6	maj	0.488	0.2501	0.978	3	274	263
4	1.20E-03	120.04	109.66	87.3	maj	0.407	0.3001	0.983	1	277	267
5	1.18E-03	121.24	105.77	88.9	maj	0.489	0.2251	0.973	3	280	270
6	1.18E-03	121.64	104.80	87.7	maj	0.508	0.2751	0.971	3	284	272
7	1.19E-03	122.78	112.94	-0.2	min	0.392	0.1751	0.984	1	285	274
8	1.17E-03	125.13	110.93	1.0	min	0.463	0.1751	0.983	1	290	277
9	1.18E-03	125.92	110.91	1.2	min	0.474	0.1751	0.981	1	292	280
10	1.21E-03	119.91	115.22	4.4	min	0.277	0.3501	0.976	3	294	282
11	1.21E-03	117.67	115.07	0.0	maj	0.209	0.2001	0.984	1	296	283
12	1.18E-03	121.68	105.10	88.3	maj	0.504	0.2751	0.977	1	299	287
13	1.19E-03	119.58	109.37	87.2	maj	0.404	0.2251	0.982	1	300	289
14	1.19E-03	120.13	108.83	86.8	maj	0.424	0.2251	0.984	1	305	292
15	1.22E-03	121.20	109.03	87.3	maj	0.437	0.2751	0.984	1	306	294
16	1.18E-03	119.42	108.77	88.1	maj	0.413	0.2251	0.980	1	309	297
17	1.32E-03	128.77	104.26	-89.5	maj	0.587	0.3251	0.851	3	310	298
18	1.19E-03	120.38	108.32	86.8	maj	0.436	0.1751	0.984	1	313	301
19	1.21E-03	120.25	110.14	-88.1	maj	0.401	0.3251	0.978	1	316	304
20	1.20E-03	117.88	113.89	84.1	maj	0.258	0.2501	0.982	1	319	307
21	1.20E-03	116.59	115.76	32.1	maj	0.120	0.2001	0.983	1	321	309
22	1.21E-03	117.18	116.05	68.7	maj	0.139	0.3501	0.981	1	323	311
23	1.19E-03	119.79	108.76	86.1	maj	0.419	0.2501	0.982	1	325	313
24	1.21E-03	120.52	109.62	88.4	maj	0.415	0.3251	0.982	1	330	317
25	1.19E-03	117.84	112.90	84.6	maj	0.287	0.2001	0.983	1	331	319
26	1.22E-03	120.93	109.24	-88.8	maj	0.429	0.3251	0.982	1	334	322
27	1.19E-03	120.82	113.66	4.3	min	0.339	0.2751	0.984	1	336	324
28	1.21E-03	119.40	111.26	87.7	maj	0.363	0.3251	0.984	1	338	325
29	1.20E-03	121.73	106.20	87.7	maj	0.489	0.3501	0.980	1	340	328
30	1.18E-03	121.66	105.03	89.5	maj	0.505	0.3251	0.978	3	345	333
AVG	1.20E-03	120.55	110.15			0.386	0.2584	0.98		307.0	294.7
STD DEV	2.56E-05	2.64	3.57			0.115	0.0599	0.024			
% Error	2.13	2.19	3.24			29.79	23.19	2.45			

Table A.4 Data for Droplet Generation Test at 75 Torr Pressure.

TRIAL	VOLUME	MAJOR AXIS	MINOR AXIS	ORIENTATION	ROTATION	ECCENTRICITY	THRESHOLD	SOLIDITY	ACCURACY	PRESSURE	
#	in^3	Pixels	Pixels	Degrees						H2O Torr	Chamber Torr
1	1.29E-03	127.40	115.51	3.8	min	0.422	0.3001	0.985	1	67	52
2	1.19E-03	121.32	113.42	0.9	min	0.355	0.2001	0.983	1	70	56
3	1.20E-03	117.99	113.33	-85.5	maj	0.278	0.2251	0.984	1	75	61
4	1.19E-03	119.96	114.34	16.1	min	0.302	0.2501	0.981	1	78	64
5	1.19E-03	121.30	106.16	-49.5	maj	0.484	0.3001	0.982	1	81	67
6	1.20E-03	120.04	109.06	79.1	maj	0.418	0.3251	0.983	3	84	69
7	1.20E-03	119.35	111.07	76.4	maj	0.366	0.3501	0.980	1	86	72
8	1.20E-03	120.56	108.15	-66.4	maj	0.442	0.2501	0.982	1	90	75
9	1.20E-03	117.26	115.07	5.8	maj	0.192	0.3251	0.984	1	92	78
10	1.21E-03	120.81	109.33	-51.9	maj	0.425	0.3001	0.984	1	95	80
11	1.18E-03	118.88	110.03	88.4	maj	0.379	0.2501	0.984	1	97	82
12	1.20E-03	118.94	111.56	44.2	maj	0.347	0.2501	0.984	1	100	85
13	1.20E-03	118.85	111.28	-65.2	maj	0.351	0.2501	0.984	1	103	89
14	1.17E-03	120.21	106.70	85.0	maj	0.461	0.2001	0.978	3	105	90
15	1.18E-03	120.37	106.65	85.4	maj	0.464	0.2001	0.981	1	107	93
16	1.21E-03	121.12	108.46	-56.3	maj	0.445	0.2751	0.983	1	112	98
17	1.18E-03	117.28	112.32	80.8	maj	0.288	0.2251	0.982	1	75	60
18	1.20E-03	120.57	108.52	68.6	maj	0.436	0.3501	0.969	3	78	63
19	1.20E-03	120.30	109.16	88.5	maj	0.420	0.3501	0.969	3	81	67
20	1.32E-03	120.32	119.67	8.4	maj	0.104	0.3251	0.983	1	84	69
21	1.16E-03	121.15	112.16	4.8	min	0.378	0.3001	0.984	1	88	73
22	1.23E-03	118.95	114.56	-15.2	maj	0.269	0.2501	0.984	1	89	74
23	1.20E-03	122.31	113.77	13.3	min	0.367	0.2751	0.984	1	93	78
24	1.15E-03	119.62	112.47	-6.1	min	0.340	0.3001	0.983	1	94	80
25	1.16E-03	119.51	107.13	84.3	maj	0.443	0.2001	0.979	3	95	81
26	1.19E-03	118.91	111.02	-64.7	maj	0.358	0.2001	0.985	1	97	82
27	1.22E-03	121.69	107.92	82.5	maj	0.462	0.2501	0.983	1	99	83
28	1.28E-03	119.77	117.17	27.4	maj	0.207	0.4001	0.975	3	100	85
29	1.17E-03	121.94	112.51	16.7	min	0.386	0.2001	0.983	1	102	86
30	1.21E-03	117.50	115.20	21.9	maj	0.197	0.3751	0.984	1	103	88
AVG	1.20E-03	120.14	111.46			0.360	0.2751	0.98		90.7	76.0
STD DEV	3.67E-05	1.91	3.37			0.094	0.0576	0.400			
% Error	3.05E+00	1.59	3.02			26.19	20.94	40.75			

Table A.5 Data for Droplet Generation Test at 20-50 Torr Pressure.

TRIAL	VOLUME	MAJOR AXIS	MINOR AXIS	ORIENTATION	ROTATION	ECCENTRICITY	THRESHOLD	SOLIDITY	ACCURACY	CHAMBER PRESSURE
#	in^3	Pixels	Pixels	Degrees						Torr
1	1.20E-03	116.65	116.00	78.2	maj	0.105	0.2001	0.984	1	38
2	8.21E-04	104.21	99.36	78.6	maj	0.302	0.2251	0.980	1	40
3	1.22E-03	118.40	114.83	80.0	maj	0.244	0.2501	0.985	1	44
5	1.25E-03	118.68	116.89	-9.9	maj	0.173	0.2501	0.977	3	42
6	1.24E-03	119.06	114.88	88.9	maj	0.263	0.2251	0.984	1	47
7	9.39E-04	108.76	104.38	-77.4	maj	0.281	0.2251	0.983	1	33
8	3.59E-04	79.16	75.26	78.9	maj	0.310	0.2251	0.978	1	39
9	1.12E-03	120.90	110.35	-19.9	min	0.409	0.2251	0.984	1	43
10	1.14E-03	125.32	109.13	19.0	min	0.492	0.2001	0.983	1	47
10-2	1.36E-03	121.80	120.29	62.0	maj	0.157	0.2001	0.984	1	47
11	2.91E-04	77.62	70.20	12.6	min	0.427	0.2251	0.976	1	31
12	9.20E-04	110.75	104.50	1.6	min	0.331	0.2501	0.984	1	41
12-2	5.94E-04	117.42	81.52	-50.5	min	0.720	0.3501	0.979	1	41
13	1.26E-03	119.36	116.09	-27.5	maj	0.232	0.2751	0.984	1	47
13-2	1.22E-03	118.41	114.76	60.2	maj	0.246	0.2501	0.981	1	47
14	3.55E-04	77.76	77.22	65.8	maj	0.117	0.2001	0.979	1	35
14-2	5.89E-04	108.29	84.56	10.7	min	0.625	0.2251	0.981	1	35
15	9.45E-04	109.04	104.49	-46.8	maj	0.286	0.2001	0.983	1	39
16	1.23E-03	122.64	107.66	-77.5	maj	0.479	0.2001	0.984	1	45
16-2	1.15E-03	121.07	111.79	9.2	min	0.384	0.2251	0.985	1	45
17	9.31E-04	109.37	102.28	-55.3	maj	0.354	0.3501	0.982	1	37
18	1.23E-03	119.26	114.12	36.7	maj	0.290	0.2001	0.984	1	45
18-2	1.18E-03	119.40	114.00	12.3	min	0.297	0.2251	0.985	1	45
18-3	1.11E-03	123.30	109.01	40.9	min	0.467	0.2251	0.984	1	45
18-4	1.22E-03	119.22	112.94	-66.6	maj	0.320	0.2001	0.983	1	45
19	1.05E-03	118.59	108.11	1.8	min	0.411	0.3751	0.983	1	47
19-2	1.21E-03	119.29	112.07	-58.4	maj	0.343	0.2001	0.984	1	47
20	1.24E-03	118.48	116.36	0.2	maj	0.188	0.2751	0.984	1	47
20-2	1.33E-03	122.06	116.91	33.2	maj	0.287	0.2251	0.985	1	47
20-3	1.06E-03	111.95	111.20	-0.1	maj	0.115	0.2751	0.982	1	47
AVG	1.03E-03	113.21	105.71			0.322	0.2393	0.98		42.6
STD DEV	3.01E-04	12.93	13.75			0.142	0.0467	0.003		
% Error	29.32	11.42	13.01			44.12	19.53	0.25		

Table A.6 Data for Degassed Water Droplet Generation Test at 20-50 Torr Pressure.

TRIAL	VOLUME	MAJOR AXIS	MINOR AXIS	ORIENTATION	ROTATION	ECCENTRICITY	THRESHOLD	SOLIDITY	ACCURACY	PRESSURE	
#	in^3	Pixels	Pixels	Degrees						H2O	Cham-ber
										Torr	Torr
1	1.19E-03	115.30	103.09	89.74	maj	0.448	0.3500	0.97	1	50	31
2	1.18E-03	112.94	109.69	-0.19	min	0.238	0.4250	0.98	1	50	34
3	1.05E-03	112.88	103.45	19.93	min	0.400	0.3500	0.98	1	52	37
4	1.17E-03	111.25	109.98	-10.48	min	0.151	0.4000	0.97	3	55	39
5	1.17E-03	112.98	105.33	87.20	maj	0.362	0.3000	0.98	1	58	41
6	1.10E-03	108.95	107.50	13.07	min	0.162	0.4000	0.97	3	50	30
6A	1.22E-03	112.46	111.43	-34.48	min	0.135	0.4250	0.98	1	50	30
7	1.18E-03	115.20	101.85	88.03	maj	0.467	0.3500	0.98	1	51	34
8	1.18E-03	114.92	102.78	-89.99	maj	0.447	0.3500	0.97	3	53	37
8A	1.19E-03	114.16	104.97	87.64	maj	0.393	0.3000	0.98	1	53	37
9	1.20E-03	116.28	108.72	-3.29	min	0.355	0.4000	0.97	3	56	40
10	1.19E-03	114.82	103.21	88.06	maj	0.438	0.3750	0.98	1	59	45
11	1.28E-03	115.20	112.90	52.97	min	0.199	0.4000	0.98	3	61	25
12	1.23E-03	115.85	110.42	4.49	min	0.303	0.3500	0.98	1	50	31
12A	1.24E-03	115.19	106.84	70.15	maj	0.374	0.4500	0.98	3	50	31
12B	1.22E-03	116.73	102.86	85.83	maj	0.473	0.3500	0.98	1	50	31
13	1.20E-03	116.17	101.92	88.00	maj	0.480	0.3000	0.97	3	50	37
14	1.16E-03	112.52	104.69	87.44	maj	0.367	0.4000	0.98	1	55	39
15	1.09E-03	110.92	106.10	-15.99	min	0.291	0.3000	0.98	1	57	41
16	1.15E-03	115.87	106.86	-2.14	min	0.387	0.4000	0.98	1	62	47
17	1.15E-03	110.98	107.59	62.74	maj	0.245	0.3500	0.97	1	50	27
18	1.30E-03	116.66	109.33	89.45	maj	0.349	0.3000	0.97	3	50	33
19	1.02E-03	106.03	104.01	-25.30	maj	0.194	0.3000	0.98	1	52	35
20	1.17E-03	114.58	102.19	-89.41	maj	0.452	0.3750	0.98	1	54	38
21	1.22E-03	113.90	107.50	88.12	maj	0.330	0.3000	0.98	1	55	39
22	1.19E-03	115.55	102.42	-88.55	maj	0.463	0.3000	0.97	3	60	43
23	1.18E-03	113.41	105.12	-82.14	maj	0.375	0.4500	0.97	3	62	47
24	1.22E-03	112.62	111.57	14.28	min	0.136	0.3500	0.98	1	50	31
24A	1.16E-03	110.95	108.44	82.05	maj	0.211	0.4000	0.97	3	50	31
25	7.85E-04	99.58	90.85	-53.35	maj	0.410	0.4000	0.98	1	53	37
25A	1.20E-03	115.93	102.46	87.93	maj	0.468	0.3000	0.97	3	53	37
26	1.17E-03	114.53	102.32	-86.66	maj	0.449	0.2750	0.97	3	63	47
AVG	1.17E-03	113.29	105.57			0.342	0.3586	0.98		53.88	36.31
STD DEV	8.94E-05	3.46	4.22			0.112	0.0502	0.00			
% ERROR	7.66	3.06	4.00			32.82	14.01	0.47			

Table A.7 Data for Top Dual View Droplet Size Test at Atmospheric Pressure.

TRIAL	VOLUME	MAJOR AXIS	MINOR AXIS	ORIENTATION	ROTATION	ECCENTRICITY	THRESHOLD	SOLIDITY	ACCURACY
#	in^3	Pixels	Pixels	Degrees					
1	1.19E-03	61.69	59.80	-14.5	min	0.246	0.0500	0.94	1
2	1.29E-03	63.89	58.80	-12.4	maj	0.391	0.3250	0.96	1
3	1.27E-03	63.02	59.32	-28.9	maj	0.338	0.3000	0.97	4
4	1.25E-03	66.64	58.95	-8.7	min	0.466	0.4500	0.95	1
5	1.27E-03	62.09	61.01	-50.1	maj	0.186	0.4500	0.97	1
6	1.24E-03	66.15	59.00	-8.0	min	0.452	0.4500	0.97	1
7	1.26E-03	65.54	59.82	-9.6	min	0.408	0.4000	0.97	1
8	1.28E-03	64.77	60.49	-11.3	min	0.358	0.4000	0.97	1
9	1.29E-03	68.01	59.32	-10.9	min	0.489	0.5000	0.96	3
10	1.22E-03	67.12	58.07	-9.2	min	0.501	0.4000	0.94	3
11	1.33E-03	64.61	59.23	-34.8	maj	0.399	0.4000	0.95	1
12	1.27E-03	66.27	59.59	-11.7	min	0.437	0.4000	0.97	1
13	1.23E-03	65.34	59.11	-12.1	min	0.426	0.4000	0.96	1
14	1.25E-03	65.26	59.73	-14.4	min	0.403	0.4000	0.95	1
15	1.32E-03	63.73	60.38	-48.0	maj	0.320	0.3000	0.93	3
16	1.27E-03	66.89	59.40	-8.6	min	0.460	0.4500	0.98	1
17	1.31E-03	63.68	60.09	-23.9	maj	0.331	0.4500	0.96	1
18	1.25E-03	67.20	58.79	-9.1	min	0.484	0.4250	0.97	1
19	1.36E-03	65.05	59.69	-23.4	maj	0.397	0.5750	0.96	3
20	1.44E-03	67.08	59.56	-19.7	maj	0.460	0.5000	0.97	3
21	1.25E-03	65.68	59.53	-8.7	min	0.422	0.4000	0.97	1
22	1.27E-03	62.53	60.09	-32.7	maj	0.277	0.5000	0.95	1
23	1.26E-03	67.16	59.00	-9.1	min	0.478	0.4000	0.96	1
24	1.28E-03	66.27	59.83	-9.9	min	0.430	0.4500	0.98	1
25	1.25E-03	67.05	58.83	-7.7	min	0.480	0.4500	0.98	1
26	1.29E-03	62.87	60.74	-26.9	maj	0.258	0.4000	0.97	1
27	1.27E-03	65.82	59.97	-12.2	min	0.412	0.4000	0.97	1
28	1.31E-03	63.46	60.59	-12.4	maj	0.297	0.4000	0.97	1
29	1.29E-03	63.55	59.51	-16.8	maj	0.351	0.4750	0.95	3
30	1.26E-03	67.19	58.93	-6.8	min	0.481	0.4000	0.97	1
AVG	1.28E-03	65.19	59.57			0.395	0.4100	0.96	
STD DEV	4.65E-05	1.771683	0.665402			0.082	0.0890	0.01	
% Error	3.64	2.72	1.12			20.84	21.70	1.35	

Table A.8 Data for Bottom Dual View Droplet Size Test at Atmospheric Pressure.

TRIAL	VOLUME	MAJOR AXIS	MINOR AXIS	ORIENTATION	ROTATION	ECCENTRICITY	THRESHOLD	SOLIDITY	ACCURACY
#	in^3	Pixels	Pixels	Degrees					
1	1.19E-03	64.13	58.64	12.2	min	0.405	0.3000	0.96	1
2	1.27E-03	62.66	60.14	10.0	max	0.281	0.3000	0.98	1
3	1.21E-03	64.04	59.12	2.8	min	0.385	0.4500	0.94	4
4	1.26E-03	62.30	60.09	32.2	max	0.264	0.3000	0.97	4
5	1.23E-03	65.04	59.27	1.7	min	0.412	0.5000	0.98	1
6	1.24E-03	61.73	60.27	21.0	min	0.216	0.2000	0.97	1
7	1.23E-03	65.59	59.10	1.0	min	0.434	0.6000	0.97	1
8	1.27E-03	63.90	57.84	76.6	max	0.425	0.3000	0.98	4
9	1.28E-03	62.35	61.06	54.4	max	0.202	0.3000	0.96	4
10	1.22E-03	61.39	60.08	25.7	max	0.205	0.3000	0.97	4
11	1.22E-03	64.77	59.01	0.4	min	0.412	0.5000	0.97	1
12	1.25E-03	61.99	60.58	38.4	max	0.212	0.3500	0.95	4
13	1.18E-03	63.42	58.79	4.4	min	0.375	0.3000	0.97	1
14	1.25E-03	65.68	59.38	3.1	min	0.427	0.3000	0.95	3
15	1.23E-03	64.88	59.35	0.4	min	0.404	0.3000	0.97	1
16	1.23E-03	63.81	56.10	88.5	max	0.476	0.4000	0.94	4
17	1.23E-03	65.02	59.23	0.9	min	0.412	0.4000	0.98	1
18	1.23E-03	61.68	59.99	42.1	max	0.232	0.2000	0.97	4
19	1.21E-03	64.85	58.92	2.2	min	0.418	0.4500	0.98	1
20	1.27E-03	62.25	60.65	36.5	max	0.225	0.3000	0.95	1
21	1.24E-03	65.14	59.37	1.1	min	0.412	0.5000	0.98	1
22	1.20E-03	64.72	58.56	0.9	min	0.426	0.4500	0.98	1
23	1.24E-03	61.69	60.29	54.2	max	0.212	0.2000	0.97	4
24	1.23E-03	63.61	56.57	83.4	max	0.457	0.2000	0.97	4
25	1.24E-03	62.07	59.91	74.9	max	0.261	0.4000	0.95	4
26	1.24E-03	65.52	59.19	-0.4	min	0.429	0.5000	0.98	1
27	1.25E-03	64.22	56.25	85.0	max	0.482	0.3000	0.95	4
28	1.25E-03	65.66	59.33	1.3	min	0.429	0.5000	0.98	1
29	1.22E-03	64.81	59.13	-0.8	min	0.409	0.6000	0.98	1
30	1.23E-03	62.79	57.91	80.3	max	0.387	0.2000	0.97	4
AVG	1.23E-03	63.72	59.14			0.358	0.3633	0.97	
STD DEV	2.35E-05	1.412428	1.219711			0.095	0.1189	0.01	
% Error	1.91	2.22	2.06			26.53	32.71	1.25	

APPENDIX B

POTENTIAL MATERIAL DATA

Table B.1 Temperatures for Elements at Various Vapor Pressures (Eberl, 2004).

Symbol	Element	Melt Point	Temperature (^{o}C) at Indicated Vapor Pressure			
		^{o}C (at ATM)	10^{-2} Torr	10^{-4} Torr	10^{-6} Torr	10^{-8} Torr
Ag	Silver	962	1027	832	685	574
Al	Aluminium	660	1217	972	812	685
As	Arsenic	817	277	204	150	104
Au	Gold	1064	1397	1132	947	807
B	Boron	2080	2027	1707	1467	1282
Ba	Barium	725	610	462	354	272
Be	Beryllium	1280	1227	997	832	707
Bi	Bismuth	271	672	517	409	347
C	Carbon	3550	2457	2137	1867	1657
Ca	Calcium	839	597	459	357	282
Cd	Cadmium	321	265	177	119	74
Co	Cobalt	1495	1517	1257	1067	922
Cr	Chromium	1857	1397	1157	977	837
Cu	Copper	1083	1257	1027	852	722
Dy	Dysprosium	1409	1117	897	747	625
Er	Erbium	1529	1177	947	777	649
Eu	Europium	822	611	466	361	283
Fe	Iron	1535	1477	1227	1032	892
Ga	Gallium	30	1132	907	742	619
Ge	Germanium	937	1397	1137	947	812
Hg	Mercury	-39	46	7	-44	-72
In	Indium	157	947	742	597	488
K	Potassium	63	208	123	65	21
La	Lanthanum	920	1727	1422	1192	1022
Li	Lithium	181	537	404	306	235

Table B.1 (continued).

Symbol	Element	Melt Point	Temperature (^oC) at Indicated Vapor Pressure			
		^oC (at ATM)	10^{-2} Torr	10^{-4} Torr	10^{-6} Torr	10^{-8} Torr
Mg	Magnesium	649	439	327	246	185
Mn	Manganese	1244	937	747	611	505
Mo	Molybdenum	2610	2527	2117	1822	1592
Na	Sodium	98	289	193	123	74
Nb	Niobium	2468	2657	2277	1987	1762
Ni	Nickel	1453	1527	1262	1072	927
P	Phosphorus	44	185	129	88	54
Pb	Lead	328	715	547	429	342
Pd	Palladium	1554	1462	1192	992	842
Pt	Platinum	1772	2097	1747	1492	1292
Re	Rhenium	3180	3067	2587	2217	1947
Rh	Rhodium	1966	2037	1707	1472	1277
S	Sulfur	113	109	55	17	-10
Sb	Antimony	631	533	425	345	279
Sc	Scandium	1541	1377	1107	917	772
Se	Selenium	217	243	164	107	63
Si	Silicon	1410	1632	1337	1147	992
Sn	Tin	232	1247	997	807	682
Sr	Strontium	769	537	394	309	241
Ta	Tantalum	2996	3057	2587	2237	1957
Te	Tellurium	450	374	280	209	155
Tl	Thallium	304	609	463	359	283
Ti	Titanium	1660	1737	1442	1227	1062
W	Tungsten	3410	3227	2757	2407	2117
Y	Yttrium	1523	1632	1332	1117	957
Yb	Ytterbium	819	557	417	317	247
Zn	Zinc	420	344	247	177	123

Table B.2 Vapor Pressures at 0°C and 20°C (Yaws, 1995). Red Denotes Unusable Ranges. Yellow Denotes Ranges that Apply to Only One Temperature.

					TEMP (K)	
			Tmin	Tmax	273.15	293.15
#	FORMULA	NAME	K	K	Pressure (Torr)	
1	Ag	SILVER	1234	6410	1.26E-46	9.37E-43
2	AgCl	SILVER CHLORIDE	1185.15	1837.15	2.98E-31	2.07E-28
3	Agl	SILVER IODIDE	1093.15	1779.15	5.10E-30	4.48E-27
4	Al	ALUMINUM	933	2329.1	3.08E-42	8.59E-39
5	AIB3H12	ALUMINUM BOROHYDRIDE	220.95	319.05	1.20E+02	2.90E+02
6	AlBr3	ALUMINUM BROMIDE	354.45	529.45	1.68E-07	9.05E-05
7	AIC13	ALUMINUM CHLORIDE	373.15	465.75	8.29E-07	3.05E-05
8	AIF3	ALUMINUM FLUORIDE	1511.15	1810.15	0.00E+00	0.00E+00
9	AII3	ALUMINUM IODIDE	451.15	658.65	8.08E-11	1.22E-08
10	A1203	ALUMINUM OXIDE	2421.1	3253.1	9.61E-92	1.03E-84
11	AI2S3012	ALUMINUM SULFATE	845.15	1043.2	6.65E+56	4.18E+48
12	Ar	ARGON	83.78	150.86	1.35E+06	2.41E+06
13	As	ARSENIC	420	885	1.66E-16	1.49E-14
14	AsBr3	ARSENIC TRIBROMIDE	314.95	493.15	4.93E-02	2.36E-01
15	AsCl3	ARSENIC TRICHLORIDE	261.75	403.55	2.30E+00	8.27E+00
16	AsF3	ARSENIC TRIFLUORIDE	270.65	329.45	4.67E+01	1.43E+02
17	AsF5	ARSENIC PENTAFLUORIDE	155.25	220.35	3.02E+03	2.22E+03
18	AsH3	ARSINE	156.23	373	6.77E+03	1.11E+04
19	Asl3	ARSENIC TRIIODIDE	437.15	602.65	1.58E-05	1.67E-04
20	As203	ARSENIC TRIOXIDE	485.65	730.35	2.13E-05	8.47E-06
21	At	ASTATINE	279	607	4.32E-07	6.95E-06
22	Au	GOLD	1226	3120	0.00E+00	0.00E+00
23	B	BORON	1821	4133	3.12E-113	2.04E-104
24	BBr3	BORON TRIBROMIDE	273.15	361.05	1.89E+01	5.43E+01
25	BC13	BORON TRICHLORIDE	166.15	451.95	4.71E+02	9.92E+02
26	BF3	BORON TRIFLUORIDE	144.78	260.9	5.65E+04	1.09E+05
27	BH2CO	BORINE CARBONYL	133.95	209.15	1.13E+04	1.73E+04
28	BH303	BORIC ACID	293.15	401.15	8.19E-01	1.94E+00
29	B2D6	DEUTERODIBORANE	118.25	179.25	1.47E+04	1.83E+04
30	B2H5Br	DIBORANE HYDROBROMIDE	179.85	289.45	3.88E+02	8.46E+02
31	B2H6	DIBORANE	107.65	289.8	2.01E+04	3.02E+04
32	B3N3H6	BORINE TRIAMINE	210.15	323.75	8.34E+01	2.19E+02
33	B4H10	TETRABORANE	182.25	289.25	3.89E+02	8.67E+02
34	B5H9	PENTABORANE	232.75	568.45	6.29E+01	1.66E+02
35	B5H11	TETRAHYDROPENTABORANE	222.95	340.15	3.42E+01	9.96E+01

Table B.2 (continued).

					TEMP (K)	
			Tmin	Tmax	273.15	293.15
#	FORMULA	NAME	K	K	Pressure (Torr)	
36	B10H14	DECABORANE	333.15	436.95	1.55E-05	2.39E-03
37	Ba	BARIUM	638	1907	1.12E-25	1.94E-23
38	Be	BERYLLIUM	1097	2744	2.20E-54	4.53E-50
39	BeB2H8	BERYLLIUM BOROHYDRIDE	274.15	363.15	9.01E-01	5.18E+00
40	BeBr2	BERYLLIUM BROMIDE	562.15	747.15	3.33E-25	5.73E-20
41	BeCl2	BERYLLIUM CHLORIDE	564.15	760.15	1.61E-06	2.24E-06
42	BeF2	BERYLLIUM FLUORIDE	1145.55	1372.15	3.21E-49	7.13E-44
43	BeI2	BERYLLIUM IODIDE	556.15	760.15	4.95E-30	2.46E-23
44	Bi	BISMUTH	569	1700	1.31E-55	1.07E-46
45	BiBr3	BISMUTH TRIBROMIDE	534.15	734.15	7.40E-11	4.40E-09
46	BiCl3	BISMUTH TRICHLORIDE	503.65	710.55	2.26E-06	1.86E-05
47	BrF5	BROMINE PENTAFLUORIDE	203.85	313.55	1.26E+02	3.22E+02
48	Br2	BROMINE	265.85	584.15	6.50E+01	1.70E+02
49	C	CARBON	3259.1	4399.1	1.99E-89	7.74E-83
50	CC120	PHOSGENE	145.37	455	5.60E+02	1.19E+03
51	CF20	CARBONYL FLUORIDE	161.89	297	2.31E+04	3.92E+04
52	CH4N20	UREA	340.65	368.05	4.81E-07	6.67E-06
53	CH4N2S	THIOUREA	454.15	854	1.13E-03	7.79E-03
54	CNBr	CYANOGEN BROMIDE	273.01	313.09	2.02E+01	8.47E+01
55	CNCI	CYANOGEN CHLORIDE	266.65	449	4.43E+02	1.01E+03
56	CNF	CYANOGEN FLUORIDE	196.75	226.35	4.70E+03	8.31E+03
57	CO	CARBON MONOXIDE	68.15	132.92	3.40E+07	1.14E+08
58	COS	CARBONYL SULFIDE	134.3	378.8	4.86E+03	8.43E+03
59	COSe	CARBON OXYSELENIDE	156.05	251.25	1.89E+03	3.80E+03
60	C02	CARBON DIOXIDE	216.58	304.19	2.62E+04	4.31E+04
61	CS2	CARBON DISULFIDE	161.11	552	1.26E+02	2.96E+02
62	CSeS	CARBON SELENOSULFIDE	225.85	358.75	2.54E+01	6.88E+01
63	C2N2	CYANOGEN	177.35	252.15	1.66E+03	1.19E+03
64	C3S2	CARBON SUBSULFIDE	287.15	403.95	3.95E-01	1.48E+00
65	Ca	CALCIUM	625	1762	8.34E-24	7.08E-22
66	CaF2	CALCIUM FLUORIDE	1691	2806.5	1.90E-79	8.45E-73
67	CbF5	COLUMBIUM FLUORIDE	359.45	498.15	7.61E-02	3.02E-01
68	Cd	CADMIUM	393	1043	7.17E-13	1.49E-11
69	CdCl2	CADMIUM CHLORIDE	891.15	1240.15	1.96E+112	4.40E+90
70	CdF2	CADMIUM FLUORIDE	1385.15	2024.15	6.75E+162	6.41E+139
71	CdI2	CADMIUM IODIDE	689.15	1069.15	3.15E+01	7.35E-01
72	CdO	CADMIUM OXIDE	1273.15	1832.15	8.21E-40	3.05E-36

Table B.2 (continued).

					TEMP (K)	
			Tmin	Tmax	273.15	293.15
#	FORMULA	NAME	K	K	Pressure (Torr)	
73	CIF	CHLORINE MONOFLUORIDE	129.75	172.65	1.42E+05	2.51E+05
74	CIF03	PERCHLORYL FLUORIDE	125.41	368.4	4.47E+03	7.95E+03
75	CIF3	CHLORINE TRIFLUORIDE	192.75	284.65	4.88E+02	1.02E+03
76	CIF5	CHLORINE PENTAFLUORIDE	193.95	297.95	1.29E+03	2.49E+03
77	CIH03S	CHLOROSULFONIC ACID	193.15	700	5.31E-01	2.32E+00
78	CIH04	PERCHLORIC ACID	171.95	631	1.12E+01	3.12E+01
79	C102	CHLORINE DIOXIDE	213.55	465	4.83E+02	1.06E+03
80	C12	CHLORINE	172.12	417.15	2.77E+03	5.10E+03
81	C120	CHLORINE MONOXIDE	174.65	275.35	6.93E+02	1.51E+03
82	C1207	CHLORINE HEPTOXIDE	227.85	351.95	2.23E+01	6.50E+01
83	Co	COBALT	1095	2528	1.11E-57	5.32E-53
84	CoCl2	COBALT CHLORIDE	1043.15	1323.15	7.50E-23	2.51E-20
85	CONC304	COBALT NITROSYL TRICARBONYL	271.85	353.15	2.49E+01	7.47E+01
86	Cr	CHROMIUM	1229	2840	3.61E-55	2.47E-51
87	CrC606	CHROMIUM CARBONYL	309.15	424.15	5.34E-02	2.49E-01
88	Cr02Cl2	CHROMIUM OXYCHLORIDE	254.75	390.25	4.07E+00	1.47E+01
89	Cs	CESIUM	295	959	8.89E-08	8.30E-07
90	CsBr	CESIUM BROMIDE	1021.15	1573.15	1.83E-93	6.31E-80
91	CsCi	CESIUM CHLORIDE	1017.15	1573.15	3.01E-41	3.78E-36
92	CsF	CESIUM FLUORIDE	985.15	1524.15	5.86E-99	2.92E-84
93	Csl	CESIUM IODIDE	1011.15	1553.15	5.45E-37	1.01E-32
94	Cu	COPPER	1130	3150	1.69E-50	6.69E-47
95	CuBr	CUPROUS BROMIDE	845.15	1628.15	3.64E-27	7.92E-24
96	CuCl	CUPROUS CHLORIDE	703	1763.1	3.07E-16	1.54E-14
97	CuC12	CUPRIC CHLORIDE	582.85	794.15	1.09E+09	1.16E+07
98	Cul	COPPER IODIDE	883.15	1609.15	2.61E-48	4.67E-41
99	DCM	DEUTERIUM CYANIDE	204.25	299.35	2.46E+02	6.03E+02
100	D2	DEUTERIUM	18.73	38.35	1.20E+09	2.60E+09
101	D20	DEUTERIUM OXIDE	276.97	643.89	3.81E+00	1.51E+01
102	Eu	EUROPIUM	640	1742	1.43E-25	1.98E-23
103	F2	FLUORINE	53.48	144.31	2.53E+06	4.58E+06
104	F20	FLUORINE OXIDE	77.05	128.55	5.03E+05	9.03E+05
105	Fe	IRON	1808.15	3008.2	3.18E-62	2.31E-57
106	FeC505	IRON PENTACARBONYL	266.65	378.15	7.39E+00	2.31E+01
107	FeCl2	FERROUS CHLORIDE	973.15	1299.15	1.30E+13	4.47E+08
108	FeC13	FERRIC CHLORIDE	467.15	592.15	4.33E-114	1.54E-72

Table B.2 (continued).

					TEMP (K)	
			Tmin	Tmax	273.15	293.15
#	FORMULA	NAME	K	K	Pressure (Torr)	
109	Fr	FRANCIUM	267	879	1.99E-06	1.42E-05
110	Ga	GALLIUM	954	2517	3.20E-42	7.04E-39
111	GaCl3	GALLIUM TRICHLORIDE	350.9	694	4.57E-02	2.60E-01
112	Gd	GADOLINIUM	728	1770	7.52E-32	4.04E-29
113	Ge	GERMANIUM	1230	3125	1.50E-60	9.45E-56
114	GeBr4	GERMANIUM BROMIDE	316.45	462.15	2.72E-01	1.19E+00
115	GeCl4	GERMANIUM CHLORIDE	228.15	357.15	2.53E+01	7.12E+01
116	GeHCl3	TRICHLORO GERMANE	231.85	348.15	2.35E+01	7.32E+01
117	GeH4	GERMANE	107.26	308	1.75E+04	2.90E+04
118	Ge2H6	DIGERMANE	184.45	304.65	2.43E+02	5.14E+02
119	Ge3H8	TRIGERMANE	236.25	383.95	1.07E+01	2.97E+01
120	HBr	HYDROGEN BROMIDE	185.15	363.15	9.72E+03	1.63E+04
121	HCN	HYDROGEN CYANIDE	259.83	456.65	2.65E+02	6.12E+02
122	HCl	HYDROGEN CHLORIDE	158.97	324.65	1.92E+04	3.15E+04
123	HF	HYDROGEN FLUORIDE	189.79	461.15	3.61E+02	7.70E+02
124	HI	HYDROGEN IODIDE	222.38	423.85	2.85E+03	5.18E+03
125	HN03	NITRIC ACID	231.55	376.1	1.42E+01	4.79E+01
126	H2	HYDROGEN	13.95	33.18	6.52E+16	3.24E+18
127	H20	WATER	273.16	647.13	4.58E+00	1.75E+01
128	H202	HYDROGEN PEROXIDE	272.74	730.15	2.76E-01	1.37E+00
129	H2S	HYDROGEN SULFIDE	187.68	373.53	7.98E+03	1.38E+04
130	H2S04	SULFURIC ACID	283.15	603.15	2.41E-06	3.26E-05
131	H2S2	HYDROGEN DISULFIDE	229.95	337.15	2.76E+01	9.07E+01
132	H2Se	HYDROGEN SELENIDE	157.85	232.5	3.90E+03	6.24E+03
133	H2Te	HYDROGEN TELLURIDE	176.75	271.15	8.29E+02	1.56E+03
134	H3N03S	SULFAMIC ACID	293.15	373.15	4.05E-03	6.00E-03
135	He	HELIUM-3	1.01	3.31	INF	INF
136	He	HELIUM-4	1.76	5.2	1.12E+37	2.83E+39
137	Hf	HAFNIUM	2117	5960	1.46E-62	1.06E-59
138	Hg	MERCURY	234.31	1735	2.01E-04	1.28E-03
139	HgBr2	MERCURIC BROMIDE	409.65	592.15	2.64E+01	4.75E-01
140	HgCl2	MERCURIC CHLORIDE	409.35	577.15	5.50E-15	3.55E-10
141	HgI2	MERCURIC IODIDE	430.65	627.15	3.84E+11	1.07E+06
142	IF7	IODINE HEPTAFLUORIDE	186.15	277.15	6.20E+02	1.60E+03
143	I2	IODINE	242	819.15	3.80E-02	2.60E-01
144	In	INDIUM	850	2323	1.07E-41	7.28E-38
145	Ir	IRIDIUM	1944	4450	5.19E-68	1.40E-64
146	K	POTASSIUM	336.35	2223	6.29E-10	8.66E-09
147	KBr	POTASSIUM BROMIDE	1068.15	1656.15	2.50E-32	4.34E-29
148	KCl	POTASSIUM CHLORIDE	1044	3470	3.76E-28	1.14E-25
149	KF	POTASSIUM FLUORIDE	1158.15	1775.15	9.77E-37	3.75E-33
150	KI	POTASSIUM IODIDE	1018.15	1597.15	5.74E-30	6.58E-27
151	KOH	POTASSIUM HYDROXIDE	679	1600	7.01E-24	1.28E-21

Table B.2 (continued).

					TEMP (K)	
			Tmin	Tmax	273.15	293.15
#	FORMULA	NAME	K	K	Pressure (Torr)	
152	Kr	KRYPTON	115.78	209.35	1.98E+05	3.21E+05
153	La	LANTHANUM	1441.5	3643	9.25E-98	4.74E-89
154	Li	LITHIUM	453.69	4085	1.06E-22	1.25E-20
155	LiBr	LITHIUM BROMIDE	1021.15	1583.15	2.13E-28	1.40E-25
156	LiCi	LITHIUM CHLORIDE	1056.15	1655.15	3.03E-102	1.89E-87
157	LiF	LITHIUM FLUORIDE	1320.15	1954.15	1.37E-43	1.41E-39
158	Li	LITHIUM IODIDE	996.15	1444.15	1.07E-30	1.25E-27
159	Lu	LUTETIUM	1057	2535	4.89E-47	1.46E-43
160	Mg	MAGNESIUM	517	1376	4.47E-19	2.22E-17
161	MgCl2	MAGNESIUM CHLORIDE	1051.15	1691.15	1.80E-86	2.24E-74
162	MgO	MAGNESIUM OXIDE	3105	5950	1.76E-56	1.50E-52
163	Mn	MANGANESE	924	2392	3.45E-38	1.48E-35
164	MnCl2	MANGANESE CHLORIDE	1009.15	1463.15	2.81E-78	6.62E-67
165	Mo	MOLYBDENUM	1677	5100	2.16E-127	1.82E-117
166	MoF6	MOLYBDENUM FLUORIDE	207.65	309.15	1.58E+02	4.20E+02
167	Mo03	MOLYBDENUM OXIDE	1007.15	1424.15	2.39E-200	2.73E-171
168	NCl3	NITROGEN TRI CHLORIDE	246.15	367.15	3.77E+01	1.05E+02
169	ND3	HEAVY AMMONIA	199.15	239.75	3.15E+03	6.15E+03
170	NF3	NITROGEN TRIFLUORIDE	66.36	233.85	8.39E+04	1.25E+05
171	NH3	AMMONIA	195.41	405.65	3.22E+03	6.42E+03
172	NH30	HYDROXYLAMINE	306.25	383	9.10E-02	8.18E-01
173	NH4Br	AMMONIUM BROMIDE	471.45	669.15	5.93E-08	9.13E-07
174	NH4CI	AMMONIUM CHLORIDE	553.15	793.15	1.83E-08	2.45E-07
175	NH4I	AMMONIUM IODIDE	484.05	678.05	2.62E-08	3.94E-07
176	NH50	AMMONIUM HYDROXIDE	203.15	353.15	8.20E+02	1.80E+03
177	NH5S	AMMONIUM HYDROGENSULFIDE	222.05	306.45	9.92E+01	3.59E+02
178	NO	NITRIC OXIDE	109.5	180.15	1.13E+06	1.99E+06
179	NOCI	NITROSYL CHLORIDE	213.55	440.65	9.55E+02	2.03E+03
180	NOF	NITROSYL FLUORIDE	141.15	217.15	4.59E+03	5.32E+03
181	N02	NITROGEN DIOXIDE	261.95	431.35	2.63E+02	7.20E+02
182	N2	NITROGEN	63.15	126.1	3.08E+06	5.56E+06
183	N2F4	TETRAFLUOROHYDRAZINE	111.65	309.35	1.12E+04	1.89E+04
184	N2H4	HYDRAZINE	274.68	653.15	2.74E+00	1.06E+01
185	N2H4C	AMMONIUM CYANIDE	222.55	304.85	1.03E+02	3.86E+02
186	N2H6C02	AMMONIUM CARBAMATE	247.05	331.45	1.27E+01	6.25E+01
187	N20	NITROUS OXIDE	182.3	309.57	2.40E+04	3.85E+04

Table B.2 (continued).

					TEMP (K)	
			Tmin	Tmax	273.15	293.15
#	FORMULA	NAME	K	K	Pressure (Torr)	
188	N203	NITROGEN TRI OX IDE	170	425	6.85E+02	1.64E+03
189	N204	NITROGEN TETRAOXIDE	261.9	320.65	2.11E+02	5.28E+02
190	N205	NITROGEN PENTOXIDE	236.35	305.55	5.19E+01	2.88E+02
191	Na	SODIUM	370.97	2573	5.55E-13	1.26E-11
192	NaBr	SODIUM BROMIDE	1020	1720	9.89E-28	3.39E-25
193	NaCN	SODIUM CYANIDE	836.85	1769.1	4.27E-24	5.71E-22
194	NaCi	SODIUM CHLORIDE	1073.9	1738.1	5.05E-30	2.62E-27
195	NaF	SODIUM FLUORIDE	1269	2060	4.68E-34	3.60E-31
196	NaI	SODIUM IODIDE	1040.15	1577.15	2.07E-30	2.09E-27
197	NaOH	SODIUM HYDROXIDE	596	1830	9.90E-15	9.79E-14
198	Na2S04	SODIUM SULFATE	1173.1	1223.1	6.67E-50	4.65E-46
199	Nb	NIOBIUM	2250	5115	1.51E-116	1.51E-108
200	Nd	NEOOYMIUM	1144	3384	3.12E-63	1.35E-57
201	Ne	NEON	24.56	44.4	1.37E-05	1.63E-07
202	Ni	NICKEL	1061	2415	3.28E-52	2.99E-48
203	NiC404	NICKEL CARBONYL	250.15	315.65	1.33E+02	3.22E+02
204	NiF2	NICKEL FLUORIDE	1350.15	1556.15	2.38E-113	1.49E-100
205	Np	NEPTUNIUM	1617.99	2073.99	8.06E-88	1.23E-80
206	O2	OXYGEN	54.35	154.58	8.55E+05	1.31E+06
207	O3	OZONE	80.15	261	5.93E+04	1.04E+05
208	Os	OSMIUM	2234	4880	2.26E-80	1.63E-76
209	OsOF5	OSMIUM OXIDE PENTAFLUORIDE	304.8	330.9	3.89E-02	8.87E+00
210	OsO4	OSMIUM TETROXIDE - YELLOW	276.35	403.15	9.94E-01	5.64E+00
211	OsO4	OSMIUM TETROXIDE - WHITE	267.55	403.15	1.62E+00	6.98E+00
212	P	PHOSPHORUS - WHITE	404.15	590.15	1.52E-03	1.06E-02
213	PBr3	PHOSPHORUS TRIBROMIDE	280.95	448.45	5.82E-01	2.18E+00
214	PC12F3	PHOSPHORUS DI CHLORIDE TRIFLUORIDE	193.35	250.35	6.62E+02	1.41E+03
215	PC13	PHOSPHORUS TRI CHLORIDE	181.15	374.15	3.59E+01	9.62E+01
216	PC15	PHOSPHORUS PENTACHLORIDE	433.15	465	1.14E-02	1.36E-01
217	PH3	PHOSPHINE	139.37	324.75	1.68E+04	2.64E+04
218	PH4Br	PHOSPHONIUM BROMIDE	229.45	311.45	5.85E+01	2.42E+02
219	PH4CI	PHOSPHONIUM CHLORIDE	182.15	246.15	4.07E+03	1.11E+04
220	PH4I	PHOSPHONIUM IODIDE	247.95	335.45	1.09E+01	5.26E+01
221	POC13	PHOSPHORUS OXYCHLORIDE	274.33	378.65	8.90E+00	2.78E+01

Table B.2 (continued).

					TEMP (K)	
			Tmin	Tmax	273.15	293.15
#	FORMULA	NAME	K	K	Pressure (Torr)	
222	PSBr3	PHOSPHORUS THIOBROMIDE	323.15	448.15	9.71E-03	7.73E-02
223	PSC13	PHOSPHORUS THIOCHLORIDE	236.95	398.15	3.69E+00	1.24E+01
224	P406	PHOSPHORUS TRIOXIDE	312.85	446.25	4.70E-01	1.68E+00
225	P4010	PHOSPHORUS PENTOXIDE	693.15	758.15	2.22E-06	2.75E-05
226	P4S10	PHOSPHORUS PENTASULFIDE	561.15	1291	3.29E-09	5.35E-08
227	Pb	LEAD	708	2024	2.42E-28	5.46E-26
228	PbBr2	LEAD BROMIDE	786.15	1187.15	7.64E-14	4.12E-13
229	PbCl2	LEAD CHLORIDE	820.15	1227.15	2.37E-27	4.07E-24
230	PbF2	LEAD FLUORIDE	1134.15	1566.15	1.90E-73	6.75E-64
231	PbI2	LEAD IODIDE	752.15	1145.15	1.84E-55	4.42E-46
232	PbO	LEAD OXIDE	1216.15	1745.15	7.81E-12	2.85E-12
233	PbS	LEAD SULFIDE	1125.15	1554.15	4.14E+107	1.77E+89
234	Pd	PALLADIUM	1336	3385	3.56E-79	1.77E-72
235	Po	POLONIUM	448	1235	2.42E-18	4.16E-16
236	Pt	PLATINUM	1744	3980	2.46E-116	7.22E-107
237	Ra	RADIUM	593	1809	1.36E-24	2.95E-22
238	Rb	RUBIDIUM	310	978	1.49E-08	1.67E-07
239	RbBr	RUBIDIUM BROMIDE	1054.15	1625.15	3.46E-31	4.42E-28
240	RbCl	RUBIDIUM CHLORIDE	1065.15	1654.15	6.01E-33	1.30E-29
241	RbF	RUBIDIUM FLUORIDE	1194.15	1681.15	0.00E+00	0.00E+00
242	Rbl	RUBIDIUM IODIDE	1021.15	1577.15	2.05E-30	2.54E-27
243	Re	RHENIUM	2480	5915	6.25E-121	1.59E-112
244	Re207	RHENIUM HEPTOXIDE	485.65	635.55	INF	INF
245	Rh	RHODIUM	1735	3940	1.29E-94	6.71E-88
246	Rn	RADON	128.95	211.75	4.62E+03	6.41E+03
247	Ru	RUTHENIUM	2051	4500	1.32E-120	1.19E-111
248	RuF5	RUTHENIUM PENTAFLUORIDE	322.75	429.95	1.67E-03	1.49E-02
249	S	SULFUR	388.36	1313	1.38E-07	2.63E-06
250	SF4	SULFUR TETRAFLUORIDE	160.85	223.95	3.29E+03	5.68E+03
251	SF6	SULFUR HEXAFLUORIDE	223.15	318.69	9.68E+03	1.62E+04
252	SOBr2	THIONYL BROMIDE	266.45	412.65	1.58E+00	5.46E+00
253	SOC12	THIONYL CHLORIDE	172	372.15	3.63E+01	9.57E+01
254	SOF2	SULFUROUS OXYFLUORIDE	174.42	229.05	4.39E+03	7.61E+03
255	S02	SULFUR DIOXIDE	197.67	430.75	1.16E+03	2.52E+03
256	S02C12	SULFURYL CHLORIDE	222	545	4.03E+01	1.11E+02
257	S03	SULFUR TRIOXIDE	289.95	490.85	4.62E+01	1.93E+02

Table B.2 (continued).

					TEMP (K)	
			Tmin	Tmax	273.15	293.15
#	FORMULA	NAME	K	K	Pressure (Torr)	
258	S2C12	SULFUR MONOCHLORIDE	265.75	411.15	1.73E+00	6.55E+00
259	Sb	ANTIMONY	617	1898	8.62E-34	2.73E-30
260	SbBr3	ANTIMONY TRIBROMIDE	367.05	548.15	1.56E-03	8.26E-03
261	SbCl3	ANTIMONY TRICHLORIDE	346.55	794	2.97E-02	1.70E-01
262	SbCl5	ANTIMONY PENTACHLORIOE	295.85	387.25	1.85E-01	8.30E-01
263	SbH3	STIBINE	177.87	440.35	1.49E+03	2.83E+03
264	Sbl3	ANTIMONY TRIIODIDE	436.75	674.15	INF	INF
265	Sb203	ANTIMONY TRIOXIDE	847.15	1698.15	1.87E-169	3.29E-142
266	Sc	SCANDIUM	1110	2700	1.33E-23	8.78E-24
267	Se	SELENIUM	397	930	7.15E-20	1.95E-16
268	SeC14	SELENIUM TETRACHLORIDE	347.15	464.65	6.06E-04	6.68E-03
269	SeF6	SELENIUM HEXAFLUORIDE	154.55	227.35	8.50E+03	1.95E+04
270	SeOCl2	SELENIUM OXYCHLORIDE	307.95	441.15	6.97E-02	3.46E-01
271	Se02	SELENIUM DIOXIDE	430.15	590.15	1.83E-06	2.01E-05
272	Si	SILICON	1997.1	2560.1	3.27E-163	5.75E-148
273	SiBrCl2F	BROMODICHLOROFLUO ROSI LANE	186.65	474.3	2.24E+02	4.73E+02
274	SiBrF3	TRIFLUOROBROMOSILA NE	203.35	354.9	3.83E+03	7.07E+03
275	SiBr2ClF	DIBROMOCHLOROFLUO ROSI LANE	207.95	515.92	7.38E+01	1.79E+02
276	S1-CIF3	TRIFLUOROCHLOROSILA NE	129.15	308.83	1.06E+04	1.81E+04
277	SiCl2F2	DICHLORODIFLUOROSIL ANE	148.45	367.35	2.47E+03	4.65E+03
278	SiCl3F	TRICHLOROFLUOROSILA NE	180.55	434.85	4.71E+02	9.98E+02
279	SiC14	SILICON TETRACHLORIDE	204.3	507	7.61E+01	1.92E+02
280	SiF4	SILICON TETRAFLUORIDE	186.35	259	4.42E+04	9.37E+04
281	SiHBr3	TRIBROMOSILANE	242.65	617.5	8.11E+00	2.43E+01
282	SIHC13	TRICHLOROSILANE	144.95	479	2.16E+02	4.92E+02
283	SiHF3	TRIFLUOROSILANE	121.15	276.65	2.55E+04	4.70E+04
284	SiH2Br2	DIBROMOSILANE	212.25	559.24	5.15E+01	1.27E+02
285	S1H2C12	DICHLOROSILANE	151.15	449	5.48E+02	1.14E+03
286	S1H2F2	DIFLUOROSILANE	126.45	310.75	1.23E+04	2.01E+04
287	SiH2l2	DIIODOSILANE	276.95	683.81	4.35E+00	1.07E+01
288	SiH3Br	MONOBROMOSILANE	187.45	455.15	6.88E+02	1.40E+03

Table B.2 (continued).

					TEMP (K)	
			Tmin	Tmax	273.15	293.15
#	FORMULA	NAME	K	K	Pressure (Torr)	
289	S1H3CI	MONOCHLOROSILANE	155.35	396.79	2.30E+03	4.18E+03
290	Sl'H3F	MONOFLUOROSILANE	120.15	285.87	2.42E+04	3.83E+04
291	S1H3I	IODOSILANE	220.15	524.59	1.26E+02	2.95E+02
292	SiH4	SILANE	88.48	269.7	3.96E+04	6.51E+04
293	Si02	SILICON DIOXIDE	1883	2503.2	2.08E-44	1.10E-42
294	Si2Cl6	HEXACHLORODISILANE	277.15	412.15	7.51E-01	3.09E+00
295	Si2F6	HEXAFLUORODISILANE	192.15	254.25	3.13E+03	1.17E+04
296	SI2H5CI	DISILANYL CHLORIDE	226.95	291.15	1.45E+02	3.44E+02
297	Si2H6	DISILANE	143.85	432	1.25E+03	2.34E+03
298	Si20Cl3F3	TRICHLOROTRIFLUORODISILOXANE	235.15	316.35	1.23E+02	3.05E+02
299	Si20Cl6	HEXACHLORODISILOXANE	268.15	408.75	1.44E+00	5.79E+00
300	S120H6	DISILOXANE	160.65	257.75	1.39E+03	2.77E+03
301	S13C18	OCTACHLOROTRISILANE	319.45	484.55	3.93E-02	1.81E-01
302	Si3H8	TRISILANE	204.25	326.25	9.37E+01	2.25E+02
303	Si3H9N	TRISILAZANE	204.45	321.85	1.06E+02	2.60E+02
304	Si4H10	TETRASILANE	245.45	373.15	7.61E+00	2.53E+01
305	Sm	SAMARIUM	733	1874	7.30E-30	1.63E-27
306	Sn	TIN	1096	2995	1.46E-47	5.95E-44
307	SnBr4	STANNIC BROMIDE	331.45	477.85	1.17E-01	5.11E-01
308	SnCl2	STANNOUS CHLORIDE	589.15	896.15	1.98E-15	4.62E-13
309	SnCl4	STANNIC CHLORIDE	250.45	386.15	5.35E+00	1.81E+01
310	SnH4	STANNIC HYDRIDE	133.15	220.85	5.16E+03	8.97E+03
311	Snl4	STANNIC IODIDE	429.15	621.15	6.44E-04	3.37E-03
312	Sr	STRONTIUM	582	1630	2.99E-21	1.47E-19
313	SrO	STRONTIUM OXIDE	2341.15	2683.15	0.00E+00	0.00E+00
314	Ta	TANTALUM	2511	5565	1.49E-162	5.72E-150
315	Tc	TECHNETIUM	1660	5000	5.27E-74	2.15E-70
316	Te	TELLURIUM	497	1285	6.03E-22	1.17E-19
317	TeCl4	TELLURIUM TETRACHLORIDE	506.15	665.15	5.78E-09	2.30E-07
318	TeF6	TELLURIUM HEXAFLUORIDE	161.85	234.55	4.99E+03	1.08E+04
319	Ti	TITANIUM	1508	3442	3.40E-64	2.31E-60
320	Ti-Cl4	TITANIUM TETRACHLORIDE	249.05	638	2.73E+00	9.40E+00
321	Tl	THALLIUM	636	1745	3.73E-30	4.74E-27
322	TiBr	THALLOUS BROMIDE	763.15	1092.15	8.00E-16	5.51E-14
323	Til	THALLOUS IODIDE	713.15	1096.15	4.02E-18	5.99E-16
324	Tm	THULIUM	661	1237	8.42E-50	2.82E-44
325	U	URANIUM	1600	4135	6.85E-79	5.95E-73
326	UF6	URANIUM FLUORIDE	234.35	328.85	2.93E+01	1.11E+02
327	V	VANADIUM	1604	3665	4.39E-96	1.89E-88

Table B.2 (continued).

					TEMP (K)	
			Tmin	Tmax	273.15	293.15
#	FORMULA	NAME	K	K	Pressure (Torr)	
328	VC14	VANADIUM TETRACHLORIDE	247.45	697	1.81E+00	5.84E+00
329	VOC13	VANADIUM OXYTRI CHLORIDE	193.65	400	4.85E+00	1.50E+01
330	U	TUNGSTEN	2667	5645	7.02E-141	5.77E-131
331	WF6	TUNGSTEN FLUORIDE	201.55	290.45	3.46E+02	9.29E+02
332	Xe	XENON	161.36	289.74	3.10E+04	4.68E+04
333	Yb	YTTERBIUM	599	1660	8.46E-23	6.81E-21
334	Yt	YTTRIUM	1246	3055	1.07E-44	2.53E-42
335	Zn	ZINC	692.7	3170	1.78E-14	4.44E-13
336	ZnCl2	ZINC CHLORIDE	701.15	1005.15	7.11E-20	2.34E-17
337	ZnF2	ZINC FLUORIDE	1243.15	1770.15	INF	INF
338	ZnO	ZINC OXIDE	1773.1	2223.1	1.56E-48	1.37E-44
339	ZnS04	ZINC SULFATE	293.15	378.15	4.25E+00	1.52E+01
340	Zr	ZIRCONIUM	1975	4598	9.04E-126	1.08E-115
341	ZrBr4	ZIRCONIUM BROMIDE	480.15	630.15	2.73E-10	9.39E-09
342	ZrCl4	ZIRCONIUM CHLORIDE	463.15	604.15	5.44E-10	2.19E-08
343	ZrI4	ZIRCONIUM IODIDE	537.15	704.15	3.32E+98	5.98E+98

Table B.3 Compounds with Acceptable Temperatures and Vapor Pressures at 20°C (Yaws, 1995).

					TEMP (K)
			Tmin	Tmax	293.15
#	FORMULA	NAME	K	K	
21	At	ASTATINE	279	607	7.0E-06
109	Fr	FRANCIUM	267	879	1.4E-05
130	H2S04	SULFURIC ACID	283.15	603.15	3.3E-05
138	Hg	MERCURY	234.31	1735	1.3E-03
134	H3N03S	SULFAMIC ACID	293.15	373.15	6.0E-03
143	I2	IODINE	242	819.15	2.6E-01
128	H202	HYDROGEN PEROXIDE	272.74	730.15	1.37
64	C3S2	CARBON SUBSULFIDE	287.15	403.95	1.48
28	BH303	BORIC ACID	293.15	401.15	1.94
213	PBr3	PHOSPHORUS TRIBROMIDE	280.95	448.45	2.18
77	CIH03S	CHLOROSULFONIC ACID	193.15	700	2.32
294	Si2Cl6	HEXACHLORODISILANE	277.15	412.15	3.09
39	BeB2H8	BERYLLIUM BOROHYDRIDE	274.15	363.15	5.18
252	SOBr2	THIONYL BROMIDE	266.45	412.65	5.46
210	OsO4	OSMIUM TETROXIDE - YELLOW	276.35	403.15	5.64
299	Si20Cl6	HEXACHLORODISILOXANE	268.15	408.75	5.79
328	VC14	VANADIUM TETRACHLORIDE	247.45	697	5.84
258	S2C12	SULFUR MONOCHLORIDE	265.75	411.15	6.55
211	OsO4	OSMIUM TETROXIDE - WHITE	267.55	403.15	6.98
15	AsCl3	ARSENIC TRICHLORIDE	261.75	403.55	8.27
320	Ti-Cl4	TITANIUM TETRACHLORIDE	249.05	638	9.40

Table B.4 Compounds with Acceptable Temperatures and Vapor Pressures at 0°C (Yaws, 1995).

			Tmin	Tmax	TEMP (K)
#	FORMULA	NAME	K	K	273.15
109	Fr	FRANCIUM	267	879	1.99E-06
138	Hg	MERCURY	234.31	1735	2.01E-04
143	I2	IODINE	242	819.15	3.80E-02
128	H202	HYDROGEN PEROXIDE	272.74	730.15	2.76E-01
77	CIH03S	CHLOROSULFONIC ACID	193.15	700	5.31E-01
294	Si2Cl6	HEXACHLORODISILANE	277.15	412.15	7.51E-01
39	BeB2H8	BERYLLIUM BOROHYDRIDE	274.15	363.15	9.01E-01
210	OsO4	OSMIUM TETROXIDE - YELLOW	276.35	403.15	9.94E-01
299	Si20Cl6	HEXACHLORODISILOXANE	268.15	408.75	1.44E+00
252	SOBr2	THIONYL BROMIDE	266.45	412.65	1.58E+00
211	OsO4	OSMIUM TETROXIDE - WHITE	267.55	403.15	1.62E+00
258	S2C12	SULFUR MONOCHLORIDE	265.75	411.15	1.73E+00
328	VC14	VANADIUM TETRACHLORIDE	247.45	697	1.81E+00
15	AsCl3	ARSENIC TRICHLORIDE	261.75	403.55	2.30E+00
320	Ti-Cl4	TITANIUM TETRACHLORIDE	249.05	638	2.73E+00
184	N2H4	HYDRAZINE	274.68	653.15	2.74E+00
223	PSC13	PHOSPHORUS THIOCHLORIDE	236.95	398.15	3.69E+00
101	D20	DEUTERIUM OXIDE	276.97	643.89	3.81E+00
88	Cr02Cl2	CHROMIUM OXYCHLORIDE	254.75	390.25	4.07E+00
287	SiH2l2	DIIODOSILANE	276.95	683.81	4.35E+00
59	COSe	CARBON OXYSELENIDE	156.05	251.25	1.89E+03
127	H20	WATER	273.16	647.13	4.58E+00
329	VOC13	VANADIUM OXYTRI CHLORIDE	193.65	400	4.85E+00
309	SnCl4	STANNIC CHLORIDE	250.45	386.15	5.35E+00
63	C2N2	CYANOGEN	177.35	252.15	1.66E+03
106	FeC505	IRON PENTACARBONYL	266.65	378.15	7.39E+00
304	Si4H10	TETRASILANE	245.45	373.15	7.61E+00
281	SiHBr3	TRIBROMOSILANE	242.65	617.5	8.11E+00
221	POC13	PHOSPHORUS OXYCHLORIDE	274.33	378.65	8.90E+00

APPENDIX C

MATLAB CODE FOR IMAGE PROCESSING

C.1 DropComparison.m - M File Controlling Image Manipulation and Data Recording

```
clear all;
close all;
clc;
PicNum=input('Enter total number of droplet pictures for comparison.');
Scale
VOLUME=zeros(PicNum,1);
MAJAXIS=zeros(size(VOLUME));
MINAXIS=zeros(size(VOLUME));
SOLID=zeros(size(VOLUME));
ECCEN=zeros(size(VOLUME));
ORIENT=zeros(size(VOLUME));
ACCURATE=zeros(size(VOLUME));
THRESHOLD=zeros(size(VOLUME));
for t=1:PicNum;
   Edgefind;
   FillUp;
   Reduce;
   DropStats;
   VolumeCalc;
   t
   Volume
   disp('Review all file names and pictures to ensure accuracy.')
   disp('Are all filenames accurate and pictures filled.');
   Quest=input('Type 1 for yes, 2 for inaccurate file name, or 3 for poor fill.');
   ACCURATE(t,1)=Quest;
   MAJAXIS(t,1)=Majaxis;
   MINAXIS(t,1)=Minaxis;
   SOLID(t,1)=Solid;
   ECCEN(t,1)=Eccen;
   ORIENT(t,1)=Orient;
   VOLUME(t,1)=Volume;
   THRESHOLD(t,1)=THRESH;
```

```
end
AVG=sum(VOLUME)/PicNum;
STDDEV=std(VOLUME);
disp('Total # of samples')
disp(PicNum);
disp('   ');
disp('AVG Volume');
disp(AVG);
disp('   ');
disp('Standard Deviation');
disp(STDDEV);
```

C.2 Scale.m – M file Used to Determine Image Scale in Inches Per Pixel

```
Image=input('Type file name for desired scale image. (Format is 14JanLOC2.bmp):','s');
ScaleA=imread(Image);
imshow(ScaleA);
THRESH=.2;
Logic=0;
while Logic==0;
   ScaleB=edge(ScaleA,'canny',THRESH);
   figure, imshow(ScaleB);
   title(['Edge of ',num2str(Image)]);
   disp('Does a good scale edge show?');
   Logic=input('Type 1 for yes and 0 for no:');
   if Logic==0;
      THRESH=input('Enter value to increase threshold:')+THRESH;
      THRESH;
      disp('THRESH=');
      disp(THRESH);
   end
   if Logic~=1 & Logic~=0;
      disp('Incorrect entry');
      Logic=0;
   end
end
fscale=input('Enter value to erase below');
Logic=0;
while Logic==0;
   ScaleC=ScaleB;
   for j=fscale:200;
      ScaleC(j,:)=0;
   end
   figure, imshow(ScaleC);
   disp('Was erase conducted properly?');
   Logic=input('Type 1 for yes and 0 for no:');
```

```
    if Logic==0;
        fscale=input('Enter value to change erase line:')+fscale;
        disp('Erase below pixal #=');
        disp(fscale);
    end
    if Logic~=1 & Logic~=0;
        disp('Incorrect entry');
        Logic=0;
    end
end
[ScaleCj,ScaleCi]=find(ScaleC);
ScaleC(fscale-1,:)
PixNum=input('Enter number of pixels for scale calculation.');
Len=input('Enter length of scale image in mm.')*0.0393701;
SCALE=Len/PixNum;
disp('Image scale (in/pixal) =');
disp(SCALE);
close all;
clc;
```

C.3 Edgefind.m M File Used to Find Droplet Edges

```
clear B*;
clear I*;
clear L*;
clear a*;
clear f*;
close all;
clc;
Image=input('Type file name for desired droplet image. (Format is
14Jan#10000000.bmp):','s');
A=imread(Image);
imshow(A);
title([num2str(Image)]);
THRESH=.3;
disp('THRESH=');
disp(THRESH);
Logic=0;
while Logic==0;
    B=edge(A,'canny',THRESH);
    figure, imshow(B);
    title(['Edge of ',num2str(Image)]);
    disp('Does a complete circle/ellipse show?');
    Logic=input('Type 1 for yes and 0 for no:');
    if Logic==0;
        THRESH=input('Enter value to increase threshold:')+THRESH;
```

```
        THRESH;
        disp('THRESH=');
        disp(THRESH);
    end
    if Logic~=1 & Logic~=0;
        disp('Incorrect entry');
        Logic=0;
    end
end
imshow (B);
title(['Edge of ',num2str(Image)]);
[Bj,Bi]=find(B);
filename=input('Type filename for saving edge picture. (Format is
14Jan#1Edge.bmp):','s');
saveas(gcf,filename)
```

C.4 FillUp.m - M File Used to Fill In Center of Droplet

```
Quest=0;
while Quest==0;
    Bf=B;
    minj=min(Bj);
    maxj=max(Bj);
    mini=min(Bi);
    maxi=max(Bi);
    for j=minj:maxj;
        first=1;
        last=644;
        mark=1;
        for i=mini:maxi;
            if B(j,i)>0 & mark==1;
                first=i;
                mark=2;
            end
        end
        for i=mini:maxi;
            if B(j,i)>0;
                last=i;
            end
        end
        for i=first:last;
            Bf(j,i)=1;
        end
    end
    figure, imshow(Bf);
    disp('Was the circle/ellipse properly filled in?');
```

```
    Quest2=input('Type 1 for yes and 0 for no:');
    if Quest2==0;
        Bf=B;
        disp('Confirm complete circle/ellipse in B. Make any necessary changes to B.');
        figure, imshow(Bf);
        CORRECT=input('Input number of X corrections to make.');
        if CORRECT~=0;
            for R=1:CORRECT;
                LowX=input('Input pixel number of lower X limit.');
                HighX=input('Input pixel number of upper X limit.');
                R
                for r=LowX:HighX;
                    B(:,r)=0;
                end
            end
        end
        CORRECT=input('Input number of Y corrections to make.');
        if CORRECT~=0;
            for R=1:CORRECT;
                LowY=input('Input pixel number of lower X limit.');
                HighY=input('Input pixel number of upper X limit.');
                R
                for r=LowY:HighY;
                    B(r,:)=0;
                    R
                end
            end
        end
        [Bj,Bi]=find(B);
        figure, imshow(B);
    end
    if Quest2==1;
        Quest=Quest2;
    end
end
```

C.5 Reduce.m - M File Used to Remove Extraneous Portions of Image

```
jtot=maxj-minj+1;
itot=maxi-mini+1;
Bfill=zeros(jtot,itot);
for j2=1:jtot;
    for i2=1:itot;
        Bfill(j2,i2)=Bf(j2+minj-1,i2+mini-1);
    end
end
```

```
figure, imshow(Bfill);
filename=input('Type filename for saving fill picture. (Format is 14Jan#1Fill.bmp):','s');
saveas(gcf,filename)
```

C.6 DropStats.m - M File Used to Determine Filled Area Properties

```
Bfillstats = bwlabel(Bfill);
Bstats = regionprops(Bfillstats,'all');
Majaxis=Bstats.MajorAxisLength;
Minaxis=Bstats.MinorAxisLength;
Solid=Bstats.Solidity;
Eccen=Bstats.Eccentricity;
Orient=Bstats.Orientation;
Orient2=abs(Orient);
```

C.7 VolumeCalc.m - M File Used to Determine Droplet Rotation and Resulting Volume

```
clear Volume;
CorrectRotate=0;
if Orient2 <= 10;
   Volume=(pi*(Minaxis*SCALE)^2*Majaxis*SCALE)/6;
   CorrectRotate=1;
elseif Orient2 >= 80;
      Volume=(pi*(Majaxis*SCALE)^2*Minaxis*SCALE)/6;
      CorrectRotate=1;
else
    while CorrectRotate==0
       disp('Determine if the ellipse should be rotated about the major or minor axis.');
       disp('If the droplet is streched lengthwise rotate about the minor axis.');
       disp('       (ie minor axis = x&z dimensions / major axis = y dimension)');
       disp('If the droplet is compressed lengthwise rotate about the major axis.');
       disp('         (ie major axis = x&z dimensions / minor axis = y dimension)');
       disp('         ');
       rotate=input('For major axis rotation type 1, for minor axis rotation type 2.');
       if rotate==1;
          Volume=(pi*(Majaxis*SCALE)^2*Minaxis*SCALE)/6;
          CorrectRotate=1;
       elseif rotate==2;
             Volume=(pi*(Minaxis*SCALE)^2*Majaxis*SCALE)/6;
             CorrectRotate=1;
       elseif rotate~=1 & rotate~=2;
             disp('Incorrect Entry')
       end
    end
 end
```

APPENDIX D

ERROR ANALYSIS

This appendix will cover the details of the error analysis. There were three portions of the error analysis: bias error due to the scale determination for each test, random error, and total error generated by a combination of these two sources. The uncertainty of an indirect measurement y, dependent on N independent measurements x_i, is defined in Equation D.1. The uncertainty associated with an indirect measurement is analogous to the standard deviation of a statistical population.

$$U^2 = \sum_{i=1}^{N} \left(\frac{\partial y}{\partial x_i} U_i \right)^2 \tag{D.1}$$

D.1 Scale Bias Error

The scale rod was graduated in 1mm increments and the error in these increments was estimated to be $\pm$ 0.1mm using a digital caliper that measured to the nearest 0.01mm. The pixel count (C) from each scale image is determined by finding the centerline of the two outside lines in the scale image and calculating the difference between the two. The scale (S) is simply the overall length (L) divided by the pixel count (C). The centerlines in the image Loc2-14Jan.bmp (the scale image for all droplet generation tests - Figure D.1) were analyzed to determine the variation in the centerline pixel locations (Table D.1 and Table D.2). From these variations the error in the pixel length for scale calculations was

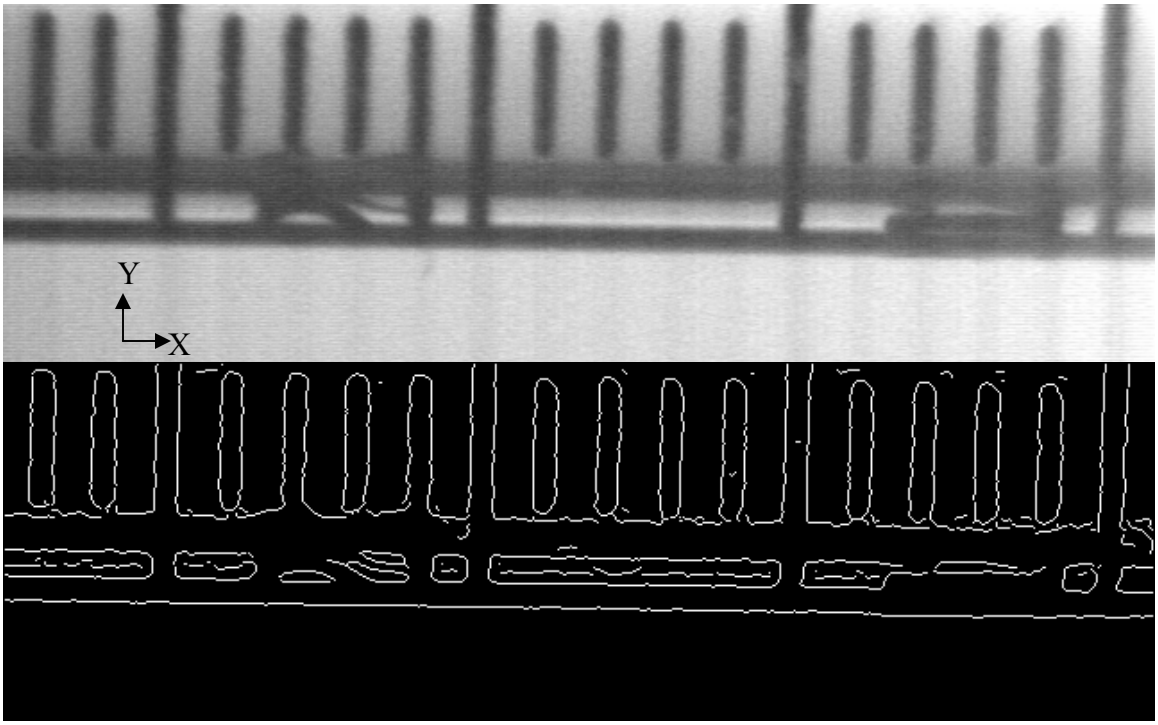

Figure D.1 Scale Image Used to Determine Pixel Count (C) Uncertainty. Bottom Shows Edge of Figure Generated by Scale.m.

Table D.1 Sample of Centerline Analysis.

X Pixel	Y Pixel	Centerline X Pixel
17	9	23
29	9	
17	10	23
29	10	
17	11	23.5
30	11	
17	12	23
29	12	
17	13	23
29	13	
17	14	23
29	14	
17	15	23
29	15	
17	16	23.5
30	16	

Statistical Results from Excel Data Analysis	
Mean	23.1346
Median	23
Mode	23
Standard Deviation	0.362
Minimum	22.5
Maximum	23.5
Range	1
Count	26

Table D.2 Summary of Centerline Analysis.

Line #	Minimum	Maximum	Standard Deviation	Range
1	22.5	23.5	0.362	1.0
2	56.5	58.0	0.550	1.5
3	92.5	93.5	0.280	1.0
4	128.0	129.5	0.301	1.5
5	163.5	166.0	0.599	2.5
6	198.5	199.5	0.289	1.0
7	233.0	235.0	0.467	2.0
8	269.0	270.0	0.298	1.0
9	303.0	305.0	0.550	2.0
10	339.5	340.5	0.286	1.0
11	373.5	375.0	0.429	1.5
12	409.0	410.0	0.270	1.0
13	444.5	446.0	0.491	1.5
14	480.0	481.0	0.300	1.0
15	515.5	516.5	0.267	1.0
16	550.5	552.0	0.528	1.5
17	585.5	587.0	0.576	1.5
18	621.5	623.5	0.619	2.0

determined to be 1.2 pixels, the largest standard deviation in the centerlines multiplied by 2. The scale bias error (U_S) was determined using the formula in equation D.2. Equation D.3 shows the formula that was utilized for calculating volume based on average values of the major axis length (Maj), minor axis length (Min), and scale (S); this formula uses the standard equation for the volume of an ellipsoid and is adjusted to account for rotations about the major and minor axis. The scale bias errors were then used to determine a volumetric bias error (U_{Vb}) using equation D.4; no bias error is associated with the major and minor axis lengths therefore only one term is present. Table D.3 shows the calculated scale and volumetric bias errors.

$$U_s^{\,2} = \left(\frac{\partial S}{\partial C} * U_C\right)^2 + \left(\frac{\partial S}{\partial L} * U_L\right)^2 = \left(\frac{-L}{C^2} * 1.2\right)^2 + \left(\frac{1}{C} * 0.1\right)^2 \tag{D.2}$$

$$V = \frac{\pi S^3}{6}\left(\begin{pmatrix} Fraction \\ Rotated \\ About\,Major \end{pmatrix}\left(Maj^2 Min\right) + \begin{pmatrix} Fraction \\ Rotated \\ About\,Minor \end{pmatrix}\left(Min^2 Maj\right)\right) \tag{D.3}$$

$$U_{Vb}^{\,2} = \left(\frac{\partial V}{\partial S} * U_S\right)^2 \tag{D.4}$$

$$= \left[\frac{\pi S^2}{2}\left(\begin{pmatrix} Fraction \\ Rotated \\ About\,Major \end{pmatrix}\left(Maj^2 Min\right) + \begin{pmatrix} Fraction \\ Rotated \\ About\,Minor \end{pmatrix}\left(Min^2 Maj\right)\right) * U_S\right]^2$$

Table D.3 Scale and Volumetric Bias Errors.

	Length		**Pixels**	**Scale**	**Scale U_b**		**Volume U_b**
Trial	**mm**	**in**	**#**	**in/pixel**	**mm/pixel**	**in/pixel**	**in^3**
ATM	17	0.669	598	1.13E-03	1.8E-04	7.0E-06	2.2E-05
300							2.2E-05
75							2.2E-05
20-50							2.2E-05
Degas	18	0.709	598	1.19E-03	1.8E-04	7.0E-06	2.1E-05
Top	29	1.142	525.5	2.17E-03	2.3E-04	9.1E-06	1.6E-05
Bot	30	1.181	543	2.18E-03	2.2E-04	8.8E-06	1.5E-05

D.2 Volumetric Random Error

The random error (U_a) was calculated by using a multiplier of 2 on the standard deviations of the volume values. A second manner for determining random error is to utilize the standard deviation in the major and minor axis lengths and calculate the propagated error in volume (U_{Va}). The propagated error in volume was calculated using equation D.5. Table D.4 compares the two different values for volumetric random error;

further calculations were conducted using the random error generated by the standard deviations in volume.

$$U_{Va}{}^{2} = \left(\frac{\partial V}{\partial Maj} * U_{Maj}\right)^{2} + \left(\frac{\partial V}{\partial Min} * U_{Min}\right)^{2} \tag{D.5}$$

$$= \left[\frac{\pi S^{3}}{6}\left(2 * \begin{pmatrix} Fraction \\ Rotated \\ About\,Major \end{pmatrix}(Maj * Min) + \begin{pmatrix} Fraction \\ Rotated \\ About\,Minor \end{pmatrix}(Min^{2})\right) * U_{Maj}\right]^{2} +$$

$$\left[\frac{\pi S^{3}}{6}\left(\begin{pmatrix} Fraction \\ Rotated \\ About\,Major \end{pmatrix}(Maj^{2}) + 2 * \begin{pmatrix} Fraction \\ Rotated \\ About\,Minor \end{pmatrix}(Maj * Min)\right) * U_{Min}\right]^{2}$$

Table D.4 Volumetric Random Error Comparison.

	MAJ Axis	**MAJ Axis 2*STD Dev**	**MIN Axis**	**MIN Axis 2*STD Dev**	**Average Volume**	**Volume U_a (2*STD Dev)**	**Volume U_{Va} (Propagated)**
Trial	**Pixels**	**Pixels**	**Pixels**	**Pixels**	**in^3**	**in^3**	**in^3**
ATM	120.1	4.25	110.2	7.52	1.19E-03	3.0E-05	7.7E-05
300	120.3	4.34	110.4	6.90	1.20E-03	2.7E-05	7.9E-05
75	119.9	2.80	110.8	5.56	1.19E-03	3.7E-05	5.1E-05
20-50	119.7	5.51	113.4	6.79	1.20E-03	1.6E-04	1.0E-04
Degas	114.2	3.44	105.8	6.53	1.19E-03	4.8E-05	6.5E-05
Top	65.12	3.53	59.57	1.35	1.27E-03	7.0E-05	1.3E-04
Bot	63.72	2.82	59.14	2.44	1.23E-03	4.7E-05	1.0E-04

D.3 Volumetric Total Error

The total error was determined using equation D.6; this is a combination of the volumetric bias error (U_{Vb}) and the random error measured by the standard deviation in volume multiplied by 2 (U_a). Table D.5 shows the results of these calculations.

$$U_{Total}{}^{2} = (U_{Vb})^{2} + (U_{a})^{2} \tag{D.6}$$

Table D.5 Total Volumetric Error.

	Average Volume	Volume U_b	Volume U_a (2*STD Dev)	Volume U_{Tot}	Total Percent Error
Trial	**in^3**	**in^3**	**in^3**	**in^3**	**%**
ATM	1.19E-03	2.2E-05	3.0E-05	3.7E-05	3.1
300	1.20E-03	2.2E-05	2.7E-05	3.5E-05	2.9
75	1.19E-03	2.2E-05	3.7E-05	4.3E-05	3.6
20-50	1.20E-03	2.2E-05	1.6E-04	1.6E-04	13.1
Degas	1.19E-03	2.1E-05	4.8E-05	5.2E-05	4.4
Top	1.27E-03	1.6E-05	7.0E-05	7.2E-05	5.6
Bot	1.23E-03	1.5E-05	4.7E-05	4.9E-05	4.0

REFERENCES

Abdel-Khalik, S. I. and Hunter, T. O., Assessment of surface heating problems in laser fusion reactors, ASME J. Heat Transfer 100 (1978) 311-318.

Abdelall, F. F., "Experimental and numerical studies of the Rayleigh-Taylor instability for bounded liquid films with injection through the boundary," Ph.D. thesis, California Institute of Technology.

Abdou, M. A., et al. Critical technical issues and evaluation and comparison studies for inertial fusion energy reactors, Fusion Engineering and Design, 23, (1993) 251-297.

Abdou, M.A., Ying, A., Morley, N., Gulec, K., Smolentsev, S., Kotschenreuther, M., Malang, S., Zinkle, S., Rognlien, T., Fogarty, P., Nelson, R., Nygren, R., McCarthy, K., Youssef, M.Z., Ghoniem, N., Sze, D., Wong, C., Sawan, M., Khater, H., Woolley, R., Mattas, R., Moir, R., Sharafat, S., Brooks, J., Hassanein, A., Petti, D., Tillack, M., Ulrickson, and M., Uchimoto, T., 2001, "On the exploration of innovative concepts for fusion chamber technology," *Fusion Eng. and Des.*, 54, 181-247.

Battelle, UT, LLC, 2005, http://www.sns.gov/aboutsns/what-why.htm, UT-Battelle LLC

Brow, S.C., 2005, http://www.absoluteastronomy.com/encyclopedia/L/La/Langmuir_probe.htm, Absolute Astronomy .com Inc.

Booth, L. A., Compiler, Central station power generation by laser-driven fusion, LA-4858-MS, Los Alamos Scientific Laboratory report (1972).

Bourham, Mohamed, 31 Aug 2004, Personal Interview, North Carolina State University, Raleigh, NC.

Bourque, R.F., Meier, W.R., and Monsler, M.J., 1992 "Overview of the OSIRIS IFE reactor conceptual design," *Fusion Technol*., 21, 1465-1469.

Bova, Ben, 1971, "Fourth State of Matter; Plasma Dynamics and Tomorrow's Technology", New York, St. Martin's Press

Burke, R.J. and Cutting, J.C., 1974, "Direct conversion of neutron energy and other advantages of a large yield per pulse, inertial-confinement fusion reactor," *J. of the*

Electromechanical Soc., 1st Topical Meeting on the Technology of Controlled Nucl. Fusion, 53-62.

Durbin, S.G., 2005, "Dynamics and free-surface geometry of turbulent liquid sheets," Ph.D. thesis, California Institute of Technology.

Eberl, K., 2004, http://www.mbe-components.com/applications/vap_data.html, MBE-Komponenten GmbH

Edmund Optics Inc, 2005, http://www.edmundoptics.com/onlinecatalog/browse.cfm, Edmund Optics Inc.

Fogt, R., 1997-2002, http://www.onlineconversion.com, BlueSparks Network

Fußmann, G., 2005, http://plasma.physik.hu-berlin.de/psi/equipment/sonden.html, Institut für Physik der Humboldt-Universität zu Berlin, Lehrstuhl für Experimentelle Plasmaphysik

Hassanein, A., and Abdel-Khalik, S. I., Interaction of target debris with liquid film-protected first walls, Presented at ARIES project Meeting, San Diego, CA (January 2002).

HIBALL-A conceptual heavy ion beam driven fusion reactor study preliminary report, University of Wisconsin Report, UWFDM -450, June 1981.

House, P.A., 1999, "Beamline and first vessel wall shielding in HYLIFE-II," UCID-136107, Lawrence Livermore National Laboratory.

Koehler, T. P., 2004, "Quantification of initial conditions in turbulent liquid sheets using laser-doppler velocimetry," Master's thesis, Georgia Institute of Technology.

Konkashbaev, I., Hassanein, A., and Abdel-Khalik, S., 2003, Single droplet dynamics in vapor clouds, Argonne National laboratory and Georgia Institute of Technology.

Kulcinski, G. L., Peterson, R. R., Wittenberg, L. J., Mogahed, E. A., and Sviatoslavsky, I. N., Dry wall issues for the SOMBRERO laser fusion power plant, Fusion Engineering and Design 60 (2002) 3-15.

Latkowski, J.F. and Meier, W.R., 2001, "Heavy-ion fusion final focus magnet shielding designs", *Fusion Technol*., 39, 798-803.

Maniscalco, J.A. and Meier, W.R., 1977, "Liquid lithium 'waterfall' inertial confinement fusion reactor concept," *Transactions of the American Nuclear Society*, 26, 62-63.

Max-Planck-Institut für Plasmaphysik, http://www.ipp.mpg.de/de/for/bereiche/diagnostik/psiequipment/sonden.html/

Moir, R.W., Adamson, M.G., Bangerter, R.O., Bieri, R.L., Condit, R.H., Hartman, C.W., House, P.A., Langdon, A.B., Logan, B.G., Orth, C.D., Petzoldt, R.W., Pitts, J.H., Post, J.H., Sacks, R.F., Tobin, M.T., Williams, W.H., Dolan, T.J., Longhurst, G.R., Hoffman, M.A., Schrock, V.E., Peterson, P.F., Bai, R.Y., Chen, X.M., Liu, J., Sze, D.K., and Meier, W.R., 1991, "HYLIFE-II progress report," UCID-21816, Lawrence Livermore National Laboratory.

Moir, R.W., 1992, "HYLIFE-II inertial fusion energy power plant design," *Fusion Technol*., 21, 1475-1486.

Moir, R.W., Bieri, R.L., Chen, X.M., Dolan, T.J., Hoffman, M.A., House P.A., Leber R.L., Lee, J.D., Lee, Y.T., Liu, J.C., Longhurst, G.R.,Meier, W.R., Peterson, R.F., Petzoldt, R.W., Schrock, V. E., Tobin, M.T., and Williams, W.H., 1994, "HYLIFE-II: a molten-salt inertial fusion energy power plant design- final report," *Fusion Technol.*, 25, 5-25.

Moir, R.W., 1995, "The High-Yield Lithium-Injection Fusion-Energy (HYLIFE)-II inertial fusion energy (IFE) power plant concept and implications for IFE." *Phys. Plasmas*, 2, 2447-2452.

Moir, R.W., 1997, "Liquid first walls for magnetic fusion energy configurations," *Nucl. Fusion*, 37, 557.

Mollendorff, U. von, and Tobin, M. T., Conceptual design considerations for the reaction chamber of a heavy ion driven inertial fusion test facility, Forschungszentrum Karlsruhe, Technik und Umwelt, INR 1945 (July 1996).

Monsler, M., Maniscalco, J., Blink, J., Meier, W., and Walker, P., 1978, "Electric power from laser fusion: the HYLIFE concept*," Proc. 13th Intersociety Energy Conversion Engineering Conf*., San Diego, California, August 20-25; see also UCRL-1259, Lawrence Livermore National Laboratory.

Nave, C. R., 2005, http://hyperphysics.phy-astr.gsu.edu/hbase/kinetic/watvap.html, Department of Physics and Astronomy, Georgia State University

Osirus and Sombrero Inertial Fusion Power Plant Designs, Final Report, WJSA 9201, DOE/ER/54100-1, March 1992.

Peterson, R. R., Response of national ignition facility first wall materials to target x-rays and debris, Fusion Technology 30 (1996) 778.

Peterson, R. R., Haynes, D. A., Jr., Golovkin, I. E., and Moses, G. A., Inertial fusion energy target output and chamber response: calculations and experiments, Physics of Plasmas, 9 (2002) 2287-2292.

Peterson, P. F., and Scott, J. M., The mini-chamber, an advanced protection concept for NIF, Fusion Technology 30 (1996) 442-447.

Raffray, A. R., Haynes, D. A., Peterson, R. R., Tillack, M. S., Wang, X., and Zaghlool, M., Dry chamber wall thermo-mechanical behavior and lifetime under IFE cyclic energy deposition, IFSA-2, Kyoto (2001).

Raffray, A. R., Haynes, D. A., and Najmabadi, F., IFE chamber walls: requirements, design options, and synergy with MFE plasma facing components, Presented at PSI-15 Meeting, Gifu, Japan (2002); submitted for publication in Journal of Nuclear materials.

Renk, T. J., Olson, C. L., Tanaka, T. J., Ulrickson, M. A., Rochan, G. A., Peterson, R. R., Golovkin, I. E., Thompson, M. O., Knowles, T. R., Raffray, A. R., and Tillack, M. S., IFE chamber dry wall materials response to pulsed x-rays and ions at power-plant level fluences, Fusion Engineering and Design, volume 65, issue 3, April 2003.

Seifritz, W. and Naegele, H., 1975, "Uranium and thorium shells serving as tampers of D-T fuel pellets for electron-beam-induced fusion approach," *Trans. Am. Nucl. Soc*., 21, 18.

Smirnov, Boris M., 2001, "Physics of Ionized Gases", New York, NY, John Wiley and Sons.

Spitzer, Lyman, 1962, "Physics of Fully Ionized Gases.", New York, NY, Interscience Publishing Inc.

Varian Associates Inc., 1992, "Basic Vacuum Practice", Lexington, MA, Varian Associates, Inc.

Waganer, L. M., et al. Inertial fusion energy reactor design studies, McDonnell Douglas Report, DOE/ER-41 0 1, MDC 92EOO08, Volume III (March 1992).

Waganer, L. M., Innovation leads the way to attractive inertial fusion energy reactors - Prometheus-L and Prometheus-H, Fusion Engineering and Design, 25, (1994) 125-143.

Williams, J. M., et al., A conceptual laser controlled thermonuclear reactor power plant, Proceedings First Topical Meeting Technology of Controlled Fusion, San Diego, CA (1974).

Yaws, Carl L., 1995, "Handbook of Vapor Pressure", Volume 4, Houston, Gulf Publishing Co.